# Theoretical Studies on Catalytic Bond Activation

Gerben Theodoor de Jong

# Theoretical Studies on Catalytic Bond Activation

ISBN 9789086590872

VRIJE UNIVERSITEIT

# Theoretical Studies on Catalytic Bond Activation

ACADEMISCH PROEFSCHRIFT

ter verkrijging van de graad Doctor aan
de Vrije Universiteit Amsterdam,
op gezag van de rector magnificus
prof.dr. L.M. Bouter,
in het openbaar te verdedigen
ten overstaan van de promotiecommissie
van de faculteit der Exacte Wetenschappen
op dinsdag 24 april 2007 om 13.45 uur
in de aula van de universiteit,
De Boelelaan 1105

door

Gerben Theodoor de Jong

geboren te Sneek

| | |
|---|---|
| promotor: | prof.dr. E.J. Baerends |
| copromotor: | dr. F.M. Bickelhaupt |

*Foar Heit en Mem*
*Für Wiebke*

# Contents

# 1 General introduction

Chemistry is the science of changing matter. From the beginning of time, mankind has used the empirical knowledge arising from chemical experience to shape its environment and to develop its culture. Since the scientific revolutions in modern time, chemistry has evolved into a science in which not only empirical knowledge, but also mechanistic understanding plays a defining role. The development of quantum chemistry in the twentieth century made it possible to understand chemical reactions at a molecular and atomic level. At present, with the use of state-of-the-art computational facilities and advanced computer-code packages, it is possible to calculate enormous amounts of data. Important goals in the field of theoretical chemistry, therefore, are: (i) the critical evaluation of these data, (ii) the understanding of these data, (iii) and, perhaps most importantly, the offering of insights leading to new practical knowledge.

This thesis concentrates on the subject of catalysis, in particular homogeneous catalysis, which is of prime importance in synthetic organic chemistry. A good choice of catalyst can decrease reaction barriers, thereby providing means to selectively convert reactants to desired products under mild conditions. A catalyst is regenerated during the reaction cycle, leading to its availability to be used again. Homogeneous catalysis, in contrast with heterogeneous catalysis, refers to the fact that catalyst and reactants are dissolved in the same reaction medium. Most successful catalysts have been found by serendipity, that is, through a process of trial and error. Clearly, there is an urgent need for new tools and concepts that enable a more rational approach to designing catalysts. The main goal of the quantum chemical research described in this thesis is to contribute to the development of these tools and concepts that can be used in future investigations, both theoretical and experimental, in the field of homogeneous catalysis.

A core concept from which we proceed is the Fragment-oriented Design of Catalysts (FDC).[1] In this approach the activity of a catalyst is understood in terms of its functional units, namely, the metal core plus the effect of the ligands. Thus, in a first step, we focus on understanding the intrinsic reactivity of the metal atom. This enables one, in a second step, to understand which features in the metal's electronic structure and the resulting bonding mechanism with the substrate have to be amplified, through a clever choice of ligands, and which ones should be attenuated in order to achieve the desired activity and selectivity. Eventually, in a third step, one can also include the effect of the solvent in this model. In this way, the design of the catalyst can be achieved in a more rational fashion.

The basis of the catalytic systems investigated in this thesis is formed by the transition metal palladium (Pd). Palladium is widely used in catalytic processes. Important examples are the oxidation of alkenes by the $PdCl_2/CuCl_2$ system (Wacker process) or the activation by palladium complexes of aryl-halogen bonds for C–C coupling reactions (Heck reaction; see also below).[2,3] An important characteristic of the group of transition metals is the relative ease in changing the oxidation state of the metal, making a wide variety of reactions possible. The main reason to specifically focus attention on palladium is that the atomic ground state of palladium consists of a closed-shell $d^{10}$ configuration. This facilitates the comparison with more realistic transition metal *complexes* used in catalytic bond activation as these are in general (although not always) closed-shell species.

Oxidative addition comprises a ubiquitous class of reactions, in which a reactant adds to a metal complex, thereby oxidizing it. For example, oxidative addition of a molecule X–Y to Pd(0) leads to the cleavage of the covalent bond between X and Y and the formation of two new bonds: X–Pd–Y. Two previously nonbonding electrons of Pd are involved, giving an increase of the formal oxidation state by two: Pd(0) is oxidized to Pd(II). This is in essence similar to the formation of, for example, Grignard's reagent in the gas-phase model reaction $Mg(0) + CH_3I \rightarrow CH_3\text{–}Mg\text{–}I$. The reverse of oxidative addition is known as reductive elimination. Oxidative addition and reductive elimination reactions are important, since nearly all catalytic processes involve oxidative-addition and reductive-elimination steps.[2,4]

The cross-coupling reaction depicted in Scheme 1.1 is an example of a catalytic cycle. In this cycle, the Pd(0) activates the aryl–X bond in the oxidative-addition step. After that, a substitution of $X^-$ by a nucleophile can take place. Finally, in the reductive-elimination step, the product of the catalytic reaction is formed, and the catalyst Pd(0) is regenerated. The first step in this cycle, the oxidative-addition step can also be called the bond-activation step. This is the step mainly concentrated on in this thesis, since the bond activation is in many cases the rate-determining step and the step that determines the selectivity of the catalytic process.

This thesis contains investigations on the activation of the archetypal H–X, X–X, C–H, C–C, and C–X bonds in the simplest aliphatic systems, where X stands for one of the halogens Cl to At, by the Pd(0) atom, as well as by the complex of Pd(0) with $Cl^-$. These relatively simple model systems were chosen in order to focus on the development of computational approaches and of analytical models to rationalize the reactivity. Turning on anion assistance in the catalyst, i.e., going from Pd to $PdCl^-$, is the first step toward more complex catalysts. The effect of anion assistance is known to speed up the

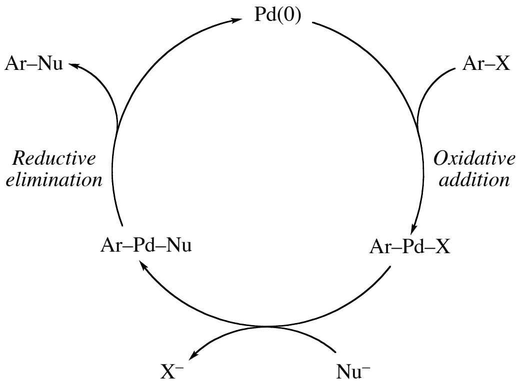

**Scheme 1.1** Catalytic cycle (adapted from p. 209 of ref. 2)

rate-determining step in various catalytic processes such as, for example, the Monsanto process.[5]

In Chapter 2, a brief overview of the theoretical methods and concepts used in this thesis is given. The results of our investigations are presented in the Chapters 3 to 11. The studies presented here can be divided into two parts. In the first part, in the Chapters 3 to 7, the results of extensive benchmarking and validation studies on density functional theory (DFT)[6-9] are described. DFT is highly efficient and the method of choice for quantum chemical calculations on organometallic compounds and reactions. Approximate DFT has, however, been criticized for underestimation of reaction barriers, which are a key issue in our investigations.[10] Therefore, we have undertaken a detailed validation study in which accurate density functionals have been identified on the basis of highly correlated *ab initio* benchmark studies. The in this way validated computational method was used in the second part of this thesis, in the Chapters 8 to 11.

The purpose of the study in Chapter 8 is to better understand the characteristic differences in reactivity between main group and transition metals, in particular, *why* transition metals are better agents for oxidative addition. The reactions are analyzed with the Activation Strain model, in which the reaction barrier is decomposed into the activation strain of the reactants and the stabilizing interaction between the reactants in the transition state geometry.

In Chapter 9 a broad investigation on the reactivity of palladium with all hydrogen halides and dihalogens is presented. This comprehensive overview leads to a good understanding of the trends in reactivity and relativistic effects. In Chapter 10, this is repeated for the palladium-catalyzed activation of the carbon-halogen bond, together with an investigation into the effects of solvation and anion assistance on the trends in reactivity. In particular, the competition between two alternative methods for oxidative addition, namely, direct oxidative insertion (OxIn) and nucleophilic substitution ($S_N2$), is examined. Importantly, both solvation and anion assistance can cause a change in preference for one of the two reaction mechanisms. This is analyzed again with the Activation Strain model, originally developed for the gas phase, which is extended here to incorporate phenomena that occur only in the condensed phase (e.g., desolvation effects).

Finally, in Chapter 11, we have extended the Activation Strain model from a single-point analysis of the transition state to an analysis along the entire reaction coordinate from reactant complex to product. This extension enables one to understand qualitatively trends in the position of the transition state along the reaction coordinate. This approach has been applied to a variety of archetypal bond activation reactions. Some of the phenomena that can now be explained are the anti-Hammond behaviour of the carbon-chlorine bond activation under anion assistance, the competition between OxIn and $S_N2$ and the significantly higher barrier for C–C bond activation than for C–H bond activation, although the C–C bond is weaker than the C–H bond. The reason for this higher barrier is the steric shielding of the C–C bond in ethane by the six surrounding C–H bonds.

# 2 Theory and method

## 2.1 Introduction

In this chapter the main theoretical concepts used in this thesis are discussed. The purpose is not to give a complete overview of the theory involved. For this, the reader is referred to the various textbooks and review articles. Rather, it is explained here on which aspects of theory this thesis focuses. To this end, first some features of *ab initio* calculations are examined. It is then argued why these *ab initio* calculations are important to benchmark the density functional theory (DFT) calculations. After that, an introduction of the Activation Strain model is given. This model has been used in rationalizing differences in reactivity between various systems. It is shown how this model can be extended, leading to a better interpretation of results. Finally, we end with a discussion of aspects of calculations in condensed phase as opposed to gas phase.

## 2.2 *Ab initio* calculations

The central problem in quantum chemistry is to solve the Schrödinger equation:[11]

$$H\Psi = i\hbar\,\partial\Psi/\partial t \tag{2.1}$$

In this equation $\Psi$ is the wavefunction and $H$ the Hamiltonian operator, which describes the energy dependence of the wavefunction. It is a postulate of quantum mechanics that all information of a system is incorporated in the wavefunction. If the Hamiltonian operator does not change in time, which is assumed throughout this thesis, the Schrödinger equation can be simplified by dividing it in a time-dependent and time-independent part. The time-independent Schrödinger equation reads:

$$H\Psi = E\Psi \tag{2.2}$$

In this eigenvalue equation the energy $E$ of the system is quantized, i.e, it adopts discrete values.

An approximation made in all calculation in this work is the Born-Oppenheimer approximation, which states that, due to the difference in mass between the nuclei and the electrons, the movement of the particles of one kind can be described independently of the movement of the other. Therefore, the distribution of the electrons at a certain configuration of the nuclei can be calculated.

It is also a postulate of quantum mechanics that the wavefunction describing the electrons has to be antisymmetric, meaning that when two electrons are exchanged, the wavefunction has to change sign. The antisymmetry of the wavefunction can be achieved by building it from so-called Slater determinants:

$$\Psi_{\mathrm{SD}} = \frac{1}{\sqrt{n!}} \begin{vmatrix} \psi_1(1) & \psi_2(1) & \cdots & \psi_n(1) \\ \psi_1(2) & \psi_2(2) & \cdots & \psi_n(2) \\ \cdots & \cdots & \cdots & \cdots \\ \psi_1(n) & \psi_2(n) & \cdots & \psi_n(n) \end{vmatrix} \tag{2.3}$$

Here, $\Psi_{\mathrm{SD}}$ is a many-electron wavefunction, $\psi_i$ are one-electron wavefunctions and $n$ is the number of electrons. A further approximation can be made in which the total electronic wavefunction $\Psi_{\mathrm{el}}$ consists of only one single determinant. This implies that the electron-electron repulsion is included in an average way, or, in other words, the Coulomb correlation between electrons is neglected, that is, the fact that electrons avoid each other because of their mutual electrostatic repulsion. This leads to the Hartree-Fock model.

Solving the Schrödinger equation now involves finding the one-electron wavefunctions $\psi_i$ that give the most accurate total wavefunction $\Psi_{\mathrm{el}}$. According to the variational principle, this is the wavefunction associated with the lowest energy. In practice, a basis-set expansion is made of the one-electron wavefunctions:

$$\psi_i = \sum_j \chi_j c_{ji} \tag{2.4}$$

The basis functions $\chi_j$ are, more or less arbitrarily, chosen beforehand. Usually, the basis functions are located on the atoms involved. In essence, the solving of the Schrödinger equation consists of the finding of the set of coefficients $c_{ji}$ that minimizes the energy of the electronic system. Important aspects determining the accuracy of the calculation are the size and the aptness of the basis set. One cannot increase the basis-set size infinitely: the computational cost increases rapidly with increasing basis-set size. Many basis sets have already been developed, each with its own advantages and disadvantages. A great part of the investigations in this study consists of extensive analyses of basis sets for all atoms involved, regarding the convergence of the computed energy as a function of the basis-set flexibility and polarization. The purpose of these analyses is to compose basis sets that yield the most accurate results for our model systems, thereby stretching our computational limits to the utmost. One of the outcomes for the model reactions in this work is the importance of including a correction for the basis set superposition error (BSSE) in the calculation of energies of complexes relative to the constituting fragments, notably in cases where electron correlation is included (*vide infra*). This correction is necessary, because of the extra stabilization in energy that a complex gets from the better description of the total wavefunction by the combination of the basis sets of the constituting fragments.[12]

In the Hartree-Fock model, Coulomb correlation between electrons is neglected. However, this correlation is important, also for the model reactions studied here. At present, there exists a range of methods to include correlation. In general in *ab initio* theory, they consist of using a multi-determinant trial wavefunction by including excited states from the reference Hartree-Fock wavefunction. The computational costs rapidly increase with a better description of electron correlation. In this thesis, we have been able to push the accuracy with which Coulomb correlation is treated up to the level of coupled-cluster theory with single and double excitations and with triple excitations treated perturbatively .

For molecular systems with heavy elements, as is the case for the model systems studied in this thesis, the electrons closest to the heavy nuclei can reach velocities approaching the speed of light. In that case, a relativistic treatment becomes necessary.[13] The basis of the formalism in relativistic quantum chemistry is the Dirac equation. This is an equation in four-dimensional space (three-dimensional position space plus time as the fourth dimension), with a Hamiltonian that accounts for relativistic effects on the energy. The wavefunction consists of four components, which can be divided into so-called “large” and “small” components. The great computational demand that a four-component method makes is mostly due to the evaluation and handling of two-electron integrals that involve the small components of the wavefunction, because the basis sets describing the small components have to be very large to satisfy the kinetic balance condition. Since these integrals contribute relatively little to the electronic energy, several approximations have been developed to neglect part of the integrals involving small components, for example the one-centre approximation.[14,15] In all four-component calculations in this thesis, all two-electron integrals involving exclusively small components were neglected and a simple Coulombic correction was applied, which has been proven remarkably reliable.[16] Various Hamiltonians have been proposed in four-component approaches that treat relativistic effects increasingly accurately. Most *ab initio* calculations were done without spin-orbit coupling using a spinfree Dirac-Coulomb Hamiltonian.[17] The nonrelativistic limit was reached using the Lévy-Leblond approximation,[18] and, for some of the model systems, the most accurate results were obtained using an unmodified Dirac-Coulomb Hamiltonian, which includes spin-orbit coupling. Other, more approximate but computationally much less demanding methods are available to incorporate relativistic effects. In some of the *ab initio* calculations, a relativistic effective core potential was used, thereby replacing the relevant electrons by a potential incorporating the predetermined relativistic effects. Finally, in the DFT calculations (see next section) relativistic effects were accounted for using the zeroth-order regular approximation (ZORA).[19]

## 2.3 Density functional theory calculations

The methods described in the previous section are based on the complicated many-electron wavefunction, which depends on several variables for each electron. In density functional theory (DFT) the many-electron wavefunction is replaced by the electron density as the basic quantity, thereby reducing greatly the number of variables.[8,9] The theorems of Hohenberg and Kohn provide the fundament of DFT, by stating that the ground-state energy $E$ of a system is uniquely determined by the corresponding electron density $\rho$, i.e., the energy is a functional of the density: $E = E[\rho]$, and by stating that the ground-state electron density minimizes the electronic energy of the system, or, in other words, that the variational principle holds in DFT.[6] However, the Hohenberg-Kohn theorems do not give the form of the functional dependence of the energy on the density.

Kohn and Sham provided the first practical computational scheme, by postulating a reference system of *noninteracting* electrons, moving in an *effective* potential.[7] This effective potential includes the external potential (of the nuclei) but also the Coulomb interaction of the electron density with itself and corrections to this averaged treatment of the electron-electron repulsion. These corrections are the exchange correlation, which originates from the fact that electrons are fermions and described by an antisymmetric wavefunction, and the Coulomb correlation, which is caused by the fact that electrons avoid each other due to their mutual electrostatic repulsion. The non-interacting reference system is then represented by a one-determinantal wavefunction, yielding the exact density of the *interacting* system and the corresponding exact energy. This is computationally highly efficient, since one is not challenged by a multi-determinantal wavefunction. However, modelling the functional dependence of the exchange-correlation energy on the electronic density is the problematic part of Kohn-Sham DFT. There is no systematic way to improve the accuracy of a certain functional. Approximations have been developed, such as the local density approximation (LDA), or generalized gradient approximations (GGAs), where different choices for the functional dependence of exchange and correlation parts on the density and different combinations thereof have lead to a wide range of available density functionals. A significant part of the research described in this thesis focuses on finding the optimal density functional for our model systems.

## 2.4 Activation Strain model of chemical reactivity

In the process of designing catalysts, one is specifically interested in the activation barrier for the desired reaction, that is, the energy of the transition state (TS) relative to the reactants, and how one can selectively lower this barrier by tuning the catalyst-substrate interaction. To gain insight into how the use of different metals and different substrates affects the activation barrier, the reactions can be analyzed using the Activation Strain model of chemical reactivity.[20-22] In this model, the activation energy $\Delta E^{\neq}$ is decomposed into the activation strain $\Delta E^{\neq}_{\text{strain}}$ and the TS interaction $\Delta E^{\neq}_{\text{int}}$:

$$\Delta E^{\neq} = \Delta E^{\neq}_{\text{strain}} + \Delta E^{\neq}_{\text{int}} \tag{2.5}$$

The activation strain $\Delta E^{\neq}_{\text{strain}}$ is the strain energy associated with deforming the reactants from their equilibrium geometry to the geometry they adopt in the activated complex. The TS interaction $\Delta E^{\neq}_{\text{int}}$ is the actual interaction energy between the deformed reactants in the transition state (see also Figure 2.1).

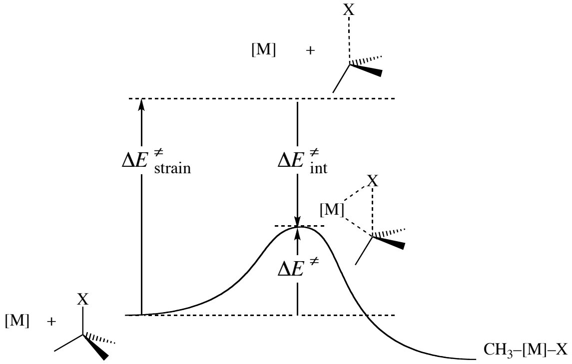

**Figure 2.1** Illustration of the Activation Strain model in the case of insertion of metal complex [M] into a C–X bond. $\Delta E^{\neq}$ is decomposed into $\Delta E^{\neq}_{\text{strain}}$ of and stabilizing $\Delta E^{\neq}_{\text{int}}$ between the reactants in the transition state.

In previous studies, this model was successfully used to rationalize differences in reactivity for different inserting metal complexes (see refs. 22-25). Also here, it has been applied to various model reactions (see Chapters 8 and 10). However, a so far unresolved issue is that the position of the TS along the reaction coordinate has a large effect on the size of the energy components. To obtain insight into how this position is determined and how this affects the barrier height, we have extended the Activation Strain model from a single-point analysis of the TS to an analysis along the reaction coordinate $\zeta$:

$$\Delta E(\zeta) = \Delta E_{\text{strain}}(\zeta) + \Delta E_{\text{int}}(\zeta) \tag{2.6}$$

In other words, the entire reaction profile is decomposed along the reaction coordinate $\zeta$ into the strain that builds up in the reactants plus the interaction between these increasingly deformed reactants. This extension enables us to understand qualitatively the trends in the position of the TS along $\zeta$ and how this position $\zeta^{\text{TS}}$ affects the height of the reaction barrier $\Delta E^{\neq} = \Delta E_{\text{strain}}(\zeta^{\text{TS}}) + \Delta E_{\text{int}}(\zeta^{\text{TS}}) = \Delta E^{\neq}{}_{\text{strain}} + \Delta E^{\neq}{}_{\text{int}}$ (see Chapter 11).

## 2.5 Solvent effects

In practice, homogeneous catalysis occurs in solution. In spite of this, most model reactions presented in this thesis were calculated in the gas phase. An important reason is that in the process of developing new catalysts, we are in first instance interested in the intrinsic reactivity of a particular metal towards the bonds in the substrate that are to be activated. Thereafter, in a second stage, we wish to find out how this intrinsic reactivity can be influenced by introducing ligands in the metal complex to steer reactivity.

Thus, for a number of model reactions, the influence of solvation on reaction characteristics has been assessed. Furthermore, an extension of the Activation Strain model (see previous section) is proposed that enables treating solvent effects in condensed-phase reactions (see Chapter 10).

To estimate solvent effects, particularly in water, a continuum solvation model was used. This implies that the solvent was not simulated with explicit solvent molecules, but instead as a continuous medium, including polarization and cavitation effects caused by the solute. The specific model of choice was the Conductor-like Screening Model (COSMO),[26] which is a dielectric model in which the solute molecule is embedded in a molecule-shaped cavity surrounded by a dielectric medium with a specific dielectric constant $\varepsilon$. Energy terms are first calculated for a conducting medium, which is relatively simple, and then scaled by a factor of $(\varepsilon - 1) / \varepsilon$. The cavity formed by the solute molecule was generated by following the path traced by a spherical solvent molecule rolling over the Van der Waals surface of the solute molecule. The atomic radii were taken from literature, and scaled to give accurate results for, e.g., hydration or complexation energies of reference systems. This approach works in general satisfactorily but it must be used with caution. For example, a complete breakdown of the model occurs if solvent molecules participate as reactants in the reaction mechanism.[27]

# 3 *Ab initio* benchmark study for the oxidative addition of the methane C–H bond to Pd. Importance of basis-set flexibility and polarization

Adapted from
G. Th. de Jong, M. Solà, L. Visscher, F. M. Bickelhaupt *J. Chem. Phys.* **2004**, *121*, 9982

## Abstract

To obtain a state-of-the-art benchmark potential energy surface (PES) for the archetypal oxidative addition of the methane C–H bond to the palladium atom, we have explored this PES using a hierarchical series of *ab initio* methods (Hartree-Fock, MP2, MP4SDQ, CCSD, and CCSD(T)) and hybrid density functional theory using the B3LYP functional, in combination with a hierarchical series of ten Gaussian-type basis sets, up to *g* polarization. Relativistic effects are taken into account either through a relativistic effective core potential for palladium or through a full four-component all-electron approach. Counterpoise corrected relative energies of stationary points are converged to within 0.1-0.2 kcal/mol as a function of the basis-set size. Our best estimate of kinetic and thermodynamic parameters is –8.1 (–8.3) kcal/mol for the formation of the reactant complex, 5.8 (3.1) kcal/mol for the activation energy relative to the separate reactants, and 0.8 (–1.2) kcal/mol for the reaction energy (zero-point vibrational energy-corrected values in parentheses). This agrees well with available experimental data. Our work highlights the importance of sufficient higher-angular momentum polarization functions, *f* and *g*, for correctly describing metal-*d*-electron correlation and, thus, for obtaining reliable relative energies. We show that standard basis sets, such as LANL2DZ+1*f* for palladium, are not sufficiently polarized for this purpose and lead to erroneous CCSD(T) results. B3LYP is associated with smaller basis set superposition errors and shows faster convergence with basis-set size but yields relative energies (in particular, a reaction barrier) that are ca. 3.5 kcal/mol higher than the corresponding CCSD(T) values.

## 3.1 Introduction

The activation of the C–H bond in alkanes is a challenging and important goal of catalysis. It is often the first step in the catalytic conversion of the abundant alkanes into more useful products.[28,29] It is difficult for the C–H bond to be activated by transition metal atoms. Alkanes are poor electron donors and acceptors. The alkane C–H bond is strong and nonpolar. Because the $\sigma$ HOMO is low lying it is unsuitable for electron donation, whereas the high-lying $\sigma^*$ LUMO is unsuitable for accepting electron density.[30] Among the transition metals, palladium is one of the most important catalysts, mostly in conjunction with ligands.[31] The insertion of the Pd atom into the C–H bond in alkanes has therefore received considerable attention, experimentally[32-36] and theoretically.[33,35,37-44] Here, the insertion of Pd into the methane C–H bond as an important example of this type of reactions is surveyed, see Scheme 3.1.

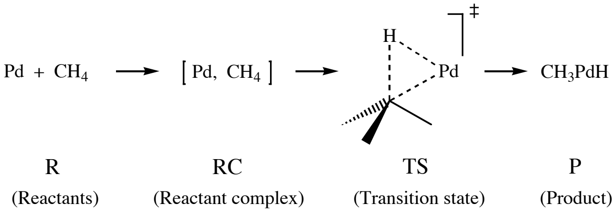

**Scheme 3.1** Model reaction and nomenclature

Experimental investigations on the kinetics of the reaction of Pd with alkanes have been carried out by Weisshaar and coworkers[34,35] and by Campbell.[36] These studies show that Pd forms collisionally stabilized complexes with alkanes, in particular also methane,[36] and that the reaction rate is extremely small to negligible. The results suggest a complexation energy of at least 8 kcal/mol for Pd-alkane complexes,[34] providing an experimental boundary condition for the stability of the Pd-methane reactant complex.

The purpose of the present study is twofold. In the first place, we wish to obtain a reliable benchmark for the potential energy surface (PES) for the archetypal organometallic reaction of methane oxidative addition to Pd(0). This is done by exploring this PES for the first time with a hierarchical series of *ab initio* and hybrid density functional methods in combination with a hierarchical series of ten Gaussian-type basis sets of increasing flexibility and polarization. The basis set superposition error (BSSE) is accounted for by counterpoise correction (CPC).[12] Relativistic effects are important for this model reaction.[22] Here, they are treated either with a relativistic effective core potential (ECP) for Pd or with a four-component all-electron approach.

The existing computational benchmark for oxidative addition of methane to Pd was obtained by Siegbahn and coworkers[35] with the parameterized configuration interaction method PCI-80,[45] in which correlation is estimated by an extrapolation procedure. Their study arrives at a complexation energy of 5.1 kcal/mol, an activation energy of 3.6 kcal/mol and a reaction energy of 2.3 kcal/mol. These values and, in particular, the activation energies are highly sensitive to the level of theory. For the activation energy a spectrum of values has been computed that ranges from +30.5 to –3.8 kcal/mol (see Table 3.1). In view of this, it is appropriate to explore to which extent the PCI-80 values are converged with respect to the order of correlation incorporated into the theoretical method and the degree of flexibility and polarization of the basis set. This work serves to clarify this. Note that, in addition to the extrapolation procedure associated with PCI-80, the computation of these benchmark values involves a further approximation. The final scaled MCPF energies of the PCI-80 study were, namely, not computed at the MCPF but, instead, the HF optimum geometry.[35,43] Here, we use a consistent set of geometries that have been fully optimized using density functional theory (DFT).[6-9]

A second purpose of our work is to find out how well standard basis sets designed for use with high-level correlated *ab initio* methods such as CCSD(T) are suited for correctly describing correlation phenomena associated with organometallic reactions involving bond breaking. The activation of the C–H bond by Pd serves as a test case.

**Table 3.1** Literature values for the energy profile (in kcal/mol) for oxidative addition of $CH_4$ to Pd

| | | Basis set quality[a] | | | | |
|---|---|---|---|---|---|---|
| Reference | Method | Pd | C and H | RC | TS | P |
| 37,38 | GVB-RCI//HF | DZP[b] | DZ | | 30.5 | 20.1 |
| 39 | CCI+Q//CASSCF | TZP[c] | DZP | | 25.1 | 17.6 |
| 39 | CCI+Q//CASSCF | TZP + 2*f*[d] | TZP | | 15.4 | 9.1 |
| 41 | MCPF//HF | TZP + *f*[e] | DZP | –4 | 16 | 9 |
| 42 | CCSD(T)//HF | TZP + 3*f*[f] | TZP | | 10.6 | 5.6 |
| 35 | PCI-80//HF | TZP + *f*[e] | DZP | –5.1[h] | 3.6[h] | –2.3[h] |
| 22 | BP86 | TZP[g] | TZ2P[g] | –10.5 | –1.6 | –7.1 |
| 44 | PBE | TZP | TZP | –11.3[h] | –3.8[h] | –8.0[h] |

a Main characteristics of the basis set used in the higher-level single-point calculations. For Pd, DZP is double-ζ for valence 4*d* shell with one set of polarization functions for 5*p* shell; TZP is triple-ζ for valence 4*d* shell with one set of polarization functions for 5*p* shell. For C and H, DZP is double-ζ with one set of polarization functions, 3*d* for C and 2*p* for H; TZP is triple-ζ with one set of polarization functions, 3*d* for C and 2*p* for H; TZ2P is triple-ζ with two sets of polarization functions, 3*d* and 4*f* for C, and 2*p* and 3*d* for H.

b ECP for [Kr] core; valence electrons: (3*s*3*p*3*d*)/[3*s*2*p*2*d*] (ref. 46).

c Augmented Huzinaga basis (ref. 47), Raffenetti contraction scheme (ref. 48): (17*s*13*p*9*d*)/[8*s*7*p*4*d*].

d Same as c but with larger primitive and contracted basis: (17*s*13*p*10*d*4*f*)/[8*s*7*p*5*d*2*f*].

e Same as c but with larger primitive and contracted basis: (17*s*13*p*9*d*3*f*)/[7*s*6*p*4*d*1*f*].

f Same as e but with three *f* functions uncontracted: (17*s*13*p*9*d*3*f*)/[7*s*6*p*4*d*3*f*].

g Slater-type orbitals.

h With ZPE correction.

## 3.2 Methods

### 3.2.1 Geometries

Geometries of the stationary points were optimized with the ADF program[49-51] using DFT at BLYP,[52,53] in combination with a large uncontracted set of Slater-type orbitals (STOs) containing diffuse functions: TZ2P. The TZ2P basis is of triple-ζ quality and has been augmented with two sets of polarization functions: 2*p* and 3*d* on H, 3*d* and 4*f* on C, and 5*p* and 4*f* on Pd. The core shells of C (1*s*) and Pd (1*s*2*s*2*p*3*s*3*p*3*d*) were treated by the frozen-core approximation.[49] An auxiliary set of *s*, *p*, *d*, *f* and *g* STOs was used to fit the molecular density and to represent the Coulomb and exchange potentials accurately in each self-consistent-field cycle.[49] Relativistic effects were accounted for using the zeroth-order regular approximation (ZORA).[19]

### 3.2.2 *Ab initio* methods

Energies of the stationary points were computed with the programs GAUSSIAN[54] and DIRAC[15,55,56] using the following hierarchy of quantum chemical methods: Hartree-Fock theory (HF), second-order Møller-Plesset perturbation theory (MP2),[57] fourth-order Møller-Plesset perturbation theory with single, double and quadruple excitations (MP4SDQ),[58] coupled-cluster theory with single and double excitations (CCSD),[59] and with triple excitations treated perturbatively (CCSD(T)[60]). Finally, DFT calculations have been done with the B3LYP functional.[53,61] In calculations with the GAUSSIAN program, relativistic effects were described using an effective core potential for Pd. On the other hand, in calculations with the DIRAC program, relativistic effects were accounted for using an all-electron four-component Dirac-Coulomb approach with a spin-free Hamiltonian (SFDC).[17] The two-electron integrals over the small components were neglected, using a simple Coulombic correction, which was shown reliable.[16]

### 3.2.3 Basis sets

For C and H, we used Dunning's correlation consistent augmented double-$\zeta$ (cc-aug-pVDZ) and triple-$\zeta$ (cc-aug-pVTZ) basis sets[62,63] in both GAUSSIAN and DIRAC calculations. For Pd, two different types of basis sets were used for the two programs, leading to two series of basis sets for our model system: A1-A4 in the GAUSSIAN calculations and B1-B6 in the DIRAC calculations (see Table 3.2). The series A1-A4 in the GAUSSIAN calculations are based on the Gaussian-type LANL2DZ basis set of Hay and Wadt for Pd.[64] This basis set involves a relativistic ECP that accounts for mass-velocity and Darwin terms. Basis set A1 corresponds to cc-aug-pVDZ for C and H and the standard LANL2DZ basis set for Pd in which, however, the original valence *p* shell has been decontracted to provide an independent function for the empty 5*p* orbital, which is important for accuracy.[65] As a first extension, in basis set A2, one set of 4*f* polarization functions was added with an exponent of 1.472, as suggested by Ehlers *et al.*[66] In basis set A3, the cc-aug-pVDZ basis set (double-$\zeta$) for C and H is replaced by cc-aug-pVTZ (triple-$\zeta$), and for Pd the LANL2DZ basis set of double-$\zeta$ quality is replaced by the LANL2TZ basis set of triple-$\zeta$ quality, with the same primitives but further decontracted, which according to Torrent and coworkers[67] leads to an increased

**Table 3.2** Basis sets used. A1-A4 for computations with GAUSSIAN, B1-B6 for computations with DIRAC

| Basis set | Pd | C and H |
|---|---|---|
| A1 | LANL2DZ | cc-aug-pVDZ |
| A2 | LANL2DZ + 1*f* | cc-aug-pVDZ |
| A3 | LANL2TZ + 1*f* | cc-aug-pVTZ |
| A4 | LANL2TZ + 3*f* | cc-aug-pVTZ |
| B1 | (24*s*16*p*13*d*)[a] | cc-aug-pVDZ[b] |
| B2 | (24*s*16*p*13*d*)[a] + 1*f* | cc-aug-pVDZ[b] |
| B3 | (24*s*16*p*13*d*)[a] + 1*f* | cc-aug-pVTZ[b] |
| B4 | (24*s*16*p*13*d*)[a] + 4*f* | cc-aug-pVTZ[b] |
| B5 | (24*s*16*p*13*d*)[a] + 4*f* + *p* | cc-aug-pVTZ[b] |
| B6 | (24*s*16*p*13*d*)[a] + 4*f* + *p* + *g* | cc-aug-pVTZ[b] |

a TZP quality.

b Completely uncontracted.

accuracy. Finally, the largest basis set in this series, A4, was created by substituting the single set of 4*f* polarization functions of Ehlers *et al.*[66] by four sets of 4*f* functions, as reported by Langhoff and coworkers,[68] with exponents 3.61217, 1.29541, 0.55471, and 0.23753. They were contracted as 211, resulting in three contracted 4*f* functions.

The series B1-B6 used with DIRAC are based on an uncontracted, Gaussian-type basis set (24*s*16*p*13*d*) for Pd, of triple-$\zeta$ quality and developed by Faegri.[69] Furthermore, Dunning's cc-aug-pVDZ and cc-aug-pVTZ basis sets[62,63] for C and H were used in uncontracted form because it is technically difficult to use contracted basis sets in the kinetic balance procedure in DIRAC.[70] Basis set B1 corresponds to cc-aug-pVDZ for C and H and the (24*s*16*p*13*d*) basis set for Pd. As a first extension, in B2, one set of 4*f* polarization functions was added with an exponent of 1.472 as reported by Ehlers.[66] In B3, the cc-aug-pVDZ basis set for C and H is replaced by cc-aug-pVTZ. In B4, the single set of 4*f* polarization functions of Ehlers is substituted by four sets of 4*f* polarization functions as reported by Langhoff[68] with exponents 3.61217, 1.29541, 0.55471, and 0.23753 that, at variance with the situation in basis set A4, were kept uncontracted. Thereafter, going to B5 an additional set of diffuse *p* functions was introduced with exponent 0.141196, as proposed by Osanai.[71] Finally, B6 was created by adding a set of *g* functions with an exponent of 1.031690071. This value is close to but not exactly equal to the exponent of the *g* functions of Osanai. Instead, it is equal to the value of one of the exponents of the *d* set of Faegri, which reduces computational costs.

## 3.3 Results and discussion

### 3.3.1 Geometries of stationary points

First, we examine the stationary points along the reaction coordinate of the oxidative insertion of Pd into a methane C–H bond. The geometries of these species were fully optimized at the ZORA-BLYP/TZ2P level of relativistic DFT and agree well with earlier relativistic DFT studies (see Figure 3.1).[22,44] The reaction proceeds from the reactants via formation of a stable reactant complex of $C_{2v}$ symmetry, in which methane coordinates in an $\eta^2$ fashion to Pd, followed by the transition state of $C_s$ symmetry, and finally a stable product, also of $C_s$ symmetry. All species have been verified through vibrational analyses to represent equilibrium structures (no imaginary frequencies) or a transition state (one imaginary frequency: 778 $i$ cm$^{-1}$). Thus, we have a set of geometries that, for all stationary points along the reaction coordinate, have been optimized consistently at the same level of theory without any structural constraint. In the following, these geometries are used in the series of high-level *ab initio* calculations that constitute our benchmark study for the oxidative addition of $CH_4$ to Pd.

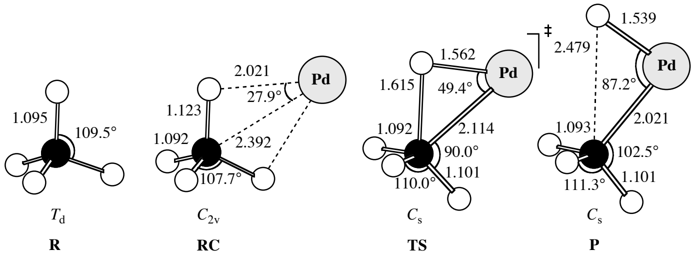

**Figure 3.1** Geometries (in Å) of the stationary points for the reaction of Pd + $CH_4$, at ZORA-BLYP/TZ2P

### 3.3.2 Energies of stationary points

As pointed out in Section 3.1, the relative energies of stationary points along the reaction profile of Pd insertion into the methane C–H bond, especially the activation energy, appear to be highly sensitive to the level of theory used, as witnessed by the large spread in values computed earlier. Here, we report the first systematic investigation of the extent to which the various thermodynamic and kinetic parameters depend on the quality of the method and the basis set as well as the extent to which these values are converged at the highest level of theory used.

The energies relative to the reactants of the stationary points for oxidative insertion of Pd into the methane C–H bond are collected in Table 3.3 and displayed in Figures 3.2 and 3.3. At all levels of theory except HF, the reaction profiles are characterized by the formation of a stable reactant complex (RC), which leads via the transition state for insertion (TS) to the oxidative-addition product (P). Three striking observations can be made: (i) the spread in values of computed relative energies, depending on the level of theory and basis set, is enormous, up to nearly 70 kcal/mol; (ii) the size of the BSSE is remarkably large, up to ca. 30 kcal/mol; (iii) most strikingly, convergence with basis-set size of the computed energies is still not reached with standard basis sets used routinely in CCSD(T) computations on organometallic compounds.

The lack of any correlation leads to a complete failure at the HF level, which yields an unbound RC, a strongly exaggerated activation barrier of ca. 45 kcal/mol and a reaction energy that differs only a few kcal/mol from the activation energy. In other words, the process is highly endothermic and has essentially no reverse barrier at the HF level for all basis sets used. The failure of HF for describing the PES of our model reaction is not unexpected because electron correlation, which is not contained in this approach, is important.[72,73] The activation energy drops significantly when electron correlation is introduced. Along HF, CCSD and CCSD(T) in combination with basis set A1, for example, the activation barrier decreases from 45.0 to 7.7 to 3.6 kcal/mol.

But also the correlated CCSD(T) values obtained with standard basis sets, such as LANL2DZ or LANL2TZ with one or three *f* functions (A2-A4) are questionable, as they are obviously not converged as a function of the basis-set size. For example, the activation energy of 3.6 kcal/mol at CCSD(T)/A1, which involves LANL2DZ for Pd, agrees exactly, that is, it coincides with that of the benchmark of Siegbahn and coworkers obtained with PCI-80. This agreement is fortuitous. The CCSD(T) value for the barrier drops from 3.6 to –3.6 and further to –18.8 kcal/mol along basis sets A1, A2, and A3, as one *f* polarization function is added and, then, the flexibility of the basis set is increased from double- to triple-$\zeta$. Thereafter, going from basis set A3 to A4, the activation energy increases again from –18.8 to –9.4 kcal/mol as polarization is increased from one to three *f* functions. This is illustrated by Figure 3.2, which shows the CCSD(T) reaction profiles and how they vary along basis sets A1-A4. Obviously, the energy values have not reached convergence. Also, an activation energy of –18.8 or –9.4 kcal/mol is not only much lower than the present benchmark value of 3.6 kcal/mol but it is also too low for a reaction that essentially does not proceed. Similar behaviour is observed for other correlated *ab initio* methods (MP2, MP4SDQ, CCSD) both in the relativistic ECP calculations with GAUSSIAN with basis sets A1-A4 and in the SFDC calculations with DIRAC with basis sets B1-B. On the other hand, the HF calculations in which electron correlation is not accounted for are relatively insensitive toward increasing the flexibility and polarization of the basis set along A1-A4 or B1-B4.

Next, we note that the BSSE (given in Table 3.4 and Figures 3.4 and 3.5) is large in the correlated *ab initio* methods, whereas it is negligible if correlation is completely neglected, i.e., in HF. The BSSE increases along A1-A3 and decreases from A3 to A4. At the CCSD(T) level, the BSSE for the TS of the reaction amounts to 16.3, 19.7, 29.5, and 18.6 along the basis sets A1-A4, whereas the corresponding BSSE values at HF are only ca. 2 kcal/mol. The increase in BSSE going from A2 to A3 reveals the imbalance that is introduced into the overall basis set by improving it for C and H (from double- to triple-$\zeta$) while leaving unchanged the basis set for Pd. Thereafter, from A3 to A4, the BSSE decreases as the quality of the Pd basis improves by increasing the number of *f*

**Table 3.3** Relative energies (in kcal/mol) of the stationary points along the reaction coordinate for oxidative addition of methane to Pd, without (no CPC) and with counterpoise correction (with CPC)

| | | RC | | TS | | P | |
|---|---|---|---|---|---|---|---|
| Method | Basis set | no CPC | with CPC | no CPC | with CPC | no CPC | with CPC |
| HF | A1 | 8.2 | 10.0 | 45.0 | 47.1 | 44.5 | 46.8 |
| | A2 | 8.0 | 9.9 | 44.4 | 46.5 | 42.7 | 45.0 |
| | A3 | 7.3 | 9.5 | 43.7 | 46.1 | 41.3 | 43.9 |
| | A4 | 7.2 | 9.4 | 43.2 | 45.7 | 40.2 | 42.9 |
| MP2 | A1 | –10.2 | 1.5 | 2.8 | 17.7 | 1.2 | 18.1 |
| | A2 | –16.0 | –0.9 | –7.7 | 11.8 | –10.5 | 11.4 |
| | A3 | –27.8 | –4.9 | –25.0 | 5.4 | –29.5 | 3.1 |
| | A4 | –21.6 | –7.5 | –15.8 | 2.6 | –16.9 | 2.4 |
| MP4SDQ | A1 | –11.7 | 1.5 | 2.3 | 18.9 | 0.9 | 19.5 |
| | A2 | –14.7 | 0.6 | –2.0 | 17.5 | –5.2 | 16.6 |
| | A3 | –25.2 | –3.4 | –15.9 | 12.8 | –20.6 | 10.0 |
| | A4 | –19.0 | –4.8 | –6.5 | 12.0 | –9.7 | 9.6 |
| CCSD | A1 | –9.1 | 3.0 | 7.7 | 23.0 | 2.1 | 19.1 |
| | A2 | –12.7 | 1.7 | 2.2 | 20.6 | –4.3 | 16.2 |
| | A3 | –22.1 | –1.9 | –10.3 | 16.5 | –18.3 | 10.3 |
| | A4 | –16.2 | –3.3 | –1.6 | 15.3 | –7.8 | 9.9 |
| CCSD(T) | A1 | –10.8 | 2.0 | 3.6 | 19.9 | –1.5 | 16.7 |
| | A2 | –15.2 | 0.2 | –3.6 | 16.0 | –10.0 | 11.9 |
| | A3 | –26.4 | –4.1 | –18.8 | 10.7 | –26.9 | 4.7 |
| | A4 | –19.9 | –5.7 | –9.4 | 9.3 | –15.6 | 4.0 |
| B3LYP | A1 | –7.3 | –4.1 | 7.5 | 11.0 | 2.3 | 6.1 |
| | A2 | –7.5 | –4.3 | 6.9 | 10.4 | 1.4 | 5.3 |
| | A3 | –8.4 | –4.7 | 6.5 | 10.6 | 0.8 | 5.0 |
| | A4 | –8.6 | –4.8 | 6.1 | 10.2 | 0.1 | 4.3 |
| SFDC-HF | B1 | 8.9 | 9.1 | 44.8 | 45.0 | 42.7 | 42.9 |
| | B2 | 8.8 | 8.9 | 44.2 | 44.4 | 40.8 | 41.1 |
| | B3 | 8.7 | 8.8 | 44.2 | 44.4 | 40.7 | 40.8 |
| | B4 | 8.6 | 8.7 | 43.8 | 44.0 | 39.6 | 39.8 |
| | B5 | 8.6 | 8.7 | 43.8 | 43.9 | 39.6 | 39.8 |
| | B6 | 8.6 | 8.7 | 43.5 | 43.7 | 39.1 | 39.3 |
| SFDC-MP2 | B1 | –6.7 | –2.4 | 4.2 | 11.5 | 2.6 | 11.2 |
| | B2 | –11.5 | –5.2 | –5.6 | 4.9 | –8.2 | 4.1 |
| | B3 | –21.1 | –7.6 | –19.4 | 0.9 | –22.7 | 0.4 |
| | B4 | –13.4 | –9.7 | –6.4 | –1.1 | –5.8 | 0.1 |
| | B5 | –12.0 | –9.8 | –5.1 | –1.2 | –4.5 | 0.0 |
| | B6 | –12.0 | –10.2 | –4.6 | –1.8 | –3.2 | 0.1 |
| SFDC-CCSD | B1 | –5.0 | –0.6 | 11.3 | 18.5 | 5.0 | 13.3 |
| | B2 | –7.7 | –2.1 | 6.6 | 15.7 | –0.6 | 9.8 |
| | B3 | –15.7 | –4.2 | –4.3 | 12.8 | –12.4 | 7.0 |
| | B4 | –8.3 | –5.1 | 7.8 | 12.4 | 1.7 | 6.8 |
| | B5 | –7.2 | –5.2 | 8.8 | 12.2 | 2.7 | 6.6 |
| | B6 | –6.7 | –5.2 | 10.1 | 12.4 | 4.5 | 7.1 |
| SFDC-CCSD(T) | B1 | –7.5 | –2.0 | 5.9 | 14.7 | –0.1 | 9.9 |
| | B2 | –10.9 | –4.1 | –0.5 | 10.3 | –7.6 | 4.8 |
| | B3 | –20.1 | –6.6 | –13.0 | 6.9 | –21.0 | 1.4 |
| | B4 | –12.3 | –7.8 | –0.1 | 6.1 | –5.9 | 0.9 |
| | B5 | –10.3 | –7.9 | 1.9 | 5.9 | –3.9 | 0.7 |
| | B6 | –9.8 | –8.1 | 3.1 | 5.8 | –2.3 | 0.8 |
| SFDC-B3LYP | B1 | –4.9 | –4.8 | 10.4 | 10.5 | 5.2 | 5.4 |
| | B2 | –5.1 | –4.9 | 9.9 | 10.0 | 4.3 | 4.5 |
| | B3 | –5.2 | –5.1 | 9.9 | 10.0 | 4.3 | 4.4 |
| | B4 | –5.3 | –5.2 | 9.5 | 9.6 | 3.7 | 3.9 |
| | B5 | –5.3 | –5.2 | 9.4 | 9.6 | 3.7 | 3.8 |
| | B6 | –5.4 | –5.3 | 9.1 | 9.3 | 3.3 | 3.5 |

**Table 3.4** Basis set superposition error (BSSE, in kcal/mol) for Pd and methane in the stationary points along the reaction coordinate for oxidative addition of methane to Pd

| | | RC | | | TS | | | P | | |
|---|---|---|---|---|---|---|---|---|---|---|
| Method | Basis set | Pd | $CH_4$ | Total | Pd | $CH_4$ | Total | Pd | $CH_4$ | Total |
| HF | A1 | 1.7 | 0.1 | 1.8 | 1.9 | 0.1 | 2.1 | 2.1 | 0.2 | 2.3 |
| | A2 | 1.7 | 0.1 | 1.8 | 1.9 | 0.1 | 2.1 | 2.1 | 0.2 | 2.3 |
| | A3 | 2.2 | 0.0 | 2.2 | 2.4 | 0.0 | 2.4 | 2.6 | 0.0 | 2.6 |
| | A4 | 2.3 | 0.0 | 2.3 | 2.5 | 0.0 | 2.5 | 2.6 | 0.0 | 2.7 |
| MP2 | A1 | 11.4 | 0.3 | 11.7 | 14.4 | 0.5 | 14.9 | 16.0 | 0.8 | 16.9 |
| | A2 | 14.8 | 0.3 | 15.1 | 18.9 | 0.6 | 19.5 | 21.1 | 0.9 | 21.9 |
| | A3 | 22.9 | 0.1 | 22.9 | 30.2 | 0.1 | 30.3 | 32.3 | 0.2 | 32.6 |
| | A4 | 14.0 | 0.1 | 14.1 | 18.1 | 0.2 | 18.4 | 18.9 | 0.4 | 19.3 |
| MP4SDQ | A1 | 12.9 | 0.3 | 13.2 | 16.2 | 0.5 | 16.6 | 17.9 | 0.6 | 18.6 |
| | A2 | 15.0 | 0.3 | 15.3 | 19.0 | 0.5 | 19.5 | 21.2 | 0.6 | 21.8 |
| | A3 | 21.7 | 0.1 | 21.8 | 28.6 | 0.1 | 28.7 | 30.5 | 0.1 | 30.6 |
| | A4 | 14.1 | 0.1 | 14.2 | 18.3 | 0.2 | 18.5 | 19.1 | 0.2 | 19.3 |
| CCSD | A1 | 11.8 | 0.3 | 12.1 | 14.9 | 0.5 | 15.3 | 16.5 | 0.6 | 17.1 |
| | A2 | 14.0 | 0.3 | 14.3 | 17.9 | 0.5 | 18.4 | 19.9 | 0.6 | 20.5 |
| | A3 | 20.2 | 0.1 | 20.2 | 26.7 | 0.1 | 26.8 | 28.5 | 0.1 | 28.6 |
| | A4 | 12.8 | 0.1 | 12.9 | 16.8 | 0.2 | 16.9 | 17.5 | 0.2 | 17.7 |
| CCSD(T) | A1 | 12.5 | 0.3 | 12.8 | 15.8 | 0.5 | 16.3 | 17.5 | 0.7 | 18.1 |
| | A2 | 15.1 | 0.3 | 15.4 | 19.1 | 0.5 | 19.7 | 21.2 | 0.7 | 21.9 |
| | A3 | 22.2 | 0.1 | 22.3 | 29.4 | 0.1 | 29.5 | 31.4 | 0.1 | 31.6 |
| | A4 | 14.1 | 0.1 | 14.2 | 18.5 | 0.2 | 18.6 | 19.3 | 0.2 | 19.5 |
| B3LYP | A1 | 3.0 | 0.2 | 3.2 | 3.3 | 0.2 | 3.4 | 3.6 | 0.3 | 3.8 |
| | A2 | 3.0 | 0.2 | 3.2 | 3.3 | 0.2 | 3.4 | 3.6 | 0.3 | 3.8 |
| | A3 | 3.8 | 0.0 | 3.8 | 4.1 | 0.0 | 4.1 | 4.2 | 0.0 | 4.3 |
| | A4 | 3.8 | 0.0 | 3.8 | 4.1 | 0.0 | 4.1 | 4.2 | 0.0 | 4.2 |
| SFDC-HF | B1 | 0.1 | 0.0 | 0.2 | 0.1 | 0.1 | 0.2 | 0.1 | 0.1 | 0.2 |
| | B2 | 0.1 | 0.0 | 0.2 | 0.1 | 0.1 | 0.2 | 0.1 | 0.1 | 0.2 |
| | B3 | 0.1 | 0.0 | 0.1 | 0.1 | 0.0 | 0.2 | 0.2 | 0.0 | 0.2 |
| | B4 | 0.1 | 0.0 | 0.2 | 0.2 | 0.0 | 0.2 | 0.2 | 0.0 | 0.2 |
| | B5 | 0.1 | 0.0 | 0.1 | 0.1 | 0.0 | 0.1 | 0.1 | 0.0 | 0.1 |
| | B6 | 0.1 | 0.0 | 0.1 | 0.1 | 0.0 | 0.1 | 0.1 | 0.0 | 0.2 |
| SFDC-MP2 | B1 | 4.0 | 0.2 | 4.3 | 6.6 | 0.7 | 7.3 | 7.6 | 1.1 | 8.6 |
| | B2 | 6.1 | 0.3 | 6.3 | 9.8 | 0.7 | 10.5 | 11.3 | 1.1 | 12.4 |
| | B3 | 13.4 | 0.1 | 13.5 | 20.1 | 0.2 | 20.3 | 22.8 | 0.3 | 23.1 |
| | B4 | 3.6 | 0.1 | 3.7 | 5.0 | 0.3 | 5.3 | 5.5 | 0.4 | 5.9 |
| | B5 | 2.1 | 0.1 | 2.2 | 3.5 | 0.3 | 3.8 | 4.0 | 0.5 | 4.5 |
| | B6 | 1.6 | 0.2 | 1.8 | 2.4 | 0.3 | 2.8 | 2.8 | 0.5 | 3.3 |
| SFDC-CCSD | B1 | 4.1 | 0.2 | 4.3 | 6.6 | 0.6 | 7.2 | 7.5 | 0.8 | 8.3 |
| | B2 | 5.3 | 0.2 | 5.6 | 8.5 | 0.6 | 9.1 | 9.7 | 0.8 | 10.5 |
| | B3 | 11.4 | 0.1 | 11.5 | 17.0 | 0.1 | 17.1 | 19.2 | 0.2 | 19.4 |
| | B4 | 3.1 | 0.1 | 3.2 | 4.3 | 0.2 | 4.5 | 4.8 | 0.2 | 5.0 |
| | B5 | 1.8 | 0.1 | 2.0 | 3.2 | 0.2 | 3.4 | 3.6 | 0.3 | 3.9 |
| | B6 | 1.3 | 0.1 | 1.4 | 2.1 | 0.2 | 2.3 | 2.3 | 0.3 | 2.6 |
| SFDC-CCSD(T) | B1 | 5.3 | 0.2 | 5.5 | 8.1 | 0.7 | 8.8 | 9.2 | 0.8 | 10.0 |
| | B2 | 6.6 | 0.2 | 6.8 | 10.1 | 0.7 | 10.8 | 11.5 | 0.8 | 12.3 |
| | B3 | 13.5 | 0.1 | 13.6 | 19.7 | 0.1 | 19.8 | 22.2 | 0.2 | 22.4 |
| | B4 | 4.4 | 0.1 | 4.6 | 6.0 | 0.2 | 6.2 | 6.5 | 0.3 | 6.7 |
| | B5 | 2.2 | 0.1 | 2.3 | 3.8 | 0.2 | 4.0 | 4.3 | 0.3 | 4.6 |
| | B6 | 1.6 | 0.1 | 1.8 | 2.5 | 0.3 | 2.7 | 2.8 | 0.3 | 3.1 |
| SFDC-B3LYP | B1 | 0.1 | 0.0 | 0.1 | 0.1 | 0.1 | 0.1 | 0.1 | 0.1 | 0.2 |
| | B2 | 0.1 | 0.0 | 0.1 | 0.1 | 0.1 | 0.1 | 0.1 | 0.1 | 0.2 |
| | B3 | 0.1 | 0.0 | 0.1 | 0.1 | 0.0 | 0.1 | 0.1 | 0.0 | 0.1 |
| | B4 | 0.1 | 0.0 | 0.1 | 0.1 | 0.0 | 0.1 | 0.1 | 0.0 | 0.2 |
| | B5 | 0.1 | 0.0 | 0.1 | 0.1 | 0.0 | 0.1 | 0.1 | 0.0 | 0.2 |
| | B6 | 0.1 | 0.0 | 0.1 | 0.1 | 0.0 | 0.1 | 0.1 | 0.0 | 0.2 |

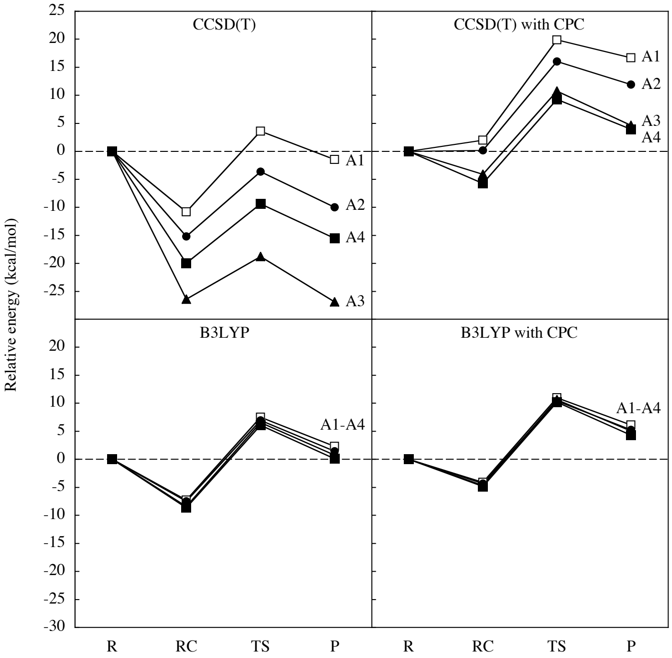

**Figure 3.2** Reaction profiles for oxidative addition of methane to Pd obtained using GAUSSIAN with CCSD(T) and B3LYP for various basis sets, without (left) and with counterpoise correction (right)

functions from one to three. The BSSE values obtained with basis sets B1-B4 are smaller than those obtained with A1-A4, but they display a similar trend as the latter. The BSSE increases going from RC to TS to P. The reason for this is that the C and H atoms and, thus, their basis functions come closer and begin to surround the Pd atom. This improves the flexibility and polarization of the basis set and thus the description of the wavefunction around the Pd atom. Note also that the BSSE stems nearly entirely from the improvement of the stabilization of Pd as methane ghost functions are added. The energy lowering of methane due to adding Pd ghost functions is in all cases small.

The above points out the prominent role that electron correlation plays in our model systems. And, more importantly, it also reveals the inadequacy of basis sets A1-A4 and B1-B4 for describing it. This may be somewhat surprising in view of earlier reports that basis sets of a quality comparable to that of A3, A4 and B3, B4 yield satisfactory energies for organometallic and coordination compounds (see, for example, refs. 72 and 73). On the other hand, it is consistent with the large variation of values obtained in earlier theoretical studies on this model reaction. One reason for the increased sensitivity that we find toward the quality of the theoretical approach is that the presence of *f* polarization functions is only the minimum requirement for describing the correlation of Pd-4*d* electrons. In this respect, the Pd basis sets in A3, A4 and B3, B4 should be

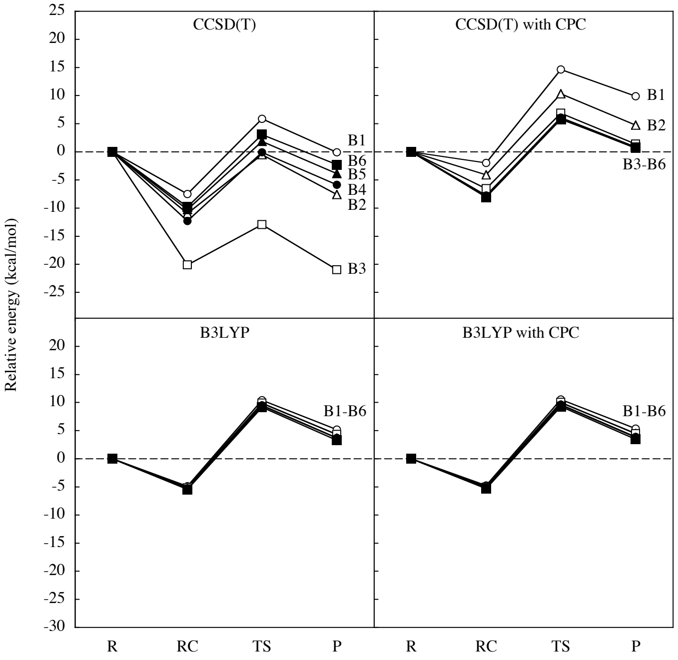

**Figure 3.3** Reaction profiles for oxidative addition of methane to Pd obtained using DIRAC with CCSD(T) and B3LYP for various basis sets, without (left) and with counterpoise correction (right)

considered minimal and cannot be expected to have achieved convergence. Furthermore, the consequences of any inadequacy in the basis set shows up more severely in processes that involve a bare, uncoordinated transition metal atom as one of the reactants because here the effect of the additional assistance of basis functions on the substrate is more severe than in situations where the transition metal fragment is already surrounded by, for example, ligands. This shows up in the large BSSE values.

We have been able to achieve virtual convergence of the CCSD(T) relative energies by further increasing the flexibility and polarization of the Pd basis set and by correcting for the BSSE through counterpoise correction. Let us first point out why the CCSD(T)/A4 and CCSD(T)/B4 values cannot be trusted without further scrutiny. This is an important issue because inspection of Table 3.3 and Figures 3.2 and 3.3 suggests that the *counterpoise-corrected* energies do converge from A3 to A4 and from B3 to B4. For example, the counterpoise-corrected activation energies computed with A3 and A4 at CCSD(T) are equal within 2 kcal/mol. Note however that the BSSE of 14-20 kcal/mol is still larger than the relative energies we wish to compute. It is therefore necessary to explore the behaviour of the reaction profile if the basis set is further increased. In particular, we wish to achieve a situation, in which the BSSE at least becomes smaller than the relative energies. Thus, we have introduced an additional diffuse *p* function

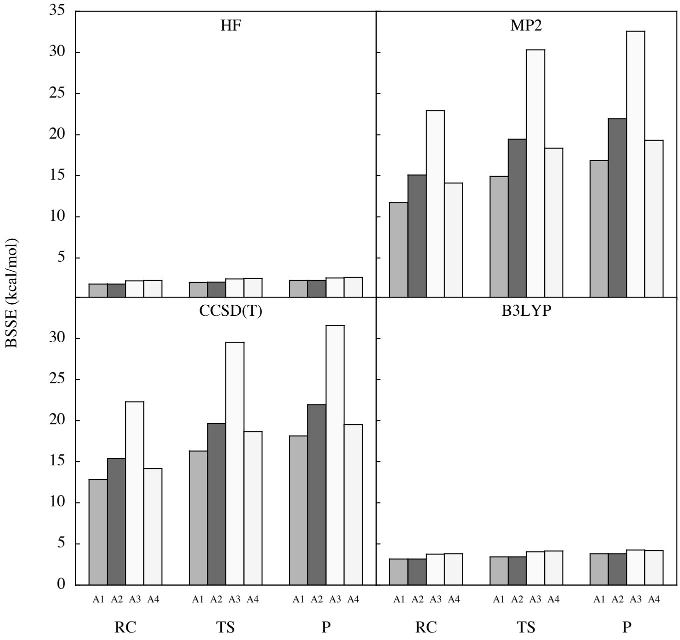

**Figure 3.4** Basis set superposition error (BSSE) for stationary points along the reaction coordinate of oxidative addition of methane to Pd obtained using GAUSSIAN with various methods and basis sets

(going to B5) and a *g* polarization function (going to B6). We have chosen the B series of basis sets (based on Faegri's 24*s*16*p*13*d* basis for Pd) for further improvements because they are superior to the A series (based on Hay and Wadt's LANL2TZ basis) in the sense that they yield a significantly smaller BSSE (compare A1-A4 with B1-B4 in Figures 3.4 and 3.5). Indeed, along B3-B6, the BSSE in, for example, the CCSD(T) activation energy decreases monotonically 19.8 to 6.2 to 4.0 to 2.7 kcal/mol and is thus clearly smaller than the relative energies that we compute. The counterpoise-corrected relative energies at CCSD(T) are converged within a few tenths of kcal/mol along B1-B6. For example, the activation energy at CCSD(T) amounts to 14.7, 10.3, 6.9, 6.1, 5.9, and 5.8 kcal/mol. Our best estimate, obtained at CCSD(T)/B6 with CPC, is –8.1 kcal/mol for the formation of the reactant complex, 5.8 kcal/mol for the activation energy relative to the separate reactants and 0.8 kcal/mol for the reaction energy. If we take into account zero-point vibrational energy effects computed at BLYP/TZ2P, this yields –8.3 kcal/mol for the formation of the reactant complex, 3.1 kcal/mol for the activation energy relative to the reactants and –1.2 kcal/mol for the reaction energy.

Our benchmark values agree well with earlier results at PCI-80 and therefore further consolidate the theoretical reaction profile. They also agree well with the experimental result, in fact slightly better so than PCI-80, that the reactant complex is bound by at least 8 kcal/mol. The fact that the experimental reaction rate is extremely small to

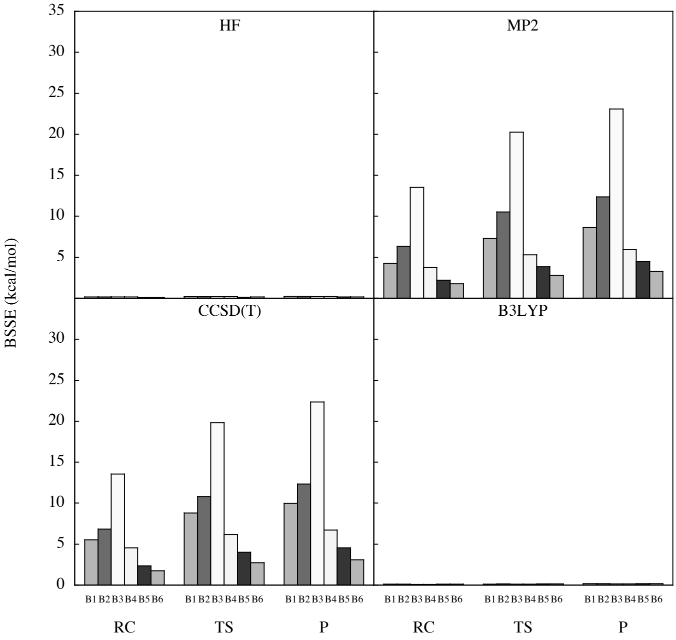

**Figure 3.5** Basis set superposition error (BSSE) for stationary points along the reaction coordinate of oxidative addition of methane to Pd obtained using DIRAC with various methods and basis sets

negligible in spite of a moderate energy barrier of 3.1 kcal/mol is consistent with an important statistical or entropic bottleneck[22] (associated with the decrease in the number of available quantum states as one goes from reactants to transition state) and the extremely short lifetime of the internally hot reactant complex that has been invoked to explain why this complex has not been observed in experiments.[34]

Finally, we note that the BSSE is small not only in uncorrelated *ab initio* calculations (HF) but also in the DFT calculations (B3LYP). This robustness of DFT is due to the *way* in which the correlation hole is described in this method rather than to the *absence* of correlation as in HF. In general, correlated *ab initio* methods depend more strongly on the extent of polarization of the basis set because the polarization functions are essential to generate the configurations through which the wavefunction can describe the correlation hole. In DFT, on the other hand, the correlation hole is built-in into the potential and the energy functional and polarization functions mainly play the much less delicate role of describing polarization of the electron density. Interestingly, in the HF and B3LYP calculations with GAUSSIAN, we observe a small but non-negligible BSSE of 2-4 kcal/mol, which does not decrease with increasing basis-set size along A1-A4 (see Table 3.4 and Figure 3.4). In the DIRAC calculations, however, the BSSE for both HF and B3LYP is essentially zero (less than 0.2 kcal/mol) for all basis sets B1-B6. This difference between the GAUSSIAN and DIRAC calculations can be ascribed to the fact that an ECP for Pd is used in the former whereas the latter are all-electron calculations. Ideally, the ECP should account for the fact that the valence orbitals must be orthogonal to the core orbitals. It is likely however that, effectively, the ECP used with the LANL2 basis sets of Pd is not able to completely project out the palladium-core components of the methane orbitals. In the DIRAC all-electron calculations this problem is of course not present. We conclude that the best B3LYP reaction profile with an activation energy of 9.3 kcal/mol is obtained at the relativistic SFDC-B3LYP/B6 level with CPC.

## 3.4 Conclusions

We have computed a benchmark for the archetypal oxidative addition of the methane C–H bond to Pd that derives from a hierarchical series of relativistic *ab initio* methods and highly polarized basis sets. Our best estimate is –8.1 kcal/mol for the formation of the reactant complex, 5.8 kcal/mol for the activation energy relative to the reactants, and 0.8 kcal/mol for the reaction energy. This is obtained at the counterpoise-corrected, four-component spin-free Dirac-Coulomb CCSD(T)/(24*s*16*p*13*d*+4*f*+*p*+*g*) level, which is virtually converged with respect to the basis-set size.

Our benchmark values agree well with earlier results obtained with the PCI-80 method and slightly better than the latter with experimental data. This agreement and, importantly, the fact that our CCSD(T) benchmark PES derives from a converged hierarchical series of basis sets consolidates the theoretical PES for this model reaction.

Our findings stress the importance of sufficient higher-angular momentum polarization functions, *f* and *g*, as well as counterpoise correction for obtaining reliable activation energies. We show that standard basis sets, such as LANL2DZ+1*f* for Pd, are not sufficiently polarized for this purpose and lead to erroneous results at CCSD(T).

# 4 DFT validation study for the oxidative addition of the methane C–H bond to Pd. Performance of various density functionals

Adapted from
G. Th. de Jong, D. P. Geerke, A. Diefenbach, F. M. Bickelhaupt *Chem. Phys.* **2005**, *313*, 261

## Abstract

We have evaluated the performance of 24 popular density functionals for describing the potential energy surface (PES) of the archetypal oxidative addition reaction of the methane C–H bond to the palladium atom by comparing the results with our *ab initio* (CCSD(T)) benchmark study of this reaction. The density functionals examined cover the local density approximation (LDA), the generalized gradient approximation (GGA), meta-GGAs as well as hybrid density functional theory. Relativistic effects are accounted for through the zeroth-order regular approximation (ZORA). The basis-set dependence of the density-functional-theory (DFT) results is assessed for the BLYP functional using a hierarchical series of Slater-type orbital (STO) basis sets ranging from unpolarized double-$\zeta$ (DZ) to quadruply polarized quadruple-$\zeta$ quality (QZ4P). Stationary points on the reaction surface have been optimized using various GGA functionals, all of which yield geometries that differ only marginally. Counterpoise-corrected relative energies of stationary points are converged to within a few tenths of a kcal/mol if one uses the doubly polarized triple-$\zeta$ (TZ2P) basis set and the basis-set superposition error (BSSE) drops to 0.0 kcal/mol for our largest basis set (QZ4P). Best overall agreement with the *ab initio* benchmark PES is achieved by functionals of the GGA, meta-GGA, and hybrid-DFT type, with mean absolute errors of 1.3 to 1.4 kcal/mol and errors in activation energies ranging from +0.8 to –1.4 kcal/mol. Interestingly, the well-known BLYP functional compares very reasonably with an only slightly larger mean absolute error of 2.5 kcal/mol and an underestimation by –1.9 kcal/mol of the overall barrier (i.e., the difference in energy between the TS and the separate reactants). For comparison, with B3LYP we arrive at a mean absolute error of 3.8 kcal/mol and an overestimation of the overall barrier by 4.5 kcal/mol.

## 4.1 Introduction

Density functional theory (DFT)[6-9] is a popular tool for electronic structure calculations with a wide range of chemical applications.[9,67,74] One such application, for which DFT performs particularly well in terms of a high computational efficiency combined with a relatively high accuracy, is the investigation of organometallic and coordination compounds, which are often computationally too demanding to be tackled at sufficiently accurate levels of conventional *ab initio* theory. A general concern, however, associated with the application of DFT to the investigation of chemical reactions is its notorious tendency to underestimate activation energies.[10] In the previous chapter, we have obtained a reliable benchmark for the potential energy surface (PES) of the organometallic reaction of methane oxidative addition to Pd(0), see Scheme 3.1.

This reaction is archetypal for C–H bond activation, which is the key step in many processes of catalytic conversion of the abundant but rather inert alkanes into more useful products,[28,29] and Pd complexes are one of the most important groups of catalysts for such processes.[31] The insertion of the Pd atom into the C–H bond in alkanes has therefore received considerable attention, experimentally[32-36] and theoretically.[33,35,37-44]

In the present study, we have evaluated the performance of 24 popular density functionals for describing the PES of the oxidative addition reaction of the methane C–H bond to the Pd atom by comparing the results with the above-mentioned *ab initio* benchmark. The latter yields the following key kinetic and thermodynamic parameters: –8.1 kcal/mol for the formation of the reactant complex, 5.8 kcal/mol for the activation energy relative to the separate reactants and 0.8 kcal/mol for the reaction energy. These values were obtained at the counterpoise-corrected, CCSD(T)/(24$s$16$p$13$d$+4$f$+$p$+$g$) level including relativistic effects through a full four-component all-electron approach, and are converged to within 0.1-0.2 kcal/mol as a function of the basis-set size. Whereas this result is satisfactory in terms of accuracy and reliability, the approach is prohibitively expensive if one wishes to study more realistic model catalysts and substrates. Instead, we use this result as a benchmark for evaluating the performance of a series of approximate density functionals. The latter cover the local density approximation (LDA), the generalized gradient approximation (GGA), meta-GGAs as well as hybrid density functional theory. We also evaluate the dependence of the resulting PES on the basis-set size and on the use of the frozen-core approximation. Our purpose is to arrive at a ranking of density functional approaches in terms of the accuracy with which they describe our model reaction, in particular the activation energy, and to hopefully find a functional that performs well and can be used in future investigations of more complex catalytic systems. We focus on the overall activation energy, that is, the difference in energy between the TS and the separate reactants, which is decisive for the rate of chemical reactions in the gas phase, in particular, if they occur under low-pressure conditions in which the reaction system is (in good approximation) thermally isolated.[34,75] But we also address the central barrier, that is, the difference in energy between the TS and the reactant complex. Here, we anticipate that the well-known BLYP functional performs very satisfactorily and, in the case of the overall activation energy, even slightly better than the much-advocated B3LYP hybrid functional.

## 4.2 Methods

### 4.2.1 Geometries

The ADF program was used for all calculations.[49-51] The evaluation of density functionals has been carried out in three stages. First, we have compared the performance of seven GGA functionals for computing the geometries and relative energies of the stationary points along the PES of our model reaction. These functionals are BP86,[52,76] BLYP,[52,53] PW91,[77] PBE,[78] revPBE,[79] RPBE,[80] and OLYP.[53,81] Apart from using other functionals than BLYP, the same computational settings were used as described in Section 3.2.1, i.e., using ZORA, the TZ2P basis set and the frozen-core approximation. Note that the geometries resulting from using BLYP in this approach are exactly the same as in the *ab initio* benchmark study in the previous chapter.

Enthalpies at 298.15 K and 1 atmosphere were calculated from 0 K electronic energies according to Eq. 4.1, assuming an ideal gas:

$$\Delta H_{298} = \Delta E + \Delta E_{\text{trans},298} + \Delta E_{\text{rot},298} + \Delta E_{\text{vib},0} + \Delta(\Delta E_{\text{vib},0})_{298} + \Delta(pV). \tag{4.1}$$

$\Delta E_{\text{trans},298}$, $\Delta E_{\text{rot},298}$ and $\Delta E_{\text{vib},0}$ are the relative differences in translational, rotational and zero-point vibrational energy; $\Delta(\Delta E_{\text{vib},0})_{298}$ is the change in the vibrational energy difference going from 0 to 298.15 K. The vibrational energy corrections are based on our frequency calculations. The molar work term $\Delta(pV)$ is $(\Delta n)RT$; $\Delta n = -1$ for two reactants combining to one species. Thermal corrections for the electronic energy are neglected.

### 4.2.2 Basis sets

In a second stage, based on the ZORA-BLYP/TZ2P geometries, we have evaluated in a series of single-point calculations the dependence of the ZORA-BLYP relative energies of the stationary points on the basis-set size for four different all-electron (i.e., no frozen-core approximation) STO basis sets, namely, ae-DZ, ae-TZP, ae-TZ2P and ae-QZ4P, and on the use of the frozen-core approximation. In the course of this evaluation, we have also computed the basis-set superposition error (BSSE), which can be accounted for by counterpoise correction.[12] The ae-DZ basis set is of double-$\zeta$ quality, is unpolarized for H and C but has been augmented with a set of 5*p* polarization functions for Pd. The ae-TZP basis set is of triple-$\zeta$ quality and has been augmented with one set of polarization functions on every atom: 2*p* on H, 3*d* on C, and 5*p* on Pd. The ae-TZ2P basis set is the all-electron counterpart corresponding to the TZ2P basis that is used with the frozen-core approximation. The ae-QZ4P basis set is of quadruple-$\zeta$ quality and has been augmented with four sets of polarization functions on each atom: two 2*p* and two 3*d* sets on H, two 3*d* and two 4*f* sets on C, and two 5*p* and two 4*f* sets on Pd.

### 4.2.3 Density functionals

Finally, in stage three, based again on the ZORA-BLYP/TZ2P geometries, we have computed in a post-SCF manner, i.e., using in all cases the electron density obtained at ZORA-BLYP/ae-TZ2P, the relative energies of stationary points along the PES for various LDA, GGA, meta-GGA and hybrid functionals. In addition to those used in stage one for geometry optimizations, the following density functionals were examined: the LDA functional VWN;[82] the GGA functionals Becke88x + BR89c,[83] FT97,[84] HCTH/93,[85] BOP,[52,86] HCTH/120,[87] HCTH/147,[87] and HCTH/407;[88] the meta-GGA functionals BLAP3,[89] VS98,[90] KCIS,[91] PKZB,[92] Bm$\tau$1,[93] OLAP3,[81,89] and TPSS;[94] and the hybrid functionals B3LYP[61] (based on VWN5[95]) and TPSSh.[94]

## 4.3 Results and discussion

### 4.3.1 Geometries and energies of stationary points

First, we examine the geometries of the stationary points for the model reaction, computed with the GGA functionals BP86, BLYP, PW91, PBE, revPBE, RPBE and OLYP in combination with the TZ2P basis set, the frozen-core approximation, and ZORA to account for relativistic effects. Geometry parameters are defined in Figure 4.1 and their values optimized with each of the functionals are collected in Table 4.1.

For all functionals, the reaction proceeds from the reactants via formation of a stable reactant complex, in which methane coordinates in an $\eta^2$ fashion to Pd, followed by a

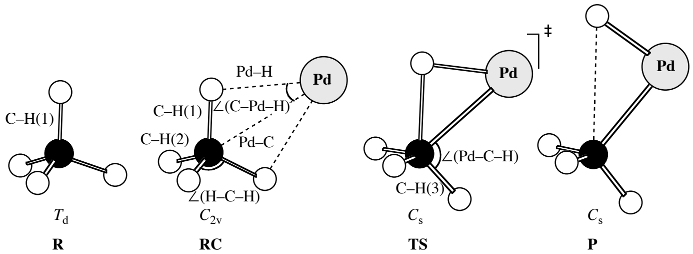

**Figure 4.1** Structures of the stationary points. See also Table 4.1

**Table 4.1** Geometry parameters[a] (in Å, degrees), optimized with various density functionals,[b] of the stationary points along the reaction coordinate for the oxidative insertion of Pd into the methane C–H bond

| Method | | C–H(1) | C–H(2) | C–H(3) | Pd–C | Pd–H | ∠(C–Pd–H) | ∠(H–C–H) | ∠(Pd–C–H) |
|---|---|---|---|---|---|---|---|---|---|
| BP86 | R | 1.096 | | | | | | | |
| | RC | 1.135 | 1.094 | | 2.288 | 1.942 | 29.7 | 107.3 | |
| | TS | 1.605 | 1.095 | 1.105 | 2.073 | 1.552 | 50.1 | 109.6 | 90.4 |
| | P | 2.413 | 1.096 | 1.103 | 1.995 | 1.528 | 85.4 | 111.0 | 102.6 |
| BLYP | R | 1.095 | | | | | | | |
| | RC | 1.123 | 1.092 | | 2.392 | 2.021 | 27.9 | 107.7 | |
| | TS | 1.615 | 1.092 | 1.101 | 2.114 | 1.562 | 49.4 | 110.0 | 90.0 |
| | P | 2.479 | 1.093 | 1.101 | 2.021 | 1.539 | 87.2 | 111.3 | 102.5 |
| PW91 | R | 1.094 | | | | | | | |
| | RC | 1.133 | 1.092 | | 2.287 | 1.942 | 29.7 | 107.4 | |
| | TS | 1.611 | 1.094 | 1.103 | 2.066 | 1.551 | 50.5 | 109.6 | 90.7 |
| | P | 2.405 | 1.094 | 1.102 | 1.992 | 1.528 | 85.1 | 111.0 | 102.6 |
| PBE | R | 1.096 | | | | | | | |
| | RC | 1.136 | 1.094 | | 2.284 | 1.941 | 29.8 | 107.3 | |
| | TS | 1.618 | 1.095 | 1.105 | 2.066 | 1.552 | 50.7 | 109.5 | 90.9 |
| | P | 2.404 | 1.096 | 1.104 | 1.992 | 1.529 | 85.1 | 111.0 | 102.6 |
| revPBE | R | 1.097 | | | | | | | |
| | RC | 1.131 | 1.095 | | 2.345 | 1.985 | 28.8 | 107.6 | |
| | TS | 1.626 | 1.096 | 1.105 | 2.083 | 1.554 | 50.6 | 109.6 | 91.2 |
| | P | 2.427 | 1.097 | 1.104 | 2.004 | 1.533 | 85.6 | 110.9 | 102.8 |
| RPBE | R | 1.097 | | | | | | | |
| | RC | 1.129 | 1.095 | | 2.366 | 2.001 | 28.4 | 107.6 | |
| | TS | 1.630 | 1.096 | 1.105 | 2.087 | 1.555 | 50.6 | 109.6 | 91.2 |
| | P | 2.434 | 1.097 | 1.105 | 2.008 | 1.534 | 85.7 | 111.0 | 102.8 |
| OLYP | R | 1.093 | | | | | | | |
| | RC | 1.120 | 1.091 | | 2.389 | 2.018 | 27.9 | 107.8 | |
| | TS | 1.651 | 1.092 | 1.101 | 2.065 | 1.539 | 52.1 | 109.5 | 92.4 |
| | P | 2.408 | 1.093 | 1.100 | 1.994 | 1.522 | 85.3 | 110.8 | 102.8 |

[a] See Figure 4.1 for definition.

[b] With TZ2P basis set and frozen-core approximation. Relativistic effects treated with ZORA.

transition state and, finally, a stable product. The imaginary frequency in the transition state associated with the normal mode that connects reactant complex and product varies, depending on the functional, between 707 and 778 *i* $\text{cm}^{-1}$.

The geometries obtained with the various GGA functionals do not show significant mutual discrepancies, and they agree well with earlier DFT studies.[22,44] The C–H bond distance values are very robust with respect to changing the functional, with variations in the order of a few thousandths of an Å. Note that variations in the length of the activated C–H bond become larger, up to 0.07 Å in the product, as the reaction progresses. This is in line with the fact that this bond is being broken along the reaction coordinate, which causes the PES to become increasingly soft in this coordinate and, thus, sensitive to changes in the computational method. More pronounced variations are found for the weak Pd–C and Pd–H bonds. This holds especially for the loosely bound RC, which shows fluctuations of up to one tenth of an Å for Pd–C and a few hundredths for Pd–H. The variations in these bond distances drop to a few hundredths or even a few thousandths of an Å as the reaction proceeds to TS and P in which more stable coordination bonds are formed. Thus, only moderate variations in bond distances occur along the various functionals and they are more pronounced for the softer bonds. This is also reflected by the variations in bond angles. These variations are very small as long as firmly bound triplets of atoms are involved (e.g., for H–C–H angles) whereas they become larger for angles opposite to a soft bond (e.g., for C–Pd–H or Pd–C–H angles).

Next, we examine the relative energies of the stationary points obtained with the same functional that was used for optimizing the geometry. As pointed out above, we first focus on the overall activation energy, that is, the difference in energy between the TS and the separate reactants, which is decisive for the rate of chemical reactions in the gas phase, in particular, if they occur under low-pressure conditions. Later on, in Section 4.3.4, we also address the central barrier, that is, the difference in energy between the TS and the reactant complex. Relative energies, with and without zero-point vibrational energy correction, as well as relative enthalpies are collected in Table 4.2. Relative energies are also graphically represented in Figure 4.2. The performance of the various functionals is assessed by a systematic comparison of the resulting PESs with our CCSD(T) benchmark, which is converged to within 0.1 to 0.2 kcal/mol regarding the basis-set size (see Chapter 3). For comparison, we have included in Table 4.2 an earlier *ab initio* benchmark obtained by Siegbahn and coworkers with the PCI-80 method, in which correlation energy is accounted for by a parameterization scheme.[35]

The investigated GGAs fall into three groups regarding their agreement with the benchmark results. BP86, PBE and PW91 overestimate the metal-substrate bonding and arrive at a too firmly bound reactant complex, a significantly underestimated barrier (by nearly 10 kcal/mol for PW91), and a too exothermic reaction energy. The situation is opposite for OLYP, which underestimates metal-substrate bonding and yields a too weakly bound reactant complex, a barrier that is too high by 4 kcal/mol, and a too endothermic reaction energy. On the other hand, BLYP and the two revisions of PBE, i.e., revPBE and RPBE, achieve quite satisfactory agreement with the coupled-cluster

**Table 4.2** Relative energies without ($\Delta E$) and with zero-point vibrational energy correction ($\Delta E + \Delta ZPE$), and relative enthalpies at 298.15 K ($\Delta H$) of the stationary points[a] for oxidative insertion of Pd into the $H_3C$–H bond (in kcal/mol), computed with various functionals,[b] and compared to *ab initio* benchmarks[c]

| | $\Delta E$ | | | $\Delta E + \Delta ZPE$ | | | $\Delta H$ | | |
|---|---|---|---|---|---|---|---|---|---|
| Method | RC | TS | P | RC | TS | P | RC | TS | P |
| *DFT computations (this study)* | | | | | | | | | |
| BP86 | –11.0 | –2.6 | –8.5 | –11.3 | –5.2 | –10.4 | –12.0 | –6.0 | –11.1 |
| BLYP | –6.7 | 3.9 | –3.4 | –6.9 | 1.2 | –5.4 | –7.4 | 0.5 | –6.1 |
| PW91 | –12.4 | –3.7 | –9.3 | –12.5 | –6.3 | –11.0 | –13.2 | –7.6 | –11.7 |
| PBE | –11.9 | –3.3 | –8.7 | –12.3 | –6.0 | –10.6 | –12.9 | –6.7 | –11.3 |
| revPBE | –6.5 | 2.9 | –2.8 | –6.9 | 0.2 | –4.8 | –7.4 | –0.5 | –5.4 |
| RPBE | –6.0 | 3.8 | –1.9 | –6.3 | 1.2 | –3.9 | –6.8 | 0.4 | –4.6 |
| OLYP | –1.4 | 9.8 | 4.9 | –1.7 | 7.1 | 2.8 | –2.2 | 6.4 | 2.2 |
| *Ab initio benchmarks* | | | | | | | | | |
| CCSD(T) // BLYP | –8.1 | 5.8 | 0.8 | –8.3 | 3.1 | –1.2 | | | |
| PCI-80 // HF | | | | –5.1 | 3.6 | –2.3 | | | |

a Geometries and energies computed at the same level of theory.

b With TZ2P basis set with frozen-core approximation. Relativistic effects treated with ZORA.

c CCSD(T) benchmark from Chapter 3 and PCI-80 from ref. 35.

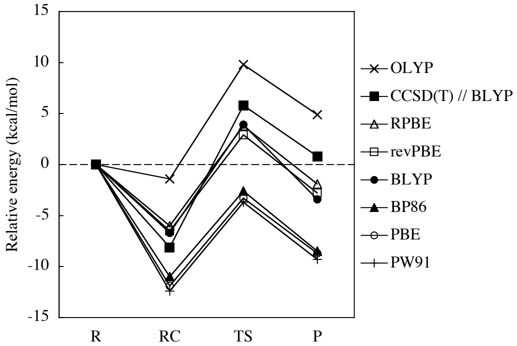

**Figure 4.2** Reaction profiles for the model reaction obtained with various density functionals and the TZ2P basis set with frozen-core approximation (geometries and energies computed at the same level of theory)

PES, with mean absolute errors of 2.3 to 2.7 kcal/mol. The reaction barrier is only slightly underestimated by these functionals, namely, by 1.9 (BLYP), 2.9 (revPBE) and 2.0 kcal/mol (RPBE), with BLYP performing a little better than the other functionals. Based on this result and the fact that BLYP is robust and well established, we choose this functional in the following sections to carry out further performance analyses.

### 4.3.2 Basis sets and frozen-core approximation

We proceed with examining the convergence of the (all-electron) BLYP relative energies of stationary points as the basis set increases along ae-DZ, ae-TZP, ae-TZ2P and ae-QZ4P, using the ZORA-BLYP/TZ2P geometries mentioned above. We also investigate the convergence of the BSSE and the effect of using the frozen-core approximation. The results are shown in Tables 4.3 and 4.4, and in Figure 4.3.

In the first place, we note that it is perfectly valid to use the frozen-core approximation as it has hardly any effect on the relative energies. This becomes clear if one compares the frozen-core BLYP/TZ2P results in Table 4.2 (–6.7, 3.9 and –3.4 kcal/mol for RC, TS and P) with the all-electron BLYP/ae-TZ2P data in Table 4.3 (no CPC: –6.7, 3.9 and –3.6 kcal/mol for RC, TS and P). The frozen-core and all-electron

**Table 4.3** Relative energies (in kcal/mol) of the stationary points[a] computed with BLYP and various basis sets with all electrons treated variationally, without and with counterpoise correction (CPC)[b]

| | RC | | TS | | P | |
|---|---|---|---|---|---|---|
| Basis set | no CPC | with CPC | no CPC | with CPC | no CPC | with CPC |
| ae-DZ | –3.5 | –1.7 | 10.0 | 12.0 | 2.0 | 4.2 |
| ae-TZP | –6.2 | –6.0 | 5.0 | 5.3 | –2.2 | –1.9 |
| ae-TZ2P | –6.7 | –6.5 | 3.9 | 4.2 | –3.6 | –3.3 |
| ae-QZ4P | –6.8 | –6.8 | 3.4 | 3.4 | –4.0 | –4.0 |

a Geometries optimized at ZORA-BLYP/TZ2P with frozen-core approximation.

b Relativistic effects treated with ZORA.

**Table 4.4** Basis-set superposition error (in kcal/mol) in the stationary points[a] for oxidative insertion of Pd into the $H_3C–H$ bond, computed with BLYP and various basis sets with all electrons treated variationally[b]

| Basis set | | RC | TS | P |
|---|---|---|---|---|
| ae-DZ | Pd | 1.3 | 1.3 | 1.4 |
| | $CH_4$ | 0.5 | 0.7 | 0.9 |
| | *Total* | *1.8* | *2.0* | *2.3* |
| ae-TZP | Pd | 0.1 | 0.1 | 0.1 |
| | $CH_4$ | 0.1 | 0.2 | 0.2 |
| | *Total* | *0.2* | *0.3* | *0.3* |
| ae-TZ2P | Pd | 0.1 | 0.1 | 0.1 |
| | $CH_4$ | 0.1 | 0.2 | 0.2 |
| | *Total* | *0.2* | *0.3* | *0.3* |
| ae-QZ4P | Pd | 0.0 | 0.0 | 0.0 |
| | $CH_4$ | 0.0 | 0.0 | 0.0 |
| | *Total* | *0.0* | *0.0* | *0.0* |

a Geometries optimized at ZORA-BLYP/TZ2P with frozen-core approximation.

b Relativistic effects treated with ZORA.

values for RC and TS are identical and for P the difference amounts to only 0.2 kcal/mol.

Next, the issues of basis-set convergence and BSSE are addressed. The data in Table 4.3 show that the relative energies of stationary points are already converged to within a few tenths of a kcal/mol with the ae-TZ2P basis set. The BSSE drops to 0.3 kcal/mol or less for this basis set and virtually vanishes if one goes to ae-QZ4P (see Table 4.4). For example, the activation energy without counterpoise correction varies from 10.0 to 5.0 to 3.9 to 3.4 kcal/mol along ae-DZ, ae-TZP, ae-TZ2P and ae-QZ4P. The corresponding BSSE amounts to 2.0, 0.3, 0.3 and 0.0 kcal/mol. Note that in fact the BSSE is only significant for the ae-DZ basis set and that it mainly originates from adding ghost functions of $CH_4$ to the description of Pd. This is in line with the work in Chapter 3, in which it was found that basis-set convergence and elimination of the BSSE are achieved much earlier for DFT than for correlated *ab initio* methods (see discussion there). In conclusion, the TZ2P basis in combination with the frozen-core approximation yields an efficient and accurate description of the relative energies of our stationary points.

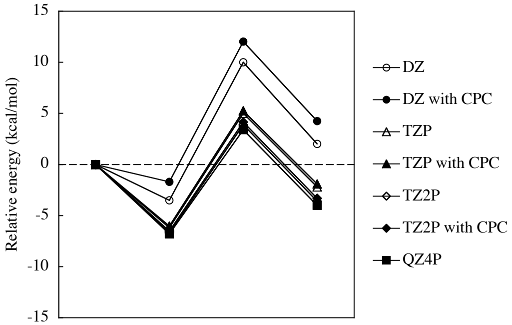

**Figure 4.3** Reaction profiles computed with ZORA-BLYP and various basis sets with all electrons treated variationally, without and with CPC. Geometries optimized using the frozen-core approximation

### 4.3.3 Performance of other density functionals

Finally, on the basis of the ZORA-BLYP/TZ2P geometries discussed above, we have computed the relative energies of the stationary points for various LDA, GGA, meta-GGA and hybrid functionals in combination with the all-electron ae-TZ2P basis set and ZORA for relativistic effects. This was done in a post-SCF manner, i.e., using the functionals with the electron density obtained at ZORA-BLYP/ae-TZ2P. The performance of the functionals is discussed by comparison with the *ab initio* CCSD(T) benchmark from Chapter 3, which is based on the same geometries. The results of this survey are collected in Table 4.5, which shows energies relative to the reactants (R).

For clarity, we wish to point out that the above procedure for computing the relative energies shown in Table 4.5 differs in three respects from that used for computing the relative energies with the seven GGA functionals shown in Table 4.2: (i) an all-electron approach is used instead of the frozen-core approximation, (ii) for all functionals, the

**Table 4.5** Energies (in kcal/mol) of the stationary points[a] relative to the separate reactants, computed for 24 functionals with the ae-TZ2P basis set with all electrons treated variationally[b,c]

| Method | RC | TS | P | Mean abs. err. rel. to R | Err. in barr. rel. to R |
|---|---|---|---|---|---|
| *LDA* | | | | | |
| VWN | –22.7 | –19.0 | –23.7 | 21.3 | –24.8 |
| *GGAs* | | | | | |
| BP86 | –10.4 (–10.5) | –2.2 (–2.3) | –8.4 (–8.5) | 6.5 | –8.0 |
| BLYP | –6.7 | 3.9 | –3.6 | 2.5 | –1.9 |
| Becke88x+BR89c | –7.3 | 4.3 | –4.0 | 2.4 | –1.5 |
| PW91 | –11.8 (–11.8) | –3.3 (–3.4) | –9.1 (–9.2) | 7.6 | –9.1 |
| PBE | –11.3 (–11.3) | –2.8 (–3.0) | –8.4 (–8.5) | 7.0 | –8.6 |
| FT97 | –12.0 | 3.4 | –4.0 | 3.7 | –2.4 |
| revPBE | –6.3 (–6.4) | 3.2 (3.1) | –2.7 (–2.8) | 2.6 | –2.6 |
| HCTH/93 | –1.0 | 10.8 | 6.0 | 5.8 | 5.0 |
| RPBE | –5.7 (–5.8) | 4.2 (4.0) | –1.7 (–1.9) | 2.2 | –1.6 |
| BOP | –3.5 | 7.5 | 0.0 | 2.4 | 1.7 |
| HCTH/120 | –5.3 | 6.6 | 1.4 | 1.4 | 0.8 |
| HCTH/147 | –4.7 | 6.7 | 1.7 | 1.8 | 0.9 |
| HCTH/407 | –2.5 | 11.9 | 6.8 | 5.9 | 6.1 |
| OLYP | –0.7 (–1.2) | 10.3 (10.1) | 5.3 (5.1) | 5.5 | 4.5 |
| *Meta-GGAs* | | | | | |
| BLAP3 | –0.6 | 13.8 | 6.1 | 6.9 | 8.0 |
| VS98 | –10.3 | 5.0 | 0.0 | 1.3 | –0.8 |
| KCIS | –8.0 | 0.1 | –6.3 | 4.3 | –5.7 |
| PKZB | –6.6 | 1.7 | –5.2 | 3.9 | –4.1 |
| Bmτ1 | –0.2 | 14.5 | 6.6 | 7.5 | 8.7 |
| OLAP3 | 5.4 | 20.2 | 15.1 | 14.1 | 14.4 |
| TPSS | –8.6 | 0.8 | –5.5 | 3.9 | –5.0 |
| *Hybrid functionals* | | | | | |
| B3LYP | –4.9 | 10.3 | 4.6 | 3.8 | 4.5 |
| TPSSh | –7.4 | 4.4 | –1.2 | 1.4 | –1.4 |
| *Ab initio benchmark* | | | | | |
| CCSD(T) | –8.1 | 5.8 | 0.8 | | |

[a] Geometries optimized at ZORA-BLYP/TZ2P with frozen-core approximation.

[b] Computed post-SCF using the BLYP electron density, unless stated otherwise. Values in parentheses computed self-consistently, i.e., with the potential and electron density corresponding to the functional indicated. Relativistic effects treated with ZORA.

[c] Mean absolute error for the energies of the three stationary points RC, TS and P relative to the separate reactants (R), and error in the overall barrier, i.e., in the energy of the TS relative to R, compared with the CCSD(T) benchmark from Chapter 3.

BLYP optimized geometries are used instead of geometries optimized with the same functional, and (iii) for all functionals, the BLYP density is used for computing the energy instead of the density corresponding to that functional. The effect of going from frozen-core (TZ2P) to all-electron calculations (ae-TZ2P), i.e., point (i), is negligible, causing a stabilization of 0.2 kcal/mol or less, and has already been discussed in Section 4.3.2. The differences between the values in Tables 4.2 and 4.5 derive mainly from the combined effect of points (ii) and (iii) that causes a destabilization of up to 0.6 kcal/mol of the relative energies if one goes from Table 4.2 to Table 4.5. Both effects are in the order of a few tenths of a kcal/mol. For the TS, the single-point approach contributes generally somewhat more (0.2-0.3 kcal/mol) to this destabilization than the post-SCF approach (0.1-0.2 kcal/mol). This was assessed by computing the relative energies using approximation (ii) but not (iii), i.e., computing them with the density corresponding to the functional under consideration but with the BLYP geometries; the resulting values are provided in parentheses in Table 4.5. In conclusion, the combined effect of approximations (i)-(iii) on the relative energies is in the order of half a kcal/mol.

Finally, we extend our survey to the full range of density functionals that, except for LDA and the seven GGAs discussed above, have been implemented in the ADF program in a post-SCF manner. For all 24 functionals, we have computed the mean absolute error in the relative energies of reactant complex, transition state and product relative to the CCSD(T) benchmark (see Table 4.5). The mean absolute error drops significantly if one goes from LDA (mean abs. err. = 21.3 kcal/mol), which suffers from its infamous overbinding, to GGA functionals (mean abs. err. = 1.4 to 7.6 kcal/mol). However, no significant improvement occurs if one goes from GGA to the more recently developed meta-GGA (mean abs. err. = 1.3-14.1 kcal/mol) and hybrid functionals (mean abs. err. = 1.4-3.8 kcal/mol). Best overall agreement with the *ab initio* benchmark PES is achieved by functionals of the GGA (HCTH/120), meta-GGA (VS98), as well as hybrid-DFT type (TPSSh), with mean absolute errors of 1.3 to 1.4 kcal/mol and errors in activation energies ranging from +0.8 to –1.4 kcal/mol. Interestingly, the well-known BLYP functional compares very reasonably with an only slightly larger mean absolute error of 2.5 kcal/mol and an underestimation of the barrier of –1.9 kcal/mol. Among the meta-GGAs, only the VS98 functional performs better, with an average error of 1.3 kcal/mol and an underestimation of the barrier by 0.8 kcal/mol. Note also that the widely used B3LYP hybrid functional does not perform better, with a mean absolute error of 3.8 kcal/mol and an overestimation of the barrier by 4.5 kcal/mol.

### 4.3.4 Performance for the central barrier

So far, we have concentrated on the overall barrier, i.e., the difference in energy between the TS and the separate reactants, which is decisive for the rate of chemical reactions in the gas phase, in particular, under low-pressure conditions in which the reaction system is (in good approximation) thermally isolated.[34,75] Here, we address the central barrier, that is, the difference in energy between the TS and the RC. The latter becomes decisive in the high-pressure regime, when termolecular collisions are sufficiently efficient to cool the otherwise rovibrationally hot reactant complex, causing it to be in thermal equilibrium with the environment. It may be tempting to conceive the central barrier of the gas-phase reaction as the barrier of the same process in solution. This is, however, not in general the case, because differential solvation of RC and TS can affect the barrier height substantially, even to the extent that relative heights of barriers for competing processes can be inverted (see, for example, Chapter 10). In Table 4.6 the energies of the stationary points relative to the reactant complex are collected.

Of course, the mean absolute error in relative energies changes by changing the point of reference from the separate reactants (in Table 4.5) to the reactant complex (in Table

**Table 4.6** Energies (in kcal/mol) of the stationary points[a] relative to the reactant complex, computed for 24 functionals with the ae-TZ2P basis set with all electrons treated variationally[b,c]

| Method | R | TS | P | Mean abs. err. rel. to RC | Err. in barr. rel. to RC |
|---|---|---|---|---|---|
| *LDA* | | | | | |
| VWN | 22.7 | 3.7 | –1.0 | 11.6 | –10.2 |
| *GGAs* | | | | | |
| BP86 | 10.4 | 8.2 | 2.0 | 5.0 | –5.7 |
| BLYP | 6.7 | 10.6 | 3.1 | 3.5 | –3.3 |
| Becke88x+BR89c | 7.3 | 11.6 | 3.3 | 2.9 | –2.3 |
| PW91 | 11.8 | 8.5 | 2.7 | 5.1 | –5.4 |
| PBE | 11.3 | 8.5 | 2.9 | 4.9 | –5.4 |
| FT97 | 12.0 | 15.4 | 8.0 | 2.1 | 1.5 |
| revPBE | 6.3 | 9.5 | 3.6 | 3.8 | –4.4 |
| HCTH/93 | 1.0 | 11.8 | 7.0 | 3.7 | –2.1 |
| RPBE | 5.7 | 9.9 | 4.0 | 3.8 | –4.0 |
| BOP | 3.5 | 11.0 | 3.5 | 4.3 | –2.9 |
| HCTH/120 | 5.3 | 11.9 | 6.7 | 2.3 | –2.0 |
| HCTH/147 | 4.7 | 11.4 | 6.4 | 2.8 | –2.5 |
| HCTH/407 | 2.5 | 14.4 | 9.3 | 2.2 | 0.5 |
| OLYP | 0.7 | 11.0 | 6.0 | 4.4 | –2.9 |
| *Meta-GGAs* | | | | | |
| BLAP3 | 0.6 | 14.4 | 6.7 | 3.4 | 0.5 |
| VS98 | 10.3 | 15.3 | 10.3 | 1.7 | 1.4 |
| KCIS | 8.0 | 8.1 | 1.7 | 4.4 | –5.8 |
| PKZB | 6.6 | 8.3 | 1.4 | 4.9 | –5.6 |
| Bmτ1 | 0.2 | 14.7 | 6.8 | 3.6 | 0.8 |
| OLAP3 | –5.4 | 14.8 | 9.7 | 5.1 | 0.9 |
| TPSS | 8.6 | 9.4 | 3.1 | 3.6 | –4.5 |
| *Hybrid functionals* | | | | | |
| B3LYP | 4.9 | 15.2 | 9.5 | 1.7 | 1.3 |
| TPSSh | 7.4 | 11.8 | 6.2 | 1.8 | –2.1 |
| *Ab initio benchmark* | | | | | |
| CCSD(T) | 8.1 | 13.9 | 8.9 | | |

a Geometries optimized at ZORA-BLYP/TZ2P with frozen-core approximation.

b Computed post-SCF using the BLYP electron density. Relativistic effects treated with ZORA.

c Mean absolute error for the energies of the three stationary points R, TS and P relative to RC and error in the central barrier, i.e., in the energy of the TS relative to RC, compared with the CCSD(T) benchmark from Chapter 3.

4.6), but doing so does not change much our conclusions concerning the performance of the various functionals, in particular, the observation that BLYP (mean abs. err = 3.5 kcal/mol) performs remarkably well, only slightly worse so than B3LYP (mean abs. err. = 1.7). Note, also, that regarding the performance for computing the activation energy, the situation is different. Whereas BLYP is slightly better for computing the overall barrier (i.e., TS relative to R), it is B3LYP that outperforms BLYP for the central barrier (i.e., TS relative to RC). We recall that BLYP underestimates the overall barrier by only –1.9 kcal/mol whereas B3LYP overestimates this barrier by 4.5 kcal/mol (see Table 4.5). The origin of the latter overestimation is that B3LYP yields a too weakly bound reactant complex. Once this deficiency is switched off, by taking the reactant complex as the point of reference, B3LYP performs very well (see Table 4.6): it overestimates the central barrier by only 1.3 kcal/mol whereas BLYP underestimates the central barrier by –3.3 kcal/mol. All together, we conclude that both BLYP and B3LYP are reasonable approaches for tackling the oxidative addition of the methane C–H bond to Pd.

## 4.4 Conclusions

We have evaluated the performance of 24 relativistic density functionals for describing the PES, i.e., geometries and relative energies of stationary points, of the archetypal oxidative addition of the methane C–H bond to palladium. Excellent agreement with the best available relativistic four-component coupled-cluster benchmark PES is achieved by functionals of the GGA, meta-GGA as well as hybrid DFT approaches, each of which have a representative in the top three, with mean absolute errors as small as 1.4 kcal/mol or less.

Neither hybrid DFT nor the meta-GGA represents a significant improvement over GGA functionals. Interestingly, the well-known BLYP functional still performs satisfactorily with a mean absolute error of 2.5 kcal/mol and an underestimation of the overall barrier (i.e. TS relative to reactants) by 1.9 kcal/mol and of the central barrier (i.e., TS relative to reactant complex) by 3.3 kcal/mol. Note that also the much advocated B3LYP hybrid functional performs well but not significantly better than BLYP, with a mean absolute error of 3.8 kcal/mol and an overestimation of the overall barrier by 4.5 kcal/mol and of the central barrier by 1.3 kcal/mol.

Our results have been verified to be converged with the basis-set size at ZORA-BLYP/TZ2P and to be unaffected by the frozen-core approximation for the core shells of C and Pd. We consider this a sound and efficient approach for the routine investigation of catalytic bond activation, also in larger, more realistic model systems.

# 5 *Ab initio* benchmark and DFT validation study for the oxidative addition of the ethane C–C bond to Pd

Adapted from
G. Th. de Jong, D. P. Geerke, A. Diefenbach, M. Solà, F. M. Bickelhaupt
*J. Comp. Chem.* **2005**, *26*, 1006

## Abstract

We have computed a state-of-the-art benchmark potential energy surface (PES) for the archetypal oxidative addition of the ethane C–C bond to the palladium atom and have used this to evaluate the performance of 24 popular density functionals, covering LDA, GGA, meta-GGA and hybrid density functionals, for describing this reaction. The *ab initio* benchmark is obtained by exploring the PES using a hierarchical series of *ab initio* methods (HF, MP2, CCSD, CCSD(T)) in combination with a hierarchical series of five Gaussian-type basis sets, up to *g* polarization. Relativistic effects are taken into account either through a relativistic effective core potential for palladium or through a full four-component all-electron approach. Our best estimate of kinetic and thermodynamic parameters is –10.8 (–11.3) kcal/mol for the formation of the reactant complex, 19.4 (17.1) kcal/mol for the activation energy relative to the separate reactants, and –4.5 (–6.8) kcal/mol for the reaction energy (zero-point vibrational energy-corrected values in parentheses). Our work highlights the importance of sufficient higher-angular momentum polarization functions for correctly describing metal-*d*-electron correlation. Best overall agreement with our *ab initio* benchmark is obtained by functionals from all three categories, GGA, meta-GGA, and hybrid DFT, with mean absolute errors of 1.5 to 2.5 kcal/mol and errors in activation energies ranging from –0.2 to –3.2 kcal/mol. Interestingly, the well-known BLYP functional compares very reasonably with a slight underestimation of the overall barrier by –0.9 kcal/mol. For comparison, with B3LYP we arrive at an overestimation of the overall barrier by 5.8 kcal/mol. On the other hand, B3LYP performs excellently for the central barrier (i.e., relative to the reactant complex), which it underestimates by only –0.1 kcal/mol.

## 5.1 Introduction

Alkanes, the "noble gases of organic chemistry," are rather inert chemical substances, which is reflected in their trivial name, paraffins, from the Latin *parum affinis* (without affinity).[29] The activation of the C–H or C–C bonds of alkanes is one of the great challenges in organic chemistry and catalysis, as it is often the first step in the catalytic conversion of the abundant but nonreactive alkanes into more useful products.[28] In the group of the transition metal elements, palladium is one of the most important catalysts, mostly in conjunction with ligands.[31] The insertion of the palladium atom into C–H and C–C bonds in alkanes has therefore received considerable attention, both experimentally[32-36] and theoretically.[33,35,37-44,96,97] In the previous chapters, we have investigated the insertion of the Pd-$d^{10}$ atom into the C–H bond of methane as an important example of this type of reactions. Among others, we have demonstrated the importance of taking into account sufficient higher-angular momentum polarization functions, $f$ and $g$, for correctly describing metal-$d$-electron correlation and, thus, for obtaining reliable relative energies (see Chapter 3). Furthermore, it was shown that density functional theory[6-9] (DFT) is able to reproduce the best *ab initio* results within one to two kcal/mol (see Chapter 4). A systematic comparison of functionals revealed that the well-known BLYP functional still performs as one of the best functionals, even better than most of the high-level meta-GGA and hybrid functionals. In this chapter, these investigations are extended to the oxidative addition of the ethane C–C bond to the Pd-$d^{10}$ atom, see Scheme 5.1. This reaction is archetypal for the activation of C–C single bonds in alkanes. At the same time, it constitutes the reverse reaction of the important class of C–C coupling through reductive elimination, which is therefore also covered.

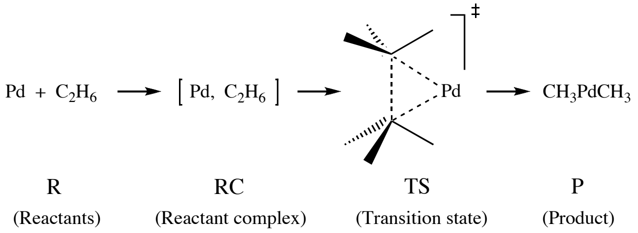

**Scheme 5.1** Model reaction and nomenclature

Experimental investigations on the reaction of Pd with alkanes have been carried out by Weisshaar and coworkers,[34,35] and, more recently, by Campbell, specifically for Pd and methane.[36] These studies show that Pd forms collisionally stabilized complexes with alkanes and that the rate of conversion of the educts is very small. The results suggest a complexation energy of at least 8 kcal/mol for Pd-alkane complexes.[34] This provides us with an experimental boundary condition for the stability of the RC of Pd + ethane.

The purpose of the present study is twofold. In the first place, we wish to obtain a reliable benchmark for the potential energy surface (PES) for the oxidative addition of the C–C bond of ethane to Pd(0). This is done by exploring this PES with a hierarchical series of *ab initio* methods (Hartree-Fock (HF), second order Møller-Plesset perturbation theory (MP2),[57] and coupled cluster theory[98] with single and double excitations (CCSD),[59] and with triple excitations treated perturbatively (CCSD(T))[60]) in combination with a hierarchical series of Gaussian-type basis sets of increasing flexibility and polarization (up to *g* functions). The basis set superposition error (BSSE) is accounted for by counterpoise correction (CPC).[12] Relativistic effects are treated with a full four-component all-electron approach.

The existing computational benchmark for oxidative addition of ethane to Pd was obtained by Siegbahn and coworkers[35] with the parameterized configuration interaction method PCI-80, in which the effect of correlation is estimated by an extrapolation procedure.[45] The PCI-80 study arrives at a Pd + ethane complexation energy of 6.6 kcal/mol, an activation energy of 19.5 kcal/mol and a reaction energy of 5.5 kcal/mol (see Table 5.1). These values and, in particular, the activation energies appear to be rather sensitive to the level of theory used. The activation energy ranges from 38.6 to 12.5 kcal/mol. In view of this situation, it is appropriate to explore to which extent the PCI-80 values are converged with respect to both the order of correlation incorporated into the theoretical method and the degree of flexibility and polarization of the basis set.

The second purpose of our work is to evaluate the performance of 24 popular density functionals, covering LDA, GGA, meta-GGA and hybrid functionals, for describing the oxidative addition of the ethane C–C bond to Pd, using our new *ab initio* benchmark as reference point. Here, we anticipate that although the latter turns out to be satisfactory in

**Table 5.1** Literature values for relative energies (in kcal/mol) of the stationary points along the reaction coordinate for the oxidative insertion of Pd into the ethane C–C bond

| | | Basis set quality$^{a}$ | | | | |
|---|---|---|---|---|---|---|
| Reference | Method | Pd | C and H | RC | TS | P |
| 37,38 | GVB-RCI//HF | DZP$^{b}$ | DZ | | 38.6 | 16.0 |
| 39 | CCI+Q//CASSCF | TZP$^{c}$ | DZP | | 39.2 | 19.7 |
| 39 | CCI+Q//CASSCF | TZP + 2$f^{d}$ | TZP | | 31.5 | 7.5 |
| 96 | CCSD(T)//HF | TZP + 3$f^{e}$ | TZP | | 23.1 | –0.2 |
| 35 | PCI-80//HF | TZP + $f^{f}$ | DZP | –6.6$^{h}$ | 19.5$^{h}$ | –5.5$^{h}$ |
| 22 | BP86 | TZP$^{g}$ | TZ2P$^{g}$ | –10.5 | 12.5 | –11.8 |

a Main characteristics of the basis set used in the higher-level single-point calculations. For Pd, DZP is double-ζ for valence 4*d* shell with one set of polarization functions for 5*p* shell; TZP is triple-ζ for valence 4*d* shell with one set of polarization functions for 5*p* shell. For C and H, DZP is double-ζ with one set of polarization functions, 3*d* for C and 2*p* for H; TZP is triple-ζ with one set of polarization functions, 3*d* for C and 2*p* for H; TZ2P is triple-ζ with two sets of polarization functions, 3*d* and 4*f* for C, and 2*p* and 3*d* for H.

b ECP for [Kr] core; valence electrons: (3*s*3*p*3*d*)/[3*s*2*p*2*d*] (ref. 46).

c Augmented Huzinaga basis (ref. 47), Raffenetti contraction scheme (ref. 48): (17*s*13*p*9*d*)/[8*s*7*p*4*d*].

d Same as c but with larger primitive and contracted basis: (17*s*13*p*10*d*4*f*)/[8*s*7*p*5*d*2*f*].

e Same as c but with larger primitive and contracted basis: (17*s*13*p*9*d*3*f*)/[7*s*6*p*4*d*3*f*].

f Same as e but with three *f* functions contracted: (17*s*13*p*9*d*3*f*)/[7*s*6*p*4*d*1*f*].

g Slater-type orbitals.

h With ZPE correction.

terms of accuracy and reliability, it is prohibitively expensive if one wishes to study more realistic catalysts and substrates. Our survey of 24 functionals serves to validate one or more of these DFT approaches as a computationally more efficient alternative to high-level *ab initio* theory in future investigations in the field of computational catalysis. A general concern, however, associated with the application of DFT to the investigation of chemical reactions is its notorious tendency to underestimate activation energies.[10] Thus, we arrive at a ranking of density functional approaches in terms of the accuracy with which they describe the PES of our model reaction, in particular the activation energy. We focus on the overall barrier, that is, the difference in energy between the TS and the separate reactants, which is decisive for the rate of chemical reactions in the gas phase, in particular, if they occur under low-pressure conditions in which the reaction system is (in good approximation) thermally isolated.[34,75] But we also address the central barrier, that is, the difference in energy between the TS and the RC. Here, we anticipate that, in line with previous work on C–H activation in methane (see Chapter 4), the well-known BLYP GGA functional is found to perform very satisfactorily, in fact, as good as the much advocated B3LYP hybrid functional.

## 5.2 Methods

### 5.2.1 Geometries

All geometry optimizations have been done with DFT using the ADF program.[49-51] For seven different GGA functionals, the performance for computing the geometries and relative energies of the stationary points along the PES of our model reaction was compared. These density functionals are BP86,[52,76] BLYP,[52,53] PW91,[77] PBE,[78] revPBE,[79] RPBE[80] and OLYP.[53,81] The same computational settings were used as described in Sections 3.2.1 and 4.2.1, i.e., using ZORA, the TZ2P basis set and the frozen-core approximation.

### 5.2.2 *Ab initio* calculations

Based on the ZORA-BLYP/TZ2P geometries, energies of stationary points were computed in a series of single-point calculations with the program package DIRAC[55,99] using the following hierarchy of methods: HF, MP2, CCSD and CCSD(T). Relativistic effects are accounted for using an all-electron four-component Dirac-Coulomb approach with a spin-free Hamiltonian.[17] The two-electron integrals over exclusively the small components have been neglected and corrected with a simple Coulombic correction.[16]

A hierarchical series of Gaussian-type basis sets, BS1-BS5, was used (see Table 5.2), which is based on the series B1-B6 used in Chapter 3 on the oxidative addition of methane to Pd (see Table 3.2 and the discussion in Section 3.2.3), differing, however, in some respects. BS1 and BS2 are exactly equal to B1 and B2. However, from B2 to B3, the C and H basis sets in Chapter 3 ($CH_4$ + Pd) are extended from uncontracted cc-aug-pVDZ to uncontracted cc-aug-pVTZ. This was not possible for the present, larger system ($C_2H_6$ + Pd), as it causes the required memory to exceed our available allotment. Therefore, in this study, we used only uncontracted cc-aug-pVDZ for C and H. Note, however, that regarding Pd BS2-BS5 corresponds with B3-B6 in Chapter 3. We have tested how the results of Chapter 3 are affected if the present approach for $C_2H_6$ + Pd (i.e., BS1-BS5 instead of B1-B6) is used also for $CH_4$ + Pd. At the highest level of theory, namely, counterpoise-corrected CCSD(T)/BS5, the energy of formation of the RC of $CH_4$ + Pd is –7.0 kcal/mol, the activation barrier is 6.9 kcal/mol and the reaction energy amounts to 1.7 kcal/mol. These relative energies are consistently ca. 1 kcal/mol higher than and, thus, compare reasonably well with the corresponding counterpoise-corrected CCSD(T)/B6 values of Chapter 3, which are –8.1, 5.8, and 0.8 kcal/mol.

**Table 5.2** Basis sets used in the *ab initio* calculations

| Basis set | Pd | C and H |
|---|---|---|
| BS1 | $(24s16p13d)^a$ | cc-aug-pVDZ$^b$ |
| BS2 | $(24s16p13d)^a + 1f$ | cc-aug-pVDZ$^b$ |
| BS3 | $(24s16p13d)^a + 4f$ | cc-aug-pVDZ$^b$ |
| BS4 | $(24s16p13d)^a + 4f + p$ | cc-aug-pVDZ$^b$ |
| BS5 | $(24s16p13d)^a + 4f + p + g$ | cc-aug-pVDZ$^b$ |

a TZP quality.

b Completely uncontracted.

### 5.2.3 DFT calculations

On the basis of the ZORA-BLYP/TZ2P geometries, we have computed in a post-SCF manner, i.e., using in all cases the electron density obtained at ZORA-BLYP/ae-TZ2P, the relative energies of stationary points for various LDA, GGAs, meta-GGAs and hybrid functionals. The ae-TZ2P basis set is the all-electron counterpart corresponding to the above-mentioned TZ2P basis that is used in conjunction with the frozen-core approximation. In addition to the ones used in the geometry optimizations, the same functionals were used as described in Section 4.2.3.

## 5.3 Results and discussion

### 5.3.1 Geometries of stationary points

First, we examine the geometries of stationary points for the oxidative insertion of Pd into the ethane C–C bond, computed with the GGA functionals BP86, BLYP, PW91, PBE, revPBE, RPBE and OLYP in combination with the TZ2P basis set, the frozen-core approximation, and ZORA to account for relativistic effects. Geometry parameters are defined in Figure 5.1 and their values optimized with each of the seven GGA functionals are collected in Table 5.3. For all functionals, the reaction proceeds from the reactants via formation of a stable reactant complex of $C_s$ symmetry, in which one of the methyl groups of ethane coordinates in an $\eta^2$ fashion to Pd, followed by the transition state of $C_2$ symmetry and, finally, a stable product of $C_{2v}$ symmetry. All species have been verified to represent equilibrium structures (no imaginary frequencies) or a transition state (one imaginary frequency). The imaginary frequency in the transition state associated with the normal mode that connects reactant complex and product varies, depending on the functional, between 487 and 493 $i$ cm$^{-1}$.

The geometries obtained with the various GGA functionals do not show significant mutual discrepancies (see Table 5.3). The C–H bond distance values are very robust with respect to changing the functional, with variations in the order of a few thousandths of an Å. Note that variations in the length of the activated C–C bond become larger, up to 0.09 Å in the product, as the reaction progresses. This is in line with the fact that this bond is being broken along the reaction coordinate, which causes the PES to become increasingly soft in this coordinate and, thus, sensitive to changes in the computational method. More pronounced variations are found for the weak Pd–C and Pd–H bonds. This holds especially for the loosely bound reactant complex, which shows fluctuations of up to one tenth of an Å for Pd–C and in the order of hundredths for Pd–H. The variations in these bond distances drop to a few hundredths or even a few thousandths of an Å as the reaction proceeds to transition state and product in which more stable coordination bonds are formed. Thus, only moderate variations in bond distances occur along the various functionals and they are more pronounced for the softer (or broken) bonds. This is also reflected by the variations in bond angles. These variations are very small as firmly bound triplets of atoms are involved, but can become somewhat larger for angles opposite to a soft bond (e.g., up to 2° for the C–Pd–C angle).

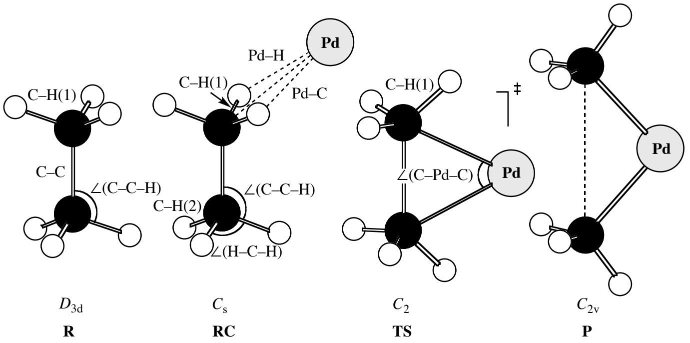

**Figure 5.1** Structures and point group symmetries of the stationary points along the reaction coordinate for the oxidative insertion of Pd into the ethane C–C bond. See Table 5.3 for values of geometry parameters

**Table 5.3** Geometry parameters[a] (in Å, degrees), optimized with seven different density functionals,[b] of the stationary points along the reaction coordinate for the oxidative insertion of Pd into the ethane C–C bond

| Method | | C–H(1) | C–H(2) | C–C | Pd–C | Pd–H | ∠(C–C–H) | ∠(H–C–H) | ∠(C–Pd–C) |
|---|---|---|---|---|---|---|---|---|---|
| BP86 | R | 1.099 | | 1.532 | | | 111.4 | | |
| | RC | 1.137 | 1.099 | 1.532 | 2.313 | 1.941 | 111.3 | 107.8 | |
| | TS | 1.133 | 1.091 | 1.927 | 2.111 | 2.059 | 133.8 | 107.7 | 54.3 |
| | P | 1.104 | 1.096 | 2.960 | 1.998 | 2.491 | 145.2 | 110.7 | 95.6 |
| BLYP | R | 1.098 | | 1.541 | | | 111.3 | | |
| | RC | 1.126 | 1.098 | 1.541 | 2.418 | 2.023 | 111.3 | 107.9 | |
| | TS | 1.123 | 1.089 | 1.945 | 2.167 | 2.102 | 133.2 | 108.7 | 53.3 |
| | P | 1.101 | 1.094 | 3.028 | 2.025 | 2.513 | 144.6 | 111.0 | 96.7 |
| PW91 | R | 1.097 | | 1.529 | | | 111.4 | | |
| | RC | 1.136 | 1.098 | 1.528 | 2.311 | 1.941 | 111.3 | 107.8 | |
| | TS | 1.130 | 1.090 | 1.926 | 2.107 | 2.063 | 134.0 | 107.9 | 54.4 |
| | P | 1.102 | 1.095 | 2.932 | 1.995 | 2.491 | 146.0 | 110.7 | 94.6 |
| PBE | R | 1.099 | | 1.530 | | | 111.4 | | |
| | RC | 1.138 | 1.099 | 1.530 | 2.308 | 1.940 | 111.3 | 107.8 | |
| | TS | 1.133 | 1.092 | 1.928 | 2.105 | 2.066 | 134.1 | 107.8 | 54.5 |
| | P | 1.104 | 1.097 | 2.937 | 1.996 | 2.492 | 145.9 | 110.7 | 94.8 |
| revPBE | R | 1.100 | | 1.537 | | | 111.4 | | |
| | RC | 1.133 | 1.100 | 1.537 | 2.374 | 1.988 | 111.4 | 107.8 | |
| | TS | 1.131 | 1.093 | 1.933 | 2.127 | 2.088 | 134.0 | 108.1 | 54.1 |
| | P | 1.105 | 1.097 | 2.971 | 2.008 | 2.504 | 145.5 | 110.6 | 95.4 |
| RPBE | R | 1.100 | | 1.538 | | | 111.4 | | |
| | RC | 1.131 | 1.101 | 1.539 | 2.396 | 2.005 | 111.4 | 107.8 | |
| | TS | 1.130 | 1.093 | 1.935 | 2.133 | 2.093 | 134.1 | 108.1 | 54.0 |
| | P | 1.105 | 1.098 | 2.976 | 2.012 | 2.508 | 145.6 | 110.6 | 95.4 |
| OLYP | R | 1.096 | | 1.529 | | | 111.4 | | |
| | RC | 1.122 | 1.096 | 1.530 | 2.426 | 2.027 | 111.6 | 107.7 | |
| | TS | 1.124 | 1.089 | 1.932 | 2.109 | 2.090 | 134.7 | 108.0 | 54.5 |
| | P | 1.100 | 1.093 | 2.961 | 1.997 | 2.492 | 145.4 | 110.5 | 95.7 |

[a] See Figure 5.1 for definition.

[b] With TZ2P basis set with frozen-core approximation. Relativistic effects treated with ZORA.

Thus, the various functionals yield essentially the same geometries. Later on, in Section 5.3.3, we show that BLYP also performs excellently in terms of relative energies of stationary points. Based on these findings, and the fact that BLYP is robust and well established, we choose the geometries of this functional, that is, ZORA-BLYP/TZ2P, to compute an *ab initio* benchmark PES in the next section.

### 5.3.2 Benchmark energies from *ab initio* calculations

As pointed out above, the relative energies of stationary points along the reaction profile of Pd insertion into the ethane C–C bond, especially the activation energy, appear to be highly sensitive to the level of theory used, as witnessed by the large spread in values computed earlier (see Table 5.1). Here, we report the first systematic investigation of the extent to which these values are converged at the highest level of theory used. This survey is based on geometries of stationary points that were optimized at the ZORA-BLYP/TZ2P level of relativistic DFT. The results of our *ab initio* computations are collected in Table 5.4 and graphically displayed in Figure 5.2.

At all levels of theory except Hartree-Fock, the reaction profiles are characterized by the formation of a stable reactant complex (RC), which leads via the transition state for insertion (TS) to the oxidative addition product (P). Three striking observations can be made: (i) the spread in values of computed relative energies, depending on the level of theory and basis set, is enormous, up to nearly 60 kcal/mol; (ii) the size of the BSSE is also remarkably large, up to ca. 14 kcal/mol; (iii) convergence with basis-set size of the computed energies is still not reached with standard basis sets used routinely in CCSD(T) computations on organometallic and coordination compounds.

The lack of any correlation leads to a complete failure at the HF level, which yields an unbound RC and a strongly exaggerated activation barrier of ca. 57 kcal/mol. The failure of HF for describing the PES of our model reaction is not unexpected because electron correlation, which is not contained in this approach, is important.[72,73] The activation energy drops significantly when electron correlation is introduced. Along HF, CCSD and CCSD(T) in combination with basis set BS1, for example, the activation barrier decreases from 57.4 to 25.0 to 18.4 kcal/mol. But also the correlated CCSD(T) values obtained with basis sets BS1 up to BS3, comparable in quality to standard basis sets such as LANL2DZ[64,65] without or with up to four *f* functions added, are questionable, as they are obviously not converged as a function of the basis-set size.[a] For example, the activation energy of 18.4 kcal/mol at CCSD(T)/BS1 agrees remarkably well with the PCI-80 value of 19.5 kcal/mol obtained by Siegbahn and coworkers (see

**Table 5.4** Relative energies (in kcal/mol) of the stationary points for oxidative insertion of Pd into the ethane C–C bond, with and without counterpoise correction (CPC), computed at several levels of *ab initio* theory

| | | RC | | TS | | P | |
|---|---|---|---|---|---|---|---|
| Method | Basis set | no CPC | with CPC | no CPC | with CPC | no CPC | with CPC |
| HF | BS1 | 5.0 | 5.5 | 57.4 | 58.0 | 40.8 | 41.2 |
| | BS2 | 4.8 | 5.3 | 57.0 | 57.6 | 38.7 | 39.0 |
| | BS3 | 4.6 | 5.2 | 56.3 | 57.0 | 36.8 | 37.2 |
| | BS4 | 4.7 | 5.2 | 56.3 | 57.1 | 36.8 | 37.2 |
| | BS5 | 4.6 | 5.1 | 56.2 | 56.9 | 36.2 | 36.6 |
| MP2 | BS1 | –11.5 | –6.4 | 17.5 | 25.2 | –5.0 | 4.8 |
| | BS2 | –16.6 | –9.1 | 8.1 | 19.0 | –16.8 | –2.9 |
| | BS3 | –15.4 | –12.3 | 8.5 | 13.3 | –11.4 | –5.7 |
| | BS4 | –14.3 | –12.5 | 9.6 | 13.1 | –10.4 | –6.0 |
| | BS5 | –14.8 | –13.0 | 8.5 | 11.9 | –10.5 | –6.3 |
| CCSD | BS1 | –9.7 | –4.5 | 25.0 | 32.7 | –0.1 | 9.1 |
| | BS2 | –12.5 | –5.9 | 20.5 | 30.0 | –6.2 | 5.5 |
| | BS3 | –10.4 | –7.7 | 23.0 | 27.1 | –1.6 | 3.0 |
| | BS4 | –9.6 | –8.0 | 23.8 | 26.9 | –0.9 | 2.7 |
| | BS5 | –9.6 | –8.1 | 23.6 | 26.6 | –0.4 | 2.9 |
| CCSD(T) | BS1 | –12.5 | –5.9 | 18.4 | 27.7 | –6.5 | 4.7 |
| | BS2 | –16.0 | –8.0 | 12.4 | 23.7 | –14.7 | –0.9 |
| | BS3 | –14.0 | –10.2 | 14.9 | 20.4 | –9.9 | –3.9 |
| | BS4 | –12.4 | –10.5 | 16.5 | 20.1 | –8.3 | –4.3 |
| | BS5 | –12.5 | –10.8 | 16.1 | 19.4 | –8.2 | –4.5 |

[a] Indeed, preliminary calculations with the program GAUSSIAN[54] at CCSD(T) with basis sets cc-aug-pVDZ for C and H, and LANL2DZ (–13.0, 16.2 and –4.7 kcal/mol for RC, TS and P) and LANL2DZ + *f* (–17.6, 8.7 and –14.1 kcal/mol for RC, TS and P), respectively, for Pd yield similar trends in the PES as the calculations with the program DIRAC at CCSD(T) with basis sets BS1 and BS2, respectively.

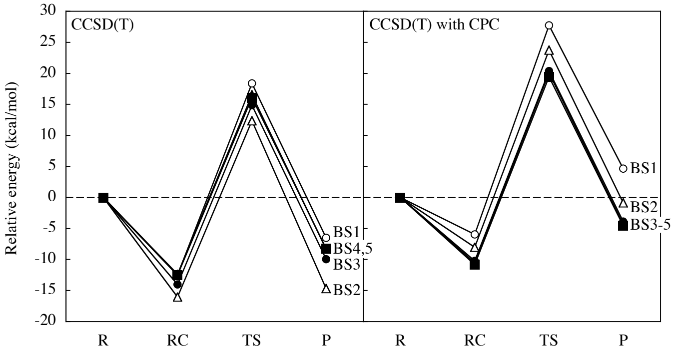

**Figure 5.2** Reaction profiles computed with CCSD(T) for various basis sets, without (left diagram) and with counterpoise correction (right diagram). Based on geometries optimized at ZORA-BLYP/TZ2P

Table 5.1). This agreement is, however, fortuitous. The activation energy computed at CCSD(T) drops further from 18.4 kcal/mol for basis set BS1 to 12.4 kcal/mol for basis set BS2 in which one *f* polarization function has been added. Thereafter, along BS2 to BS5, the activation energy increases again, although not monotonically, from 12.4 to 16.1 kcal/mol, as three more sets of *f* functions, an additional set of diffuse *p* functions and a set of *g* functions are added to the basis set of Pd. This is illustrated by Figure 5.2, left, which shows the CCSD(T) reaction profiles and how they vary along BS1-BS5.

Next, we note that the BSSE takes on large values in the correlated *ab initio* methods, whereas it is negligible if correlation is completely neglected, i.e., in HF (see Table 5.3, difference between values with and without CPC). The BSSE increases somewhat going from BS1 to BS2, and decreases from BS2 to BS5. At the CCSD(T) level, for example, the BSSE for TS amounts to 9.3 to 3.4 kcal/mol along the basis sets BS1 to BS5, whereas the corresponding BSSE values at HF are only ca. 0.7 kcal/mol. The BSSE increases along the reaction coordinate, that is, going from RC to TS to P. The reason for this is that along this series, the C and H atoms and, thus, their basis functions come closer and begin to surround the Pd atom. This effectively improves the flexibility and polarization of the basis set and thus the description of the wavefunction in the region of the Pd atom. Note that the total BSSE at CCSD(T) has been considerably decreased, that is, from 11.4 kcal/mol for BS2 to only 3.4 kcal/mol for BS5 and is thus clearly smaller than the relative energies that we compute, notably the activation barrier.

The high sensitivity of the PES for oxidative addition of the ethane C–C bond to Pd highlights the prominent role that electron correlation plays in our model systems. It is striking that the relative CCSD(T) energies have still not reached convergence for basis set BS3, which is of a quality comparable to that of standard basis sets such as LANL2DZ,[64] augmented with four *f* polarization functions, for Pd (see Table 5.3 and Figure 5.2, left). This may be somewhat surprising in view of earlier reports that such basis sets yield satisfactory energies for organometallic and coordination compounds.[72,73] On the other hand, it is consistent with the large variation of values for the thermodynamic and kinetic parameters obtained in earlier theoretical studies of the present model reaction, as shown in Table 5.1. It is also consistent with our findings in Chapter 3 for the PES for oxidative addition of the methane C–H bond to Pd, which shows exactly the same sensitivity and behaviour. One reason for the increased sensitivity that we find towards the quality of the theoretical approach is that the presence of *f* polarization functions is only the minimum requirement for describing the electron correlation of palladium 4*d* electrons. In this respect, the palladium basis sets in BS1, BS2 and BS3 should be considered minimal and cannot be expected to have achieved convergence. Furthermore, the consequences of any inadequacy in the basis set shows up more severely in processes such as ours, which involve a bare, uncoordinated transition-metal atom as one of the reactants because here the effect of additional assistance of basis functions on the substrate is more severe than in situations where the transition-metal fragment is already surrounded by, for example, ligands. This shows up in the relatively large BSSE values for CCSD(T)/BS1-BS3.

Thus, we have been able to achieve virtual convergence of the CCSD(T) relative energies by using a larger than standard basis set and by correcting for the BSSE (see Table 5.3 and Figure 5.2, right). Our best estimate for the kinetic and thermodynamic parameters of the oxidative insertion of Pd into the ethane C–C bond, obtained at CCSD(T)/BS5 with CPC, is –10.8 kcal/mol for the formation of the RC, 19.4 kcal/mol for the activation energy relative to the reactants, and –4.5 kcal/mol for the reaction energy. If we take into account zero-point vibrational energy (ZPE) effects computed at BLYP/TZ2P, this yields –11.3 kcal/mol for the formation of the reactant complex, +17.1 kcal/mol for the activation energy relative to the separate reactants, and –6.8 kcal/mol for the reaction energy. Our benchmark values, in particular the activation energy, agree reasonably well with those obtained by Siegbahn and coworkers at PCI-80,[35] namely, –6.6, +19.5 and –5.5 kcal/mol for RC, TS and P and, therefore, further consolidate the theoretical reaction profile. They also agree well, in fact slightly better so than PCI-80, with the experimental result that the reactant complex is bound by at least 8 kcal/mol.[34]

### 5.3.3 Validation of DFT

Next, we examine the relative energies of stationary points computed with the GGA functionals BP86, BLYP, PW91, PBE, revPBE, RPBE and OLYP in combination with the TZ2P basis set, the frozen-core approximation, and ZORA to account for relativistic effects. Note that for each functional we use consistently the geometries optimized with that functional, for example, BP86//BP86 or BLYP//BLYP. As pointed out above, we first focus on the overall activation energy, that is, the difference in energy between the

TS and the separate reactants, which is decisive for the rate of chemical reactions in the gas phase, in particular, if they occur under low-pressure conditions. Later on, in the next section, we also address the central barrier, that is, the difference in energy between the TS and the reactant complex. Relative energies, with and without zero-point vibrational energy correction, as well as relative enthalpies are collected in Table 5.5. Relative energies are also graphically represented in Figure 5.3. The performance of the various GGA functionals is assessed by a comparison of the resulting PESs with our relativistic CCSD(T) benchmark. For comparison, we have also included in Table 5.5 the earlier *ab initio* benchmark obtained by Siegbahn and coworkers with the PCI-80 method.

It is clear, especially from Figure 5.3, that the investigated GGAs fall into three groups regarding their agreement with the benchmark results. OLYP clearly underestimates metal-substrate bonding and yields a too weakly bound reactant complex, a barrier that is too high by almost 6 kcal/mol, and an endothermic reaction energy, where it should be exothermic. The situation is opposite for BP86, PBE and PW91, which seem to overestimate metal-substrate bonding. Although this leads to nice agreement for the RC with the coupled-cluster result, it gives a significantly underestimated barrier (by nearly 10 kcal/mol for PW91) and a too exothermic reaction energy. On the other hand, BLYP and the two revisions of PBE, i.e., revPBE and RPBE, achieve quite satisfactory agreement with the coupled-cluster PES, especially for the barrier, which is underestimated by only 1.1 (BLYP), 2.1 (revPBE), and 1.2 kcal/mol (RPBE), with BLYP performing slightly better than the other functionals. Thus, we arrive at the conclusion that was anticipated earlier, namely, that BLYP performs excellently for computing relative energies. Furthermore, we notice the same order of relative performance of the various GGA functionals as we found in Chapter 4 on the reaction of Pd + C–H, in which BLYP also performed better than other functionals.

**Table 5.5** Relative energies without ($\Delta E$) and with zero-point vibrational energy correction ($\Delta E + \Delta ZPE$), and relative enthalpies at 298.15 K ($\Delta H$) of the stationary points,[a] computed with several functionals[b,c]

| | $\Delta E$ | | | $\Delta E + \Delta ZPE$ | | | $\Delta H$ | | |
|---|---|---|---|---|---|---|---|---|---|
| Method | RC | TS | P | RC | TS | P | RC | TS | P |
| *DFT computations (this study)* | | | | | | | | | |
| BP86 | −11.0 | 11.3 | −13.4 | −11.5 | 8.8 | −15.8 | −11.9 | 8.2 | −15.7 |
| BLYP | −6.8 | 18.3 | −9.3 | −7.2 | 15.9 | −11.5 | −7.5 | 15.4 | −11.5 |
| PW91 | −12.4 | 9.7 | −14.3 | −12.9 | 7.3 | −16.5 | −13.3 | 6.7 | −16.5 |
| PBE | −11.9 | 10.2 | −13.5 | −12.5 | 7.7 | −15.9 | −12.9 | 7.1 | −15.8 |
| revPBE | −6.5 | 17.3 | −7.7 | −7.1 | 14.8 | −10.0 | −7.3 | 14.3 | −10.0 |
| RPBE | −6.0 | 18.2 | −6.9 | −6.5 | 15.7 | −9.3 | −6.8 | 15.2 | −9.2 |
| OLYP | −1.3 | 25.1 | 0.8 | −1.8 | 22.8 | −1.5 | −2.0 | 22.2 | −1.5 |
| *Ab initio benchmarks* | | | | | | | | | |
| CCSD(T) // BLYP | −10.8 | 19.4 | −4.5 | −11.3 | 17.1 | −6.8 | | | |
| PCI-80 // HF | | | | −6.6 | 19.5 | −5.5 | | | |

a Geometries and energies computed at the same level of theory.

b With TZ2P basis set with frozen-core approximation. Relativistic effects treated with ZORA.

c CCSD(T) benchmark from this study and PCI-80 from ref. 35.

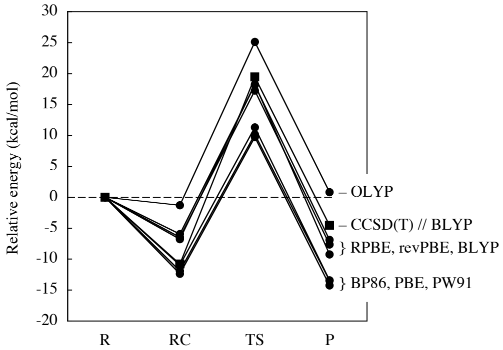

**Figure 5.3** Reaction profiles obtained with several functionals, using ZORA and the TZ2P basis set with frozen-core approximation (geometries and energies computed at the same level of theory)

Finally, based again on the ZORA-BLYP/TZ2P geometries discussed above, we have computed the relative energies of stationary points along the PES for various LDA, GGA, meta-GGA and hybrid functionals in combination with the all-electron ae-TZ2P basis set and ZORA for relativistic effects. This was done in a post-SCF manner, that is, using density functionals with the electron density obtained at ZORA-BLYP/ae-TZ2P. The performance of the density functionals is discussed by comparing the resulting PESs with that of the CCSD(T) benchmark discussed above. The results of this survey are collected in Table 5.6, which shows energies relative to the separate reactants.

For clarity, we wish to point out that the above procedure for computing the relative energies shown in Table 5.6 differs in three respects from that used for computing the relative energies with the seven GGA functionals shown in Table 5.5: (i) an all-electron approach is used instead of the frozen-core approximation; (ii) for all functionals, the BLYP optimized geometries are used instead of geometries optimized with the same functional; and (iii) for all functionals, the BLYP electron density is used for computing the energy instead of the electron density corresponding to that functional. The effect of going from frozen-core (TZ2P) to all-electron calculations (ae-TZ2P), that is, point (i), is negligible, causing a stabilization of 0.2 kcal/mol or less (compare BLYP values in Tables 5.5 and 5.6). The differences between the values in Tables 5.5 and 5.6 derive mainly from the combined effects of points (ii) and (iii), which causes a destabilization of up to 1.7 (for the OLYP transition state) of the relative energies if one goes from Table 5.5 to Table 5.6. Both effects are in the order of a few tenths of a kcal/mol up to maximally one kcal/mol and, for the different GGA functionals and stationary points, contribute to this destabilization with varying relative importance. For the TS, the single-point approach contributes generally somewhat more (0.6-1.0 kcal/mol) to this destabilization than the post-SCF approach (0.1-0.4 kcal/mol, with an exceptionally high value of 0.8 kcal/mol for OLYP). This has been assessed by computing the relative energies of stationary points using approximation (ii) but not (iii), that is, computing them with the electron density corresponding to the functional under consideration but with the BLYP geometries; the resulting values are provided in parentheses in Table 5.6. In conclusion, the combined effect of approximations (i)-(iii) on the relative energies of stationary points is in the order of one kcal/mol with an upper limit of 1.7 kcal/mol.

Now, we extend our survey to the full range of density functionals that, except for LDA and the seven GGAs discussed above, have been implemented in the ADF program in a post-SCF manner. For all 24 functionals, we have computed the mean absolute error in the relative energies of RC, TS and P, and the error in the barrier, as compared with the CCSD(T) benchmark (see Table 5.6). Both the mean absolute error and the error in the barrier drop significantly going from LDA (mean abs. err. = 19.7 kcal/mol), which suffers from its infamous overbinding, to GGA functionals (mean abs. err. = 2.5 to 8.2

**Table 5.6** Energies (in kcal/mol) of the stationary points[a] relative to the separate reactants, and dissociation energy of ethane into two methyl radicals ($D_{CC}$), computed for 24 functionals with the ae-TZ2P basis set with all electrons treated variationally[b,c]

| Method | RC | TS | P | Mean abs. err. rel. to R | Err. in barr. rel. to R | $D_{CC}$ | Err. in $D_{CC}$ |
|---|---|---|---|---|---|---|---|
| *LDA* | | | | | | | |
| VWN | –22.7 (–23.0) | –5.2 (–5.5) | –27.2 (–27.3) | 19.7 | –24.7 | 114.5 | 24.0 |
| *GGAs* | | | | | | | |
| BP86 | –10.4 (–10.4) | 12.3 (12.1) | –13.3 (–13.4) | 5.4 | –7.1 | 93.0 | 2.5 |
| BLYP | –6.7 | 18.5 | –9.5 | 3.4 | –0.9 | 90.0 | –0.5 |
| Becke88x+BR89c | –7.4 | 17.3 | –11.6 | 4.2 | –2.1 | 91.3 | 0.8 |
| PW91 | –11.8 (–11.8) | 10.8 (10.7) | –14.1 (–14.0) | 6.4 | –8.6 | 96.2 | 5.7 |
| PBE | –11.3 (–11.3) | 11.5 (11.2) | –13.2 (–13.2) | 5.7 | –7.9 | 96.3 | 5.8 |
| FT97 | –11.9 | 12.2 | –14.8 | 6.2 | –7.2 | 93.5 | 3.0 |
| revPBE | –6.2 (–6.3) | 18.3 (17.9) | –7.6 (–7.6) | 2.9 | –1.1 | 90.5 | 0.0 |
| HCTH/93 | –1.0 | 27.2 | 2.4 | 8.2 | 7.8 | 91.2 | 0.7 |
| RPBE | –5.7 (–5.8) | 19.2 (18.8) | –6.7 (–6.8) | 2.5 | –0.2 | 89.9 | –0.6 |
| BOP | –3.5 | 22.7 | –5.8 | 4.0 | 3.3 | 89.3 | –1.2 |
| HCTH/120 | –5.4 | 21.7 | –2.7 | 3.2 | 2.3 | 93.2 | 2.7 |
| HCTH/147 | –4.7 | 22.3 | –2.2 | 3.7 | 2.9 | 93.2 | 2.7 |
| HCTH/407 | –2.6 | 26.9 | 2.5 | 7.6 | 7.5 | 91.6 | 1.1 |
| OLYP | –0.5 (–1.1) | 26.8 (26.0) | 1.6 (1.1) | 7.9 | 7.4 | 91.3 | 0.8 |
| *Meta-GGAs* | | | | | | | |
| BLAP3 | –0.8 | 29.9 | 0.3 | 8.4 | 10.5 | 91.8 | 1.3 |
| VS98 | –10.9 | 16.2 | –5.8 | 1.5 | –3.2 | 89.9 | –0.6 |
| KCIS | –8.3 | 13.6 | –11.1 | 5.0 | –5.8 | 91.7 | 1.2 |
| PKZB | –6.8 | 15.2 | –10.4 | 4.7 | –4.2 | 89.8 | –0.7 |
| Bm$\tau$1 | –0.5 | 30.6 | 0.6 | 8.9 | 11.2 | 90.2 | –0.3 |
| OLAP3 | 5.5 | 38.3 | 11.5 | 17.0 | 18.9 | 93.1 | 2.6 |
| TPSS | –8.6 | 14.8 | –11.4 | 4.6 | –4.6 | 90.3 | –0.2 |
| *Hybrid functionals* | | | | | | | |
| B3LYP | –4.9 | 25.2 | 0.2 | 5.4 | 5.8 | 90.4 | –0.1 |
| TPSSh | –7.3 | 18.6 | –6.2 | 2.0 | –0.8 | 90.1 | –0.4 |
| *Ab initio benchmark* | | | | | | | |
| CCSD(T) | –10.8 | 19.4 | –4.5 | | | 90.5 | |

[a] Geometries optimized at ZORA-BLYP/TZ2P with frozen-core approximation.

[b] Computed post-SCF using the BLYP electron density, unless stated otherwise. Values in parentheses computed self-consistently, that is, with the potential and electron density corresponding to the functional indicated. Relativistic effects treated with ZORA.

[c] Mean absolute error for the energies of the three stationary points RC, TS and P relative to the separate reactants (R), error in the overall barrier, that is, in the energy of the TS relative to R, and error in dissociation energy of the ethane C–C bond compared with the CCSD(T) benchmark.

kcal/mol). However, no significant improvement occurs going from GGA to the more recently developed meta-GGA (mean abs. err. = 1.5-17.0 kcal/mol) and hybrid functionals (mean abs. err. = 2.0-5.4 kcal/mol). Best overall agreement with the *ab initio* benchmark PES is achieved by functionals of the GGA (RPBE), meta-GGA (VS98), as well as hybrid-DFT type (TPSSh), with mean absolute errors of 1.5 to 2.5 kcal/mol and errors in the barrier ranging from –3.3 to –0.3 kcal/mol. Interestingly, the well-known BLYP functional compares very reasonably with an only slightly larger mean absolute error of 3.4 kcal/mol and an underestimation of the barrier of only –0.9 kcal/mol. Apart from RPBE, only one other functional performs better in calculating the activation barrier, namely, the TPSSh hybrid functional, with an underestimation of the barrier of only –0.8 kcal/mol. Note also that the widely used B3LYP hybrid functional does not perform better for this PES, with a significantly higher mean absolute error of 5.4 kcal/mol and an overestimation of the barrier by not less than 5.8 kcal/mol.

The above agrees with and further corroborates our previous finding for the Pd + methane system in which B3LYP was also found to perform slightly worse than BLYP (see Chapter 4). Our results also nicely agree with experimental findings by Weisshaar and coworkers,[100] who already noted a general tendency for the B3LYP functional to overestimate reaction barrier heights for insertion of 3*d* transition metal ions, and in particular $Co^+$, into C–H and C–C bonds. They proved that, using a statistical rate model, B3LYP energies cannot fit experiment at all. However, adjusting the reaction barrier heights (relative to reactants) downward with 4-7 kcal/mol leads to good agreement with experiment. Independently, we reach the same result, namely, that B3LYP overestimates the barrier (relative to reactants) by almost 6 kcal/mol.

### 5.3.4 Performance for the central barrier

So far, we have concentrated on the overall barrier, i.e., the difference in energy between the transition state and the separate reactants, which, as pointed out earlier, is decisive for the rate of chemical reactions in the gas phase, in particular, if they occur under low-pressure conditions in which the reaction system is (in good approximation) thermally isolated.[34,75] Here, we address the central barrier, the difference in energy between the TS and the reactant complex, which becomes decisive in the high-pressure regime, when termolecular collisions are sufficiently efficient to cool the otherwise rovibrationally hot reactant complex, causing it to be in thermal equilibrium with the environment. In Table 5.7 the energies of the separate reactants (R), the transition state (TS) and the product (P) relative to the reactant complex are collected.

Now, B3LYP (mean abs. err. = 2.4 kcal/mol) performs significantly better than BLYP (mean abs. err. = 6.1 kcal/mol) and is only surpassed by the performance of the GGA functional VS98 (mean abs. err. = 1.5 kcal/mol). Whereas BLYP is better for computing the overall barrier (i.e., TS relative to R), it is B3LYP that outperforms BLYP for the central barrier (i.e., TS relative to RC). We recall that BLYP underestimates the overall barrier by only –0.9 kcal/mol whereas B3LYP overestimates this barrier by 5.8 kcal/mol (see Table 5.6). The latter overestimation originates partially from the fact that B3LYP yields a too weakly bound reactant complex. Once this deficiency is switched off, by taking the reactant complex as the point of reference, B3LYP performs very well (see Table 5.7): it underestimates the barrier by only –0.1 kcal/mol whereas BLYP underestimates the central barrier by –5.0 kcal/mol.

We have verified that errors made by BLYP or B3LYP in overall or central barriers do not originate from a failure in describing the C–C bond dissociation. To this end, we have first computed an *ab initio* benchmark for the C–C bond strength, that is, the dissociation energy $D_{CC}$ associated with the reaction $H_3C–CH_3 \rightarrow 2\ CH_3^{\bullet}$, at the same levels of theory as we did for the PES of the oxidative addition of the ethane C–C bond

**Table 5.7** Energies (in kcal/mol) of the stationary points[a] relative to the reactant complex, computed for 24 functionals with the ae-TZ2P basis set with all electrons treated variationally[b,c]

| Method | R | TS | P | Mean abs. err. rel. to RC | Err. in barr. rel. to RC |
|---|---|---|---|---|---|
| *LDA* | | | | | |
| VWN | 22.7 | 17.5 | –4.5 | 11.8 | –12.7 |
| *GGAs* | | | | | |
| BP86 | 10.4 | 22.7 | –2.9 | 5.7 | –7.5 |
| BLYP | 6.7 | 25.2 | –2.8 | 6.1 | –5.0 |
| Becke88x+BR89c | 7.4 | 24.7 | –4.2 | 6.5 | –5.5 |
| PW91 | 11.8 | 22.6 | –2.3 | 5.7 | –7.6 |
| PBE | 11.3 | 22.8 | –1.9 | 5.4 | –7.4 |
| FT97 | 11.9 | 24.1 | –2.9 | 5.5 | –6.1 |
| revPBE | 6.2 | 24.5 | –1.4 | 6.0 | –5.7 |
| HCTH/93 | 1.0 | 28.2 | 3.4 | 4.9 | –2.0 |
| RPBE | 5.7 | 24.9 | –1.0 | 5.9 | –5.3 |
| BOP | 3.5 | 26.2 | –2.3 | 6.6 | –4.0 |
| HCTH/120 | 5.4 | 27.1 | 2.7 | 4.1 | –3.1 |
| HCTH/147 | 4.7 | 27.0 | 2.5 | 4.4 | –3.2 |
| HCTH/407 | 2.6 | 29.5 | 5.1 | 3.3 | –0.7 |
| OLYP | 0.5 | 27.3 | 2.1 | 5.8 | –2.9 |
| *Meta-GGAs* | | | | | |
| BLAP3 | 0.8 | 30.7 | 1.1 | 5.2 | 0.5 |
| VS98 | 10.9 | 27.1 | 5.1 | 1.5 | –3.1 |
| KCIS | 8.3 | 21.9 | –2.8 | 6.6 | –8.3 |
| PKZB | 6.8 | 22.0 | –3.6 | 7.4 | –8.2 |
| Bmτ1 | 0.5 | 31.1 | 1.1 | 5.5 | 0.9 |
| OLAP3 | –5.5 | 32.8 | 6.0 | 6.4 | 2.6 |
| TPSS | 8.6 | 23.4 | –2.8 | 6.0 | –6.8 |
| *Hybrid functionals* | | | | | |
| B3LYP | 4.9 | 30.1 | 5.1 | 2.4 | –0.1 |
| TPSSh | 7.3 | 25.9 | 1.1 | 4.3 | –4.3 |
| *Ab initio benchmark* | | | | | |
| CCSD(T) | 10.8 | 30.2 | 6.3 | | |

a Geometries optimized at ZORA-BLYP/TZ2P with frozen-core approximation.

b Computed post-SCF using the BLYP electron density. Relativistic effects treated with ZORA.

c Mean absolute error for the energies of the three stationary points R, TS and P relative to RC and error in the central barrier, in the energy of the TS relative to RC, compared with the CCSD(T) benchmark.

to Pd. This was done again using the BLYP-optimized geometries, which yield a C–H bond length of 1.084 Å for the $D_{3h}$ symmetric methyl radical. Thus, we arrive at a dissociation energy of 90.5 kcal/mol at CCSD(T) (HF: 68.0, MP2: 94.0, and CCSD: 88.4 kcal/mol), in nice agreement with previous findings (for example, Robertson *et al.*: 94.0[101] and 87.6 kcal/mol;[102] Lorant *et al.*: 95.8 kcal/mol[103]). Most functionals are able to describe the dissociation energy reasonably well, yielding errors, compared with the CCSD(T) benchmark, in the order of a kcal/mol or less. For BLYP and B3LYP, the dissociation energy $D_{CC}$ is underestimated by only 0.5 and 0.1 kcal/mol respectively (see Table 5.6). All together, we conclude that both BLYP and B3LYP are reasonable approaches for tackling the oxidative addition of the ethane C–C bond to palladium.

## 5.4 Conclusions

We have computed an *ab initio* benchmark for the archetypal oxidative addition of the ethane C–C bond to palladium that derives from a hierarchical series of relativistic methods and highly polarized basis sets for the palladium atom, up to the counterpoise corrected, four-component spin-free Dirac-Coulomb CCSD(T)/(24*s*16*p*13*d*+4*f*+*p*+*g*) level, which is converged with respect to the basis-set size within less than a kcal/mol. Our findings stress the importance of sufficient higher-angular momentum polarization functions as well as counterpoise correction for obtaining reliable activation energies.

This benchmark is used to evaluate the performance of 24 relativistic density functionals for describing geometries and relative energies of the stationary points. Excellent agreement with our *ab initio* benchmark for energies relative to reactants, is achieved by functionals of the GGA, meta-GGA as well as hybrid DFT approaches, each of which have a representative in the top three, with mean absolute errors as small as 2.5 kcal/mol or less. Neither hybrid DFT nor the meta-GGA represents a systematic improvement over GGA functionals. Interestingly, the BLYP functional still performs satisfactorily with mean absolute errors of 3.4 and 6.1 kcal/mol for energies relative to reactants and reactant complex, respectively, and an underestimation of the overall barrier (i.e., TS relative to reactants) by only –0.9 kcal/mol and of the central barrier (i.e., TS relative to RC) by –5.0 kcal/mol. Note that the much advocated B3LYP hybrid functional also performs well, but not significantly better than BLYP, with mean absolute errors of 5.4 and 2.4 kcal/mol for energies relative to reactants and reactant complex, respectively, and an overestimation of the overall barrier by 5.8 kcal/mol and an underestimation of the central barrier by only –0.1 kcal/mol. These results parallel our previous finding for the oxidative addition of the methane C–H bond to Pd.

All together, we consider ZORA-BLYP/TZ2P a sound and efficient approach for the routine investigation of catalytic bond activation, also in larger, more realistic systems.

# 6 *Ab initio* benchmark and DFT validation study for the oxidative addition of the fluoromethane C–F bond to Pd

Adapted from
G. Th. de Jong, F. M. Bickelhaupt *J. Phys. Chem. A* **2005**, *109*, 9685

## Abstract

We have computed a state-of-the-art benchmark potential energy surface (PES) for two reaction pathways (oxidative insertion (OxIn) and $S_N2$) for oxidative addition of the fluoromethane C–F bond to the palladium atom and have used this to evaluate the performance of 26 popular density functionals, covering LDA, GGA, meta-GGA, and hybrid density functionals, for describing these reactions. The *ab initio* benchmark is obtained by exploring the PES using a hierarchical series of *ab initio* methods (HF, MP2, CCSD, CCSD(T)) in combination with a hierarchical series of seven Gaussian-type basis sets, up to *g* polarization. Relativistic effects are taken into account through a full four-component all-electron approach. Our best estimate of kinetic and thermodynamic parameters is –5.3 (–6.1) kcal/mol for the formation of the reactant complex, 27.8 (25.4) kcal/mol for the activation energy for oxidative insertion (OxIn) relative to the separate reactants, 37.5 (31.8) kcal/mol for the activation energy for the alternative $S_N2$ pathway, and –6.4 (–7.8) kcal/mol for the reaction energy (zero-point vibrational energy-corrected values in parentheses). Best overall agreement with our *ab initio* benchmark is obtained by functionals from all three categories, GGA, meta-GGA, and hybrid DFT, with mean absolute errors of 1.4 to 2.7 kcal/mol and errors in activation energies ranging from 0.3 to 2.8 kcal/mol. The B3LYP functional compares very well with a slight underestimation of the overall barrier for OxIn by –0.9 kcal/mol. For comparison, the well-known BLYP functional underestimates the overall barrier by –10.1 kcal/mol. The relative performance of these two functionals is inverted with respect to previous findings for the insertion of Pd into the C–H and C–C bonds. However, all major functionals yield correct trends and qualitative features of the PES, in particular, a clear preference for the OxIn over the alternative $S_N2$ pathway.

## 6.1 Introduction

The activation of the C–F bond in fluorocarbons provides a great challenge for synthetic chemists. Fluorocarbons are known to have a high chemical inertness and high thermal stability. This is caused by the great strength of the C–F bond. Fluorine is the most electronegative element and forms the strongest single bond with carbon of any element.[104] Examples of carbon-fluorine bond activation by metal complexes are relatively rare.[105,106] Catalytic activation of the C–F bond can provide means to selectively convert simple fragments into desired complex products via C–C bond formation. Successful examples have been found for, *inter alia*, aryl fluorides.[107] While C–H and C–C activation have been the subject in various computational investigations, the oxidative addition of the C–F or, more generally, the C–halogen bonds has received less attention.[108] Still, there is a number of theoretical studies[22-25,44,108-110] on the activation of C–X bonds by $d^{10}$ metal centres, such as Pd complexes, which is our main subject of interest because of its relevance for homogeneous catalysis.[31]

Transition-metal-induced C–F bond activation usually proceeds via an oxidative addition process in which the metal increases its formal oxidation state by two units. There has been controversy about the mechanism of this reaction.[105] One mechanism that has been proposed requires the concerted transfer of two electrons and involves either a concerted front-side displacement or a concerted nucleophilic displacement ($S_N2$) proceeding via backside attack of the C–F bond by the metal. Theoretical studies on the oxidative addition of the chloromethane C–Cl bond to the Pd atom show[23,24,109] that this process can indeed proceed via direct oxidative insertion of the metal into the C–Cl bond (OxIn) or via $S_N2$ substitution followed, in a concerted manner, by leaving-group rearrangement ($S_N2$-ra). The reaction barrier for OxIn is lower than that for the $S_N2$ pathway. Interestingly, anion assistance, e.g., coordination of a chloride anion to Pd, reverses this order in activation energies and makes $S_N2$ the preferred pathway. Note that this shift in mechanism also corresponds to a change in stereochemistry at the carbon

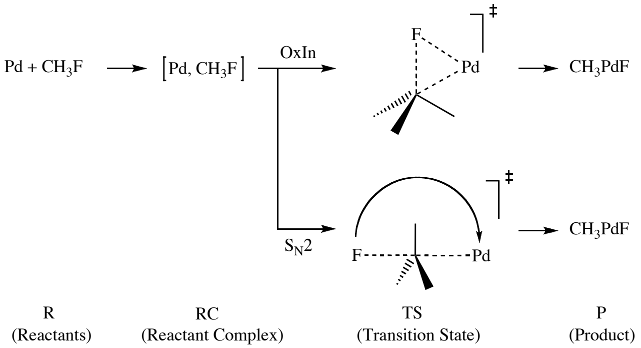

**Scheme 6.1** Model reactions and nomenclature

atom involved, namely, from retention (OxIn) to inversion of configuration ($S_N2$). This is of practical relevance for other substrates in which the carbon atom, C*, is asymmetric. Now, one may wonder if these two pathways, represented in Scheme 6.1, exist also for the corresponding activation of the stronger and more polar C–F bond.

Besides answering the above question, this study aims at two objectives. In the first place, we wish to obtain a reliable benchmark for the potential energy surface (PES) for the oxidative addition of the fluoromethane C–F bond to Pd. This is done by exploring this PES with a hierarchical series of *ab initio* methods (Hartree-Fock (HF), second-order Møller-Plesset perturbation theory (MP2),[57] and coupled-cluster theory[98] with single and double excitations (CCSD),[59] and with triple excitations treated perturbatively (CCSD(T))[60]) in combination with a hierarchical series of Gaussian-type basis sets of increasing flexibility and polarization (up to *g* functions). The basis set superposition error (BSSE) is accounted for by counterpoise correction (CPC).[12] Relativistic effects are treated with a full all-electron approach. To our knowledge these are the first benchmarking calculations at advanced correlated levels for this reaction.

In the previous chapters, with the same approach, we have investigated the insertion of the Pd-$d^{10}$ atom into the C–H bond of methane and the C–C bond of ethane as important examples of oxidative addition reactions to Pd. Density functional theory[6-9] (DFT) was shown to reproduce the highest-level *ab initio* (coupled-cluster) benchmark potential energy surfaces (PESs) within a few kcal/mol (see Chapters 4 and 5). Interestingly, the well-known BLYP functional turned out to be among the best performing functionals, providing PESs that are better than those of most of the high-level meta-GGA and hybrid functionals. The present model reaction of Pd + $CH_3F$ may possibly impose higher demands to the basis set used in the computations than the previously studied model reactions of Pd + $CH_4$ or $C_2H_6$ because the fluorine atom expands relatively much when it gains anionic character (which is what happens in an oxidative addition). Therefore, we have also investigated the oxidative addition of hydrogen fluoride to Pd. This model system is computationally less demanding than Pd + $CH_3F$ and thus allows to extend the basis set further, in fact, just far enough, in our attempt to test for convergence of the CCSD(T) energies with basis-set size.

The second purpose of our work is to evaluate the performance of 26 popular density functionals, covering LDA, GGA, meta-GGA and hybrid functionals, for describing our model reaction, using the *ab initio* benchmark as reference point. Here, we anticipate that while the latter turns out to be satisfactory in terms of accuracy and reliability, it is prohibitively expensive if one wishes to study more realistic model catalysts and substrates. Our survey of 26 functionals serves to validate one or more of these DFT approaches as a computationally more efficient alternative to high-level *ab initio* theory in future investigations in the field of computational catalysis. A general concern, however, associated with the application of DFT to the investigation of chemical reactions is its notorious tendency to underestimate activation energies.[10] Thus, we arrive at a ranking of density functional approaches in terms of the accuracy with which they describe the PES of our model reaction, in particular the activation energy. We focus on the overall barrier, that is, the difference in energy between the TS and the separate reactants, which is decisive for the rate of chemical reactions in the gas phase, in particular, if they occur under low-pressure conditions in which the reaction system is (in good approximation) thermally isolated.[34,75] But we also address the central barrier, that is, the difference in energy between the TS and the RC.

## 6.2 Methods

### 6.2.1 Geometries

All geometry optimizations have been done with DFT using the ADF program.[49-51] For several functionals, both LDA and GGA, the performance for computing the geometries and relative energies of the stationary points of our model reaction was compared. These density functionals are the LDA functional VWN[82] and the GGA functionals BP86,[52,76] BLYP,[52,53] PW91,[77] PBE,[78] revPBE,[79] RPBE[80] and OLYP.[53,81] The same computational settings were used as described in Sections 3.2.1, 4.2.1, and 5.2.1., i.e., using ZORA, the TZ2P basis set and the frozen-core approximation. For F, 1*s* was considered the core shell.

### 6.2.2 *Ab initio* calculations

On the basis of the ZORA-BLYP/TZ2P geometries, energies of the stationary points were computed in a series of single-point calculations with the program package DIRAC[55,99] using the following hierarchy of quantum chemical methods: HF, MP2, CCSD and CCSD(T). Relativistic effects are accounted for using a full all-electron four-component Dirac-Coulomb approach with a spin-free Hamiltonian.[17] The two-electron integrals over exclusively the small components have been neglected and corrected with a simple Coulombic correction, which has been shown reliable.[16]

A hierarchical series of Gaussian-type basis sets was used (see Table 6.1), which is based on the series BS1-BS5 used in Chapter 5 on the oxidative addition of the ethane C–C bond to Pd (see Table 5.2 and the discussion in Section 5.2.2). For the latter model reaction, relative energies were converged to within ca. 1 kcal/mol at BS5. In the present study, we wish to further extend the series of basis sets regarding their flexibility because of the possibly increased demands, in this respect, of fluorine. For our system $CH_3F$ + Pd, it was possible to go until BS6 and BS7, which are extensions of BS5, replacing the basis set for fluorine with uncontracted cc-aug-pVTZ and uncontracted cc-aug-pVQZ, respectively. Larger basis sets appeared to be unfeasible as this would cause the required memory to exceed our available allotment. Thus, to yet further extend our exploration of basis-set convergence, a less demanding, in terms of computational costs (in particular memory), model reaction Pd + HF was included into this investigation. This system was also studied with basis sets BS5, BS6, and BS7, but furthermore with BS6*, which is an extension of BS6, replacing the basis set for hydrogen with uncontracted cc-aug-pVTZ; and with BS8, in which an uncontracted cc-aug-pV5Z basis set is used for fluorine.

**Table 6.1** Basis sets used in the *ab initio* calculations

| Basis set | Pd | C | H | F |
|---|---|---|---|---|
| BS1 | $(24s16p13d)^{a}$ | cc-aug-pVDZ$^{b}$ | cc-aug-pVDZ$^{b}$ | cc-aug-pVDZ$^{b}$ |
| BS2 | $(24s16p13d)^{a} + 1f$ | cc-aug-pVDZ$^{b}$ | cc-aug-pVDZ$^{b}$ | cc-aug-pVDZ$^{b}$ |
| BS3 | $(24s16p13d)^{a} + 4f$ | cc-aug-pVDZ$^{b}$ | cc-aug-pVDZ$^{b}$ | cc-aug-pVDZ$^{b}$ |
| BS4 | $(24s16p13d)^{a} + 4f + p$ | cc-aug-pVDZ$^{b}$ | cc-aug-pVDZ$^{b}$ | cc-aug-pVDZ$^{b}$ |
| BS5 | $(24s16p13d)^{a} + 4f + p + g$ | cc-aug-pVDZ$^{b}$ | cc-aug-pVDZ$^{b}$ | cc-aug-pVDZ$^{b}$ |
| BS6 | $(24s16p13d)^{a} + 4f + p + g$ | cc-aug-pVDZ$^{b}$ | cc-aug-pVDZ$^{b}$ | cc-aug-pVTZ$^{b}$ |
| BS6* | $(24s16p13d)^{a} + 4f + p + g$ |  | cc-aug-pVTZ$^{b}$ | cc-aug-pVTZ$^{b}$ |
| BS7 | $(24s16p13d)^{a} + 4f + p + g$ | cc-aug-pVDZ$^{b}$ | cc-aug-pVDZ$^{b}$ | cc-aug-pVQZ$^{b}$ |
| BS8 | $(24s16p13d)^{a} + 4f + p + g$ |  | cc-aug-pVDZ$^{b}$ | cc-aug-pV5Z$^{b}$ |

[a] TZP quality.

[b] Completely uncontracted.

### 6.2.3 DFT calculations

On the basis of the ZORA-BLYP/TZ2P geometries, we have computed in a post-SCF manner, that is, using in all cases the electron density obtained at ZORA-BLYP/ae-TZ2P, the relative energies of stationary points along the PES for various LDA, GGAs, meta-GGAs and hybrid functionals. The ae-TZ2P basis set is the all-electron (i.e., no frozen-core approximation) counterpart corresponding to the above-mentioned TZ2P basis that is used in conjunction with the frozen-core approximation. In addition to the ones used in the geometry optimizations, the same functionals were examined as described in Section 4.2.3, with the addition of the hybrid functionals O3LYP[111] and X3LYP[112] (both based on VWN5[95]).

## 6.3 Results and discussion

### 6.3.1 Geometries of stationary points and reaction characteristics

First, we examine the geometries of stationary points along the reaction coordinates of the two pathways for oxidative addition of the C–F bond of fluoromethane to Pd, computed with the LDA functional VWN and the GGA functionals BP86, BLYP, PW91, PBE, revPBE, RPBE, and OLYP in combination with the TZ2P basis set, the frozen-core approximation, and ZORA to account for relativistic effects. Geometry parameters for selected stationary points are defined in Figure 6.1, and their values optimized with each of the eight functionals are collected in Table 6.2.

For each of the functionals the reaction characteristics are similar. For both reaction pathways, OxIn and $S_N2$-ra, the reaction proceeds from the reactants R via formation of a stable reactant complex RC of $C_s$ symmetry, in which fluoromethane coordinates via two hydrogen atoms in an $\eta^2$ fashion to Pd (see Figure 6.1), completely analogous to the corresponding reactant complexes of Pd + methane and Pd + ethane (see Figures 4.1 and 5.1). In the OxIn pathway, the reaction proceeds from this RC via a transition state $TS_{OxIn}$ of $C_s$ symmetry to the final product P of $C_s$ symmetry. The alternative $S_N2$-ra pathway brings the system from the same reactant complex RC in three different steps, i.e., in a more complex manner than suggested in Scheme 6.1, to the same product P. Interestingly, the minimal energy path of the Pd-atom approach to the C atom in a backside fashion first leads to insertion into a C–H bond. The transition state for insertion of Pd into the fluoromethane C–H bond, $TS_{CH}$, (3.0 kcal/mol above reactants, computed at BLYP) is similar to the corresponding transition state for Pd + methane (3.9 kcal/mol above reactants, see Chapter 4), but the resulting product of this insertion, intermediate $IM_{CH}$ (at –7.1 kcal/mol), is somewhat more stabilized with respect to the reactants than the corresponding species for methane (at –3.4 kcal/mol, see Chapter 4). Thereafter, in the second step, the inserted Pd does not approach much further; however, the $F^-$ leaving group is expelled from carbon and in a concerted movement, via transition state $TS_{S_N2}$ (26.4 kcal/mol), it abstracts the newly formed hydrogen ligand, as a proton, from Pd. The product of this second elementary step, intermediate $IM_{S_N2}$ (12.1 kcal/mol relative to reactants), can be conceived as a complex between the relatively stable $PdCH_2$

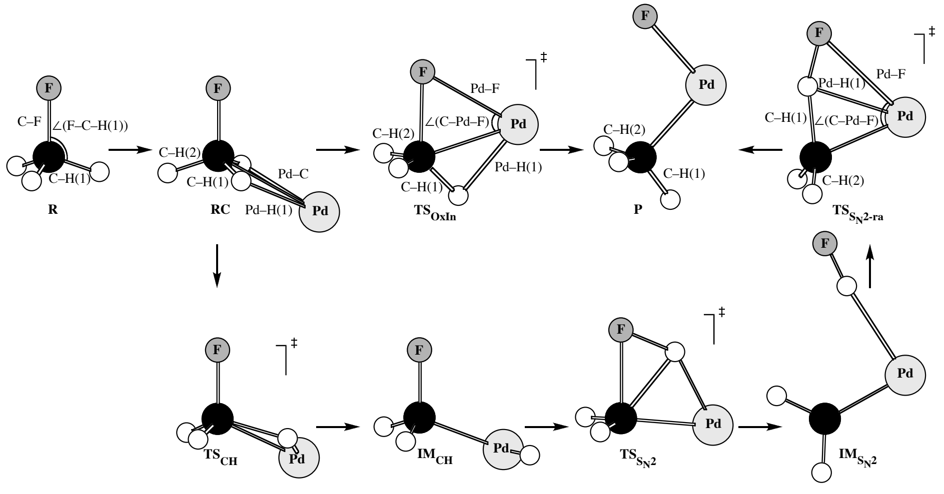

**Figure 6.1** Structures of stationary points of the two pathways for oxidative addition of the $CH_3$–F bond to Pd

**Table 6.2** Selected geometry parameters[a] (in Å, degrees), optimized with various functionals,[b] of stationary points for the OxIn and $\mathrm{S_N2}$-type pathways for oxidative addition of the fluoromethane C–F bond to Pd

| Method | | C–F | C–H(1) | C–H(2) | Pd–C | Pd–F | Pd–H(1) | ∠(F–C–H(1)) | ∠(C–Pd–F) |
|---|---|---|---|---|---|---|---|---|---|
| VWN | R | 1.374 | 1.102 | | | | | 109.3 | |
| | RC | 1.373 | 1.161 | 1.100 | 2.125 | | 1.846 | 108.9 | |
| | $\mathrm{TS_{OxIn}}$ | 1.756 | 1.201 | 1.094 | 1.970 | 2.173 | 1.834 | 136.6 | 49.9 |
| | $\mathrm{TS_{S_N2\text{-}ra}}$ | 2.573 | 1.542 | 1.107 | 1.934 | 2.433 | 2.062 | 8.3 | 71.1 |
| | P[c] | 2.756 | 1.104 | 1.099 | 1.936 | 1.882 | 2.462 | 121.1 | 92.4 |
| BP86 | R | 1.400 | 1.098 | | | | | 108.7 | |
| | RC | 1.399 | 1.137 | 1.096 | 2.273 | | 1.943 | 108.4 | |
| | $\mathrm{TS_{OxIn}}$ | 1.783 | 1.182 | 1.090 | 2.045 | 2.266 | 1.869 | 136.6 | 48.5 |
| | $\mathrm{TS_{S_N2\text{-}ra}}$ | 2.569 | 1.513 | 1.104 | 1.991 | 2.498 | 2.117 | 7.9 | 68.8 |
| | P | 2.894 | 1.104 | 1.095 | 1.978 | 1.923 | 2.465 | 143.9 | 95.8 |
| BLYP | R | 1.413 | 1.095 | | | | | 108.4 | |
| | RC | 1.411 | 1.123 | 1.094 | 2.390 | | 2.031 | 108.2 | |
| | $\mathrm{TS_{OxIn}}$ | 1.785 | 1.158 | 1.086 | 2.129 | 2.297 | 1.907 | 134.3 | 47.4 |
| | $\mathrm{TS_{S_N2\text{-}ra}}$ | 2.569 | 1.501 | 1.101 | 2.025 | 2.526 | 2.148 | 7.9 | 67.7 |
| | P | 2.949 | 1.102 | 1.093 | 2.004 | 1.944 | 2.483 | 143.1 | 96.7 |
| PW91 | R | 1.398 | 1.096 | | | | | 108.8 | |
| | RC | 1.397 | 1.135 | 1.095 | 2.271 | | 1.942 | 108.4 | |
| | $\mathrm{TS_{OxIn}}$ | 1.779 | 1.180 | 1.088 | 2.042 | 2.267 | 1.867 | 136.9 | 48.4 |
| | $\mathrm{TS_{S_N2\text{-}ra}}$ | 2.568 | 1.514 | 1.102 | 1.987 | 2.506 | 2.111 | 7.7 | 68.6 |
| | P[c] | 2.857 | 1.098 | 1.093 | 1.977 | 1.926 | 2.496 | 121.1 | 94.1 |
| PBE | R | 1.398 | 1.098 | | | | | 108.8 | |
| | RC | 1.397 | 1.138 | 1.096 | 2.268 | | 1.941 | 108.4 | |
| | $\mathrm{TS_{OxIn}}$ | 1.779 | 1.183 | 1.090 | 2.039 | 2.266 | 1.867 | 137.1 | 48.5 |
| | $\mathrm{TS_{S_N2\text{-}ra}}$ | 2.569 | 1.512 | 1.104 | 1.987 | 2.513 | 2.121 | 7.7 | 68.5 |
| | P | 2.886 | 1.104 | 1.096 | 1.974 | 1.925 | 2.464 | 144.2 | 95.5 |
| revPBE | R | 1.405 | 1.099 | | | | | 108.7 | |
| | RC | 1.404 | 1.132 | 1.097 | 2.338 | | 1.990 | 108.4 | |
| | $\mathrm{TS_{OxIn}}$ | 1.792 | 1.179 | 1.090 | 2.060 | 2.296 | 1.882 | 137.3 | 48.2 |
| | $\mathrm{TS_{S_N2\text{-}ra}}$ | 2.567 | 1.492 | 1.106 | 2.003 | 2.544 | 2.139 | 7.5 | 67.6 |
| | P | 2.921 | 1.105 | 1.096 | 1.986 | 1.940 | 2.475 | 144.0 | 96.2 |
| RPBE | R | 1.407 | 1.099 | | | | | 108.7 | |
| | RC | 1.406 | 1.130 | 1.097 | 2.361 | | 2.008 | 108.3 | |
| | $\mathrm{TS_{OxIn}}$ | 1.794 | 1.178 | 1.090 | 2.067 | 2.307 | 1.886 | 137.4 | 48.0 |
| | $\mathrm{TS_{S_N2\text{-}ra}}$ | 2.568 | 1.495 | 1.106 | 2.007 | 2.553 | 2.146 | 7.5 | 67.3 |
| | P | 2.931 | 1.105 | 1.097 | 1.989 | 1.945 | 2.477 | 143.9 | 96.4 |
| OLYP | R | 1.395 | 1.095 | | | | | 108.8 | |
| | RC[d] | 1.389 | 1.128 | 1.094 | 3.088 | | 1.966 | 108.8 | |
| | $\mathrm{TS_{OxIn}}$ | 1.798 | 1.165 | 1.086 | 2.055 | 2.295 | 1.899 | 138.4 | 48.4 |
| | $\mathrm{TS_{S_N2\text{-}ra}}$ | 2.546 | 1.472 | 1.102 | 1.993 | 2.569 | 2.147 | 7.2 | 66.4 |
| | P | 2.938 | 1.101 | 1.092 | 1.970 | 1.944 | 2.455 | 143.4 | 97.3 |

[a] See Figure 6.1 for definition.

[b] With TZ2P basis set with frozen-core approximation; relativistic effects treated with ZORA.

[c] Pd–F bond in product orientated eclipsed with respect to C–H(2) bond, at variance with other functionals.

[d] Substrate coordinated to Pd in $\eta^1$ instead of $\eta^2$ fashion, i.e., via one instead of two H atoms, namely, H(1).

entity and HF (this complex is bound by –6.6 kcal/mol, again at BLYP). In $\mathrm{IM_{S_N2}}$, the $\mathrm{CH_2}$-end can rotate almost freely, with a rotation barrier of 0.9 kcal/mol. Because of the presence of this intermediate, there will be racemization, which is a notable difference with the OxIn pathway in which there is retention of configuration. This difference will, of course, only be noticed for chiral substrates and not for our simple, achiral model fluoromethane. Finally, the third and last elementary step proceeds from intermediate $\mathrm{IM_{S_N2}}$ via transition state $\mathrm{TS_{S_N2\text{-}ra}}$ to the same final product P as for the OxIn pathway. Transition state $\mathrm{TS_{S_N2\text{-}ra}}$ is 30.2 kcal/mol (again at BLYP) above the reactants and, thus, constitutes the highest point on the PES along the $S_N2$-ra pathway. As this will be the rate-determining point, at least for the gas-phase process occurring in the low-pressure regime, and for economic reasons, we confine our determination of a high-level *ab initio* benchmark PES for the $S_N2$-ra pathway to the stationary points R, RC, $TS_{S_N2\text{-ra}}$, and P.

We wish to point out the two marked differences between the $S_N2$-ra mechanism of the present Pd + $CH_3F$ system and that of Pd + $CH_3Cl$, which is discussed in more detail in the next chapter. In both cases, there are two competing reaction channels, direct oxidative insertion (OxIn) and an alternative pathway with strong $S_N2$ character ($S_N2$-ra). In the first place, however, the C–F bond is much stronger than the C–Cl bond, and activation of the former is associated with significantly higher barriers (via both OxIn and $S_N2$). Thus, at variance with the situation for Pd + $CH_3Cl$ (see next chapter), the minimum energy path for Pd approaching $CH_3F$ from the backside is, in a sense, redirected from straight nucleophilic substitution and proceeds instead via the relatively low-energy saddle point $TS_{CH}$ for insertion into a C–H bond. Furthermore, for both, Pd + $CH_3F$ and Pd + $CH_3Cl$, the highest point on the PES of the $S_N2$-ra pathway has the character of a migrating leaving group, i.e., $F^-$ and $Cl^-$, respectively. However, the much higher basicity of $F^-$ compared to $Cl^-$ causes the former, after its expulsion in $TS_{S_N2}$ and on its way toward Pd, to abstract a proton, under formation of the intermediate complex $IM_{S_N2}$. At variance, in the case of Pd + $CH_3Cl$, the expelled $Cl^-$ leaving group migrates directly to Pd *without abstracting a proton* and, thus, without forming an additional intermediate complex involving the conjugate acid HCl.

All species in both reaction pathways have been verified to represent equilibrium structures (no imaginary frequencies) or transition states (one imaginary frequency). Furthermore, it has been verified that each transition state connects the stable stationary points as reported. The imaginary frequency in transition state $TS_{OxIn}$ associated with the normal mode that connects RC and P varies for the investigated functionals from 453 to 501 $i\,cm^{-1}$. The imaginary frequency in transition state $TS_{S_N2\text{-ra}}$ associated with the normal mode that connects $IM_{S_N2}$ and P varies from 683 to 1005 $i\,cm^{-1}$.

The geometries obtained with the various LDA and GGA functionals do not show significant mutual discrepancies (see Table 6.2). The two most eye-catching, but not essential, differences are the reactant complex RC computed with OLYP and the product P computed with VWN and PW91. Contrary to the situation found previously for methane and ethane substrates (see Chapters 4 and 5), OLYP yields an $\eta^1$ instead of an $\eta^2$ reactant complex. It should be noted, however, that forcing Pd in RC into an $\eta^2$ geometry will raise the energy with only a mere 0.6 kcal/mol. Likewise, VWN and PW91 yield a product in which the methyl group is in an eclipsed instead of a staggered conformation relative to the Pd–F bond but, again, this difference is not exactly dramatic if one realizes that the eclipsed is higher in energy than the staggered conformer by only

0.2 kcal/mol for VWN and a virtually negligible 0.03 kcal/mol for PW91. In fact, the essential physics here is that the methyl group is virtually a free internal rotor.

The C–H bond distances are very robust with respect to changing the functional, with variations in the order of a few hundredths, or less, of an Å. Note that variations in the length of the C–F bond become larger as the reaction progresses, in product P up to 0.09 Å along the various GGA functionals. This is in line with the fact that this bond is being broken along the reaction coordinate, which causes the PES to become increasingly soft in this coordinate and, thus, sensitive to changes in the method. More pronounced variations are found for the weak Pd–C and Pd–H bonds. This holds especially for the loosely bound RC, which for the GGA functionals shows fluctuations of up to one tenth of an Å for Pd–C and in the order of some hundredths up to one tenth for Pd–H. The variations in these bond distances drop to a few hundredths or even a few thousandths of an Å as the reaction proceeds to P in which more stable coordination bonds are formed. Thus, only moderate variations in bond distances occur along the various functionals, and they are more pronounced for the softer bonds. This is also reflected by the variations in bond angles. These variations are very small as firmly bound triplets of atoms are involved, but can become larger for angles opposite to a soft bond.

Thus, the various functionals yield essentially the same geometries. Since we found in Chapters 4 and 5 on the reactions of Pd with methane and ethane that BLYP performs excellently in terms of relative energies of stationary points for those model reactions and because BLYP is robust and well established, we choose the geometries of this functional to compute the *ab initio* benchmark PES in the next section.

### 6.3.2 Benchmark energies from *ab initio* calculations

Here, we report the first systematic *ab initio* calculations into relative energies of the model addition reaction of the C–F bond of fluoromethane to the Pd atom. This survey is based on geometries of stationary points that were optimized at the ZORA-BLYP/TZ2P level of relativistic DFT. The results are collected in Table 6.3.

At all levels of theory except Hartree-Fock, the reaction profiles are characterized by the formation of a stable RC, which leads via $TS_{OxIn}$ or via $TS_{S_N2\text{-ra}}$ to product P. Three striking observations can be made: (i) the spread in values of computed relative energies, depending on the level of theory and basis set, is enormous, up to nearly 45 kcal/mol; (ii) the size of the BSSE is also remarkably large, up to ca. 13 kcal/mol; and (iii) convergence with basis-set size of the computed energies is still not reached with standard basis sets used routinely in CCSD(T) computations on organometallic compounds. The lack of any correlation leads to a complete failure at the HF level, which yields an unbound RC and strongly exaggerated activation barriers: ca. 62 kcal/mol for $TS_{OxIn}$ and ca. 71 kcal/mol for $TS_{S_N2\text{-ra}}$. The failure of HF for describing the

PES of our model reaction is not unexpected because electron correlation, which is not contained in this approach, is important.[72,73] The activation energies for both pathways drop significantly when correlation is introduced. Along HF, CCSD and CCSD(T) in combination with basis set BS1, for example, the activation barrier for direct oxidative insertion decreases from 60.7 to 30.2 to 22.8 kcal/mol. But also the correlated CCSD(T) values obtained with basis sets BS1 up to BS3, comparable in quality to standard basis sets such as LANL2DZ[64,65] without or with up to four *f* functions added, are questionable, as they are obviously not converged as a function of the basis-set size. For example, at CCSD(T)/BS1 the activation energy for direct insertion is 22.8 kcal/mol. This drops to 18.3 kcal/mol for BS2 in which one *f* polarization function has been added. Thereafter, along BS2 to BS5, the activation energy increases again, although not monotonically, from 21.5 to 22.9 kcal/mol, as three more sets of *f* functions, an additional set of diffuse *p* functions and a set of *g* functions are added to the basis set of Pd. When the basis set for F is also increased, to uncontracted cc-aug-pVTZ (BS6) and cc-aug-pVQZ (BS7), the barrier increases to 24.4 and 25.3 kcal/mol, respectively.

Next, we note that the BSSE takes on large values in the correlated *ab initio* methods, whereas it is negligible if correlation is completely neglected, i.e., in HF (see

**Table 6.3** Relative energies (in kcal/mol) of stationary points of the two pathways for oxidative addition of the $CH_3$–F bond to Pd, without and with counterpoise correction (CPC), at several levels of *ab initio* theory

| | | RC | | $TS_{OxIn}$ | | $TS_{S_N2\text{-}ra}$ | | P | |
|---|---|---|---|---|---|---|---|---|---|
| Method | Basis set | no CPC | with CPC | no CPC | with CPC | no CPC | with CPC | no CPC | with CPC |
| HF | BS1 | 9.9 | 10.5 | 60.7 | 61.3 | 71.9 | 72.5 | 26.3 | 27.0 |
| | BS2 | 9.8 | 10.4 | 60.1 | 60.8 | 70.9 | 71.5 | 23.4 | 24.1 |
| | BS3 | 9.5 | 10.2 | 59.4 | 60.2 | 69.7 | 70.4 | 20.5 | 21.4 |
| | BS4 | 9.4 | 10.1 | 59.4 | 60.1 | 69.6 | 70.3 | 20.3 | 21.2 |
| | BS5 | 9.4 | 10.0 | 59.2 | 59.9 | 69.3 | 70.0 | 19.6 | 20.4 |
| | BS6 | 9.5 | 10.0 | 60.9 | 61.5 | 70.4 | 71.0 | 21.0 | 21.7 |
| | BS7 | 9.5 | 10.0 | 61.4 | 61.9 | 70.8 | 71.3 | 21.5 | 22.1 |
| MP2 | BS1 | –5.1 | –0.4 | 24.0 | 29.9 | 34.5 | 40.2 | –8.4 | 0.5 |
| | BS2 | –9.7 | –3.0 | 17.3 | 25.9 | 28.4 | 36.5 | –16.4 | –3.6 |
| | BS3 | –9.1 | –5.9 | 19.1 | 23.2 | 32.9 | 36.9 | –7.3 | –1.9 |
| | BS4 | –8.0 | –6.2 | 20.2 | 23.0 | 34.0 | 36.6 | –6.5 | –2.3 |
| | BS5 | –8.5 | –6.8 | 19.5 | 22.2 | 33.8 | 36.4 | –5.9 | –2.0 |
| | BS6 | –8.5 | –6.9 | 20.7 | 23.2 | 35.1 | 37.5 | –4.9 | –1.5 |
| | BS7 | –8.5 | –7.0 | 21.4 | 23.9 | 36.0 | 38.4 | –4.1 | –0.6 |
| CCSD | BS1 | –3.8 | 1.0 | 30.2 | 36.2 | 37.0 | 42.7 | –8.9 | –0.1 |
| | BS2 | –6.4 | –0.4 | 26.9 | 34.5 | 34.5 | 41.7 | –14.0 | –2.9 |
| | BS3 | –4.8 | –2.1 | 30.0 | 33.6 | 39.3 | 42.8 | –7.9 | –3.2 |
| | BS4 | –4.1 | –2.4 | 30.8 | 33.3 | 40.1 | 42.6 | –7.5 | –3.7 |
| | BS5 | –4.2 | –2.6 | 30.7 | 33.1 | 40.5 | 42.9 | –6.8 | –3.3 |
| | BS6 | –4.1 | –2.7 | 32.4 | 34.6 | 42.0 | 44.2 | –5.3 | –2.2 |
| | BS7 | –4.1 | –2.8 | 33.4 | 35.6 | 43.1 | 45.3 | –4.2 | –1.0 |
| CCSD(T) | BS1 | –6.3 | –0.4 | 22.8 | 30.2 | 29.6 | 36.7 | –14.4 | –3.9 |
| | BS2 | –9.6 | –2.4 | 18.3 | 27.4 | 25.4 | 34.0 | –21.0 | –8.0 |
| | BS3 | –8.2 | –4.4 | 21.5 | 26.3 | 30.5 | 35.3 | –14.7 | –8.5 |
| | BS4 | –6.7 | –4.8 | 23.1 | 26.0 | 32.1 | 35.0 | –13.3 | –8.9 |
| | BS5 | –6.9 | –5.1 | 22.9 | 25.7 | 32.5 | 35.2 | –12.8 | –8.8 |
| | BS6 | –6.8 | –5.3 | 24.4 | 26.9 | 33.9 | 36.4 | –11.5 | –7.7 |
| | BS7 | –6.8 | –5.3 | 25.3 | 27.8 | 35.0 | 37.5 | –10.5 | –6.4 |

Table 6.3, difference between values with and without CPC). The BSSE increases somewhat going from BS1 to BS2, decreases from BS2 to BS5, and remains more or less constant from BS5 to BS7. At the CCSD(T) level, for example, the BSSE for $TS_{OxIn}$ amounts to 7.4, 9.1, 4.8, 2.9, 2.7, 2.5, and 2.5 kcal/mol along the basis sets BS1-BS7, whereas the corresponding BSSE values at HF are only ca. 0.7 kcal/mol. The BSSE increases along the reaction coordinate. The reason for this is that along the reaction coordinate, the C, H, and F atoms and, thus, their basis functions come closer and begin to surround the Pd atom. This effectively improves the flexibility and polarization of the basis set and thus the description of the wavefunction around the Pd atom. Note that the BSSE at CCSD(T) has been considerably decreased, for example, for $TS_{OxIn}$, from 9.1 kcal/mol for BS2 to only 2.5 kcal/mol for BS7 and is thus clearly smaller than the relative energies that we wish to be able to compute, in particular activation energies, such as that for OxIn, which amounts to 25.3 kcal/mol; see CCSD(T)/BS7 in Table 6.3.

The high sensitivity of the PES for oxidative addition of the C–F bond to Pd highlights the prominent role that electron correlation plays in this system. It is striking that the relative CCSD(T) energies have still not reached convergence for basis set BS3, which is of a quality comparable to that of standard basis sets such as LANL2DZ,[64] augmented with four *f* polarization functions, for Pd (see Table 6.3). This may be somewhat surprising in view of earlier reports that such basis sets yield satisfactory energies for organometallic and coordination compounds.[72,73] On the other hand, it is consistent with our findings for the reactions of Pd with the C–H and C–C bonds, which show the same behaviour (see Chapters 3 and 5). One reason for the increased sensitivity toward the quality of the theoretical approach is that the presence of *f* polarization functions is only the minimum requirement for describing the correlation of Pd-4*d* electrons. In this respect, the Pd basis sets in BS1 to BS3 should be considered minimal and cannot be expected to have achieved convergence. Furthermore, the consequences of any inadequacy in the basis set shows up more severely in processes such as ours, which involve a bare transition-metal atom as one of the reactants because here the effect of assistance of basis functions on the substrate is more severe than in situations where the transition-metal fragment is already surrounded by ligands, before it combines with the substrate. This shows up in the relatively large BSSE values for CCSD(T)/BS1-BS3.

To ensure that convergence is reached for the basis-set size of the substrate atoms, particularly the fluorine atom, we have extended our investigations to the oxidative insertion of Pd into the H–F bond of hydrogen fluoride. This model reaction, in which fluorine also occurs in a polar bond, is computationally less demanding and therefore enables us to use larger basis sets than would be possible for our main model system $CH_3F$. Geometries of stationary points were obtained at ZORA-BLYP/TZ2P and are given in Figure 6.2. The insertion of Pd into the H–F bond has a significant barrier and is

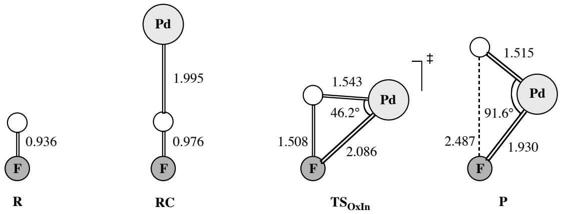

**Figure 6.2** Geometries (in Å) for Pd + H–F, at ZORA-BLYP/TZ2P, with frozen-core approximation

slightly endothermic (complexation, activation and reaction energy at BLYP, respectively, –5.0, 12.1, and 0.5 kcal/mol). The results of the *ab initio* calculations for Pd + HF with basis sets BS5, BS6, BS6* (new), BS7 and BS8 (new) are collected in Table 6.4. Note that along BS5 to BS8, the basis set for Pd is the same and corresponds to the largest one used for Pd + $CH_3F$. Only the basis sets for H and F are varied.

The PES for Pd + HF shows similar trends along HF, MP2, CCSD, and CCSD(T) as Pd + $CH_3F$. The lack of any correlation at Hartree-Fock leads again to a highly exaggerated activation barrier and an unbound reactant complex. Furthermore, relative energies are reasonably, that is, within ca. one kcal/mol, converged at all basis sets used for fluorine and hydrogen, i.e., BS5-BS8. For example, the activation energy (i.e., $TS_{OxIn}$ relative to R) for Pd + HF at CCSD(T) with CPC varies from 21.8, 21.4, 20.6, 21.2, to 21.9 kcal/mol along the basis sets BS5, BS6, BS6*, BS7, and BS8. The variations found for the complexation (i.e., RC relative to R) and reaction energy (i.e., P relative to R) are not larger. We conclude that, for the oxidative insertion of Pd into a polar bond involving fluorine, the relative energies calculated with a basis set at triple- or

**Table 6.4** Relative energies (in kcal/mol) of the stationary points for oxidative addition of H–F to Pd, without (no CPC) and with counterpoise correction (with CPC), computed at several levels of *ab initio* theory

| | | RC | | $TS_{OxIn}$ | | P | |
|---|---|---|---|---|---|---|---|
| Method | Basis set | no CPC | with CPC | no CPC | with CPC | no CPC | with CPC |
| HF | BS5 | 3.3 | 3.5 | 52.9 | 53.6 | 31.1 | 31.9 |
| | BS6 | 3.4 | 3.5 | 54.3 | 54.8 | 32.2 | 32.7 |
| | BS6* | 3.4 | 3.4 | 54.5 | 55.0 | 32.5 | 33.0 |
| | BS7 | 3.4 | 3.5 | 54.5 | 54.9 | 32.4 | 32.8 |
| | BS8 | 3.5 | 3.6 | 54.6 | 55.1 | 32.6 | 33.0 |
| MP2 | BS5 | –2.2 | –1.5 | 20.4 | 22.9 | 19.0 | 22.3 |
| | BS6 | –2.1 | –1.7 | 20.0 | 22.1 | 18.4 | 21.1 |
| | BS6* | –2.9 | –0.9 | 18.5 | 21.1 | 16.8 | 20.0 |
| | BS7 | –2.2 | –1.7 | 19.5 | 21.7 | 17.9 | 20.7 |
| | BS8 | –2.2 | –0.6 | 19.1 | 22.6 | 17.4 | 20.7 |
| CCSD | BS5 | –1.5 | –0.8 | 25.4 | 27.5 | 10.9 | 13.5 |
| | BS6 | –1.3 | –1.0 | 25.8 | 27.6 | 11.0 | 13.2 |
| | BS6* | –2.0 | –0.4 | 24.7 | 27.0 | 9.9 | 12.6 |
| | BS7 | –1.3 | –1.0 | 25.8 | 27.6 | 10.8 | 13.1 |
| | BS8 | –1.4 | –0.1 | 25.3 | 28.3 | 10.3 | 13.2 |
| CCSD(T) | BS5 | –2.5 | –1.7 | 19.2 | 21.8 | 6.7 | 9.6 |
| | BS6 | –2.4 | –1.9 | 19.3 | 21.4 | 6.4 | 8.9 |
| | BS6* | –3.3 | –1.3 | 18.0 | 20.6 | 5.2 | 8.2 |
| | BS7 | –2.4 | –2.0 | 19.1 | 21.2 | 6.1 | 8.8 |
| | BS8 | –2.5 | –1.1 | 18.7 | 21.9 | 5.6 | 8.8 |

quadruple-$\zeta$ level for fluorine are reliable to within a kcal/mol. This further corroborates the benchmark calculations for the oxidative addition reactions of Pd + $CH_3F$.

Thus, we have achieved virtual convergence of the CCSD(T) relative energies by using a larger than standard basis set and by using counterpoise correction. Our best estimate is, obtained at CCSD(T)/BS7 with CPC, –5.3 kcal/mol for the formation of the RC, 27.8 kcal/mol for the barrier of the OxIn pathway, 37.5 kcal/mol for the barrier of the $S_N2$ pathway, and –6.4 kcal/mol for the reaction energy. If we take into account zero-point vibrational energy effects computed at BLYP/TZ2P, this yields –6.1 kcal/mol for the formation of the RC, 25.4 kcal/mol for the barrier for the OxIn pathway, 31.8 kcal/mol for the barrier for the $S_N2$ pathway, and –7.8 kcal/mol for the reaction energy.

### 6.3.3 Validation of DFT

Next, we examine the relative energies of stationary points computed with the LDA functional VWN and the GGA functionals BP86, BLYP, PW91, PBE, revPBE, RPBE and OLYP in combination with ZORA-TZ2P with the frozen-core approximation. Note that for each functional we use consistently the geometries optimized with that functional. As pointed above, we first focus on the overall activation energy, that is, the difference in energy between the TS and the separate reactants, which is decisive for the rate of chemical reactions in the gas phase, in particular, if they occur under low-pressure conditions. Relative energies, with and without zero-point vibrational energy correction, as well as relative enthalpies are collected in Table 6.5. The performance of the different functionals is assessed by a comparison with our CCSD(T) benchmark.

It is clear from Table 6.5 that LDA suffers here from its infamous overbinding providing barriers that are too low and complexation and reaction energies that are too high. The GGA functionals fall into three groups regarding their agreement with the benchmark results. OLYP is clearly the best performing functional, with activation

**Table 6.5** Relative energies (in kcal/mol) without ($\Delta E$) and with zero-point vibrational energy correction ($\Delta E + \Delta ZPE$), and relative enthalpies at 298.15 K ($\Delta H$) of stationary points,[a] computed with various functionals[b]

| | $\Delta E$ | | | | $\Delta E + \Delta ZPE$ | | | | $\Delta H$ | | | |
|---|---|---|---|---|---|---|---|---|---|---|---|---|
| Method | RC | $\mathrm{TS_{Oxin}}$ | $\mathrm{TS_{S_N2\text{-}ra}}$ | P | RC | $\mathrm{TS_{Oxin}}$ | $\mathrm{TS_{S_N2\text{-}ra}}$ | P | RC | $\mathrm{TS_{Oxin}}$ | $\mathrm{TS_{S_N2\text{-}ra}}$ | P |
| *DFT computations* | | | | | | | | | | | | |
| VWN | –26.1 | –0.8 | 15.3 | –30.8 | –27.2 | –3.2 | 10.2 | –32.2 | –27.8 | –4.0 | 9.7 | –32.5 |
| BP86 | –9.7 | 14.0 | 27.3 | –18.3 | –10.6 | 11.5 | 21.8 | –19.8 | –11.0 | 10.8 | 21.3 | –20.0 |
| BLYP | –5.5 | 17.7 | 30.2 | –15.8 | –6.2 | 15.3 | 24.5 | –17.2 | –6.4 | 14.7 | 24.1 | –17.4 |
| PW91 | –11.3 | 12.4 | 26.0 | –19.6 | –12.0 | 10.0 | 20.5 | –21.0 | –12.5 | 9.3 | 20.1 | –21.2 |
| PBE | –10.8 | 12.8 | 26.4 | –18.9 | –11.7 | 10.3 | 20.9 | –20.5 | –12.1 | 9.7 | 20.4 | –21.2 |
| revPBE | –5.4 | 18.3 | 30.9 | –14.1 | –6.2 | 15.9 | 25.3 | –15.6 | –6.5 | 15.2 | 24.9 | –15.8 |
| RPBE | –4.9 | 18.8 | 31.3 | –13.6 | –5.7 | 16.3 | 25.6 | –15.1 | –6.0 | 15.7 | 25.2 | –15.2 |
| OLYP | –1.1 | 25.3 | 37.6 | –6.2 | –1.4 | 22.9 | 31.9 | –7.7 | –1.6 | 22.2 | 31.5 | –7.9 |
| *Ab initio benchmark* | | | | | | | | | | | | |
| CCSD(T) // BLYP | –5.3 | 27.8 | 37.5 | –6.4 | –6.1 | 25.4 | 31.8 | –7.8 | | | | |

a See Figure 6.1. Geometries and energies computed at the same level of theory.

b With TZ2P basis set with frozen-core approximation. Relativistic effects treated with ZORA. CCSD(T) benchmark from this study.

barriers that agree within ca. 2 kcal/mol with the CCSD(T) benchmark. The other functionals overestimate metal-substrate bonding in the RC, and provide a too low barrier and a too exothermic reaction energy. The apparent overbinding is more pronounced for BP86, PBE and PW91 than for BLYP, revPBE and RPBE. For example, PW91 underestimates the barrier for direct insertion by 15.4 kcal/mol and the barrier for the $S_N2$-ra pathway by 11.5 kcal/mol, whereas BLYP underestimates these barriers by 10.1 and 7.3 kcal/mol. Note however that all GGA functionals yield the same relative order in barriers and reaction energies, that is, OxIn well beneath $S_N2$, in nice agreement with the benchmark. This parallels our findings in the previous chapters for the insertion of Pd into the C–H and C–C bonds. However, for C–H and C–C activation, BLYP agrees excellently with CCSD(T) and OLYP *overestimates* barriers by 5-7 kcal/mol, at variance with the present case of C–F activation for which it is OLYP that agrees excellently with CCSD(T) and BLYP that *underestimates* barriers by 7-10 kcal/mol.

Finally, based again on the ZORA-BLYP/TZ2P geometries discussed above, we have computed the relative energies of the stationary points for a wide range of functionals in combination with the all-electron ae-TZ2P basis set. This was done in a post-SCF manner, i.e., using the functionals with the electron density obtained at ZORA-BLYP/ae-TZ2P. The results are collected in Table 6.6.

For clarity, we wish to point out that this computational procedure differs in three respects from that used for Table 6.5: (i) an all-electron approach is used instead of the frozen-core approximation, (ii) for all functionals, the BLYP-optimized geometries are used instead of geometries optimized with the same functional, and (iii) for all functionals, the BLYP electron density is used for computing the energy instead of the density corresponding to that functional. The effect of point (i) is in the order of up to 0.5 kcal/mol (compare BLYP values in Tables 6.5 and 6.6). The differences between the values in Tables 6.5 and 6.6 derive mainly from the combined effect of points (ii) and (iii), which is, in the case of the GGA functionals, in the order of up to 1.4 kcal/mol. Both effects are mostly in the order of a few tenths of a kcal/mol and, for the different GGA functionals and stationary points, contribute to this destabilization with varying importance. This was tested by computing the relative energies using approximation (ii) but not (iii), i.e., computing them with the density corresponding to the functional under consideration but with the BLYP geometries; the resulting values are provided in parentheses in Table 6.6. In conclusion, for the GGA functionals, the combined effect of approximations (i)-(iii) on the relative energies is small, up to 1.4 kcal/mol.

Now, we extend our survey to the full range of density functionals that, except for LDA and the GGAs discussed above, have been implemented in the ADF program in a post-SCF manner. For all 26 functionals, we have computed mean absolute errors and the errors in the barriers, as compared with the CCSD(T) benchmark (see Table 6.6).

Both the mean absolute error and the error in the barrier drop significantly if one goes from LDA (mean abs. err. = 21.4 kcal/mol), which suffers from its infamous overbinding, to GGA functionals (mean abs. err. = 2.1-11.1 kcal/mol). However, no significant improvement occurs going from GGA to the more recently developed meta-GGA functionals (mean abs. err. = 2.7-10.0 kcal/mol). The hybrid functionals again give improvement (mean abs. err. = 1.4-5.6 kcal/mol). Best agreement with the benchmark is achieved by functionals of the GGA (HCTH/407 and OLYP) and meta-GGA (BLAP3 and Bm$\tau$1), as well as hybrid type (B3LYP and X3LYP), with mean errors of 1.4 to 2.2 kcal/mol and errors in the barriers ranging from –2.1 to –0.9 kcal/mol for the OxIn pathway and from 0.3 to 2.8 kcal/mol for the $S_N2$-ra pathway. Note that the outstanding performance of BLYP for insertion of Pd into the C–H and C–C bonds, does not hold for

**Table 6.6** Energies (in kcal/mol) of the stationary points[a] relative to separate reactants, and dissociation energy of fluoromethane into a methyl radical and fluorine atom ($D_{CF}$), computed for 26 functionals[b,c]

| Method | RC | $TS_{OxIn}$ | $TS_{S_N2\text{-ra}}$ | P | Mean abs. err. rel. to R | Err. in OxIn barr. rel. to R | Err. in $S_N2$-ra barr. rel. to R | $D_{CF}$ | Err. in $D_{CF}$ |
|---|---|---|---|---|---|---|---|---|---|
| *LDA* | | | | | | | | | |
| VWN | –21.4 (–21.7) | 2.3 (2.0) | 16.6 (16.7) | –29.4 (–29.5) | 21.4 | –25.4 | –20.9 | 142.2 | 30.3 |
| *GGAs* | | | | | | | | | |
| BP86 | –9.0 (–9.1) | 14.6 (14.5) | 27.5 (27.5) | –18.6 (–18.6) | 9.8 | –13.2 | –10.0 | 116.6 | 4.7 |
| BLYP | –5.4 | 17.7 | 30.1 | –16.3 | 6.9 | –10.1 | –7.4 | 114.6 | 2.7 |
| Becke88x+BR89c | –6.1 | 17.4 | 29.6 | –18.7 | 7.8 | –10.4 | –7.8 | 115.5 | 3.6 |
| PW91 | –10.5 (–10.5) | 13.1 (13.0) | 26.1 (26.2) | –19.7 (–19.8) | 11.1 | –14.7 | –11.4 | 119.3 | 7.5 |
| PBE | –10.0 (–10.1) | 13.7 (13.4) | 26.6 (26.6) | –19.0 (–19.2) | 10.6 | –14.0 | –10.9 | 118.8 | 6.9 |
| FT97 | –10.8 | 15.5 | 26.6 | –17.6 | 9.9 | –12.2 | –10.8 | 111.7 | –0.2 |
| revPBE | –5.0 (–5.1) | 19.0 (18.7) | 31.1 (31.0) | –14.3 (–14.5) | 5.9 | –8.8 | –6.4 | 112.1 | 0.2 |
| HCTH/93 | 0.1 | 26.6 | 39.4 | –5.1 | 2.5 | –1.2 | 2.0 | 114.7 | 2.8 |
| RPBE | –4.5 (–4.7) | 19.4 (19.1) | 31.5 (31.4) | –13.8 (–14.0) | 5.6 | –8.4 | –6.0 | 111.2 | –0.7 |
| BOP | –2.1 | 21.5 | 33.3 | –13.0 | 5.1 | –6.2 | –4.2 | 113.2 | 1.3 |
| HCTH/120 | –4.2 | 21.6 | 35.1 | –9.6 | 3.2 | –6.2 | –2.4 | 117.0 | 5.1 |
| HCTH/147 | –3.5 | 22.2 | 35.8 | –9.2 | 3.0 | –5.5 | –1.7 | 116.9 | 5.1 |
| HCTH/407 | –1.6 | 25.6 | 38.8 | –5.1 | 2.1 | –2.1 | 1.4 | 115.7 | 3.8 |
| OLYP | 0.3 (–0.2) | 26.0 (25.6) | 38.5 (37.9) | –6.2 (–6.5) | 2.2 | –1.8 | 1.0 | 113.7 | 1.9 |
| *Meta-GGAs* | | | | | | | | | |
| BLAP3 | 0.4 | 26.6 | 37.8 | –10.1 | 2.7 | –1.1 | 0.3 | 116.9 | 5.0 |
| VS98 | –9.3 | 12.2 | 29.0 | –18.6 | 10.0 | –15.6 | –8.5 | 111.7 | –0.1 |
| KCIS | –7.0 | 15.0 | 29.0 | –18.4 | 8.8 | –12.8 | –8.5 | 111.6 | –0.3 |
| PKZB | –5.5 | 16.4 | 30.9 | –17.8 | 7.4 | –11.4 | –6.6 | 109.2 | –2.6 |
| Bm$\tau$1 | 0.7 | 26.9 | 37.9 | –10.0 | 2.7 | –0.9 | 0.5 | 115.2 | 3.4 |
| OLAP3 | 6.2 | 34.9 | 46.2 | –0.1 | 8.4 | 7.1 | 8.7 | 116.1 | 4.2 |
| TPSS | –7.0 | 15.9 | 31.5 | –18.6 | 7.9 | –11.8 | –6.0 | 113.5 | 1.6 |
| *Hybrid functionals* | | | | | | | | | |
| B3LYP | –3.4 | 26.9 | 40.2 | –7.0 | 1.5 | –0.9 | 2.7 | 110.9 | –1.0 |
| O3LYP | 0.3 | 31.0 | 45.2 | –0.4 | 5.6 | 3.3 | 7.7 | 116.1 | 4.3 |
| X3LYP | –3.9 | 26.8 | 40.3 | –6.9 | 1.4 | –1.0 | 2.8 | 111.2 | –0.6 |
| TPSSh | –5.7 | 20.8 | 36.4 | –13.6 | 3.9 | –7.0 | –1.0 | 111.0 | –0.8 |
| *Ab initio benchmark* | | | | | | | | | |
| CCSD(T) | –5.3 | 27.8 | 37.5 | –6.4 | | | | 111.9 | |

a Geometries optimized at ZORA-BLYP/TZ2P with frozen-core approximation.

b Computed post-SCF using BLYP electron density, unless stated otherwise. Values in parentheses computed self-consistently, that is, with the potential and electron density corresponding to the functional indicated. Using ZORA and ae-TZ2P basis set without frozen-core approximation.

c Mean absolute error for the energies of the stationary points RC, $TS_{OxIn}$, $TS_{S_N2\text{-ra}}$ and P relative to separate reactants, error in the overall barriers, and error in dissociation energy of the C–F bond, compared with the CCSD(T) benchmark.

insertion of Pd into the C–F bond. Here, BLYP has a mean error of 6.9 kcal/mol, which has to be compared with 2.2 kcal/mol for OLYP and even 1.5 kcal/mol for B3LYP. In particular, BLYP underestimates the OxIn barrier by –10.1 kcal/mol and the $S_N2$-ra barrier by –7.4 kcal/mol. Again, note that OLYP and B3LYP perform much better for these barriers: both slightly underestimate the OxIn barrier (by –1.8 and –0.9 kcal/mol) and slightly overestimate that for $S_N2$-ra (by 1.0 and 2.7 kcal/mol).

### 6.3.4 Performance for the central barrier

So far, we have concentrated on the overall barrier, that is, the difference in energy between the TS and the separate reactants, which is decisive for the rate of chemical reactions in the gas phase, in particular, if they occur under low-pressure conditions in which the reaction system is (in good approximation) thermally isolated.[34,75] Here, we

**Table 6.7** Energies (in kcal/mol) of stationary points[a] relative to RC, computed for 26 functionals[b,c]

| Method | R | $TS_{OxIn}$ | $TS_{S_N2\text{-ra}}$ | P | Mean abs. err. rel. to RC | Err. in OxIn barr. rel. to RC | Err. in $S_N2$-ra barr. rel. to RC |
|---|---|---|---|---|---|---|---|
| *LDA* | | | | | | | |
| VWN | 21.4 | 23.8 | 38.0 | –8.0 | 9.3 | –9.3 | –4.8 |
| *GGAs* | | | | | | | |
| BP86 | 9.0 | 23.6 | 36.5 | –9.6 | 7.0 | –9.5 | –6.3 |
| BLYP | 5.5 | 23.2 | 35.5 | –10.8 | 6.8 | –9.9 | –7.3 |
| Becke88x+BR89c | 6.1 | 23.4 | 35.7 | –12.6 | 7.3 | –9.7 | –7.1 |
| PW91 | 10.5 | 23.7 | 36.6 | –9.2 | 7.2 | –9.4 | –6.2 |
| PBE | 10.0 | 23.7 | 36.5 | –9.0 | 7.1 | –9.4 | –6.3 |
| FT97 | 10.8 | 26.4 | 37.4 | –6.8 | 5.8 | –6.7 | –5.3 |
| revPBE | 5.0 | 24.0 | 36.1 | –9.3 | 6.1 | –9.1 | –6.7 |
| HCTH/93 | –0.1 | 26.5 | 39.3 | –5.3 | 4.9 | –6.6 | –3.5 |
| RPBE | 4.5 | 23.9 | 36.0 | –9.3 | 6.3 | –9.2 | –6.8 |
| BOP | 2.1 | 23.7 | 35.4 | –10.9 | 7.5 | –9.4 | –7.3 |
| HCTH/120 | 4.2 | 25.8 | 39.3 | –5.4 | 4.1 | –7.3 | –3.5 |
| HCTH/147 | 3.5 | 25.8 | 39.3 | –5.6 | 4.3 | –7.3 | –3.5 |
| HCTH/407 | 1.6 | 27.2 | 40.4 | –3.6 | 3.6 | –5.9 | –2.4 |
| OLYP | –0.3 | 25.6 | 38.1 | –6.6 | 5.8 | –7.5 | –4.7 |
| *Meta-GGAs* | | | | | | | |
| BLAP3 | –0.4 | 26.3 | 37.4 | –10.5 | 6.8 | –6.8 | –5.4 |
| VS98 | 9.3 | 21.5 | 38.2 | –9.3 | 7.1 | –11.6 | –4.6 |
| KCIS | 7.0 | 22.0 | 36.0 | –11.4 | 7.5 | –11.1 | –6.8 |
| PKZB | 5.5 | 21.9 | 36.4 | –12.3 | 7.3 | –11.2 | –6.4 |
| Bm$\tau$1 | –0.7 | 26.1 | 37.2 | –10.7 | 7.1 | –7.0 | –5.6 |
| OLAP3 | –6.2 | 28.7 | 40.0 | –6.3 | 6.0 | –4.4 | –2.8 |
| TPSS | 7.0 | 22.9 | 38.5 | –11.6 | 6.7 | –10.2 | –4.3 |
| *Hybrid functionals* | | | | | | | |
| B3LYP | 3.4 | 30.2 | 43.5 | –3.6 | 2.0 | –2.9 | 0.7 |
| O3LYP | –0.3 | 30.8 | 44.9 | –0.6 | 2.6 | –2.3 | 2.1 |
| X3LYP | 3.9 | 30.8 | 44.2 | –2.9 | 1.8 | –2.3 | 1.4 |
| TPSSh | 5.7 | 26.5 | 42.1 | –7.9 | 3.6 | –6.6 | –0.7 |
| *Ab initio benchmark* | | | | | | | |
| CCSD(T) | 5.3 | 33.1 | 42.8 | –1.1 | | | |

[a] Geometries optimized at ZORA-BLYP/TZ2P with frozen-core approximation.

[b] Computed post-SCF using BLYP electron density. Using ZORA and ae-TZ2P basis set without frozen-core approximation.

[c] Mean absolute error for the energies of the four stationary points R, $TS_{OxIn}$, $TS_{S_N2\text{-ra}}$ and P relative to RC and error in the central barriers, that is, in the energy of $TS_{OxIn}$, respectively $TS_{S_N2\text{-ra}}$, relative to RC, compared with the CCSD(T) benchmark from this study.

address the central barrier, that is, the difference in energy between the TS and the RC. The latter becomes decisive in the high-pressure regime, when termolecular collisions are sufficiently efficient to cool the otherwise rovibrationally hot reactant complex, causing it to be in thermal equilibrium with the environment. In Table 6.7, we have collected the energies of the separate reactants (R), the transition states of both reaction pathways ($TS_{OxIn}$ and $TS_{S_N2\text{-ra}}$) and the product (P) relative to the reactant complex (RC).

Best overall performance is again achieved by the hybrid functionals X3LYP (mean abs. err. = 1.8 kcal/mol) and B3LYP (2.0 kcal/mol). They outperform BLYP (6.8 kcal/mol) and also OLYP (5.8 kcal/mol). Here, B3LYP appears to perform remarkably well for both, energies relative to reactants and relative to the reactant complex.

We have verified to which extent errors made in the barriers originate from a failure in describing the C–F bond dissociation. To this end, we have first computed an *ab initio* benchmark for the C–F bond strength ($D_{CF}$), using again BLYP-optimized geometries. Thus, we arrive at a dissociation energy of 111.9 kcal/mol at CCSD(T)/BS7 with CPC (HF: 75.8, MP2: 118.3, and CCSD: 108.5 kcal/mol), in nice agreement with the experimental value for the enthalpy at 0 K, namely, 113.3 ± 3.8 kcal/mol.[113] Most functionals describe $D_{CF}$ reasonably well, yielding errors in the order of a few kcal/mol. BLYP overestimates it by only 2.7 kcal/mol, while B3LYP underestimates it by a mere 1.0 kcal/mol (see Table 6.6). This agrees well with computations of the C–F bond strength by Wiener and Politzer,[114] who find that the B3LYP value is 4 kcal/mol less bonding than the BLYP one. In conclusion, the underestimation of the barriers by BLYP cannot be ascribed to a failure in describing the bond dissociation.

### 6.3.5 BLYP//LDA: A compromise between accuracy and economy

The above shows that BLYP is a sound and efficient alternative computationally immensely demanding *ab initio* methods for the routine investigation of catalytic bond activation in larger, more realistic model systems. But one can, of course, always raise the size of a model system and thus the computational costs beyond the limits associated with the available computing resources. The question is: can we push these limits even a bit further, that is, can we find a DFT approach that is not much less accurate than BLYP and yet significantly more efficient. A substantial improvement of the efficiency is easily achieved with LDA. However, it is well-known and confirmed here that LDA fails miserably regarding the accuracy of its PES. On the other hand, we have also seen that although LDA (VWN) geometries of stationary points differ somewhat more from the GGA ones than the latter differ among each other, this discrepancy in geometries is not dramatic. Therefore, in an attempt to achieve the utmost in terms of efficiency, we have also computed the BLYP//LDA PESs associated with the oxidative addition reactions of the $CH_3$–F bond to Pd, that is, using LDA-optimized geometries of the stationary points at which then, in a single-point fashion, BLYP energies are computed (using ZORA and the TZ2P basis with frozen-core approximation). The relative energies are –2.0 kcal/mol for RC, 19.7 kcal/mol for $TS_{OxIn}$, 31.2 kcal/mol for $TS_{S_N2\text{-}ra}$ and –14.3 kcal/mol for P. This compares reasonably well with the values obtained with a full BLYP//BLYP approach (see Table 6.5). The BLYP//LDA relative energies are somewhat higher than those obtained with BLYP//BLYP, namely, 3.5, 2.1, 1.0, and 1.5 kcal/mol, respectively, for RC, $TS_{OxIn}$, $TS_{S_N2\text{-}ra}$, and P. Thus, the more approximate BLYP//LDA PES agrees even somewhat better with the CCSD(T) benchmark than BLYP//BLYP. While this is most probably fortuitous, it shows that the more approximate BLYP//LDA approach differs in this case only a few kcal/mol from the principally more accurate BLYP//BLYP approach, while a significant reduction in computational cost in the most demanding part of the computations, the geometry optimization, is achieved.

## 6.4 Conclusions

We have computed an *ab initio* benchmark for the archetypal oxidative addition of the fluoromethane C–F bond to Pd that derives from a hierarchical series of relativistic *ab initio* methods and highly polarized basis sets for the Pd atom, up to the counterpoise-corrected, four-component spin-free Dirac-Coulomb CCSD(T)/(24*s*16*p*13*d*+4*f*+*p*+*g*) level, which is converged with respect to the basis-set size within a few tenths of a kcal/mol. We stress the importance of sufficient higher-angular momentum polarization functions as well as counterpoise correction for obtaining reliable activation energies.

This benchmark is used to evaluate the performance of 26 density functionals. Excellent agreement is achieved by functionals of the GGA and meta-GGA as well as hybrid DFT approaches, with mean absolute errors as small as 2.7 kcal/mol or less. The outstanding performance of BLYP as found for insertion of Pd into C–H and C–C bonds (see Chapters 4 and 5), is not found for insertion into the C–F bond. Here, BLYP has a mean error of 6.9 kcal/mol, which has to be compared with 2.2 kcal/mol for OLYP and even 1.5 kcal/mol for B3LYP. In particular, BLYP underestimates the OxIn barrier by –10.1 kcal/mol and the barrier for $S_N2$-ra by –7.4 kcal/mol. For comparison, OLYP and B3LYP only slightly underestimate the OxIn barrier by –1.8 and –0.9 kcal/mol, and slightly overestimate the barrier for $S_N2$-ra, by 1.0 and 2.7 kcal/mol.

However, all important features of the CCSD(T) benchmark are reproduced by functionals such as BLYP, OLYP and B3LYP. Thus, while none of these functionals is the “best one” for each individual reaction, they all agree with the benchmark in the following order of the barriers: C–F ($S_N2$-ra) > C–F (OxIn) ≥ C–C (OxIn) > C–H (OxIn).

All together, we consider ZORA-BLYP/TZ2P a sound and efficient approach for the investigation of catalytic bond activation, also in larger, more realistic systems.

# 7 *Ab initio* benchmark and DFT validation study for the oxidative addition of the chloromethane C–Cl bond to Pd

Adapted from
G. Th. de Jong, F. M. Bickelhaupt *J. Chem. Theory Comput.* **2006**, *2*, 322

## Abstract

We have computed a state-of-the-art benchmark potential energy surface (PES) for the archetypal oxidative addition of the chloromethane C–Cl bond to the palladium atom and have used this to evaluate the performance of 26 popular density functionals, covering LDA, GGA, meta-GGA and hybrid functionals, for describing this reaction. The *ab initio* benchmark is obtained by exploring the PES using a hierarchical series of *ab initio* methods (HF, MP2, CCSD, CCSD(T)) in combination with a hierarchical series of seven Gaussian-type basis sets, up to *g* polarization. Relativistic effects are taken into account through a full four-component all-electron approach. Our best estimate of kinetic and thermodynamic parameters is –11.2 (–10.8) kcal/mol for the formation of the most stable reactant complex, 3.8 (2.7) kcal/mol for the activation energy of direct oxidative insertion (OxIn), and –28.0 (–28.8) kcal/mol for the reaction energy (all energies relative to separate reactants, zero-point vibrational energy-corrected values in parentheses). The best overall agreement with our *ab initio* benchmark is obtained by functionals from all three categories, GGA, meta-GGA, and hybrid DFT, with mean absolute errors of 0.8-3.0 kcal/mol and errors in activation energies for OxIn ranging from 0.0 to 1.2 kcal/mol. For example, three well-known functionals, BLYP, OLYP and B3LYP, compare very reasonably with, respectively, an underestimation of the barrier for OxIn of –4.2 kcal/mol and overestimations of 4.2 and 1.6 kcal/mol. Interestingly, all important features of the CCSD(T) benchmark potential energy surfaces for the Pd-induced activation of C–H, C–C, C–F and C–Cl bonds are reproduced correctly within a few kcal/mol by BLYP, OLYP and B3LYP, while, at the same time, none of these functionals is the "best one" in each individual case. This follows from an overall comparison of the results of this chapter as well as the preceding chapters.

## 7.1 Introduction

The activation of the C–Cl bond is an efficient tool for selectively converting simple educts, via C–C bond formation, into more complex compounds. This process, which is often based on catalytically active Pd complexes, is therefore of major importance for synthetic chemistry. The most intensively used substrates for such C–C coupling reactions are aryl halides, whereas it is more difficult in this context to exploit alkyl halides.[115] While C–H and C–C activation have been the subject in various theoretical investigations, the oxidative addition of C–Cl or, more generally, C–halogen bonds has received less attention.[108] Still, there have been done computational studies on the activation of C–X bonds by $d^{10}$ metal centres,[20,22-25,44,108,110] such as Pd complexes, which is a main subject of interest because of its relevance for homogeneous catalysis.[31]

Transition-metal-induced C–Cl bond activation usually proceeds via an oxidative addition process in which the metal increases its formal oxidation state by two units. There has been controversy about the mechanism of this reaction.[105] One mechanism that has been proposed requires the concerted transfer of two electrons and involves either a concerted front-side displacement or a concerted nucleophilic displacement ($\mathrm{S_N2}$) proceeding via backside attack of the C–Cl bond by the metal. Theoretical studies on the oxidative addition of the C–Cl bond in chloromethane to the Pd atom show that this process can indeed proceed via direct oxidative insertion of the metal into the C–Cl bond (OxIn) or via $\mathrm{S_N2}$ substitution followed, in a concerted manner, by leaving-group rearrangement ($\mathrm{S_N2}$-ra).[20,23,24] The reaction barrier for OxIn is lower than that for the $\mathrm{S_N2}$ pathway. The two pathways are schematically summarized in Scheme 7.1.

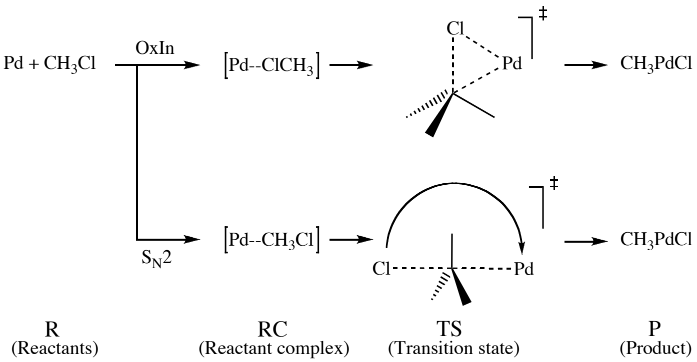

**Scheme 7.1** Model reactions and nomenclature

The purpose of the present study is twofold. In the first place, we wish to obtain a reliable benchmark for the potential energy surface (PES) for the oxidative addition of the $CH_3$–Cl bond to Pd(0). This is done using a hierarchical series of *ab initio* methods (Hartree-Fock (HF), second order Møller-Plesset perturbation theory (MP2),[57] and coupled cluster theory[98] with single and double excitations (CCSD)[59] and with triple excitations treated perturbatively (CCSD(T))[60]) in combination with a hierarchical series of basis sets of increasing flexibility and polarization, including counterpoise correction.[12] Relativity is treated with an all-electron approach. To our knowledge these are the first benchmarking calculations at advanced correlated level for this reaction.

The second purpose of our work is to evaluate the performance of 26 popular density functionals for describing the present model reaction, using the *ab initio* benchmark as a reference point. In Chapters 4 to 6, with the same approach as has been used in the present study, we have investigated the insertion of the Pd-$d^{10}$ atom into the methane C–H bond, the ethane C–C bond and the fluoromethane C–F bond as important archetypal examples of oxidative addition reactions. DFT turned out to reproduce the highest level *ab initio* benchmark within a few kcal/mol. Interestingly, in the case of Pd-induced C–H and C–C bond activation, the well-known BLYP functional turned out to be among the best performing functionals, better than most of the high-level meta-GGA and hybrid functionals. On the other hand, the activation of the C–F bond turns out to be somewhat better described by OLYP and B3LYP. Here, we are interested in how far the same conclusions hold for C–Cl activation. We conclude with an overview for all bonds for which we have carried out a benchmarking study: C–H, C–C, C–F, and C–Cl.

## 7.2 Methods

### 7.2.1 Geometries

All geometry optimizations have been done with DFT using the ADF program.[49-51] For several LDA and GGA functionals the performance for computing the geometries and relative energies of the stationary points was compared. These functionals are the LDA functional VWN[82] and the GGA functionals BP86,[52,76] BLYP,[52,53] PW91,[77] PBE,[78] revPBE,[79] RPBE[80] and OLYP.[53,81] The same computational settings were used as described in Sections 3.2.1, 4.2.1, 5.2.1, and 6.2.1, i.e., using ZORA, the TZ2P basis set and the frozen-core approximation. For Cl, 1*s*2*s*2*p* was considered the core shell.

### 7.2.2 *Ab initio* calculations

Based on the ZORA-BLYP/TZ2P geometries, energies of the stationary points were computed in a series of single-point calculations with the program package DIRAC[55,99] using the following hierarchy of methods: HF, MP2, CCSD and CCSD(T). Relativistic effects are accounted for using an all-electron Dirac-Coulomb approach with a spin-free Hamiltonian.[17] The two-electron integrals exclusively over the small components have been neglected and corrected with a reliable simple Coulombic correction.[16]

A hierarchical series of Gaussian-type basis sets was used (see Table 6.1), which is based on the series BS1-BS5 used in the previous chapters on the reactions of Pd + C–C and C–F (see Tables 5.2 and 6.1 and the discussions in Sections 5.2.2 and 6.2.2), with an extra uncontracted cc-aug-pVTZ basis set for Cl. For C–C addition, concerning the cc-aug-pVDZ basis set for C and H, relative energies were converged to within ca. 1 kcal/mol at BS5 (see Section 5.2.2). For the present reaction, we have investigated more extensively how well the relative energies are converged with respect to the basis-set sizes of C, H and Cl. To this end, basis sets BS2(–) and BS2(+) were constructed. BS2(–) is equal to BS2, but with a cc-aug-pVDZ instead of a cc-aug-pVTZ basis set for Cl. BS2(+) also corresponds to BS2, but with a cc-aug-pVTZ basis set for C, H and Cl.

**Table 7.1** Basis sets used in the *ab initio* calculations

| Basis set | Pd | C | H | Cl |
|---|---|---|---|---|
| BS1 | $(24s16p13d)^a$ | cc-aug-pVDZ[b] | cc-aug-pVDZ[b] | cc-aug-pVTZ[b] |
| BS2 | $(24s16p13d)^a + 1f$ | cc-aug-pVDZ[b] | cc-aug-pVDZ[b] | cc-aug-pVTZ[b] |
| BS2(–) | $(24s16p13d)^a + 1f$ | cc-aug-pVDZ[b] | cc-aug-pVDZ[b] | cc-aug-pVDZ[b] |
| BS2(+) | $(24s16p13d)^a + 1f$ | cc-aug-pVTZ[b] | cc-aug-pVTZ[b] | cc-aug-pVTZ[b] |
| BS3 | $(24s16p13d)^a + 4f$ | cc-aug-pVDZ[b] | cc-aug-pVDZ[b] | cc-aug-pVTZ[b] |
| BS4 | $(24s16p13d)^a + 4f + p$ | cc-aug-pVDZ[b] | cc-aug-pVDZ[b] | cc-aug-pVTZ[b] |
| BS5 | $(24s16p13d)^a + 4f + p + g$ | cc-aug-pVDZ[b] | cc-aug-pVDZ[b] | cc-aug-pVTZ[b] |

a TZP quality.

b Completely uncontracted.

### 7.2.3 DFT calculations

On the basis of the ZORA-BLYP/TZ2P geometries, we have computed in a post-SCF manner, that is, using in all cases the electron density obtained at ZORA-BLYP/ae-TZ2P, the relative energies of the stationary points for various LDA, GGAs, meta-GGAs and hybrid functionals. The ae-TZ2P basis set is the all-electron counterpart corresponding to the above-mentioned TZ2P basis that is used in conjunction with the frozen-core approximation. In addition to the ones used in the geometry optimizations, the same functionals were examined as described in Section 4.2.3, with the addition of the hybrid functionals O3LYP[111] and X3LYP[112] (both based on VWN5[95]).

## 7.3 Results and discussion

### 7.3.1 Geometries of stationary points and reaction characteristics

First, we examine the geometries of stationary points along the reaction coordinates of the two pathways for oxidative addition of Pd to the chloromethane C–Cl bond, computed with the LDA functional VWN and the GGA functionals BP86, BLYP, PW91, PBE, revPBE, RPBE and OLYP in combination with the TZ2P basis set, the frozen-core approximation, and ZORA. For the BLYP functional, the results are given in

Figure 7.1. For the other functionals, the optimized geometries can be found in the supporting information of ref. 116. All species in both reaction pathways have been verified through vibrational analyses to represent equilibrium structures (no imaginary frequencies) or transition states (one imaginary frequency). Furthermore, it has been verified that each transition state connects the stable stationary points as shown.

Each functional gives similar reaction characteristics. For the OxIn pathway, the reaction proceeds from the reactants R via formation of a stable reactant complex $RC_{OxIn}$, in which the Cl atom coordinates to Pd, to a transition state $TS_{OxIn}$ and, finally, a stable product P. For the $S_N2$ pathway, the reaction proceeds from the reactants via formation of another stable reactant complex, $RC_{S_N2}$, in which chloromethane coordinates via two hydrogen atoms in an $\eta^2$ fashion to Pd, completely analogous to reactant complexes for the reactions of Pd with methane, ethane, and fluoromethane. From $RC_{S_N2}$, the reaction then occurs in concert with a rearrangement of the $Cl^-$ leaving group from C to Pd, with a transition state $TS_{S_N2\text{-ra}}$ and, finally, the same product P as in the OxIn pathway. In Chapter 6, the differences between the $S_N2$ mechanisms for the reaction of Pd with $CH_3Cl$ and with $CH_3F$ have been discussed.

The geometries obtained with the various LDA and GGA functionals do not show significant mutual discrepancies. Because we found in the studies in Chapters 4 and 5 on the reactions of Pd with methane and ethane that BLYP performs excellently in terms of relative energies of stationary points and because BLYP is robust and well established, we chose the geometries of this functional to compute the *ab initio* benchmark PES.

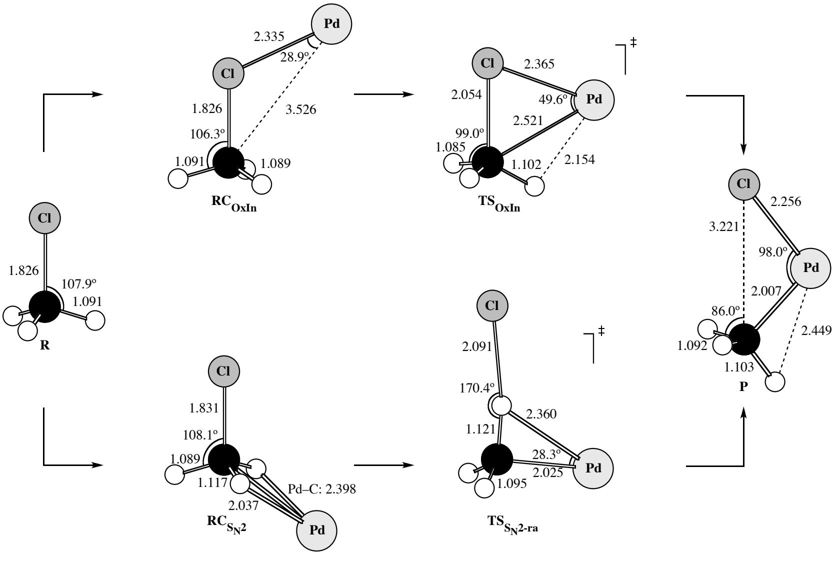

**Figure 7.1** Geometries (in Å, degrees) of stationary points along the reaction coordinates of the OxIn and $S_N2$-type pathways for the oxidative addition of the chloromethane C–Cl bond to Pd, at ZORA-BLYP/TZ2P

### 7.3.2 Benchmark energies from *ab initio* calculations

Here, we report the first systematic *ab initio* calculations into relative energies of the model addition reaction of the chloromethane C–Cl bond to the Pd atom. This survey is based on geometries of stationary points that were optimized at the ZORA-BLYP/TZ2P level of DFT. The results of our *ab initio* computations are collected in Table 7.2.

At almost all levels of theory except Hartree-Fock, the reaction profiles are characterized by the formation of stable reactant complexes $RC_{OxIn}$ and $RC_{S_N2}$, where the first one is always lower in energy than the second one, which lead via $TS_{OxIn}$ or via $TS_{S_N2\text{-ra}}$ to the product P. Three striking observations can be made: (i) the spread in values of computed relative energies, depending on the level of theory and basis set, is enormous, up to ca. 45 kcal/mol; (ii) the size of the BSSE is also remarkably large, up to ca. 14 kcal/mol; (iii) without counterpoise correction, convergence with basis-set size of the computed energies is still not reached with standard basis sets.

The lack of any correlation, which is important for this model reaction,[72,73] leads to a complete failure at the HF level, which yields unbound reactant complexes and strongly exaggerated reaction barriers. The activation energies for both pathways drop significantly when electron correlation is introduced. Along HF, CCSD and CCSD(T)

**Table 7.2** Relative energies (in kcal/mol) of the stationary points for the two pathways for oxidative addition of the $CH_3$–Cl bond to Pd, without and with counterpoise correction (CPC), at several levels of *ab initio* theory[a]

| | | $RC_{OxIn}$ | | $RC_{S_N2}$ | | $TS_{OxIn}$ | | $TS_{S_N2\text{-ra}}$ | | P | |
|---|---|---|---|---|---|---|---|---|---|---|---|
| Method | Basis set | no CPC | with CPC | no CPC | with CPC | no CPC | with CPC | no CPC | with CPC | no CPC | with CPC |
| HF | BS1 | 6.4 | 6.9 | 9.9 | 10.4 | 28.9 | 29.4 | 61.6 | 62.2 | 4.3 | 4.8 |
| | BS2 | 6.2 | 6.7 | 9.8 | 10.3 | 28.6 | 29.2 | 60.6 | 61.1 | 2.0 | 2.6 |
| | BS2(–) | 7.2 | 7.7 | 9.8 | 10.3 | 29.0 | 29.6 | 58.6 | 59.1 | 1.6 | 2.2 |
| | BS2(+) | 6.2 | 6.7 | | | 28.4 | 28.9 | | | | |
| | BS3 | 6.0 | 6.5 | 9.5 | 10.1 | 28.2 | 28.8 | 59.6 | 60.2 | 0.1 | 0.8 |
| | BS4 | 6.0 | 6.5 | 9.6 | 10.0 | 28.2 | 28.7 | 59.6 | 60.1 | 0.0 | 0.6 |
| | BS5 | 5.9 | 6.4 | 9.5 | 10.0 | 28.1 | 28.6 | 59.3 | 59.9 | –0.6 | 0.0 |
| MP2 | BS1 | –11.2 | –6.4 | –5.8 | –0.9 | 3.9 | 10.4 | 41.9 | 47.3 | –29.5 | –19.7 |
| | BS2 | –16.7 | –9.8 | –10.6 | –3.5 | –3.1 | 6.2 | 37.3 | 45.1 | –39.0 | –25.0 |
| | BS2(–) | –10.8 | –6.2 | –10.1 | –3.3 | 1.7 | 9.3 | 36.7 | 44.4 | –34.3 | –22.6 |
| | BS2(+) | –17.4 | –10.0 | | | –8.5 | 4.6 | | | | |
| | BS3 | –16.9 | –13.7 | –9.6 | –6.5 | –2.0 | 1.8 | 45.1 | 48.6 | –30.4 | –25.0 |
| | BS4 | –16.3 | –14.2 | –7.7 | –6.0 | –1.1 | 1.4 | 46.4 | 48.6 | –29.4 | –25.4 |
| | BS5 | –16.7 | –14.8 | –9.0 | –7.3 | –1.8 | 0.5 | 46.7 | 48.7 | –29.1 | –25.4 |
| CCSD | BS1 | –8.3 | –3.5 | –4.3 | 0.7 | 7.2 | 13.6 | 40.0 | 45.5 | –28.7 | –19.1 |
| | BS2 | –11.3 | –5.3 | –6.9 | –0.7 | 3.6 | 11.8 | 38.2 | 45.1 | –33.8 | –21.8 |
| | BS2(–) | –6.5 | –2.2 | –6.6 | –0.5 | 7.4 | 14.2 | 37.4 | 44.3 | –29.9 | –19.7 |
| | BS2(+) | –11.9 | –5.4 | | | –0.8 | 10.4 | | | | |
| | BS3 | –10.2 | –7.3 | –5.0 | –2.3 | 6.4 | 9.7 | 44.9 | 48.1 | –27.1 | –22.4 |
| | BS4 | –9.8 | –7.8 | –4.1 | –2.6 | 7.0 | 9.3 | 45.9 | 48.0 | –26.4 | –22.8 |
| | BS5 | –9.6 | –7.9 | –4.2 | –2.8 | 6.9 | 9.1 | 46.4 | 48.4 | –25.8 | –22.5 |
| CCSD(T) | BS1 | –11.0 | –5.1 | –7.0 | –0.8 | 2.1 | 10.0 | 35.0 | 42.0 | –33.8 | –22.3 |
| | BS2 | –14.9 | –7.7 | –10.3 | –2.7 | –2.6 | 7.1 | 31.7 | 40.2 | –40.7 | –26.5 |
| | BS2(–) | –9.4 | –4.2 | –9.9 | –2.5 | 1.9 | 10.1 | 31.1 | 39.5 | –36.1 | –24.0 |
| | BS2(+) | –15.6 | –7.9 | | | –7.7 | 5.5 | | | | |
| | BS3 | –14.1 | –10.3 | –8.5 | –4.7 | 0.2 | 4.7 | 38.5 | 43.1 | –33.6 | –27.6 |
| | BS4 | –13.1 | –11.0 | –6.8 | –5.0 | 1.6 | 4.2 | 40.3 | 43.0 | –32.0 | –28.0 |
| | BS5 | –13.1 | –11.2 | –7.0 | –5.4 | 1.4 | 3.8 | 40.7 | 43.3 | –31.7 | –28.0 |

a CCD(T) procedure not reliable for $TS_{S_N2\text{-ra}}$, see Section 7.3.2.

with basis set BS1, for example, the activation barrier for OxIn decreases from 28.9 to 7.2 to 2.1 kcal/mol. But also the correlated CCSD(T) values obtained with basis sets BS1 up to BS3, comparable in quality to standard basis sets such as LANL2DZ[64,65] without or with up to four *f* functions added, are questionable, if one does not take into account counterpoise correction, as they are obviously not converged as a function of the basis-set size. For example, at CCSD(T)/BS1 the barrier for OxIn is 2.1 kcal/mol. This drops to –2.6 kcal/mol for basis set BS2. Thereafter, along BS3 to BS5, the barrier increases again, although not monotonically, to 1.4 kcal/mol.

Next, we note that the BSSE takes on large values in the correlated methods. At the CCSD(T) level, for example, the BSSE for $TS_{OxIn}$ amounts to 7.9, 9.7, 4.5, 2.6, and 2.4 kcal/mol along the basis sets BS1 to BS5 (see Table 7.2, difference between values with CPC and without CPC), whereas the corresponding BSSE values at HF are only ca. 0.6 kcal/mol. The BSSE increases along the reaction coordinate, because along the reaction coordinate, the C, H and Cl atoms and, thus, their basis functions come closer and begin to surround the Pd atom. This effectively improves the flexibility and polarization of the basis set and, thus, the description of the wavefunction in the region of the Pd atom. Note that the total BSSE at CCSD(T) has been considerably decreased, that is, to only 2.4 kcal/mol for BS5 and is not much larger anymore than the relative energies that we compute, in particular, the OxIn barrier of 1.4 kcal/mol, see CCSD(T)/BS5 in Table 7.2.

In basis sets BS1 to BS5, mentioned above, we use consistently the same basis sets for all substrate atoms, namely, uncontracted cc-aug-pVDZ for C and H and cc-aug-pVTZ for Cl. For Pd + $CH_4$, it was shown that CCSD(T) with CPC values at BS5, that is, using cc-aug-pVDZ for C and H, are converged within ca. one kcal/mol with respect to extending the basis set for C and H to cc-aug-pVTZ (see Chapter 5). Here, we explore to what extent the corresponding values for the Pd + $CH_3Cl$ system are converged if the basis set for C and H is extended from cc-aug-pVDZ in basis set BS2 to cc-aug-pVTZ in the larger basis set BS2(+). Furthermore, we probe the dependence of the counterpoise-corrected CCSD(T) relative energies on the size of the basis set for Cl by reducing it from cc-aug-pVTZ in basis set BS2 to cc-aug-pVDZ in basis set BS2(–). The results for the modified basis sets BS2(–) and BS2(+) are also shown in Table 7.2 below the entry for basis set BS2. It appears that using cc-aug-pVDZ instead of cc-aug-pVTZ for Cl makes a significant difference for the counterpoise-corrected CCSD(T) relative energies. $TS_{OxIn}$, for example, changes from 7.1 to 10.1 kcal/mol, going from BS2 to BS2(–) (see Table 7.2, CCSD(T) with CPC). From this, we conclude that using the uncontracted cc-aug-pVTZ basis set for Cl in $CH_3Cl$ is a minimal requirement. The calculations with basis set BS2(+) are extremely expensive and were, therefore, confined to the relative energies of two stationary points: $RC_{OxIn}$ and $TS_{OxIn}$. In agreement with our earlier finding for Pd + $CH_4$ (see Chapter 5), extending the basis sets of C and H from cc-aug-pVDZ to cc-aug-pVTZ has little effect on the CCSD(T) with CPC values. $TS_{OxIn}$, for example, decreases by only one-and-a-half kcal/mol, from 7.1 to 5.5 kcal/mol, going from BS2 to BS2(+) (see Table 7.2, CCSD(T) with CPC). We conclude that using uncontracted cc-aug-pVDZ for C and H and uncontracted cc-aug-pVTZ for Cl represents a good compromise between efficiency and accuracy in our CCSD(T) computations.

Thus, we have been able to achieve virtual convergence of the CCSD(T) relative energies by using a larger than standard basis set and by correcting for the BSSE. The results are converged to within some tenths of a kcal/mol.

There are however strong indications for one of the species, namely, $TS_{S_N2\text{-ra}}$ being problematic in the sense that a single-reference *ab initio* approach to describing it (e.g., HF, MP2, or CCSD(T)) is not suitable: (i) unlike the situation for the other species, the HOMO and LUMO of $TS_{S_N2\text{-ra}}$ are degenerate within a few hundredths of an eV; (ii) in line with this, there is near degeneracy of the singlet and triplet state ($E^{\text{triplet}} - E^{\text{singlet}}$ = +1.3, –11.0, +3.7, –5.8 and –1.6 kcal/mol at BLYP/TZ2P, HF, MP2, CCSD and CCSD(T); *ab initio* values obtained with BS5 and CPC); and (iii) importantly, the resulting barrier of 43.3 kcal/mol is also much higher than all values obtained with the various density functionals, even those which normally overestimate this type of barriers. For example, the activation barriers obtained with BLYP, OLYP and B3LYP are 23.1, 31.9 and 36.3 kcal/mol, respectively, all well below the CCSD(T) value of 43.3 kcal/mol. An analysis of the electronic structure of $TS_{S_N2\text{-ra}}$ reveals the physics behind this phenomenon: the species has much of the character of a complex between $Cl^-$ and $PdCH_3^+$. Consequently, the HOMO and LUMO of $TS_{S_N2\text{-ra}}$ closely resemble a chlorine 3*p* atomic orbital (AO), pushed up in energy by the (local) excess of negative charge, and a carbon 2*p* AO on the methyl fragment in $PdCH_3^+$, pulled down in energy by the (local) excess of positive charge: these circumstances clearly promote the occurrence of a single-electron transfer from $Cl^-$ to $PdCH_3^+$. This suggests that the problem may be relieved if the LUMO is destabilized. This can be achieved, for example, by introducing an extra $Cl^-$ ligand at Pd, which neutralizes the excess positive charge in the $PdCH_3^+$ moiety of $TS_{S_N2\text{-ra}}$. Thus, we have computed and analyzed the corresponding transition state for $PdCl^-$ induced C–Cl activation, the structure of which is shown in Figure 7.2. Indeed, all indicators of a pathological situation disappear: (i) there is a clear HOMO-LUMO gap of 0.65 eV at BLYP/TZ2P; (ii) the singlet state is well below the triplet state; and (iii) the CCSD(T)/BS3[a] with CPC value again agrees perfectly with the BLYP/TZ2P value: both amount to –18.8 kcal/mol (not shown in a table).[b]

[a] Our computational resources did not allow for larger basis sets than BS3 in the case of the $PdCl^-$ + $CH_3Cl$ model system. This basis set should, however, yield relative energies that are reasonably converged with basis set size, as can be seen for other stationary points in Table 3.3.

[b] Counterpoise-corrected relative energies of $TS_{S_N2\text{-ra}}$ of $PdCl^-$ + $CH_3Cl$ are –10.2, –13.8, –17.7, and –18.8 kcal/mol at HF, MP2, CCSD, and CCSD(T), respectively, in combination with basis set BS3.

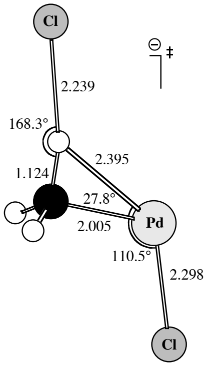

**Figure 7.2** Structure of the $\mathrm{S_N2}$-ra transition state for oxidative addition of the chloromethane C–Cl bond to $\mathrm{PdCl^-}$. Geometry optimized at ZORA-BLYP/TZ2P

In conclusion, our best estimate, obtained at CCSD(T)/BS5 with CPC, is –11.2 kcal/mol for the formation of $\mathrm{RC_{OxIn}}$, –5.4 kcal/mol for the formation of $\mathrm{RC_{S_N2}}$, 3.8 kcal/mol for the barrier $\mathrm{TS_{OxIn}}$, and –28.0 kcal/mol for the reaction energy. The barrier of 43.3 kcal/mol for the $\mathrm{S_N2}$ pathway is probably too high for the reasons pointed out above; this value should therefore be treated with great precaution. If we take into account zero-point vibrational energy effects computed at BLYP/TZ2P, we arrive at –10.8 kcal/mol for the formation of $\mathrm{RC_{OxIn}}$, –6.1 kcal/mol for the formation of $\mathrm{RC_{S_N2}}$, 2.7 kcal/mol for the barrier $\mathrm{TS_{OxIn}}$, and –28.8 kcal/mol for the reaction energy.

### 7.3.3 Validation of DFT

Next, we examine the relative energies of stationary points computed with the LDA functional VWN and the GGA functionals BP86, BLYP, PW91, PBE, revPBE, RPBE and OLYP in combination with the TZ2P basis set, the frozen-core approximation, and

**Table 7.3** Relative energies without ($\Delta E$) and with zero-point vibrational energy correction ($\Delta E + \Delta ZPE$), and relative enthalpies at 298.15 K ($\Delta H$) of the stationary points[a] (in kcal/mol), computed with eight different density functionals,[b] and compared to *ab initio* (CCSD(T)) benchmark[c]

| | $\Delta E$ | | | | | $\Delta E + \Delta ZPE$ | | | | | $\Delta H$ | | | | |
|---|---|---|---|---|---|---|---|---|---|---|---|---|---|---|---|
| Method | $\mathrm{RC_{Oxin}}$ | $\mathrm{RC_{S_N2}}$ | $\mathrm{TS_{Oxin}}$ | $\mathrm{TS_{S_N2\text{-}ra}}$ | P | $\mathrm{RC_{Oxin}}$ | $\mathrm{RC_{S_N2}}$ | $\mathrm{TS_{Oxin}}$ | $\mathrm{TS_{S_N2\text{-}ra}}$ | P | $\mathrm{RC_{Oxin}}$ | $\mathrm{RC_{S_N2}}$ | $\mathrm{TS_{Oxin}}$ | $\mathrm{TS_{S_N2\text{-}ra}}$ | P |
| *DFT computations* | | | | | | | | | | | | | | | |
| VWN | –30.1 | –25.5 | –21.8 | 15.8 | –52.1 | –29.6 | –26.6 | –22.7 | 11.8 | –52.9 | –29.9 | –27.1 | –23.2 | 11.4 | –53.1 |
| BP86 | –16.4 | –9.3 | –5.2 | 23.4 | –36.9 | –16.0 | –10.2 | –6.3 | 20.4 | –37.7 | –16.2 | –10.6 | –6.8 | 20.1 | –37.8 |
| BLYP | –12.9 | –5.1 | –0.6 | 23.1 | –33.1 | –12.5 | –5.8 | –1.7 | 20.4 | –33.9 | –12.7 | –6.0 | –2.0 | 20.1 | –34.0 |
| PW91 | –17.6 | –10.8 | –6.7 | 22.7 | –37.8 | –17.1 | –11.6 | –7.8 | 19.8 | –38.7 | –19.1 | –12.0 | –10.0 | 19.5 | –39.4 |
| PBE | –17.0 | –10.4 | –6.1 | 23.3 | –37.1 | –16.6 | –11.3 | –7.2 | 20.3 | –37.9 | –16.8 | –11.7 | –7.7 | 19.9 | –38.7 |
| revPBE | –11.9 | –5.0 | 0.1 | 26.1 | –31.4 | –11.6 | –5.9 | –1.0 | 23.5 | –32.3 | –11.8 | –6.1 | –1.4 | 23.1 | –32.4 |
| RPBE | –11.5 | –4.5 | 0.8 | 26.1 | –30.7 | –11.1 | –5.3 | –0.4 | 23.3 | –31.5 | –11.3 | –5.6 | –0.7 | 23.0 | –31.7 |
| OLYP | –6.8 | –0.1 | 7.0 | 31.2 | –23.5 | –6.4 | –0.8 | 5.8 | 28.7 | –24.4 | –6.6 | –0.9 | 5.3 | 28.4 | –24.5 |
| *Ab initio benchmark* | | | | | | | | | | | | | | | |
| CCSD(T) | –11.2 | –5.4 | 3.8 | (43.3) | –28.0 | –10.8 | –6.1 | 2.7 | (40.6) | –28.8 | | | | | |

a Geometries and energies computed at the same level of theory.

b With TZ2P basis set with frozen-core approximation. Relativistic effects treated with ZORA.

c Based on BLYP-optimized geometries. CCSD(T) procedure not reliable for $\mathrm{TS_{S_N2\text{-}ra}}$, see Section 7.3.2.

ZORA to account for relativistic effects. Note that for each functional we consistently use the geometries optimized with that functional (see Section 7.3.1). The results are collected in Table 7.3. The performance of the LDA functional VWN and the various GGA functionals is assessed by a systematic comparison with our CCSD(T) benchmark.

LDA suffers here from its infamous overbinding, providing barriers that are too low and complexation and reaction energies that are too high. The GGA functionals fall into three groups. OLYP clearly underestimates metal-substrate bonding and yields too weakly bound reactant complexes for both pathways, a barrier for the OxIn pathway that is too high by 3.2 kcal/mol, and an insufficiently exothermic reaction energy. The situation is the opposite for BP86, PBE and PW91, which overestimate metal-substrate bonding, giving rise to too strongly bound reactant complexes, a significantly underestimated barrier for the OxIn pathway and a too exothermic reaction energy. On the other hand, BLYP and the two revisions of PBE, i.e., revPBE and RPBE, perform very satisfactorily with reactant complexes that are in good agreement and a relatively small underestimation of the barrier for the OxIn pathway (i.e., by 4.4, 3.7 and 3.0 kcal/mol for BLYP, revPBE and RPBE, respectively), and somewhat too large reaction energies, but less so than in the case of the group of BP86, PBE, and PW91. Note that all functionals undershoot to an unusually high extent the CCSD(T) value of the barrier associated with the $S_N2$ pathway. It was pointed out above, that in this case the CCSD(T) value tends to be too high and should be treated with great precaution.

Finally, based again on the ZORA-BLYP/TZ2P geometries, we have computed the relative energies of the stationary points for a wide range of functionals in combination with the all-electron ae-TZ2P basis set. This was done in a post-SCF manner, that is, using the electron density obtained at ZORA-BLYP/ae-TZ2P. The performance of the functionals is discussed by comparison with our CCSD(T) benchmark. The results are collected in Table 7.4.

For clarity, we wish to point out that the above procedure differs in three respects from that used for computing the relative energies shown in Table 7.3: (i) an all-electron approach is used instead of the frozen-core approximation; (ii) for all functionals, the BLYP-optimized geometries are used instead of geometries optimized with the same functional, and (iii) for all functionals, the BLYP electron density is used for computing the energy instead of the density corresponding to that functional. The effect of point (i) is in the order of up to 0.3 kcal/mol (compare BLYP values in Tables 7.3 and 7.4). The differences between the values in Tables 7.3 and 7.4 derive mainly from the combined effect of points (ii) and (iii), which is, considering the GGA functionals, in the order of up to 1.0 kcal/mol. Both effects are mostly in the order of a few tenths of a kcal/mol and, for the different GGA functionals and stationary points, contribute with varying relative importance. For example, for $TS_{OxIn}$, the single-point approach contributes generally somewhat more (0.6-1.0 kcal/mol) to this destabilization than the post-SCF approach (up to 0.3 kcal/mol). This was tested by computing the relative energies using approximation (ii) but not (iii), i.e., computing them with the density corresponding to the functional under consideration but with the BLYP geometries; the resulting values are provided in parentheses in Table 7.4. In conclusion, for the GGA functionals, the combined effect of approximations (i)-(iii) on the relative energies is small, up to one kcal/mol.

We extend our survey to the full range of functionals that are implemented in the ADF program in a post-SCF manner. In Section 7.3.2, it was pointed out that the CCSD(T) relative energy for $TS_{S_N2\text{-ra}}$ is unreliable. Indeed, it exceeds the corresponding values obtained with the various functionals to an unusually great extent, even for those,

**Table 7.4** Energies (in kcal/mol) of the stationary points[a] relative to reactants, and dissociation energy of chloromethane into a methyl radical and chlorine atom ($D_{CCl}$), computed for 26 density functionals[b-e]

| Method | $RC_{OxIn}$ | $RC_{S_N2}$ | $TS_{OxIn}$ | $TS_{S_N2\text{-ra}}$ | P | Mean abs. err. | Mean abs. err. exl. $TS_{S_N2\text{-ra}}$ | Err. in OxIn barr. | Err. in $S_N2$-ra barr. | $D_{CCl}$ | Err. in $D_{CF}$ |
|---|---|---|---|---|---|---|---|---|---|---|---|
| *LDA* | | | | | | | | | | | |
| VWN | –27.6 (–27.7) | –20.7 (–21.0) | –18.2 (–18.4) | 18.7 (18.7) | –50.2 (–50.3) | 20.1 | 19.0 | –22.0 | –24.6 | 106.2 | 25.0 |
| *GGAs* | | | | | | | | | | | |
| BP86 | –16.0 (–16.0) | –8.6 (–8.7) | –4.5 (–4.5) | 23.8 (23.8) | –37.0 (–37.0) | 9.0 | 6.3 | –8.3 | –19.5 | 86.0 | 4.9 |
| BLYP | –12.8 | –5.1 | –0.5 | 23.1 | –33.5 | 6.4 | 2.9 | –4.2 | –20.2 | 82.1 | 1.0 |
| B88xBR89c | –13.9 | –5.8 | –0.4 | 22.6 | –35.9 | 7.2 | 3.8 | –4.2 | –20.7 | 83.4 | 2.2 |
| PW91 | –17.2 (–17.2) | –10.1 (–10.1) | –5.8 (–5.8) | 23.0 (23.1) | –38.0 (–37.9) | 10.1 | 7.6 | –9.6 | –20.3 | 88.9 | 7.7 |
| PBE | –16.4 (–16.6) | –9.5 (–9.6) | –5.1 (–5.1) | 23.6 (23.7) | –37.2 (–37.1) | 9.4 | 6.9 | –8.9 | –19.7 | 88.9 | 7.7 |
| FT97 | –12.7 | –10.5 | 3.8 | 23.5 | –36.9 | 7.1 | 3.9 | 0.0 | –19.8 | 84.7 | 3.5 |
| revPBE | –11.6 (–11.8) | –4.6 (–4.8) | 0.7 (0.7) | 26.3 (26.2) | –31.7 (–31.7) | 5.0 | 2.0 | –3.1 | –17.0 | 83.5 | 2.4 |
| HCTH/93 | –6.6 | 0.4 | 8.0 | 32.1 | –22.7 | 6.2 | 4.9 | 4.2 | –11.2 | 83.0 | 1.9 |
| RPBE | –11.1 (–11.3) | –4.1 (–4.3) | 1.4 (1.3) | 26.3 (26.2) | –30.9 (–30.9) | 4.7 | 1.7 | –2.4 | –17.0 | 82.9 | 1.8 |
| BOP | –9.6 | –1.9 | 3.4 | 25.4 | –29.9 | 5.0 | 1.8 | –0.3 | –17.9 | 81.8 | 0.6 |
| HCTH/120 | –11.0 | –3.9 | 3.0 | 28.5 | –27.5 | 3.6 | 0.8 | –0.8 | –14.8 | 84.3 | 3.2 |
| HCTH/147 | –10.4 | –3.3 | 3.6 | 29.1 | –27.0 | 3.7 | 1.0 | –0.2 | –14.2 | 84.3 | 3.1 |
| HCTH/407 | –7.8 | –1.3 | 8.0 | 30.8 | –22.7 | 5.9 | 4.2 | 4.2 | –12.4 | 83.2 | 2.1 |
| OLYP | –6.0 (–6.5) | 0.7 (0.2) | 8.0 (7.7) | 31.9 (31.3) | –23.3 (–23.7) | 6.3 | 5.0 | 4.2 | –11.4 | 83.6 | 2.4 |
| *Meta-GGAs* | | | | | | | | | | | |
| BLAP3 | –7.7 | 0.2 | 7.5 | 27.7 | –26.7 | 5.9 | 3.5 | 3.7 | –15.6 | 85.3 | 4.1 |
| VS98 | –14.2 | –8.9 | –5.7 | 25.7 | –33.5 | 7.8 | 5.4 | –9.5 | –17.6 | 81.2 | 0.1 |
| KCIS | –13.7 | –6.7 | –1.6 | 26.0 | –34.7 | 6.6 | 4.0 | –5.4 | –17.3 | 85.4 | 4.2 |
| PKZB | –12.5 | –5.2 | –0.5 | 26.6 | –34.4 | 5.8 | 3.0 | –4.3 | –16.7 | 83.6 | 2.5 |
| Bm$\tau$1 | –7.4 | 0.5 | 7.9 | 27.3 | –26.4 | 6.2 | 3.8 | 4.1 | –16.0 | 83.7 | 2.5 |
| OLAP3 | –0.9 | 6.1 | 16.0 | 36.5 | –16.5 | 10.4 | 11.3 | 12.2 | –6.8 | 86.8 | 5.6 |
| TPSS | –14.4 | –6.7 | –3.7 | 25.0 | –36.9 | 7.9 | 5.3 | –7.5 | –18.3 | 84.2 | 3.0 |
| *Hybrid functionals* | | | | | | | | | | | |
| B3LYP | –9.3 | –3.1 | 5.4 | 36.3 | –26.5 | 2.8 | 1.8 | 1.6 | –7.0 | 81.2 | 0.1 |
| O3LYP | –5.4 | 0.5 | 10.1 | 40.4 | –19.6 | 5.9 | 6.6 | 6.3 | –2.9 | 85.7 | 4.5 |
| X3LYP | –9.7 | –3.7 | 5.0 | 36.9 | –26.7 | 2.4 | 1.4 | 1.2 | –6.3 | 81.7 | 0.6 |
| TPSSh | –12.3 | –5.4 | –0.3 | 31.6 | –32.9 | 4.4 | 2.6 | –4.1 | –11.7 | 83.2 | 2.0 |
| *Ab initio benchmark* | | | | | | | | | | | |
| CCSD(T) | –11.2 | –5.4 | 3.8 | *43.3* | –28.0 | | | | | 81.2 | |

a Geometries optimized at ZORA-BLYP/TZ2P with frozen-core approximation.

b Computed post-SCF using the BLYP electron density, unless stated otherwise. Values in parentheses computed with the potential and electron density corresponding to the functional indicated. With ZORA and ae-TZ2P basis set with all electrons treated variationally

c Mean absolute error for the energies of all stationary points relative to reactants, error in the overall barriers and error in dissociation energy of the C–Cl bond, compared with the CCSD(T) benchmark.

d Furthermore, mean absolute error corresponding to footnote c, but excluding stationary point $TS_{S_N2\text{-ra}}$.

e CCSD(T) procedure not reliable for $TS_{S_N2\text{-ra}}$, see Section 7.3.2.

that normally overestimate this type of barrier, such as OLYP. For comparison, deviations of the DFT barriers are significantly smaller for $TS_{OxIn}$ and they also show the well-known scattering of individual values somewhat above and below the CCSD(T) value. Thus, for almost all functionals the mean absolute error drops significantly if one excludes $TS_{S_N2\text{-ra}}$; Table 7.4 displays both values in the columns "mean abs. err." and "mean abs. err. excl. $TS_{S_N2\text{-ra}}$". In the following, we discuss the latter.

Both the mean absolute error and the error in the OxIn barrier drop significantly if one goes from LDA (mean abs. err. = 19.0 kcal/mol), which, as mentioned above, suffers from its infamous overbinding, to GGA functionals (mean abs. err. = 0.8-7.6 kcal/mol). However, no significant improvement occurs if one goes from GGA to the more recently developed meta-GGA functionals (mean abs. err. = 3.0-11.3 kcal/mol) and hybrid functionals (mean abs. err. = 1.4-6.6 kcal/mol). The best overall agreement with the *ab initio* benchmark PES is achieved by functionals of the GGA (HCTH/120), meta-GGA (PKZB), as well as hybrid-DFT type (X3LYP), with mean absolute errors of 0.8 to 3.0 kcal/mol and errors in the OxIn barrier ranging from –4.3 to 1.2 kcal/mol. Interestingly, the well-known BLYP functional compares very reasonably with an only slightly larger mean absolute error of 2.9 kcal/mol and an underestimation of the OxIn barrier of –4.2 kcal/mol. The OLYP functional overestimates the OxIn barrier by the same amount, 4.2 kcal/mol, but has a larger mean absolute error of 5.0 kcal/mol. The hybrid functionals B3LYP and X3LYP perform remarkably well, with overestimations of the barrier by only 1.6 and 1.2 kcal/mol, and mean absolute errors of only 1.8 and 1.4 kcal/mol.

We have verified to what extent errors originate from a failure in describing the C–Cl bond dissociation. To this end, we have first computed an *ab initio* benchmark for the C–Cl bond strength ($D_{CCl}$), using again BLYP-optimized geometries. Thus, we arrive at a dissociation energy of 81.2 kcal/mol at CCSD(T)/BS5 with CPC (HF: 60.0, MP2: 86.0, and CCSD: 78.2 kcal/mol), in nice agreement with the experimental value for the enthalpy at 0 K, namely, 82.04 ± 0.26 kcal/mol.[113] Most functionals describe $D_{CCl}$ reasonably well, yielding errors in the order of a few kcal/mol. For BLYP and B3LYP, the dissociation energy is overestimated by only 1.0 and 0.1 kcal/mol, respectively. In

**Table 7.5** Reaction profiles (kcal/mol) for the oxidative addition of various bonds to Pd, with various methods[a]

| | | Reactant complex | | | | Transition state | | | | Product | | | |
|---|---|---|---|---|---|---|---|---|---|---|---|---|---|
| Bond | | CCSD(T) | BLYP | OLYP | B3LYP | CCSD(T) | BLYP | OLYP | B3LYP | CCSD(T) | BLYP | OLYP | B3LYP |
| C–H | OxIn | –8.1 | –6.7 | –0.7 | –4.9 | 5.8 | 3.9 | 10.3 | 10.3 | 0.8 | –3.6 | 5.3 | 4.6 |
| C–C | OxIn | –10.8 | –6.7 | –0.5 | –4.9 | 19.4 | 18.5 | 26.8 | 25.2 | –4.5 | –9.5 | 1.6 | 0.2 |
| C–F | OxIn | –5.3 | –5.4 | 0.3 | –3.4 | 27.8 | 17.7 | 26.0 | 26.9 | –6.4 | –16.3 | –6.2 | –7.0 |
| | $S_N2$ | c | c | c | c | 37.5 | 30.1 | 38.5 | 40.2 | c | c | c | c |
| C–Cl | OxIn | –11.2 | –12.8 | –6.0 | –9.3 | 3.8 | –0.5 | 8.0 | 5.4 | –28.0 | –33.5 | –23.3 | –26.5 |
| | $S_N2$ | –5.4 | –5.1 | 0.7 | –3.1 | (43.3)[b] | 23.1 | 31.9 | 36.3 | c | c | c | c |

a Geometries optimized at ZORA-BLYP/TZ2P with frozen-core approximation. BLYP, OLYP and B3LYP results calculated with ae-TZ2P basis set and post-SCF using the BLYP electron density.

b CCSD(T) procedure not reliable, see Section 7.3.2.

c Same as OxIn.

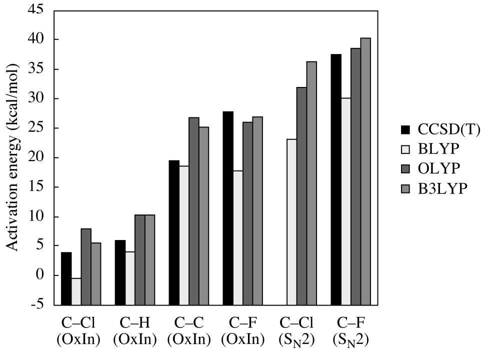

**Figure 7.3** Activation energies for the oxidative addition of various bonds to Pd, computed with various methods. For computational details, see the footnotes of Table 7.5

conclusion, the underestimation of the activation energy by BLYP cannot be ascribed to a failure in describing C–Cl bond dissociation.

### 7.3.4 Comparison of C–H, C–C, C–F and C–Cl bond activation

Finally, we have carried out a comprehensive comparison of the *ab initio* CCSD(T) benchmark PESs as well as the corresponding BLYP, OLYP and B3LYP density functional results for the Pd-induced activation of the methane C–H (OxIn), ethane C–C (OxIn), fluoromethane C–F (OxIn and S$_N$2) and chloromethane C–Cl bond (OxIn and S$_N$2) using the same computational details throughout. The energies of all stationary points relative to the reactants are collected in Table 7.5. Trends in activation energies are displayed in Figure 7.3 in which the questionable CCSD(T) value for the S$_N$2 transition state for C–Cl activation has been left out.

It is clear, especially from Figure 7.3, that all important features of the CCSD(T) benchmark PESs for Pd-induced C–H, C–C, C–F and C–Cl bond activation are reproduced by important functionals such as BLYP, OLYP and B3LYP. On the other hand, a more detailed look also shows that none of these functionals is the “best one” for each individual reaction. For example, BLYP performs best in the case of C–H and C–C bond activation whereas OLYP and B3LYP overestimate the barrier (compare values in Table 7.5). But, in the case of C–F bond activation, the BLYP functional underestimates the barriers of both OxIn and S$_N$2 pathways while OLYP and B3LYP perform very satisfactorily. For the C–Cl bond, as described above, the OxIn barrier is only slightly underestimated by BLYP and overestimated by OLYP and B3LYP. Nevertheless, they all agree with the CCSD(T) benchmark that, for example, the activation energies for oxidative addition increase in the order C–Cl (OxIn) < C–H (OxIn) < C–C (OxIn) ≤ C–F (OxIn) < C–Cl (S$_N$2-ra; no reliable benchmark) < C–F (S$_N$2-ra).

## 7.4 Conclusions

We have computed an *ab initio* benchmark for the archetypal oxidative addition of the chloromethane C–Cl bond to Pd that derives from a hierarchical series of relativistic methods and highly polarized basis sets for the Pd atom, up to the counterpoise corrected, four-component spin-free Dirac-Coulomb CCSD(T)/(24*s*16*p*13*d*+4*f*+*p*+*g*) level, which is converged with respect to the basis-set size within one kcal/mol. Our findings stress the importance of sufficient higher-angular momentum polarization functions, as well as counterpoise correction for obtaining reliable activation energies.

This benchmark is used to evaluate the performance of 26 density functionals for describing relative energies of the stationary points. Excellent agreement with our *ab initio* benchmark is achieved by GGA, meta-GGA as well as hybrid DFT functionals with mean absolute errors as small as 3.0 kcal/mol or less. All theoretical methods reveal the existence of two possible reaction mechanisms for oxidative addition: direct oxidative insertion (OxIn) with a barrier that is at least some 20 kcal/mol lower than that of an alternative $S_N2$ pathway. Interestingly, the well-known BLYP functional still performs satisfactorily with a mean absolute error of 2.9 kcal/mol and an underestimation of the OxIn barrier by –4.2 kcal/mol. Note that the much advocated B3LYP hybrid functional also performs remarkably well, with a mean absolute error of 1.8 kcal/mol and an overestimation of the OxIn barrier by only 1.6 kcal/mol.

Finally, a comprehensive comparison of the present and previous studies shows that all important features of the CCSD(T) benchmark PESs for Pd-induced C–H, C–C, C–F and C–Cl activation are reproduced by important functionals such as BLYP, OLYP, and B3LYP. Thus, while none of these functionals is the “best one” for each individual reaction, they all agree with the CCSD(T) benchmark that, for example, the activation energies for oxidative addition increase in the order C–Cl (OxIn) < C–H (OxIn) < C–C (OxIn) ≤ C–F (OxIn) < C–Cl ($S_N2$-ra; no reliable benchmark) < C–F ($S_N2$-ra).

All together, we consider ZORA-BLYP/TZ2P a sound and efficient approach for the investigation of catalytic bond activation, also in larger, more realistic systems.

# 8 Oxidative addition to main group versus transition metals. Insights from the Activation Strain model

Adapted from
G. Th. de Jong, R. Visser, F. M. Bickelhaupt *J. Organomet. Chem.* **2006**, *691*, 4341

## Abstract

We have studied the oxidative addition of the methane C–H and chloromethane C–Cl bonds to a number of main group (Be, Mg, Ca) and transition metals (Pd, Zn, Cd), using relativistic density functional theory (DFT) at ZORA-BLYP/TZ2P. The purpose is to better understand what causes the characteristic differences in reactivity between main group and transition metals towards oxidative addition. Thus, we have analyzed our model reactions using the Activation Strain model in which the activation energy $\Delta E^{\neq}$ is decomposed into the activation strain $\Delta E^{\neq}_{\text{strain}}$ of and the stabilizing TS interaction $\Delta E^{\neq}_{\text{int}}$ between the reactants in the activated complex: $\Delta E^{\neq} = \Delta E^{\neq}_{\text{strain}} + \Delta E^{\neq}_{\text{int}}$. Activation of the C–H bond goes with higher barriers than activation of the C–Cl bond because the higher bond strength of the former translates into a higher activation strain $\Delta E^{\neq}_{\text{strain}}$. The barriers for bond activation increase along Pd < Be, Ca < Mg < Zn, Cd. This can be straightforwardly understood through the TS interaction $\Delta E^{\neq}_{\text{int}}$, that is, in terms of the bonding capabilities of the metals. Pd yields the lowest barriers because it achieves the most stabilizing $\Delta E^{\neq}_{\text{int}}$. This is the result of the small HOMO-LUMO gap between its occupied 4*d* and unfilled 5*s* AOs, which makes Pd both a good electron donor and acceptor. Zn and Cd yield the highest barriers because the large HOMO-LUMO gap between the occupied valence n*s* and unfilled valence n*p* AOs makes them both poor donors and poor acceptors of electronic charge.

## 8.1 Introduction

Oxidative addition and reductive elimination are key steps in many reactions of homogeneous catalysis[117-120] and have been intensively investigated both experimentally[32-35,120-122] and theoretically.[33,35,42,43,67,108,122,123] A well-known class of processes involving oxidative addition is catalytic C–X bond activation.[31,117,118,124,125] The catalytically active species in these reactions are generally coordination complexes of transition metals. Main-group metals do have a rich chemistry[118,124,126,127] but they are commonly not involved in catalytic bond activation through oxidative insertion. An exception is carbon-halogen bond activation by ground-state magnesium through matrix deposition, which yields Grignard's reagent.[118,124,127,128]

In the present study in this chapter, we aim at obtaining more insight into *why* transition metals are better agents for oxidative insertion reactions than main-group metals such as alkaline earths. Oxidative insertion of a metal into a carbon-substituent bond is associated with increasing the oxidation state of the metal atom by +2. The particular capability of transition metals to undergo such reactions has been ascribed, among others, to the ease with which they can change their oxidation state.[118] In a sense, however, this is a reformulation of the question rather than an answer. Here, we make an attempt to trace the characteristic difference in reactivity between transition metals and main-group metals to corresponding characteristic features in their orbital electronic structure. To this end, a detailed study of the reactivity of a series of transition metals and main-group metals towards the methane C–H bond and the chloromethane C–Cl bond has been carried out using relativistic nonlocal density functional theory (DFT) at the ZORA-BLYP/TZ2P level. In the previous chapters, this approach was shown to agree excellently with highly correlated relativistic *ab initio* benchmark studies for describing the insertion of palladium into C–H, C–Cl and other bonds. Our investigation covers the group-10 transition metal palladium and the alkaline earth metals beryllium, magnesium and calcium. Furthermore, we have included the group-12 transition metals zinc and cadmium, the behaviour of which is known to resemble, to some extent, that of the alkaline earths.[118,126] Thus, all together, the potential energy surfaces (PESs) of the following archetypal model reactions (Eqs. 8.1 and 8.2) were explored and compared:

$$\mathrm{M + CH_4 \rightarrow CH_3{-}M{-}H} \qquad \mathrm{(M = Pd, Be, Mg, Ca, Zn, Cd)} \qquad (8.1)$$

$$\mathrm{M + CH_3Cl \rightarrow CH_3{-}M{-}Cl} \qquad \mathrm{(M = Pd, Mg, Zn, Cd)} \qquad (8.2)$$

These model reactions reveal the *intrinsic* characteristics of and differences between the categories of metals, that is, their behaviour in the absence of solvent molecules and ligands. While the latter may substantially affect the precise shape of PESs for real condensed-phase reactions, our study suggests that essential aspects of their behaviour are inherited from this intrinsic nature of the metal atoms.

The difference in reactivity for the various combinations of inserting metals and bonds is analyzed and interpreted in terms of the Activation Strain model of chemical reactivity (see Chapter 2). In this model, activation energies $\Delta E^{\neq}$ are decomposed into the activation strain $\Delta E^{\neq}_{\text{strain}}$ of and the stabilizing transition state (TS) interaction $\Delta E^{\neq}_{\text{int}}$ between the reactants in the activated complex: $\Delta E^{\neq} = \Delta E^{\neq}_{\text{strain}} + \Delta E^{\neq}_{\text{int}}$. The activation strain $\Delta E^{\neq}_{\text{strain}}$ depends on the strength of the activated bond and on the extent to which a particular metal expands the bond in the activated complex. The TS interaction $\Delta E^{\neq}_{\text{int}}$ is directly determined by the bonding capabilities and, thus, the frontier orbitals of the reactants. As will emerge from our analyses, much of the characteristics of Pd *versus* alkaline earths *versus* group-12 metals can be traced to the respective valence configurations: $s^0d^{10}$, $s^2d^0$ and $s^2d^{10}$, respectively. In practice, of course, catalytic activity and selectivity of *solution-phase* transition or main-group metal *complexes* are substantially affected by coordination of ligands and interaction with solvent molecules. However, the starting point in this pilot study is the investigation of the *intrinsic* reactivity of the transition metal *atom*.

## 8.2 Methods

### 8.2.1 Computational details

All calculations are based on DFT,[6-9] using the Amsterdam Density Functional (ADF) program.[49-51] The BLYP density functional was used,[52,53] in combination with a large uncontracted set of Slater-type orbitals (STOs) containing diffuse functions. This basis set is designated TZ2P: it is of triple-$\zeta$ quality and has been augmented with two sets of polarization functions on each atom. The core shells of C (1*s*), Cl (1*s*2*s*2*p*), Be (1*s*), Mg (1*s*), Ca (1*s*2*s*2*p*), Zn (1*s*2*s*2*p*), Pd (1*s*2*s*2*p*3*s*3*p*3*d*), and Cd (1*s*2*s*2*p*3*s*3*p*3*d*) were treated by the frozen-core approximation.[49] An auxiliary set of *s*, *p*, *d*, *f* and *g* STOs was used to fit the molecular density and to represent the Coulomb and exchange potentials accurately in each SCF cycle.[49] Relativistic effects were accounted for using ZORA.[19] In the previous chapters, this computational approach has been shown to be in good agreement with high-level *ab initio* calculations for this type of model reactions

Equilibrium and transition state geometries were fully optimized using analytical gradient techniques. All structures were verified by frequency calculations: for minima all normal modes have real frequencies, whereas transition states have one normal mode with an imaginary frequency. The character of the normal mode associated with the imaginary frequency was analyzed to ensure that the correct transition state was found.

### 8.2.2 Activation Strain analyses

To gain insight into how the use of different metals and different substrates affects the activation barriers of the different oxidative insertion reactions, i.e., insight into how this effect depends on the nature of the concomitant geometrical deformation and electronic structure of reacting metal and substrate, the reactions were analyzed using the Activation Strain model of chemical reactivity (see Chapter 2). In this model, the activation energy $\Delta E^{\neq}$ is decomposed into the activation strain $\Delta E^{\neq}_{\text{strain}}$ and the transition state (TS) interaction $\Delta E^{\neq}_{\text{int}}$:

$$\Delta E^{\neq} = \Delta E^{\neq}_{\text{strain}} + \Delta E^{\neq}_{\text{int}} \tag{8.3}$$

The activation strain $\Delta E^{\neq}_{\text{strain}}$ is the strain energy associated with deforming the reactants from their equilibrium geometry to the geometry they acquire in the activated complex. The TS interaction $\Delta E^{\neq}_{\text{int}}$ is the actual interaction energy between the deformed reactants in the transition state. In the present study, one of the reactants is the neutral metal atom and the other reactant is one of the substrates methane and chloromethane.

## 8.3 Results and discussion

### 8.3.1 Reaction profiles and geometries

In this section, we discuss the PESs of the various oxidative insertion reactions as well as the geometries of stationary points along the reaction coordinate. Geometries are summarized in Figure 8.1; reaction profiles in Table 8.1 and Figure 8.2. The results of the Activation Strain analyses are discussed in Section 8.3.2.

The reactions of Pd with $CH_4$ and $CH_3Cl$ have been discussed before in Chapters 3, 4 and 7. The reaction of Pd with $CH_3Cl$, may also proceed via an alternative, higher-energy $S_N2$ pathway for the details of which the reader is referred to Chapter 7. In the present study in this chapter, we will focus on oxidative insertion.

All model reactions proceed from the reactants via a transition state (TS) to a product (P), see Figure 8.1. The reactions of Pd involve, in addition, the formation of a stable reactant complex (RC) prior to advancing to the TS, see **2a** and **9a** in Figure 8.1. For all other metals, such encounter complexes are essentially unbound and thus not existent. Table 8.1 contains the relative energies of all stationary points along the reaction coordinate. These are also graphically represented in Figure 8.2. Two striking trends emerge: (i) the barriers for insertion into the C–H bond are significantly higher than those for insertion into the C–Cl bond; (ii) activation energies increase roughly in the order Pd < alkaline earths < group 12 (or more precisely Pd < Be, Ca < Mg < Zn, Cd).

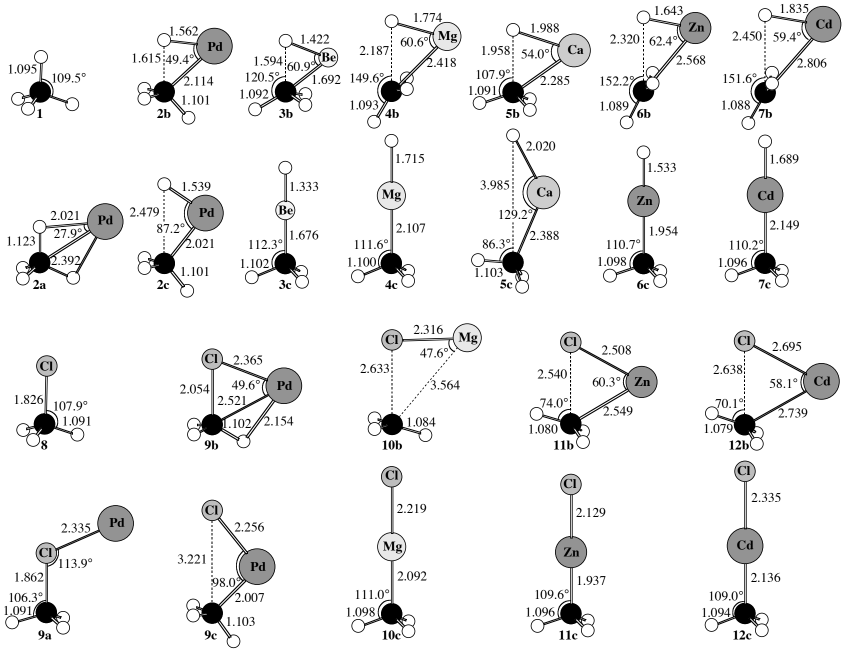

**Figure 8.1** Geometries (in Å, degrees) at ZORA-BLYP/TZ2P of stationary points for oxidative insertion of various metals into the methane C–H bond and the chloromethane C–Cl bond

The activation energies for insertion into the C–H bond are between 4 and 96 kcal/mol and are significantly higher than those for insertion into the C–Cl bond, which range from –1 up to only 46 kcal/mol. It will be shown later that the lower barrier for insertion into the C–Cl bond is related to the fact that the C–Cl bond is weaker than the C–H bond. Insertion into the C–Cl bond is overall also significantly more exothermic than insertion into the C–H bond. Most products have linear C–M–H or C–M–Cl units. Exceptions are the products of Pd and Ca insertion (**2c**, **9c** and **5c**).

Next, we have a closer look at the activation energies and TS structures for insertion into the C–H bond and how they depend on the inserting metal atom. The activation energies are 3.9 (Pd), 51.0 (Be), 76.7 (Mg), 51.7 (Ca), 91.6 (Zn) and 96.1 kcal/mol (Cd).

**Table 8.1** Reaction profiles (in kcal/mol) for oxidative insertion reactions, computed at ZORA-BLYP/TZ2P.

| Activated bond | Reactants | Reactant complex | Transition state | Product |
|---|---|---|---|---|
| C–H | Pd + $CH_4$ | –6.7 | 3.9 | –3.4 |
| | Be + $CH_4$ | a | 51.0 | –40.6 |
| | Mg + $CH_4$ | a | 76.7 | 16.0 |
| | Ca + $CH_4$ | a | 51.7 | 14.9 |
| | Zn + $CH_4$ | a | 91.6 | 20.4 |
| | Cd + $CH_4$ | a | 96.1 | 32.7 |
| C–Cl | Pd + $CH_3Cl$ | –12.9 | –0.6 | –33.1 |
| | Mg + $CH_3Cl$ | a | 24.6 | –49.7 |
| | Zn + $CH_3Cl$ | a | 44.3 | –29.6 |
| | Cd + $CH_3Cl$ | a | 46.0 | –15.5 |

a RC unbound.

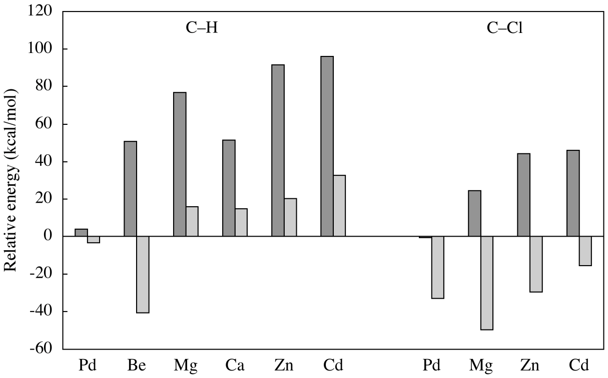

**Figure 8.2** Activation (left bars) and reaction (right bars) energies (relative to reactants) at ZORA-BLYP/TZ2P for the oxidative insertion reactions of various metals into the methane C–H and chloromethane C–Cl bonds

Thus, the transition metal Pd has by far the lowest barrier followed, with significantly higher barriers, by the alkaline earths and, finally, the group-12 transition metals. All TS structures have $C_s$ point-group symmetry and are characterized by an elongation of the activated C–H bond. The trend in C–H bond elongation along the various metals roughly reflects the trend in activation energies: it varies from +0.520 Å (Pd), to +0.499, +1.092 and +0.863 Å (Be, Mg, Ca) to +1.225 and +1.355 Å (Zn, Cd). This corresponds to percentage-wise elongations of 46-124%. In case of the TSs of Mg (**4b**), Zn (**6b**) and Cd (**7b**), the methyl group has, in addition, considerably flattened and is tilted with respect to the elongated C–H bond. In all TSs (**3b**-**7b**) except that of Pd (**2b**), the methyl group is staggered with respect to the metal. For Pd (**2b**) it is eclipsed. These differences are however not that significant. The essential physics here is that the methyl group in these structures is virtually a free internal rotor with a rotation barrier in the order of a few tenths of a kcal/mol (see also the discussion in Section 6.3.1). Later on, in Section 8.3.2, it will be shown that the above trends in activation energy and C–H bond elongation are related in a straightforward manner to the valence configuration of the metal atoms.

Similar trends are found for the activation energies and TS structures for oxidative insertion into the C–Cl bond. These activation energies are –0.6 (Pd), 24.6 (Mg), 44.3 (Zn) and 46.0 kcal/mol (Cd). Again, the transition metal Pd has by far the lowest barrier followed, with significantly higher barriers, by the alkaline earth Mg and the group-12 transition metals. All TS structures have $C_s$ point-group symmetry and are characterized by an elongation of the activated C–Cl bond. Also, the trend in C–Cl bond elongation along the various metals again roughly reflects the trend in activation energies: it varies from +0.228 (Pd), to +0.807 (Mg) to +0.714 (Zn) and +0.812 Å (Cd). This corresponds to percentage-wise elongations of 12-44%. Note that the elongation of the C–Cl bond in the TS (12-44%) is significantly lower than that of the C–H bond (46-124%). This contributes to the lower activation energies for insertion into C–Cl as compared to C–H. Furthermore, the TSs come again in two kinds regarding the conformation of the methyl group: staggered relative to the metal (**11b** and **12b**) and eclipsed relative to the metal (**9b** and **10b**). However, as pointed out above, these differences are not to be overrated because the methyl group in these structures is virtually a free internal rotor.

In conclusion, the transition metal Pd is indeed intrinsically (i.e., already as isolated atom, in the absence of environment effects) more reactive towards oxidative insertion into a C–X bond than alkaline earths and group-12 transition metals. This trend perfectly agrees with condensed-phase experiments despite the obvious modifications of the exact shape of the potential energy surface due to solvent and ligand effects. In the next section, we try to find out *why* Pd inserts more readily.

### 8.3.2 Activation Strain analyses of reactivity

The results of the Activation Strain analyses are listed in Table 8.2. Our aim is to elucidate the factors that determine the major trends in our model reactions: (i) the increase of the activation barrier from C–H to C–Cl, and (ii) the increase of the activation barrier from Pd to the alkaline earths to the group-12 transition metals.

Our analyses reveal that the higher activation energies for insertion into the C–H bond originate from the fact that the C–H bond is stronger than the C–Cl bond, 109.7 versus 82.1 kcal/mol at ZORA-BLYP/TZ2P, in line with previous studies.[23,24] To understand this, we analyze the energy profile $\Delta E(\zeta)$ for the reaction of Pd + $CH_3Cl$ in terms of the interplay between strain energy $\Delta E_{\text{strain}}(\zeta)$ of the reactants and their mutual interaction energy $\Delta E_{\text{int}}(\zeta)$ along the reaction coordinate $\zeta$. The analysis of the energy profile of Pd + $CH_3Cl$ is schematically depicted in Figure 8.3 (black curves). The strain energy $\Delta E_{\text{strain}}(\zeta)$ increases along the reaction coordinate $\zeta$ because the C–Cl bond of the substrate is stretched while the Pd-substrate interaction $\Delta E_{\text{int}}(\zeta)$ becomes more stabilizing due to the decreasing HOMO-LUMO gap of the deformed substrate. The net result is the reaction profile of $\Delta E$ with the transition state indicated by a dot. Note that the reaction coordinate can be represented as the extent of stretching of the C–Cl bond.

**Table 8.2** Activation Strain analysis of the reaction barriers for various oxidative insertion reactions

| | C–H | | | | | | C–Cl | | | |
|---|---|---|---|---|---|---|---|---|---|---|
| | Pd | Be | Mg | Ca | Zn | Cd | Pd | Mg | Zn | Cd |
| *Energy decomposition (in kcal/mol)* | | | | | | | | | | |
| $\Delta E^{\neq}$ | 3.9 | 51.0 | 76.7 | 51.7 | 91.6 | 96.1 | –0.6 | 24.6 | 44.3 | 46.0 |
| $\Delta E^{\neq}_{\text{strain}}$ | 52.2 | 42.2 | 105.0 | 74.6 | 117.6 | 122.3 | 9.9 | 39.7 | 40.4 | 46.0 |
| $\Delta E^{\neq}_{\text{int}}$ | –48.3 | 8.8 | –28.3 | –23.0 | –26.0 | –26.2 | –10.5 | –15.2 | 3.8 | 0.0 |
| *C–X bond elongation in TS* | | | | | | | | | | |
| $\Delta(\text{C–X})^{\neq}$ (in Å) | 0.520 | 0.499 | 1.092 | 0.863 | 1.225 | 1.355 | 0.228 | 0.807 | 0.714 | 0.812 |
| $\Delta(\text{C–X})^{\neq}$ (in %) | 47 | 46 | 100 | 79 | 112 | 124 | 12 | 44 | 39 | 44 |

Now, we switch from the C–Cl to the stronger C–H bond (not shown; grey curves in Figure 8.3 will be discussed later). An important effect is that the $\Delta E_{\text{strain}}(\zeta)$ curve for C–H is destabilized relative to that for C–Cl. Consequently, also the net energy profile $\Delta E(\zeta) = \Delta E_{\text{strain}}(\zeta) + \Delta E_{\text{int}}(\zeta)$ of the Pd + $CH_4$ reaction is destabilized. Of course, the interaction between reactants $\Delta E_{\text{int}}(\zeta)$ is also affected by going from C–Cl to C–H. However, $\Delta E_{\text{int}}(\zeta)$ is *more* stabilizing for C–H in the first stages of the reaction (not shown here). Clearly, the absolute effect of changing from C–Cl to C–H is larger on the $\Delta E_{\text{strain}}(\zeta)$ curve than on the $\Delta E_{\text{int}}(\zeta)$ curve. The position of the TS along the reaction coordinate is, however, influenced by the $\Delta E_{\text{int}}(\zeta)$ curve. This is not pursued further here, but will be discussed extensively in Chapter 11.

Finally, we address the issue as to *why* the transition metal Pd has *intrinsically* a better capability of inserting into C–X bonds than alkaline earths and group-12 transition metals. We begin with an inspection of the frontier-orbital levels of our series of metal atoms, which are shown in Figure 8.4, together with the frontier-orbital levels of methane and chloromethane. There is a number of striking differences between the categories of metals. In the first place, the HOMO-LUMO gap increases from only 0.6 eV for Pd to 1.9-3.6 for the alkaline earths to 5.4-5.9 eV for group 12. This translates directly into a decrease in bonding capabilities along the series because a lower-energy HOMO is a worse electron donor (it has a larger gap with the substrate-$\sigma^*_{\text{C–X}}$ acceptor), and a higher-energy LUMO a worse electron acceptor (it has a larger gap with the substrate HOMO). This nicely agrees with the computed trend in barriers, which increase in the same order as the bonding capabilities of the metal decrease.

However, the trend of decreasing bonding capabilities along Pd, alkaline earths and group-12 atoms seems, at first sight, to be *not* confirmed by the Activation Strain analyses. In the case of insertion into the C–H bond, the TS interaction $\Delta E^{\neq}_{\text{int}}$ between metal and substrate does weaken from Pd (–48 kcal/mol) to the other metals (–28 to +9 kcal/mol) but along the latter (Be, Mg, Ca, Zn, Cd) there is no correlation with the

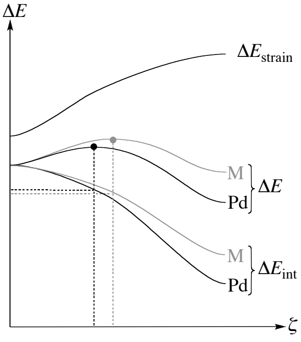

**Figure 8.3** Schematic profile of $\Delta E$ and its decomposition into $\Delta E_{\text{strain}}$ of and $\Delta E_{\text{int}}$. Going from Pd to a metal M with poorer bonding capabilities, the TS is destabilized and shifts forward along the reaction coordinate $\zeta$

HOMO-LUMO gap of the metal. For insertion into the C–Cl bond, the TS interaction $\Delta E^{\neq}_{\text{int}}$ becomes even *more stabilizing* from Pd (–11 kcal/mol) to Mg (–15 kcal/mol). It is the increase in activation strain $\Delta E^{\neq}_{\text{strain}}$ along Pd, alkaline earths and group-12 metals that causes the steady increase in overall barrier along these categories of metals.

Nevertheless, this can all be traced to the decrease in bonding capabilities from Pd to alkaline earths to group 12. We recall that the energy profile ($\Delta E$) for the reactions arises from an interplay of $\Delta E_{\text{strain}}(\zeta)$ and $\Delta E_{\text{int}}(\zeta)$. The analysis for Pd + $CH_3Cl$ is schematically depicted in Figure 8.3 (black curves). As pointed out above, $\Delta E_{\text{strain}}(\zeta)$ increases along the reaction coordinate $\zeta$ because the substrate C–Cl bond is stretched while $\Delta E_{\text{int}}(\zeta)$ becomes more stabilizing due to the decreasing HOMO-LUMO gap of the deformed substrate. The net result is the reaction profile $\Delta E$ with the TS indicated by a dot. We also recall that the reaction coordinate can be represented as the extent of stretching of the C–Cl bond. Now, we switch from Pd to the alkaline earths M. This time, the strain curve $\Delta E_{\text{strain}}(\zeta)$ is in approximation unaffected. The main effect is that $\Delta E_{\text{int}}(\zeta)$ for the alkaline earth metal (grey curve) is less stabilizing and descends initially *less* steeply along $\zeta$ than the $\Delta E_{\text{int}}(\zeta)$ curve for Pd (in black), see Figure 8.3. As a result, also the net energy profile $\Delta E(\zeta)$ of the M + $CH_3Cl$ reaction is destabilized and, because $\Delta E_{\text{int}}(\zeta)$ descends *less* steeply, the maximum of $\Delta E(\zeta)$ shifts to the right, i.e., the TS becomes more productlike. This is why the C–Cl bond expands more in the TSs involving alkaline earths and group-12 metals (i.e., by 39-44%) than in the TS involving Pd (only 12%, see Table 8.2). Interestingly, the more pronounced C–Cl bond expansion in the TS of Mg causes the corresponding TS interaction $\Delta E^{\neq}_{\text{int}}$ to become even more stabilizing than that for Pd (see dashed lines in Figure 8.3). Thus, the less stabilizing TS interaction $\Delta E^{\neq}_{\text{int}}$ occurs not because Pd has worse bonding capabilities. Rather, it occurs because of its *better* bonding capabilities, which make that the TS is reached in an early stage along the reaction coordinate: at that point, the C–Cl bond is less expanded and has

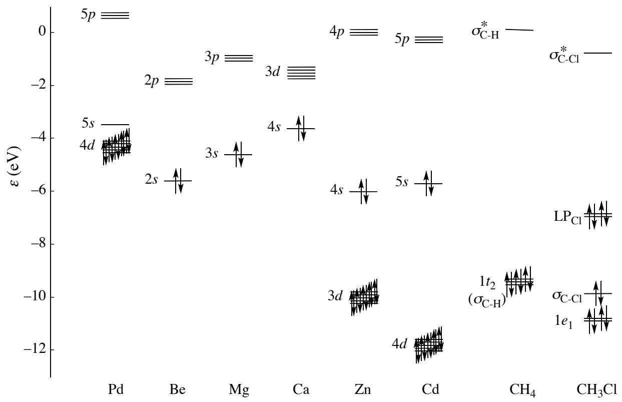

**Figure 8.4** Frontier orbital levels $\varepsilon$ with occupations of Pd, Be, Mg, Ca, Zn, Cd, $CH_4$ and $CH_3Cl$

therefore a larger HOMO-LUMO gap and, thus, poorer bonding capabilities. A similar mechanism causes the C–H bond to expand more in the TS for the oxidative insertion if we go from Pd (0.520 Å) to the alkaline earths (0.499-1.092 Å) to group 12 (1.225-1.355 Å) even though the bonding capabilities decrease along this series of metals.

Of course, the bonding capabilities of metals and substrates are not only determined by orbital-energy differences. The latter set a trend in the metal-substrate interactions but this trend can be much affected by the shape of the orbitals (through the resulting overlap) and also by electrostatic interactions. The precise role of these factors has not been resolved here. This requires a detailed analysis of all terms along a well defined reaction coordinate, which is however beyond the scope of this pilot study.

In conclusion, the fact that Pd is a better agent for oxidative insertion than alkaline earths or group-12 metals can be mainly ascribed to its excellent electron-donating and accepting capabilities associated with the high-energy 4*d* HOMO and low-energy 5*s* LUMO. Together, this causes a more stabilizing $\Delta E_{\mathrm{int}}(\zeta)$ at any point along the reaction coordinate $\zeta$ and therefore a lower barrier. The more stabilizing $\Delta E_{\mathrm{int}}(\zeta)$ can be masked by the fact that it also causes the TS to shift along $\zeta$ towards the reactant-side ("to the left" in Figure 8.3) making, on one hand, the TS interaction $\Delta E^{\neq}_{\mathrm{int}}$ less *stabilizing* but, on the other hand, the activation strain $\Delta E^{\neq}_{\mathrm{strain}} = \Delta E_{\mathrm{strain}}(\zeta^{\mathrm{TS}})$ less *destabilizing*.

## 8.4 Conclusions

The transition metal Pd is indeed intrinsically (i.e., already as isolated atom, in the absence of environment effects) more reactive towards oxidative insertion into a C–X bond than alkaline earths and group-12 transition metals. This can be mainly ascribed to its excellent electron-donating and accepting capabilities associated with the high-energy 4*d* HOMO and low-energy 5*s* LUMO. Together, this causes a more stabilizing Pd-substrate interaction $\Delta E_{\mathrm{int}}(\zeta)$ at any point along the reaction coordinate $\zeta$ and therefore a lower barrier as follows directly from our Activation Strain analysis, in which the activation energy $\Delta E^{\neq}$ arises as the sum of $\Delta E^{\neq}_{\mathrm{strain}}$ of and $\Delta E^{\neq}_{\mathrm{int}}$. In other words, the high energy of the Pd-4*d* HOMO makes it a good electron donor, promoting the oxidation process that leads to bond breaking. On the other hand, the low-energy Pd-5*s* LUMO makes it a good electron acceptor, promoting metal-adduct bonding.

Our study focuses on a selection of representative metals (Pd, Be, Mg, Ca, Zn, Cd) and bonds (C–H and C–Cl). Rather than providing a complete sweep through the Periodic Table, it is a pilot from which one can proceed in various directions. We expect that the main features that make Pd a superior agent in oxidative addition also hold for other transition metals up till group 10 (e.g., Ni and Pt) and that they are passed through also to the corresponding, catalytically active coordination complexes.

# 9 Oxidative addition of hydrogen halides and dihalogens to Pd. Trends in reactivity and relativistic effects

Adapted from
G. Th. de Jong, A. Kovács, F. M. Bickelhaupt *J. Phys. Chem. A* **2006**, *110*, 7943

## Abstract

We have theoretically studied the oxidative addition of HX and $X_2$ to palladium for X = F, Cl, Br, I and At, using both nonrelativistic and ZORA-relativistic density functional theory at BLYP/QZ4P. The purpose is threefold: (i) to obtain a set of consistent potential energy surfaces (PESs) to infer accurate trends in reactivity for simple, archetypal oxidative addition reactions; (ii) to assess how relativistic effects modify these trends along X = F, Cl, Br, I and At; and (iii) to rationalize the trends in reactivity in terms of the reactants' molecular-orbital (MO) electronic structure and the H–X and X–X bond strengths. For the latter, we provide full Dirac-Coulomb CCSD(T) benchmarks. All oxidative additions to Pd are exothermic and have a negative overall barrier, except that of HF, which is approximately thermoneutral and has a positive overall barrier. The activation barriers of the HX oxidative additions decrease systematically as X descends in group 17 of the Periodic Table; those of $X_2$ first increase, from F to Cl, but then also decrease further down group 17. On the other hand, HX and $X_2$ show clearly opposite trends regarding the heat of reaction: that of HX becomes *more* exothermic and that of $X_2$ *less* exothermic as X descends in group 17. Relativistic effects can be as large as 15-20 kcal/mol but they do not change the qualitative trends. Interestingly, the influence of relativistic effects on activation barriers and reaction energies decreases for the heavier halogens due to counteracting relativistic effects in palladium and the halogens.

## 9.1 Introduction

Oxidative addition and reductive elimination are ubiquitous as elementary reaction steps in homogeneous catalysis[117-120] and have been intensively investigated both experimentally[32-35,120-122] and theoretically.[33,35,42,43,67,108,122,123] A well-known class of processes involving oxidative addition is catalytic C–X bond activation.[31,117,118,124,125] The catalytically active species in these reactions are generally coordination complexes of palladium or other transition metals.

Here, we focus on the related processes of hydrogen-halide and dihalogen oxidative addition to palladium, for all halogens from fluorine to astatine (see Scheme 9.1). Apart from being involved in various catalytic processes,[2,117,129] the oxidative addition of hydrogen halides is also a model for the addition of more complex HX species in which X is, for example, formate or acetate.[130] Furthermore, the reactant (or precursor) complexes of dihalogen (in particular, $I_2$) complexes have been studied not only theoretically but also experimentally as models for early stages of the oxidative addition mechanism.[131]

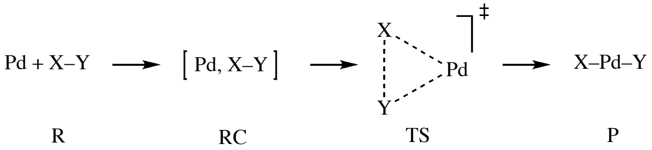

**Scheme 9.1** Model reactions and nomenclature (X = halogen, Y = H or X)

Our purpose is, in the first place, to obtain a set of consistent potential energy surfaces (PESs), which enable us to infer accurate trends in reactivity for these simple, archetypal oxidative addition reactions. A second purpose of this study is to assess how relativistic effects affect these trends along X = F, Cl, Br, I and At. In the third place, we wish to rationalize the trends in reactivity in terms of the reactants' molecular-orbital (MO) electronic structure[132] and the H–X and X–X bond strengths. Here, it is an asset of our model systems that they are simple because this facilitates the analyses and puts emphasis on the essential features in the electronic structure. Thus, we have explored the PES for oxidative addition of HX and $X_2$ to palladium for X = F, Cl, Br, I and At, using both nonrelativistic and ZORA-relativistic density functional theory at BLYP/QZ4P. In the course of our work, we have also computed highly accurate full Dirac-Coulomb CCSD(T) benchmarks for H–X and X–X bond energies that take spin-orbit coupling into account. One of our findings is that, interestingly, relativistic effects on activation barriers and reaction energies decrease for the heavier halogens. In this study, we focus on the overall barrier, that is, the difference in energy between the transition state and the separate reactants, which is decisive for the rate of chemical reactions in the gas phase, in particular, if they occur under low-pressure conditions in which the reaction system is (in good approximation) thermally isolated.[34,75]

## 9.2 Methods

### 9.2.1 DFT calculations

All density functional theory (DFT)[6-9] calculations have been carried out with the Amsterdam Density Functional (ADF) program.[49,50,133] Calculations were done either nonrelativistically or with scalar relativistic effects accounted for using the zeroth-order regular approximation (ZORA).[19] For the dissociation energies of the dihalogens and hydrogen halides, where spin-orbit coupling is expected to be important, also single-point calculations using double-group symmetry including spin-orbit effects were done. The BLYP[52,53] density functional was used, in combination with the QZ4P basis set for all elements except for hydrogen for which the TZ2P basis was used. The QZ4P basis set is a large uncontracted set of Slater-type orbitals (STOs) containing diffuse functions. It is of quadruple-$\zeta$ quality and has been augmented with several sets of polarization functions on each atom: two $3d$ and two $4f$ sets on F, three $3d$ and two $4f$ sets on Cl, two $4d$ and three $4f$ sets on Br, one $5d$ and three $4f$ sets on I, one $6d$ and two $5f$ sets on At, and two $5p$ and two $4f$ sets on Pd. The TZ2P basis set, only used for hydrogen, is of triple-$\zeta$ quality and has been augmented with two sets of polarization functions: $2p$ and $3d$. An auxiliary set of $s$, $p$, $d$, $f$ and $g$ STOs was used to fit the molecular density and to represent the Coulomb and exchange potentials accurately in each SCF cycle.[49] All electrons were treated variationally (i.e., no frozen-core approximation). Closed-shell and open-shell systems were treated using the spin-restricted and spin-unrestricted formalism, respectively. The electronic structures of Pd, HX and $X_2$ were analyzed in terms of the quantitative molecular orbital (MO) model contained in Kohn-Sham DFT.[132] In Chapters 4 to 7, it has been shown that our approach is in good agreement with high-level relativistic *ab initio* calculations for our model systems.

Equilibrium and transition state geometries were fully optimized using analytical gradient techniques. All structures were verified by frequency calculations: for minima all normal modes have real frequencies, whereas transition states have one normal mode with an imaginary frequency. The character of the normal mode associated with the imaginary frequency was analyzed to ensure that the correct transition state was found.

### 9.2.2 *Ab initio* calculations

On the basis of the ZORA-BLYP/QZ4P optimized geometries, *ab initio* dissociation energies of $X_2$ and HX were calculated at the advanced correlated CCSD(T) level[59,60,98] with the program package DIRAC.[55,99] A full all-electron four-component Dirac-Coulomb approach was used, which allowed nonrelativistic calculations with the Lévy-Leblond approximation[18] (designated here as CCSD(T)), relativistic calculations without spin-orbit coupling using a spin-free Dirac-Coulomb Hamiltonian[17] (SFDC–CCSD(T)), and relativistic calculations using the unmodified Dirac-Coulomb Hamiltonian, which includes spin-orbit coupling (DC–CCSD(T)). The two-electron integrals over the small components have been neglected and corrected with a simple Coulombic correction that has been shown reliable.[16] The basis sets used for H, F and Cl were Dunning's correlation-consistent augmented triple-$\zeta$ (aug-cc-pVTZ) basis sets,[63] and for Br, I and At Dyall's relativistically optimized triple-$\zeta$ basis sets.[134]

## 9.3 Results and discussion

### 9.3.1 Reaction profiles and geometries

In this section, we discuss the fully relativistic potential energy surfaces (PESs) of the various oxidative insertion reactions as well as the geometries of the stationary points, that is, all computed at ZORA-BLYP/QZ4P//ZORA-BLYP/QZ4P, designated R//R in the tables. Structural results are summarized in Figure 9.1 and Tables 9.1 and 9.2, and results about reaction profiles in Figure 9.2 and Table 9.3. In Section 9.3.2, we examine how relativistic effects affect the trends in reactivity. Finally, in Section 9.3.3,

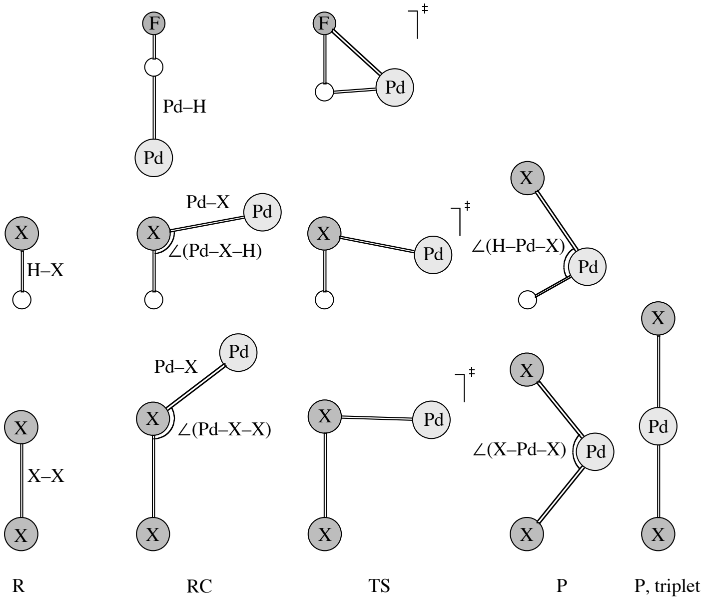

**Figure 9.1** Structures of stationary points for oxidative insertion of Pd to HX and $X_2$ with X = F, Cl, Br, I, and At (see also Tables 9.1 and 9.2). Note that structures involving HF differ from those of other HX

**Table 9.1** Geometry parameters[a] (in Å, degrees) of stationary points for Pd + HX, with X = F to At[b]

| | | H–X | | Pd–X | | Pd–H | | ∠(Pd–X–H) | | ∠(H–Pd–X) | |
|---|---|---|---|---|---|---|---|---|---|---|---|
| Substrate | | NR | R | NR | R | NR | R | NR | R | NR | R |
| H–F | R | 0.934 | 0.935 | | | | | | | | |
| | RC | 0.967 | 0.974 | 3.000 | 2.969 | 2.033 | 1.995 | 0.0 | 0.0 | 0.0 | 0.0 |
| | TS | 1.665 | 1.497 | 2.085 | 2.083 | 1.531 | 1.538 | 46.5 | 47.5 | 52.1 | 45.8 |
| | P | 2.468 | 2.487 | 1.966 | 1.925 | 1.525 | 1.511 | 38.2 | 37.4 | 89.0 | 91.6 |
| H–Cl | R | 1.291 | 1.291 | | | | | | | | |
| | RC | 1.300 | 1.306 | 2.480 | 2.343 | 3.052 | 2.922 | 103.2 | 102.7 | 24.5 | 25.9 |
| | TS | 1.307 | 1.317 | 2.515 | 2.373 | 2.575 | 2.466 | 77.7 | 78.1 | 29.7 | 31.5 |
| | P | 2.532 | 2.627 | 2.284 | 2.236 | 1.528 | 1.511 | 36.5 | 35.0 | 80.6 | 86.8 |
| H–Br | R | 1.437 | 1.435 | | | | | | | | |
| | RC | 1.451 | 1.458 | 2.553 | 2.439 | 3.221 | 3.103 | 103.7 | 102.6 | 26.0 | 27.3 |
| | TS | 1.457 | 1.467 | 2.577 | 2.461 | 2.650 | 2.575 | 76.6 | 77.4 | 32.3 | 33.8 |
| | P | 2.447 | 2.668 | 2.418 | 2.366 | 1.535 | 1.513 | 36.8 | 34.3 | 72.7 | 83.8 |
| H–I | R | 1.634 | 1.630 | | | | | | | | |
| | RC | 1.653 | 1.658 | 2.613 | 2.532 | 3.402 | 3.300 | 103.5 | 101.9 | 28.2 | 29.4 |
| | TS | 1.666 | 1.671 | 2.638 | 2.555 | 2.637 | 2.610 | 71.5 | 72.9 | 36.8 | 37.7 |
| | P | 1.987 | 2.674 | 2.640 | 2.527 | 1.616 | 1.519 | 37.7 | 33.8 | 48.7 | 78.4 |
| H–At | R | 1.738 | 1.726 | | | | | | | | |
| | RC | 1.758 | 1.759 | 2.675 | 2.619 | 3.474 | 3.397 | 101.2 | 99.9 | 29.8 | 30.7 |
| | TS | 1.773 | 1.769 | 2.697 | 2.635 | 2.672 | 2.705 | 70.0 | 72.8 | 38.5 | 38.7 |
| | P | 2.120 | 2.668 | 2.705 | 2.616 | 1.609 | 1.524 | 36.5 | 33.5 | 51.6 | 75.1 |

a See Figure 9.1 for definition.

b NR = computed *non*relativistically at BLYP/QZ4P; R = computed *relativistically* at ZORA-BLYP/QZ4P.

we try to understand the trends in reactivity in terms of the electronic structure of the reactants and the H–X and X–X bond strengths.

First, the oxidative addition reactions of HX + Pd are examined. They may all proceed from the reactants (R) via a reactant complex (RC) to a transition state (TS) that connects the RC with the product (P) in which the H–X bond is broken (see Figure 9.1 and Table 9.1). For all HX except HF, there is also a direct approach, perpendicularly to the H–X bond, without a barrier possible (*vide infra*). In the reactant complex, Pd binds to the halogen atom X with a Pd–X–H angle close to 100° for all hydrogen halides except hydrogen fluoride (see Table 9.1). In the case of the latter, Pd binds to the hydrogen atom and forms a linear Pd–H–X structure. The substrates HCl to HAt have a donor lone pair (LP) orbital on the halogen, which is fitted well for donation of electronic charge from the LP to the empty Pd-5*s* orbital, which causes Pd to bind to the halogen. The fluorine in HF is very electronegative and donates less well. Therefore, Pd will bind to the hydrogen, where it can donate electronic charge to the empty antibonding $\sigma^*_{\text{H–F}}$, which is strongly located on the hydrogen. The complexation energies between Pd and HX (i.e., the energy of RC relative to R) range from –4.9 kcal/mol for HF to –20.2 kcal/mol for HAt (see Table 9.3, R//R data). Activation barriers and reaction energies also show a pronounced trend: both decrease systematically from F to At. Only Pd + HF has a positive overall barrier and is approximately thermoneutral. The other reactions have all negative overall barriers and are pronouncedly exothermic. For example, the activation energies are +11.9 (F), –10.4 (Cl), –12.7 (Br), –18.3 (I) and –18.5 kcal/mol (At) (see Table 9.3, R//R data).

**Table 9.2** Geometry parameters[a] (in Å, degrees) of stationary points for Pd + $X_2$, with X = F to At[b]

| | | X–X | | Pd–X | | ∠(Pd–X–X) | | ∠(X–Pd–X) | |
|---|---|---|---|---|---|---|---|---|---|
| Substrate | | NR | R | NR | R | NR | R | NR | R |
| F–F[c] | R | 1.433 | 1.433 | | | | | | |
| | RC | 1.787 | 1.822 | 1.978 | 1.945 | 180.0 | 180.0 | 0.0 | 0.0 |
| | P | 2.926 | 2.973 | 1.919 | 1.891 | 40.3 | 38.2 | 99.3 | 103.6 |
| | Linear P (triplet) | 3.866 | 3.806 | 1.933 | 1.903 | 0.0 | 0.0 | 180.0 | 180.0 |
| Cl–Cl | R | 2.040 | 2.041 | | | | | | |
| | RC | 2.257 | 2.269 | 2.331 | 2.257 | 158.6 | 136.4 | 10.5 | 21.9 |
| | TS | 2.302 | 2.351 | 2.333 | 2.241 | 88.7 | 89.6 | 45.2 | 46.6 |
| | P | 3.384 | 3.453 | 2.252 | 2.215 | 41.3 | 38.8 | 97.4 | 102.4 |
| | Linear P (triplet) | 4.586 | 4.448 | 2.293 | 2.224 | 0.0 | 0.0 | 180.0 | 180.0 |
| Br–Br | R | 2.348 | 2.346 | | | | | | |
| | RC | 2.523 | 2.532 | 2.466 | 2.384 | 139.2 | 126.9 | 20.6 | 27.4 |
| | TS | 2.561 | 2.599 | 2.452 | 2.367 | 88.1 | 87.6 | 47.2 | 49.0 |
| | P | 3.508 | 3.591 | 2.390 | 2.351 | 42.8 | 40.2 | 94.4 | 99.6 |
| | Linear P (triplet) | 4.878 | 4.723 | 2.439 | 2.362 | 0.0 | 0.0 | 180.0 | 180.0 |
| I–I | R | 2.742 | 2.737 | | | | | | |
| | RC | 2.872 | 2.881 | 2.592 | 2.513 | 123.1 | 116.2 | 30.0 | 34.3 |
| | TS | 2.901 | 2.931 | 2.580 | 2.507 | 87.1 | 85.4 | 50.0 | 52.1 |
| | P | 3.612 | 3.724 | 2.565 | 2.522 | 45.2 | 42.4 | 89.5 | 95.2 |
| | Linear P (triplet) | 5.181 | 5.078 | 2.590 | 2.539 | 0.0 | 0.0 | 180.0 | 180.0 |
| At–At | R | 2.953 | 2.923 | | | | | | |
| | RC | 3.066 | 3.052 | 2.662 | 2.604 | 116.3 | 113.1 | 34.3 | 36.4 |
| | TS | 3.092 | 3.096 | 2.655 | 2.594 | 86.5 | 84.2 | 51.4 | 53.5 |
| | P | 3.662 | 3.786 | 2.660 | 2.614 | 46.5 | 43.6 | 87.0 | 92.8 |
| | Linear P (triplet) | 5.367 | 5.257 | 2.683 | 2.629 | 0.0 | 0.0 | 180.0 | 180.0 |

a See Figure 9.1 for definition.

b NR = computed *non*relativistically at BLYP/QZ4P; R = computed *relativistically* at ZORA-BLYP/QZ4P.

c No TS found because of lower-lying triplet PES.

Interestingly, the TS of Pd + HF is found to be of a different nature than the TS of the other Pd + HX reactions. For the latter, there is in fact no barrier for a direct approach of the palladium perpendicular to the H–X bond. Thus, for Pd + HCl, HBr, HI and HAt the energy increases as Pd is moving away from the equilibrium position of the RC because this weakens the coordination bond. The TS is reached as Pd is arriving at the rim of the reactive zone that surrounds the H–X bond: if Pd moves across this border,

**Table 9.3** Relative energies (in kcal/mol) of stationary points for Pd + HX and $X_2$, with X = F to At[a]

| | RC | | | TS | | | P | | | Linear P (triplet) | | |
|---|---|---|---|---|---|---|---|---|---|---|---|---|
| Substrate | NR//NR | R//NR | R//R | NR//NR | R//NR | R//R | NR//NR | R//NR | R//R | NR//NR | R//NR | R//R |
| H–F | –4.1 | –4.9 | –4.9 | 23.1 | 11.3 | 11.9 | 16.7 | 0.5 | 0.1 | b | b | b |
| H–Cl | –6.2 | –10.3 | –11.1 | –5.7 | –9.6 | –10.4 | –6.2 | –22.1 | –22.6 | b | b | b |
| H–Br | –8.4 | –12.9 | –13.6 | –7.8 | –12.1 | –12.7 | –14.2 | –29.0 | –30.0 | b | b | b |
| H–I | –14.4 | –19.5 | –20.0 | –13.0 | –17.9 | –18.3 | –23.3 | –33.8 | –37.3 | b | b | b |
| H–At | –16.7 | –20.0 | –20.2 | –15.1 | –18.3 | –18.5 | –27.1 | –38.0 | –40.4 | b | b | b |
| F–F | –39.3 | –43.8 | –44.0 | c | c | (–32)[c] | –85.8 | –100.7 | –101.3 | –96.6 | –112.9 | –113.3 |
| Cl–Cl | –21.9 | –26.4 | –27.8 | –14.7 | –21.8 | –22.6 | –46.3 | –61.2 | –61.8 | –48.2 | –65.3 | –66.5 |
| Br–Br | –21.8 | –27.7 | –28.6 | –17.5 | –24.5 | –25.1 | –42.3 | –56.0 | –56.6 | –41.4 | –58.8 | –60.1 |
| I–I | –22.5 | –29.4 | –30.0 | –20.5 | –27.6 | –28.0 | –40.0 | –52.3 | –52.9 | –35.9 | –52.8 | –53.3 |
| At–At | –23.0 | –29.2 | –29.4 | –21.7 | –27.4 | –27.6 | –39.6 | –49.1 | –49.5 | –33.8 | –48.6 | –49.1 |

a NR//NR = computed fully *non*relativistically at BLYP/QZ4P//BLYP/QZ4P; R//NR = energy computed *relativistically* but with *nonrelativistic geometries* at ZORA-BLYP/QZ4P//BLYP/QZ4P; R//R = computed fully *relativistically* at ZORA-BLYP/QZ4P//ZORA-BLYP/QZ4P.

b Not an equilibrium structure

c Accurate determination hampered due to near-degeneracy of singlet and triplet PES. R//R value of –32 kcal/mol is upper bound, estimated from singlet energy profile in Figure 9.3.

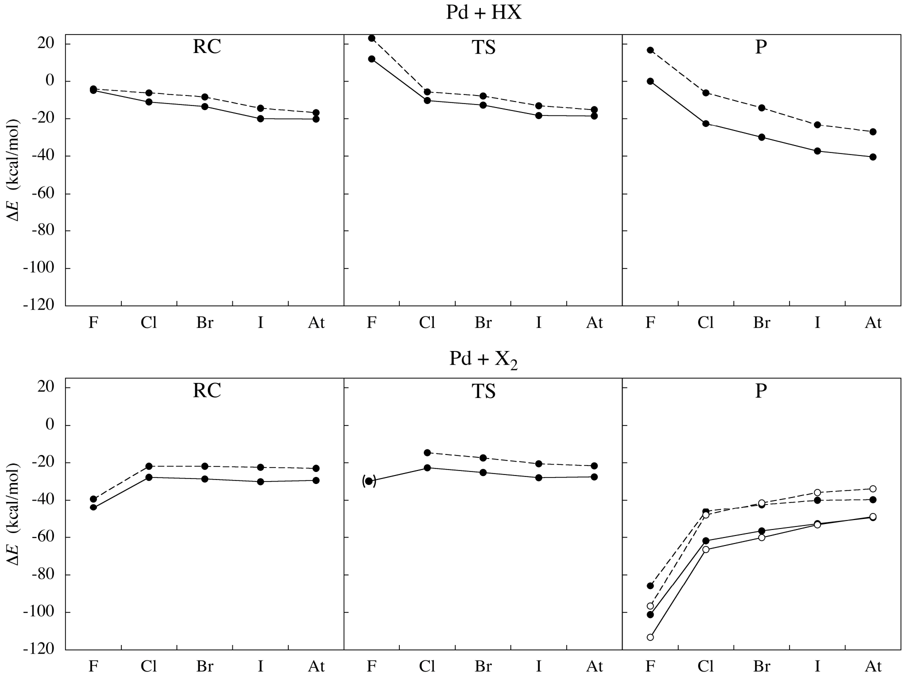

**Figure 9.2** Relative energies of the stationary points for Pd + HX and $X_2$, with X = F to At, at BLYP/QZ4P, without (dashed lines) and with ZORA relativistic effects (straight lines). For Pd + $F_2$ TS: value is an upper bound. For Pd + $X_2$ product: filled circles refer to singlet states, unfilled circles to triplet states

it spontaneously inserts (in a sense, it falls) into the H–X bond, which then gives way and breaks. At variance, the TS for Pd + HF is inherently connected with the movement of insertion into the H–F bond and it is also present in the case of a direct approach of Pd perpendicular to the H–F bond.

Next, we inspect the reactions of $X_2$ + Pd. Similar to the situation of the HX, the $X_2$ additions may all proceed from the reactants (R) via a reactant complex (RC) to a transition state (TS) that connects the RC with the product (P) in which the X–X bond is broken (see Figure 9.1 and Table 9.2). In the reactant complex, Pd binds to the halogen atom X with a Pd–X–X angle that decreases systematically from 180° for $F_2$ to 113° for $At_2$ (see Table 9.2).

Regarding the energetics, there are striking differences between oxidative addition of $X_2$ and HX. The complexation energies between Pd and $X_2$ (i.e., the energy of RC relative to the reactants) are considerably more stabilizing than in the case of Pd + HX (see Table 9.3, R//R data). The activation barriers for Pd + $X_2$ are also generally lower than those for Pd + HX. Furthermore, the barriers of Pd + $X_2$ first *increase*, from X = F to Cl, but then also decrease along X = Cl, Br, I and At (see Figure 9.2). The activation energy goes up from approximately (*vide infra*) –32 kcal/mol for $F_2$ to –22.6 for $Cl_2$ and, thereafter, goes down to –27.6 kcal/mol for $At_2$. The nature of the transition states resembles that of the corresponding Pd + HX reactions in the sense that they occur only if one proceeds from the RC while oxidative addition proceeds again barrierless if Pd approaches the dihalogen side-on, that is, perpendicular to the X–X bond. Contrary to the situation for Pd + HX, the oxidative addition $X_2$ to Pd becomes systematically *less* exothermic along X = F to At. Thus, the reaction energy for Pd + $X_2$ goes from a very exothermic –101.3 kcal/mol for X = F up to the less exothermic –49.5 kcal/mol for At. For comparison, in the case of Pd + HX, the reaction energy goes from approximately thermoneutral, +0.1 kcal/mol, for X = F to a clearly exothermic –40.4 kcal/mol for X = At.

Now, we come back to the barrier for Pd + $F_2$. The computation of an accurate value for this barrier is hampered by the fact that, only for this reaction, the triplet surface drops below the singlet one as we proceed along the reaction coordinate to the transition state. This is illustrated in Figure 9.3, which shows the singlet and triplet PESs for Pd + $F_2$ (upper) and, for comparison, those for Pd + $I_2$ as a function of the Pd–X–X angle; the latter has been varied, in steps of 5°, from 180° (corresponding to a linear RC) to 0° (linear P) while optimizing all other geometry parameters in every step. The value of approximately –32 kcal/mol (mentioned above, in Table 9.3, and indicated in Figure 9.2) for the barrier of Pd + $F_2$ refers to the highest point on the PES of the singlet spin state. However, before that point the triplet PES, which is characterized by the absence of a reaction barrier, drops below the singlet PES. It is beyond the scope of this explorative investigation to resolve the intricate problem of how this singlet-triplet crossing affects the precise mechanism and shape of the effective PES for Pd + $F_2$ reaction. It is,

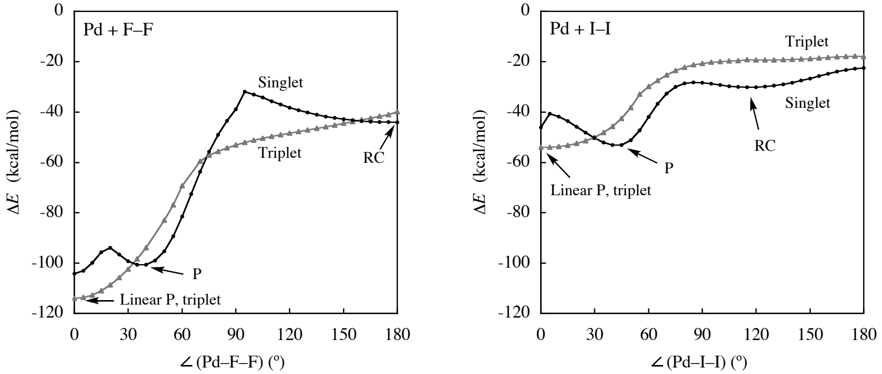

**Figure 9.3** Energy profiles for insertion of Pd into F–F and I–I bonds. Singlet and triplet energies for optimized geometries at fixed Pd–X–X angle, at ZORA-BLYP/TZ2P with frozen-core approximation. An angle of 180° means a linear Pd–X–X geometry; an angle of 0° means a linear X–Pd–X geometry

however, instructive to compare the singlet and triplet PESs of Pd + $F_2$ with those of Pd + $I_2$. In Figure 9.3, it can be nicely seen that for the reaction with $I_2$, the triplet PES is always clearly above the singlet PES until and including the product P. Only as we proceed to a linear product geometry (∠Pd–I–I = 0°), does the triplet PES become more stable than the singlet PES. We have verified that this happens for all products of dihalogen addition but not for the hydrogen halides. The linear triplet-state products of the dihalogen reactions turn out to be approximately equally stable as (At, I) up to ca. 12 kcal/mol (F) more stable than the bent products on the singlet PES (see Table 9.3).

### 9.3.2 Relativistic effects

Relativistic effects are significant but they do not change the relative order of reactivity of HX and $X_2$ oxidative addition to Pd along the series of halogens. Relativistic effects can be revealed by comparing the fully relativistic PESs discussed above (R//R data in Table 9.3) with the corresponding fully nonrelativistic PESs derived from nonrelativistic energies and nonrelativistic geometries of stationary points (NR//NR data in Table 9.3).

Relativistic effects stabilize the PESs of all HX and $X_2$ addition reactions relative to the reactants as illustrated by Figure 9.4. Reaction barriers are stabilized by up to 11 kcal/mol (for Pd + HF) and reactions become more exothermic. One might expect relativistic effects to be more pronounced for the reactions involving the heavier

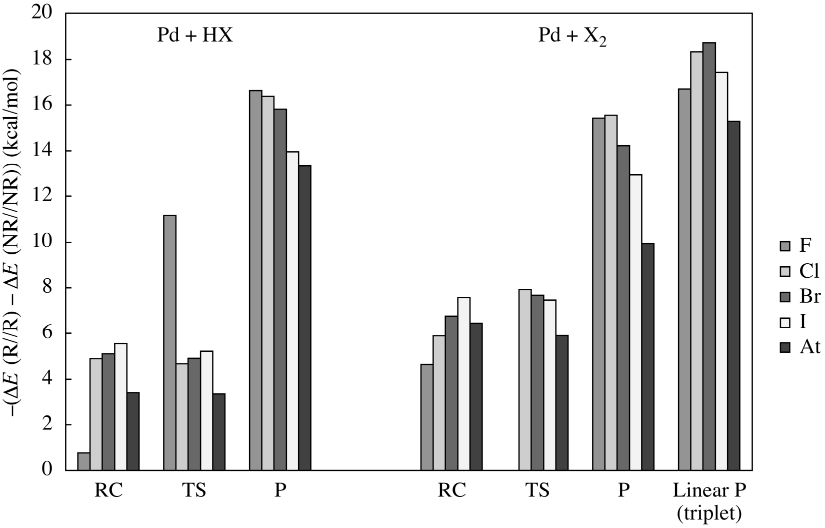

**Figure 9.4** Relativistic effects on energies of stationary points for the oxidative addition of HX and $X_2$ to Pd, with X = F, Cl, Br, I, and At, at BLYP/QZ4P, scalar relativistic effects included by ZORA

halogens. This expectation is born out of the observation that relativistic effects on H–X and X–X bond strengths increase substantially along X = F to At (*vide infra*). Interestingly, however, the relativistic stabilization of transition states and products becomes overall smaller, not stronger, along this series in X. The relativistic effects originating from the halogen atoms obviously counteract those originating from Pd.

Relativity also affects the geometries of all species involved in the HX and $X_2$ oxidative addition reactions. The most striking and general effect is a shortening of the Pd–X and, in most cases, also the Pd–H bond distance. For example, the Pd–X distance in the transition states of Pd + HX contracts relativistically by –0.002 (F), –0.142 (Cl), –0.116 (Br), –0.083 (I) and –0.062 Å (At). Note that the relativistic effects on geometries are not largest for the systems with the heaviest halogens: along Cl to At, they even decrease systematically. This more or less parallels the trend in the relativistic effects on the activation barriers.

The above suggests that relativistic effects strengthen the Pd–substrate interaction. However, the primary effect on the energetics is not directly visible because it also induces geometrical changes that may amplify or attenuate the overall effect. To separate the initial relativistic effect on the Pd-substrate interaction from geometry relaxation effects, we have again computed all PESs at ZORA/BLYP/QZ4P//BLYP/QZ4P, that is, relativistically but with the nonrelativistic geometries (designated R//NR in Table 9.3). Now, it is immediately clear that the overall relativistic effects, of the order of up to 17 kcal/mol, are hardly affected by geometrical relaxation processes, which are typically in the order of 1 kcal/mol or less (they only reach larger values of 3.5 and 2.4 kcal/mol for the reaction energies of Pd + HI and Pd + HAt, respectively). In conclusion, the relativistic stabilization of RC, TS and P of the reactions of Pd + HX and Pd + $X_2$ can indeed be attributed to a strengthening of the Pd-substrate interaction. This is in nice agreement with similar findings for the reactions of Pd + $CH_3X$ by Diefenbach *et al.*[22]

### 9.3.3 Analysis of trends in reactivity and relativistic effects

In the previous sections, we have found, among others, that the activation barrier for HX oxidative addition decreases along X = F, Cl, Br, I and At, and that the activation barrier for $X_2$ oxidative addition first increases, from X = F to Cl but then also decreases from X = Cl to At. We also found that relativistic effects further reduce the activation barrier for all model reactions. In this section, we try to rationalize these trends in terms of the reactants' electronic structures and the H–X and X–X bond strengths (see Figure 9.5 and Table 9.4).

The homolytic dissociation energies $D_{HX}$ and $D_{XX}$ of HX and $X_2$ are shown in Table 9.4. They have been computed both with BLYP/QZ4P and, to have an accurate benchmark, also with CCSD(T) (see Section 9.2.2 for details). Furthermore, relativistic effects have been investigated by carrying out both the BLYP and CCSD(T) computations nonrelativistically (BLYP, CCSD(T)), scalar relativistically, i.e., without spin-orbit coupling (ZORA-BLYP, spin-free Dirac-Coulomb or SFDC-CCSD(T)), and relativistically including spin-orbit coupling (SO-ZORA-BLYP, Dirac-Coulomb or DC-CCSD(T)). The BLYP values agree well with those of CCSD(T) at any level of treating relativistic effects. For example, $D_{\mathrm{HAt}}$ amounts to 73.9, 71.8 and 55.5 kcal/mol at BLYP, ZORA-BLYP and SO-ZORA-BLYP, which agrees within 1.2 kcal/mol with 73.1, 70.6 and 54.5 kcal/mol obtained at CCSD(T), SFDC-CCSD(T) and DC-CCSD(T), respectively, including counterpoise correction for the BSSE. Counterpoise correction is more important for coupled-cluster calculations, than for DFT calculations; see Chapters 3 and 4. For $D_{\mathrm{HX}}$ and $D_{\mathrm{XX}}$, the BSSE can reach values of up to 3.7 kcal/mol (in case of $D_{\mathrm{HI}}$). The same trends for $D_{\mathrm{HX}}$ and $D_{\mathrm{XX}}$ were found in previous calculations.[135] The DC-CCSD(T) benchmark tends to yield slightly too weak bond energies (by a few kcal/mol up to 7.9 kcal/mol for $Cl_2$) if compared to experimental values.[136] Note that relativistic effects on $D_{\mathrm{HX}}$ and $D_{\mathrm{XX}}$ are essentially caused by spin-orbit coupling. The spin-orbit term stems from the atoms ($H^{\bullet}$ and $X^{\bullet}$) that have a doublet open-shell configuration. Spin-orbit coupling is a minor term for all closed-shell systems: Pd, HX, $X_2$ as well as the species at the stationary points along the PES for our model reactions. For example, the relativistic energy *with* spin-orbit coupling of the product of Pd + $At_2$ relative to reactants is –51.2 kcal/mol (not shown in Table 9.3), which is only marginally different from the scalar relativistic value of –49.5 kcal/mol (see Table 9.3). This leads us to suggest that the scalar relativistic relative energies reported here for the stationary points for the reaction of Pd with the substrates are reliable whereas reliable dissociation energies can only be obtained if spin-orbit coupling is taken into account.

**Table 9.4** Dissociation energies (in kcal/mol) of HX ($D_{\mathrm{HX}}$) and $X_2$ ($D_{\mathrm{XX}}$) for X = F to At, at various levels of DFT and *ab initio* theory[a]

| | $D_{\mathrm{HX}}$ | | | | | $D_{\mathrm{XX}}$ | | | | |
|---|---|---|---|---|---|---|---|---|---|---|
| Method | F | Cl | Br | I | At | F | Cl | Br | I | At |
| BLYP//BLYP[b] | 140.9 | 104.5 | 91.5 | 79.5 | 73.9 | 49.0 | 58.1 | 51.6 | 45.8 | 42.9 |
| BLYP | 140.9 | 104.5 | 91.5 | 79.5 | 73.9 | 49.0 | 58.1 | 51.6 | 45.8 | 42.8 |
| ZORA-BLYP | 140.8 | 104.3 | 91.0 | 78.4 | 71.8 | 49.0 | 58.0 | 51.4 | 45.3 | 42.2 |
| SO-ZORA-BLYP | 140.7 | 104.0 | 87.5 | 71.3 | 55.5 | 49.0 | 57.5 | 44.9 | 32.4 | 17.5 |
| SO-ZORA-BLYP ($\Delta H^{298}$)[c] | 136.0 | 100.9 | 84.8 | 69.0 | 53.5 | 48.4 | 57.5 | 45.0 | 32.7 | 17.7 |
| CCSD(T) | 137.1 | 103.2 | 91.0 | 77.8 | 73.1 | 34.3 | 51.9 | 45.5 | 41.3 | 39.0 |
| SFDC-CCSD(T) | 136.9 | 103.0 | 90.3 | 76.7 | 70.6 | 34.3 | 51.8 | 45.0 | 40.5 | 36.9 |
| DC-CCSD(T) | 136.5 | 102.2 | 86.8 | 70.6 | 54.5 | 33.5 | 50.1 | 38.5 | 28.5 | 12.4 |
| Experiment[d] | 136.4 | 103.2 | 87.5 | 71.3 | | 37.9 | 58.0 | 46.1 | 36.1 | |

a Geometries optimized at ZORA-BLYP/QZ4P unless stated otherwise. BLYP = nonrelativistic BLYP/QZ4P. ZORA-BLYP = scalar ZORA-relativistic BLYP/QZ4P. SO-ZORA-BLYP = spin-orbit ZORA-relativistic BLYP/QZ4P. CCSD(T) = nonrelativistic CCSD(T). SFDC-CCSD(T) = CCSD(T) with relativistic spin-free Dirac-Coulomb Hamiltonian excluding spin-orbit coupling. DC-CCSD(T) = CCSD(T) with relativistic unmodified Dirac-Coulomb Hamiltonian including spin-orbit coupling. All CCSD(T) values have been corrected for the BSSE.

b Geometries optimized nonrelativistically at BLYP/QZ4P.

c Enthalpy.

d Obtained from corresponding enthalpies of formation at 298 K from ref. 136.

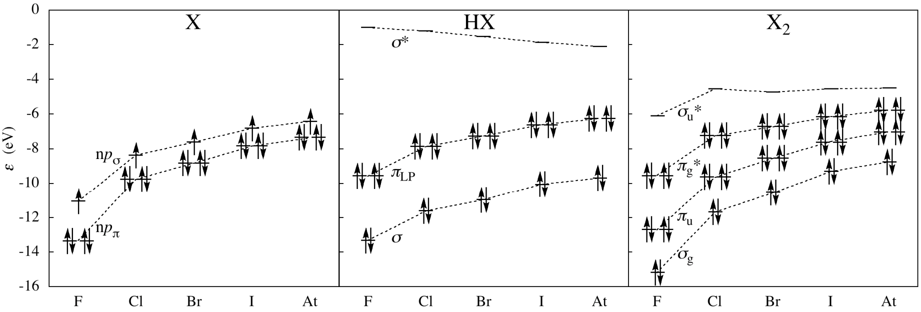

**Figure 9.5** Orbital energies $\varepsilon$ of the frontier orbitals of X, HX, and $X_2$, for X = F to At, at ZORA-BLYP/QZ4P

Now, we examine the trends in $D_{\mathrm{HX}}$ and $D_{\mathrm{XX}}$ (see Table 9.4). Two observations can be made: (i) the H–X bonds of the hydrogen halides ($D_{\mathrm{HX}}$ = 141-56 kcal/mol at SO-ZORA-BLYP) are significantly stronger than the X–X bonds of the dihalogens ($D_{\mathrm{XX}}$ = 49-18 kcal/mol at same level); (ii) both H–X and X–X bond strength decrease along X = F, Cl, Br, I and At, with one exception for $F_2$, which has a smaller bond strength than $Cl_2$ (*vide infra*). The decrease along this series is significantly more pronounced for HX than for $X_2$. This is so because in the former, a strong contribution to the trend is provided by the decreasing charge-stabilization that goes with the decreasing electronegativity difference across the H–X bond; this feature is completely absent in the homonuclear $X_2$ series. The relatively weak F–F bond originates from the very compact nature of the fluorine 2*p* AOs (which lack a *p*-type core, at variance with the n*p* valence AOs of higher periods) as a result of which a favourable $<2p_\sigma|2p_\sigma>$ bond overlap occurs at a relatively short F–F distance at which there is already significant antibonding $<2s|2s>$ overlap (see Kovács *et al.*[137] for a full account of the bonding in $F_2$).

The above trends in H–X and X–X bond strengths contribute in a straightforward manner to the trend in the activation energies. According to the Activation Strain model of chemical reactivity (see Chapter 2), the activation energy $\Delta E^{\neq}$ is decomposed into the activation strain $\Delta E^{\neq}_{\mathrm{strain}}$ of and the stabilizing TS interaction $\Delta E^{\neq}_{\mathrm{int}}$ between the reactants in the activated complex: $\Delta E^{\neq} = \Delta E^{\neq}_{\mathrm{strain}} + \Delta E^{\neq}_{\mathrm{int}}$. Here, the activation strain is entirely due to substrate bond stretching which requires more energy for HX than for $X_2$. Furthermore, the H–X bond strength decreases along X = F, Cl, Br, I and At whereas the X–X bond strength first increases, from X = F to Cl, and thereafter also decreases along X = Cl, Br, I and At. This is exactly the trend in activation energies that we find for the model reactions of Pd + HX and for Pd + $X_2$ (see Figure 9.2 and Table 9.4).

The overall trend in activation energies is also dependent on the Pd-substrate interaction, that is, the TS interaction $\Delta E^{\neq}_{\mathrm{int}}$ which is provided, among others, by the donor-acceptor orbital interactions between Pd-4*d* AOs and the substrate $\sigma^*_{\mathrm{H-X}}$ or $\sigma^*_{\mathrm{X-X}}$

LUMO. These interactions are strengthened by relativistic effects that lead to the well-known destabilization of Pd-4*d* AOs and thus to a smaller, more favourable HOMO-LUMO gap between Pd and the substrate (the effect is further reinforced by relativistic stabilization of the Pd-5*s* acceptor AO).[22] In the case of HX, the $\sigma^*_{\mathrm{H-X}}$ LUMO is mainly the $1s$–n$p_\sigma$ antibonding combination. The energy of this antibonding combination decreases along X = F, Cl, Br, I and At, because the n*p* AO becomes more diffuse and, thus, the $<1s|\mathrm{n}p_\sigma>$ overlap smaller (see Figure 9.5). This reduces the HOMO-LUMO gap between Pd and HX and thus strengthens the TS interaction $\Delta E^{\neq}_{\mathrm{int}}$ along this series. This further contributes to the trend of a decreasing activation energy $\Delta E^{\neq}$ for Pd + HX along X = F, Cl, Br, I and At (see Figure 9.2). In the case of $X_2$, the $\sigma^*_{\mathrm{X-X}}$ LUMO is mainly the n$p_\sigma$–n$p_\sigma$ antibonding combination. The energy of this antibonding combination *increases* along X = F, Cl, Br, I and At, because the energy of the n*p* AO itself also increases down group 17 (see Figure 9.5). This causes the HOMO-LUMO gap between Pd and $X_2$ to become larger and thus to weaken the TS interaction $\Delta E^{\neq}_{\mathrm{int}}$ along this series. From X = F to Cl, this effect enhances the trend set by the activation strain $\Delta E^{\neq}_{\mathrm{strain}}$: the activation energy $\Delta E^{\neq}$ for Pd + $X_2$ increases from X = F to Cl. Thereafter, along X = Cl, Br, I and At, the trend in $\Delta E^{\neq}_{\mathrm{int}}$ partially, but not completely, cancels the trend of a decreasing activation strain $\Delta E^{\neq}_{\mathrm{strain}}$ for Pd + $X_2$ (see Figure 9.2). In the products, however, this effect becomes larger and does reverse the trend over the whole series. As a consequence, the reactions of Pd + $X_2$ become *systematically less* exothermic along X = F, Cl, Br, I and At, thus showing the opposite trend for the reaction energy as compared to Pd + HX.

Finally, note that the 2*p* AO of the very electronegative fluorine atom and the resulting $\sigma^*_{\mathrm{X-X}}$ LUMO of the $F_2$ molecule are at relatively low energy. This is the reason why, in the reaction of Pd + $F_2$, we encounter a low-energy triplet PES. This corresponds to a single-electron transfer mechanism in which an electron has been transferred from Pd to the very low-energy $\sigma^*_{\mathrm{F-F}}$ LUMO of $F_2$.

## 9.4 Conclusions

The oxidative addition of both hydrogen halides (HX) and dihalogens ($X_2$) to palladium is exothermic and goes via a negative overall barrier, except for the oxidative addition of hydrogen fluoride which is approximately thermoneutral and associated with a positive overall barrier. The activation barriers of Pd + HX decrease systematically as X descends in group 17 of the Periodic Table; those of Pd + $X_2$ increase at first, from X = F to Cl, but then also decrease systematically along X = Cl, Br, I and At.

An important factor that contributes to the above trends is the strength of the H–X and X–X bonds that are broken in the process of oxidative addition: the H–X bond strength monotonically decreases along X = F, Cl, Br, I and At, whereas the X–X bond strength first increases, from X = F to Cl, and thereafter also decreases along X = Cl, Br, I and At. On the other hand, HX and $X_2$ show consistently opposite trends for the reaction energy: that of HX becomes *more* exothermic and that of $X_2$ *less* exothermic as X descends in group 17. The latter is ascribed to the weakening of the Pd-substrate interaction along this series which, for Pd + $X_2$, is strong enough to reverse the trend of decreasing X–X bond strength.

Relativistic effects reduce activation barriers and make all reactions more exothermic. This is the result of a relativistic strengthening of the Pd-substrate interaction. Interestingly, the influence of relativistic effects on activation barriers and reaction energies decreases for the heavier halogens due to counteracting relativistic effects in palladium and the halogens.

# 10 Catalytic carbon-halogen bond activation. Trends in reactivity, selectivity and solvation

Adapted from
G. Th. de Jong, F. M. Bickelhaupt *J. Chem. Theory Comput.* **2007**, *3*, in press

## Abstract

We have theoretically studied the oxidative addition of all halomethanes $CH_3X$ (with X = F, Cl, Br, I, At) to Pd and $PdCl^-$, using both nonrelativistic and ZORA-relativistic density functional theory at BLYP/QZ4P. Our study covers the gas phase as well as the condensed phase (water), where solvent effects are described with the Conductor-like Screening Model (COSMO). The activation of the C*–X bond may proceed via two stereochemically different pathways: (i) direct oxidative insertion (OxIn) which goes with *retention* of the configuration at C*; and (ii) an alternative $S_N2$ pathway which goes with *inversion* of the configuration at C*. In the gas phase, for Pd, the OxIn pathway has the lowest reaction barrier for all $CH_3X$. Anion assistance, that is, going from Pd to $PdCl^-$, changes the preference for all $CH_3X$ from OxIn to the $S_N2$ pathway. Gas-phase reaction barriers for both pathways to C–X activation generally decrease as X descends in group 17. Two striking solvent effects are (i) the shift in reactivity of Pd + $CH_3X$ from OxIn to $S_N2$ in the case of the smaller halogens, F and Cl, and (ii) the shift in reactivity of $PdCl^-$ + $CH_3X$ in the opposite direction, that is, from $S_N2$ to OxIn, in the case of the *heavier* halogens, I and At. We use the Activation Strain model to arrive at a qualitative understanding of how the competition between OxIn and $S_N2$ pathways is determined by the halogen atom in the activated C–X bond, by anion assistance, and by solvation.

## 10.1 Introduction

Oxidative addition and reductive elimination are ubiquitous as elementary reaction steps in homogeneous catalysis[117-120] and have been intensively investigated both experimentally[32-35,120-122] and theoretically.[33,35,42,43,67,108,122,123] A well-known class of processes involving oxidative addition is catalytic C–X bond activation.[31,117,118,124,125] The catalytically active species in these reactions are generally coordination complexes of palladium or other transition metals. This process is an efficient tool for selectively converting simple educts, via C–C bond formation, into more complex compounds and is therefore of major importance for synthetic chemistry. The most intensively used substrates for such C–C coupling reactions are aryl halides, whereas it is more difficult in this context to exploit alkyl halides.[115]

In the oxidative addition process, the metal increases its formal oxidation state by two units. There has been controversy about the mechanism of this reaction, notably concerning the C–Cl bond.[105] One mechanism that has been proposed requires the concerted transfer of two electrons and involves either a concerted front-side displacement or a concerted nucleophilic displacement ($S_N2$) proceeding via backside attack of the C–Cl bond by the metal. Theoretical studies on the oxidative addition of the C–Cl bond in chloromethane to the Pd atom in the gas phase show that this process can indeed proceed via direct oxidative insertion of the metal into the C–Cl bond (OxIn) or via $S_N2$ substitution followed, in a concerted manner, by leaving-group rearrangement ($S_N2$-ra).[20,24,116] The reaction barrier for OxIn is lower than that for the $S_N2$ pathway. Interestingly, anion assistance, for example, coordination of a chloride anion to Pd, reverses this order in activation energies and makes $S_N2$ the preferred pathway. Note that this shift in mechanism also corresponds to a change in stereochemistry at the carbon atom involved, namely, from retention (OxIn) to inversion of configuration ($S_N2$). The two pathways are schematically summarized in Scheme 10.1.

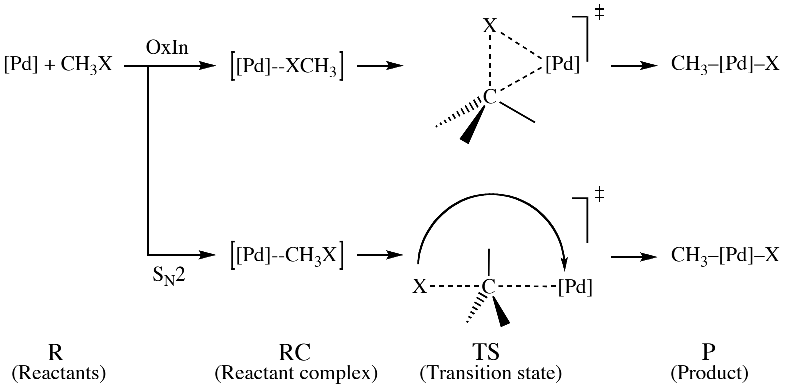

**Scheme 10.1** Model reactions and nomenclature

In the present study, we aim at obtaining insight into the trends in reactivity of palladium and all possible carbon-halogen bonds, that is, C–X, with X = F, Cl, Br, I, and At. Along this series of halogens, we are particularly interested in the preference for one of the two pathways, OxIn or $S_N2$, and how this preference is affected by three different aspects, namely, (i) anion assistance, i.e., using $PdCl^-$ instead of Pd, (ii) relativistic effects, and (iii) solvent effects, in particular, changing from the gas phase to an aqueous solution. To this end, we have calculated a set of consistent potential energy surfaces (PESs), using both nonrelativistic and relativistic density functional theory (DFT) and, for the solvent effects, using a continuum solvation model, which enables us to infer accurate trends in reactivity for these simple, archetypal oxidative addition reactions.

The differences in reactivity are analyzed and interpreted in terms of the Activation Strain model (see Chapter 2). In this model, activation energies $\Delta E^{\neq}$ are decomposed into the activation strain $\Delta E^{\neq}_{\text{strain}}$ and the transition state (TS) interaction $\Delta E^{\neq}_{\text{int}}$. The activation strain $\Delta E^{\neq}_{\text{strain}}$ depends on the strength of the activated bond and on the extent to which a particular metal expands the bond in the activated complex. The TS interaction $\Delta E^{\neq}_{\text{int}}$ is directly determined by the bonding capabilities and of the reactants. As will emerge from our analyses, much of the trends in reaction characteristics can be traced to the different strengths of the carbon-halogen bonds and the energy levels of the highest occupied and lowest unoccupied molecular orbitals in the substrates.

## 10.2 Methods

### 10.2.1 DFT calculations

All DFT[6-9] calculations have been done with the ADF program.[49,50,133] Calculations were done either nonrelativistically or with scalar relativistic effects accounted for using ZORA.[19] For the dissociation energies of the C–X bonds, where spin-orbit coupling is expected to be important, also single-point calculations using double-group symmetry including spin-orbit effects were done. The BLYP[52,53] functional was used, in combination with the QZ4P basis set for all elements except H, for which the TZ2P basis set was used. The QZ4P basis set is a large uncontracted set of Slater-type orbitals (STOs) containing diffuse functions. It is of quadruple-$\zeta$ quality and has been augmented with several sets of polarization functions on each atom: two 3*d* and two 4*f* sets on F, three 3*d* and two 4*f* sets on Cl, two 4*d* and three 4*f* sets on Br, one 5*d* and three 4*f* sets on I, one 6*d* and two 5*f* sets on At, two 3*d* and two 4*f* sets on C, and two 5*p* and two 4*f* sets on Pd. The TZ2P basis set, only used for H, is of triple-$\zeta$ quality and has been augmented with two sets of polarization functions: 2*p* and 3*d* in the case of H. An auxiliary set of *s*, *p*, *d*, *f* and *g* STOs was used to fit the molecular density and to represent the Coulomb and exchange potentials accurately in each SCF cycle.[49] All electrons were treated variationally (i.e., no frozen-core approximation). The electronic structures of Pd, $PdCl^-$ and $CH_3X$ were analyzed in terms of the molecular orbital model contained in Kohn-Sham DFT.[132] In Chapters 4 to 7, it has been shown that our approach is in good agreement with high-level *ab initio* calculations for our model reactions.

Equilibrium and transition state geometries were fully optimized using analytical gradient techniques. All structures were verified by frequency calculations.

Solvent effects in water have been estimated using the Conductor-like Screening Model (COSMO),[26] as implemented in the ADF program.[138] The same parameters were used as described in ref. 139. This implies using a solvent-excluding surface with an effective radius for water of 1.9 Å, derived from the macroscopic density and molecular mass, and a relative dielectric constant of 78.4. The empirical parameter in the scaling function in the COSMO equation was chosen to be 0.0. MM3 radii were used,[140] divided by 1.2, giving 1.350 Å for H, 1.700 Å for C, 1.425 Å for F, 1.725 Å for Cl, 1.850 Å for Br, 1.967 Å for I, 2.092 Å for At, and 1.975 Å for Pd. Using these radii gave differences of less than 3 kcal/mol between computed and experimental hydration energies of, for example, the chloride anion, tetramethylammonium cation and tert-butyl cation.[141] Furthermore, the above computational settings were tested on the complexation energy of $F^-$ and $C_2H_5F$. At ZORA-BLYP/QZ4P, this is –19.0 kcal/mol in the gas phase and a much smaller –0.2 kcal/mol when solvent effects in water are included by COSMO. This is in complete agreement with previous observations.[142]

### 10.2.2 Activation Strain analyses

To gain insight into how the use of different inserting metal complexes and different substrates affects the activation barriers, the reactions were analyzed using the Activation Strain model (see Chapter 2). In this model, the activation energy $\Delta E^{\neq}$ is decomposed into the activation strain $\Delta E^{\neq}_{\text{strain}}$ and the TS interaction $\Delta E^{\neq}_{\text{int}}$:

$$\Delta E^{\neq} = \Delta E^{\neq}_{\text{strain}} + \Delta E^{\neq}_{\text{int}} \tag{10.1}$$

$\Delta E^{\neq}_{\text{strain}}$ is the strain energy associated with deforming the reactants from their equilibrium geometry to the geometry they acquire in the activated complex. $\Delta E^{\neq}_{\text{int}}$ is the interaction energy between the deformed reactants in TS. In the present study, one of the reactants is either Pd or $PdCl^-$, and the other reactant is one of the substrates $CH_3X$.

### 10.2.3 *Ab initio* calculations

On the basis of the ZORA-BLYP/QZ4P optimized geometries, *ab initio* dissociation energies of the $CH_3$–X bonds were calculated at the CCSD(T) level[59,60,98] with the program package DIRAC.[55,99] An all-electron four-component Dirac-Coulomb approach was used, which allowed nonrelativistic calculations with the Lévy-Leblond approximation,[18] relativistic calculations without spin-orbit coupling using a spinfree Dirac-Coulomb Hamiltonian,[17] and relativistic calculations using the unmodified Dirac-Coulomb Hamiltonian, which includes spin-orbit coupling (DC–CCSD(T)). The two-electron integrals exclusively over the small components have been neglected and corrected with a reliable simple Coulombic correction.[16] The basis sets used for H, C, F and Cl were Dunning's correlation consistent augmented triple-$\zeta$ (aug-cc-pVTZ) basis sets,[63] and for Br, I, and At Dyall's relativistically optimized triple-$\zeta$ basis sets.[134]

## 10.3 Results and discussion

### 10.3.1 Reaction profiles and geometries

In this section, we discuss the fully relativistic PESs in the gas phase of the various oxidative addition reactions as well as the geometries of the stationary points, that is, all computed at ZORA-BLYP/QZ4P. In the next section, we examine how relativity has affected the trends in reactivity. Thereafter, we examine how solvent effects affect these trends. Finally, we analyze these trends in the framework of the Activation Strain model. Structural results are summarized in Figure 10.1 and Tables 10.1 (relativistically in gas phase) and 10.2 (relativistically in water), and results about reaction profiles in Table 10.3 and in Figures 10.2 and 10.3. Nonrelativistic structural results, energies with ZPE correction and enthalpies at 298.15 K of all stationary points at all levels of theory, and Cartesian coordinates of all species occurring in this study can be found in the supporting information of ref. 143. The reactions of Pd + $CH_3F$ and Pd + $CH_3Cl$ have

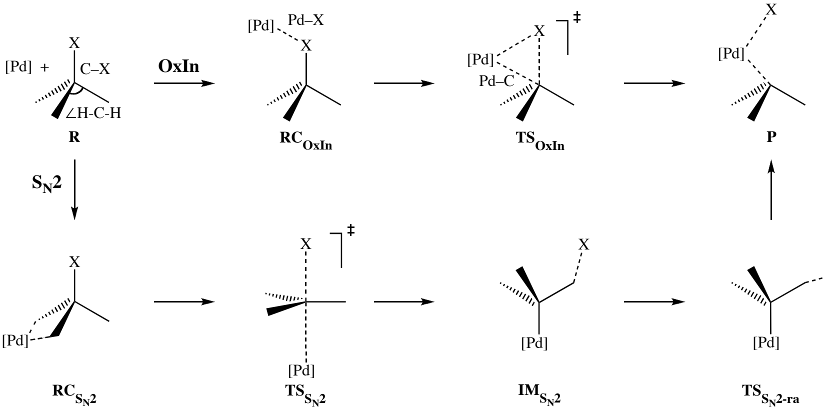

**Figure 10.1** Structures of stationary points along the reaction coordinates of the OxIn and $S_N2$-type pathways for oxidative addition of the $CH_3$–X bond to [Pd], with [Pd] = Pd and $PdCl^-$, and X = F, Cl, Br, I, and At

**Table 10.1** Geometry parameters[a] (in Å, degrees) of stationary points along the reaction coordinates of the OxIn and $S_N2$-type pathways of Pd and $PdCl^-$ addition to the halomethane C–X bond, with X = F, Cl, Br, I, and At, computed relativistically in the gas phase[b]

| | | Pd | | | | | $PdCl^-$ | | | | |
|---|---|---|---|---|---|---|---|---|---|---|---|
| | | F | Cl | Br | I | At | F | Cl | Br | I | At |
| R | C–X | 1.413 | 1.818 | 1.986 | 2.189 | 2.295 | | | | | |
| | ∠H–C–H | 108.5 | 108.1 | 107.3 | 107.1 | 106.6 | | | | | |
| $RC_{OxIn}$ | C–X | 1.411$^c$ | 1.853 | 2.030 | 2.226 | 2.336 | 1.423 | 1.901 | 2.112 | 2.298 | 2.422 |
| | Pd–X | 3.301$^c$ | 2.324 | 2.425 | 2.529 | 2.616 | 2.429 | 2.277 | 2.390 | 2.515 | 2.611 |
| | Pd–C | 2.372$^c$ | 3.516 | 3.669 | 3.817 | 3.909 | 3.133 | 3.582 | 3.850 | 4.037 | 4.228 |
| | ∠H–C–H | 110.5$^c$ | 111.8 | 112.5 | 112.4 | 112.8 | 111.3 | 112.0 | 112.8 | 112.4 | 112.7 |
| $TS_{OxIn}$ | C–X | 1.786 | 2.046 | 2.194 | 2.379 | 2.477 | 1.733 | 2.152 | 2.327 | 2.491 | 2.587 |
| | Pd–X | 2.304 | 2.355 | 2.448 | 2.554 | 2.637 | 2.227 | 2.315 | 2.424 | 2.549 | 2.639 |
| | Pd–C | 2.111 | 2.506 | 2.643 | 2.730 | 2.807 | 2.462 | 2.790 | 2.902 | 2.916 | 2.978 |
| | ∠H–C–H | 111.1 | 112.6 | 113.2 | 112.9 | 113.3 | 113.8 | 114.4 | 114.8 | 114.2 | 114.3 |
| P | C–X | 2.944 | 3.209 | 3.319 | 3.465 | 3.539 | 2.892 | 3.244 | 3.337 | 3.502 | 3.580 |
| | Pd–X | 1.938 | 2.250 | 2.381 | 2.543 | 2.632 | 2.020 | 2.352 | 2.492 | 2.658 | 2.751 |
| | Pd–C | 1.997 | 2.001 | 2.002 | 2.005 | 2.006 | 2.016 | 2.025 | 2.026 | 2.030 | 2.030 |
| | ∠H–C–H | 112.5 | 112.4 | 112.3 | 112.1 | 112.0 | 111.9 | 111.9 | 111.9 | 111.9 | 111.8 |
| $RC_{S_N2}$ | C–X | 1.411 | 1.824 | 2.004 | 2.222 | 2.390 | 1.447 | 1.899 | d | d | d |
| | Pd–X | 3.301 | 3.768 | 3.970 | 4.253 | 4.567 | 3.352 | 3.799 | d | d | d |
| | Pd–C | 2.372 | 2.383 | 2.366 | 2.352 | 2.313 | 2.308 | 2.280 | d | d | d |
| | ∠H–C–H | 110.5 | 111.2 | 112.4 | 113.4 | 117.0 | 111.4 | 112.9 | d | d | d |
| $TS_{S_N2}$ | C–X | 1.851$^e$ | d | d | d | d | 2.359 | 2.009 | d | d | d |
| | Pd–X | 2.806$^e$ | d | d | d | d | 3.843 | 3.976 | d | d | d |
| | Pd–C | 1.926$^e$ | d | d | d | d | 1.963 | 2.214 | d | d | d |
| | ∠H–C–H | 114.7$^e$ | d | d | d | d | 112.2$^f$ | 117.6 | d | d | d |
| $IM_{S_N2}$ | C–X | 3.575$^e$ | d | d | d | d | 2.856$^e$ | 2.724 | 2.911 | 3.173 | 3.232 |
| | Pd–X | 3.166$^e$ | d | d | d | d | 3.457$^e$ | 4.546 | 4.755 | 5.044 | 5.113 |
| | Pd–C | 1.859$^e$ | d | d | d | d | 1.884$^e$ | 1.998 | 2.002 | 2.007 | 2.011 |
| | ∠H–C–H | 120.0$^e$ | d | d | d | d | 107.2$^e$ | 115.0 | 114.4 | 113.9 | 113.9 |
| $TS_{S_N2\text{-ra}}$ | C–X | 2.566 | 3.192 | 3.425 | 3.641 | 3.742 | 2.604 | 3.354 | 3.570 | 3.876 | 3.981 |
| | Pd–X | 2.508 | 4.022 | 4.329 | 4.342 | 4.506 | 3.262 | 4311 | 4.517 | 4.819 | 4.912 |
| | Pd–C | 2.019 | 2.018 | 2.020 | 2.007 | 2.009 | 1.969 | 1.997 | 2.001 | 2.005 | 2.007 |
| | ∠H–C–H | 117.2 | 114.1 | 113.8 | 111.5 | 111.3 | 113.5 | 112.9 | 112.8 | 112.7 | 112.6 |

[a] See Figure 10.1; for ∠H–C–H the average of the three possible ∠H–C–H is given.

[b] At ZORA-BLYP/QZ4P level of theory.

[c] Same as $RC_{S_N2}$.

[d] Stationary point does not exist.

[e] “Anomalous” $PdCH_2\cdots HF$ structure, see text.

[f] C in methyl group pointing towards Pd.

been investigated before in Chapters 6 and 7. It was shown there that our computational method gives results that are in good agreement with high-level *ab initio* benchmark calculations. In this chapter, we present a comprehensive overview of all reactions of Pd and $PdCl^-$ with $CH_3X$.

All reactions proceed from the reactants via two distinct pathways, either via direct oxidative insertion (OxIn) or via $S_N2$ substitution, to the product, see Figure 10.1. For the OxIn pathway, the reaction proceeds from the reactants R via the formation of a stable reactant complex $RC_{OxIn}$, in which the halogen atom coordinates to the palladium atom, to a transition state $TS_{OxIn}$ and, finally, a stable product P. There is one exception, namely, the addition of $CH_3F$ to Pd. Here, the reaction proceeds from the same reactant complex as the alternative $S_N2$ pathway, because the F–Pd coordination bond is too weak to produce a stable reactant complex (*vide infra*).

**Table 10.2** Geometry parameters[a] (in Å, degrees) of stationary points along the reaction coordinates of the OxIn and $S_N2$-type pathways of Pd and $PdCl^-$ addition to the halomethane C–X bond, with X = F, Cl, Br, I, and At, computed relativistically including solvent effects in water[b]

| | | Pd | | | | | $PdCl^-$ | | | | |
|---|---|---|---|---|---|---|---|---|---|---|---|
| | | F | Cl | Br | I | At | F | Cl | Br | I | At |
| R | C–X | 1.437 | 1.832 | 1.997 | 2.192 | 2.300 | | | | | |
| | ∠H–C–H | 107.7 | 107.4 | 106.7 | 106.7 | 106.3 | | | | | |
| $RC_{OxIn}$ | C–X | 1.436[c] | 1.862 | 2.032 | 2.218 | 2.326 | 1.455 | 1.863 | 2.035 | 2.223 | 2.332 |
| | Pd–X | 3.266[c] | 2.312 | 2.416 | 2.525 | 2.611 | 2.288 | 2.320 | 2.428 | 2.548 | 2.637 |
| | Pd–C | 2.333[c] | 3.513 | 3.658 | 3.798 | 3.874 | 3.302 | 3.535 | 3.703 | 3.864 | 3.944 |
| | ∠H–C–H | 111.2[c] | 112.3 | 112.9 | 112.6 | 113.0 | 112.0 | 112.2 | 112.8 | 112.5 | 112.9 |
| $TS_{OxIn}$ | C–X | 1.861 | 2.083 | 2.222 | 2.390 | 2.484 | 1.825 | 2.149 | 2.276 | 2.432 | 2.518 |
| | Pd–X | 2.592 | 2.327 | 2.430 | 2.544 | 2.626 | 2.157 | 2.327 | 2.442 | 2.570 | 2.656 |
| | Pd–C | 2.020 | 2.583 | 2.672 | 2.718 | 2.779 | 2.503 | 2.622 | 2.680 | 2.695 | 2.743 |
| | ∠H–C–H | 109.5 | 113.7 | 113.9 | 113.3 | 113.5 | 115.3 | 114.3 | 114.2 | 113.5 | 113.5 |
| P | C–X | 2.949 | 3.203 | 3.309 | 3.444 | 3.517 | 2.928 | 3.243 | 3.320 | 3.466 | 3.571 |
| | Pd–X | 2.009 | 2.291 | 2.413 | 2.562 | 2.648 | 2.054 | 2.355 | 2.485 | 2.635 | 2.714 |
| | Pd–C | 1.993 | 1.999 | 2.000 | 2.004 | 2.005 | 2.022 | 2.031 | 2.033 | 2.038 | 2.037 |
| | ∠H–C–H | 112.9 | 112.7 | 112.6 | 112.4 | 112.2 | 111.9 | 112.0 | 111.9 | 111.8 | 111.8 |
| $RC_{S_N2}$ | C–X | 1.436 | 1.842 | 2.022 | 2.227 | d | 1.440 | 1.845 | 2.023 | 2.221 | 2.425 |
| | Pd–X | 3.266 | 3.724 | 3.921 | 4.201 | d | 3.265 | 3.687 | 3.856 | 4.084 | 4.453 |
| | Pd–C | 2.333 | 2.343 | 2.326 | 2.323 | d | 2.332 | 2.335 | 2.319 | 2.323 | 2.247 |
| | ∠H–C–H | 111.2 | 111.8 | 113.0 | 113.7 | d | 111.2 | 111.6 | 112.6 | 112.7 | 118.4 |
| $TS_{S_N2}$ | C–X | 1.838 | 2.162 | 2.266 | 2.447 | d | 1.927 | 2.173 | 2.267 | 2.504 | 2.557 |
| | Pd–X | 4.004 | 4.270 | 4.360 | 4.554 | d | 3.758 | 4.078 | 4.198 | 4.418 | 4.488 |
| | Pd–C | 2.165 | 2.185 | 2.196 | 2.195 | d | 2.044 | 2.124 | 2.152 | 2.135 | 2.152 |
| | ∠H–C–H | 119.9 | 119.6 | 119.4 | 119.4 | d | 119.6[e] | 119.9 | 119.8 | 120.0 | 119.9 |
| $IM_{S_N2}$ | C–X | 2.381 | 2.879 | 2.926 | 3.032 | 3.038 | 3.275 | 5.187 | 4.318 | 3.999 | 3.805 |
| | Pd–X | 4.398 | 4.891 | 4.946 | 5.063 | 5.078 | 4.132 | 6.961 | 6.052 | 5.976 | 5.782 |
| | Pd–C | 2.017 | 2.012 | 2.021 | 2.031 | 2.040 | 2.001 | 1.999 | 2.000 | 2.003 | 2.009 |
| | ∠H–C–H | 116.4 | 115.7 | 115.9 | 116.0 | 116.3 | 113.1 | 112.8 | 112.7 | 112.8 | 112.9 |
| $TS_{S_N2\text{-}ra}$ | C–X | 2.931 | 3.841 | 3.990 | 4.139 | 4.142 | 3.241 | 4.088 | 4.299 | 4.543 | 4.628 |
| | Pd–X | 4.611 | 4.845 | 5.001 | 5.138 | 5.147 | 4.073 | 4.775 | 5.034 | 5.294 | 5.329 |
| | Pd–C | 1.991 | 1.987 | 1.989 | 1.993 | 1.998 | 2.000 | 2.001 | 2.001 | 2.001 | 2.001 |
| | ∠H–C–H | 114.3 | 114.7 | 114.6 | 114.3 | 114.0 | 113.1 | 112.8 | 112.8 | 112.7 | 112.7 |

a See Figure 10.1; for ∠H–C–H the average of the three possible ∠H–C–H is given.

b At ZORA-BLYP/QZ4P level of theory, including solvent effects in water by COSMO.

c Same as $RC_{S_N2}$.

d Stationary point does not exist.

e C in methyl group pointing towards Pd.

The $S_N2$ pathway to oxidative addition proceeds via two consecutive stages: first the actual nucleophilic substitution followed by a rearrangement of the expelled leaving group toward Pd. The exact nature of this pathway and the shape of the reaction profile depend on the particular model reaction, that is, on the halogen atom in the C–X bond and on whether the metal experiences anion assistance ($PdCl^-$) or not (Pd). For all neutral Pd + $CH_3X$ and for $PdCl^-$ + $CH_3F$ and $CH_3Cl$, the $S_N2$ reaction proceeds from the reactants via formation of a stable reactant complex, $RC_{S_N2}$, that differs from $RC_{OxIn}$. In the $S_N2$ reactant complex $RC_{S_N2}$, $CH_3X$ coordinates either via one hydrogen atom in an $\eta^1$ fashion or via two hydrogen atoms in an $\eta^2$ fashion to Pd (see Figure 10.1), completely analogous to the reactant complexes found previously for the reactions of Pd with methane (see Chapters 3 and 4) and ethane (see Chapter 5). The distinction between coordination to one or two hydrogen atoms is not important from an energetical point of view. Thus, enforcing $\eta^2$ coordination in the case of an $\eta^1$ equilibrium structure (and *vice versa*) leads to a destabilization of not more than a few tenths of a kcal/mol. From $RC_{S_N2}$, the $S_N2$ substitution can then proceed via transition state $TS_{S_N2}$ to intermediate $IM_{S_N2}$ in which the C–X bond is broken. However, for the anion-assisted reactions of $PdCl^-$ + $CH_3Br$, $CH_3I$ and $CH_3At$, the intermediate $IM_{S_N2}$ is rather stable, and it is formed spontaneously, that is, via a barrierless substitution process lacking both a stable encounter complex $RC_{S_N2}$ and a transition state $TS_{S_N2}$.

On the other hand, for the reactions of Pd + $CH_3Cl$, $CH_3Br$, $CH_3I$ and $CH_3At$, the expulsion of the leaving group goes with (energetically highly unfavourable) charge separation. This causes the intermediate structure $IM_{S_N2}$, i.e., $PdCH_3^+{\cdots}X^-$, to become labile (i.e., it is no longer a local minimum) with respect to spontaneous back reaction $RC_{S_N2}$. Consequently, the first and only transition state encountered along the $S_N2$ pathway of Pd + $CH_3Cl$, $CH_3Br$, $CH_3I$ and $CH_3At$ is $TS_{S_N2\text{-ra}}$ which is associated with the rearrangement of the $X^-$ leaving group from carbon to palladium yielding the product P.

There are some marked differences between the $S_N2$ pathways for addition of $CH_3F$ compared to the other substrates (for a detailed discussion, see Chapter 6). In the first place, the C–F bond is much stronger than the other C–X bonds (*vide infra*) and activation of the former is associated with significantly higher barriers (via both OxIn and $S_N2$). Thus, at variance with the other substrates, the minimum energy path for Pd approaching $CH_3F$ from the backside is, in a sense, redirected from straight nucleophilic substitution and proceeds instead via a relatively low-energy transition state for insertion into a C–H bond (not shown here). Furthermore, the much higher basicity of $F^-$ compared to the other $X^-$ causes the former, after its expulsion in the actual $S_N2$ transition state $TS_{S_N2}$ and on its way toward Pd or $PdCl^-$, to abstract a proton from the methyl moiety, under formation of an "anomalous" structure $PdCH_2{\cdots}HF$ or $[PdCl]CH_2^-{\cdots}HF$ for the intermediate complex $IM_{S_N2}$ (i.e., *not* $PdCH_3^+{\cdots}F^-$ or $[PdCl]CH_3{\cdots}X^-$). From this intermediate, fluoride migrates via the normal transition state $TS_{S_N2\text{-ra}}$ toward Pd or $PdCl^-$ under formation of the product $CH_3PdF$ or $CH_3[PdCl]F^-$.

Regarding the energetics of the reaction, the following trends can be observed. Along X = F, Cl, Br, I, and At, the reactant complex $RC_{OxIn}$ becomes increasingly stable, from –13.3 kcal/mol for Pd + $CH_3Cl$ to –26.2 kcal/mol for Pd + $CH_3At$ and from –2.4 kcal/mol for $PdCl^-$ + $CH_3F$ to –27.7 kcal/mol for $PdCl^-$ + $CH_3At$, see Table 10.3 and Figure 10.2, upper diagrams. In contrast, the relative energy of the reactant complex for the $S_N2$ pathway, $RC_{S_N2}$, does not change much when the halogen in the substrate is changed. This is clearly seen from Figure 10.2, middle diagrams. In all cases the reactant complexes for addition to $PdCl^-$ are more stable than for addition to Pd.

All reaction barriers become lower along X = F, Cl, Br, I, and At. For example, the relative energy of $TS_{OxIn}$ changes from 17.2 for Pd + $CH_3F$ to –13.3 kcal/mol for Pd +

$CH_3At$. The relative ordering of barriers for the two pathways does not change along X: for addition to Pd, the relative energy of $TS_{OxIn}$ lies below the relative energy of $TS_{S_N2\text{-ra}}$ with a difference of, for example, 12.4 kcal/mol in case of $CH_3F$ and 19.1 kcal/mol in case of $CH_3At$. In contrast, for addition to $PdCl^-$ for all $CH_3X$, the relative energy of $TS_{S_N2\text{-ra}}$ lies below the relative energy of $TS_{OxIn}$ with a difference of, for example, 11.9 kcal/mol in case of $CH_3F$ and 10.2 kcal/mol in case of $CH_3At$, see Table 10.3 and Figure 10.3, middle diagrams. This change of selectivity, from OxIn as the preferred pathway for addition to Pd, to $S_N2$ as the preferred pathway for addition to $PdCl^-$ has been observed before for addition of $CH_3Cl$ and can be well understood within the Activation Strain model by the stronger, more stabilizing TS interaction $\Delta E^{\neq}_{int}$ in case of $PdCl^-$, caused by the raise of Pd-4*d*-derived orbitals in $PdCl^-$, which translates into more

**Table 10.3** Energies (in kcal/mol) relative to reactants of stationary points along the reaction coordinates of the OxIn and $S_N2$-type pathways of Pd and $PdCl^-$ addition to the halomethane C–X bond, with X = F to At[a]

| | | $RC_{OxIn}$ | $TS_{OxIn}$ | P | $RC_{S_N2}$ | $TS_{S_N2}$ | $IM_{S_N2}$ | $TS_{S_N2\text{-ra}}$ |
|---|---|---|---|---|---|---|---|---|
| *Nonrelativistic in gas phase* | | | | | | | | |
| Pd | F | –3.0[b] | 23.2 | –1.0 | –3.0 | 39.6 | 31.5[c] | 38.8 |
| | Cl | –7.8 | 5.4 | –17.5 | –2.7 | d | d | 31.4 |
| | Br | –10.3 | 0.1 | –22.0 | –2.8 | d | d | 25.5 |
| | I | –16.1 | –6.3 | –25.7 | –3.0 | d | d | 23.7 |
| | At | –18.4 | –8.9 | –27.4 | –3.3 | d | d | 20.4 |
| $PdCl^-$ | F | –12.9[b] | 13.1 | –29.4 | –12.9 | 5.8 | 4.0 | 5.1 |
| | Cl | –13.0 | –3.3 | –45.1 | –14.4 | –12.9 | –14.9 | –11.9 |
| | Br | –16.7 | –8.4 | –48.7 | d | d | –20.6 | –17.2 |
| | I | –23.8 | –14.9 | –51.1 | d | d | –24.2 | –20.8 |
| | At | –26.2 | –17.5 | –51.9 | d | d | –25.8 | –22.2 |
| *Relativistic in gas phase* | | | | | | | | |
| Pd | F | –5.6[b] | 17.2 | –16.7 | –5.6 | 25.5 | 10.9[c] | 29.6 |
| | Cl | –13.3 | –0.8 | –33.4 | –5.3 | d | d | 22.9 |
| | Br | –16.2 | –5.7 | –37.7 | –5.7 | d | d | 16.6 |
| | I | –22.4 | –12.2 | –41.5 | –6.2 | d | d | 9.9 |
| | At | –22.6 | –13.3 | –42.7 | –7.2 | d | d | 5.8 |
| $PdCl^-$ | F | –2.4 | 9.7 | –39.4 | –16.0 | –1.8 | –8.3 | –2.2 |
| | Cl | –17.6 | –6.9 | –54.7 | –17.7 | –17.2 | –21.2 | –18.3 |
| | Br | –21.1 | –11.6 | –57.8 | d | d | –26.7 | –23.4 |
| | I | –27.5 | –17.2 | –59.9 | d | d | –30.6 | –27.0 |
| | At | –27.7 | –17.9 | –59.5 | d | d | –32.2 | –28.1 |
| *Relativistic in water* | | | | | | | | |
| Pd | F | –7.6[b] | 10.5 | –27.5 | –7.6 | 3.6 | 1.5 | 3.7 |
| | Cl | –15.7 | –2.9 | –40.4 | –7.3 | –3.1 | –8.2 | –4.5 |
| | Br | –18.7 | –7.7 | –43.4 | –7.8 | –6.2 | –10.7 | –5.7 |
| | I | –25.4 | –14.4 | –45.7 | –8.2 | –7.5 | –10.9 | –3.6 |
| | At | –25.8 | –15.6 | –46.3 | d | d | –12.1 | –3.2 |
| $PdCl^-$ | F | –7.2 | 11.0 | –37.4 | –11.4 | –1.3 | –10.9 | –10.4 |
| | Cl | –19.1 | –3.5 | –45.9 | –10.8 | –7.0 | –20.4 | –18.8 |
| | Br | –21.1 | –7.3 | –47.0 | –11.2 | –9.0 | –20.9 | –19.6 |
| | I | –26.0 | –12.3 | –46.1 | –10.9 | –10.4 | –18.3 | –16.5 |
| | At | –25.7 | –12.5 | –45.6 | –11.4 | –11.3 | –17.6 | –15.6 |

a Nonrelativistic in gas phase: computed fully nonrelativistically at BLYP/QZ4P. Relativistic in gas phase: computed fully relativistically at ZORA-BLYP/QZ4P. Relativistic in water: computed fully relativistically at ZORA-BLYP/QZ4P including solvent effects in water by COSMO.

b Same as $RC_{S_N2}$.

c "Anomalous" $PdCH_2{\cdots}HF$ structure, see text.

d Stationary point does not exist.

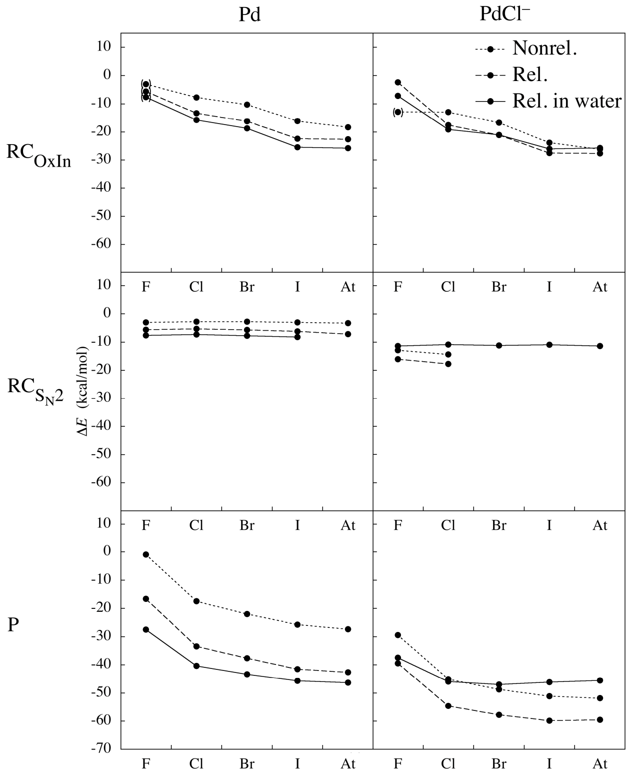

**Figure 10.2** Relative energies of the reactant complexes and the product for the OxIn and $S_N2$-type pathways for Pd and $PdCl^-$ addition to the halomethane C–X bond, with X = F, Cl, Br, I, and At. Dotted lines: calculated nonrelativistically in gas phase; dashed lines: relativistically in gas phase; solid lines: relativistically in water

stabilizing donor-acceptor orbital interactions with the substrate. See for a discussion ref. 24. It is interesting to note that this same effect extends over all $CH_3X$ additions.

The exothermicity of the reaction becomes larger along X = F, Cl, Br, I, and At, although there is a certain saturation for the largest halogens. The reaction energy changes for addition to Pd, for example, from –16.7 kcal/mol for $CH_3F$ to –33.4 kcal/mol for $CH_3Cl$ to –37.7 kcal/mol for $CH_3Br$ to –41.5 kcal/mol for $CH_3I$ to –42.7 kcal/mol for $CH_3At$. The addition to $PdCl^-$ is in all cases more exothermic than that to Pd.

In the next sections, the effects of relativity and of changing the environment from the gas phase to water on these trends will be investigated. In the last section, an analysis of the trends in reactivity will be given.

### 10.3.2 Relativistic effects

The use of a relativistic treatment is significant, but it does not change the relative order of reactivity of $CH_3X$ oxidative addition to Pd and $PdCl^-$ along the series of halogens. The effects of relativity can be revealed by comparing the fully relativistic PESs discussed above with the corresponding fully nonrelativistic PESs derived from nonrelativistic energies and nonrelativistic geometries of stationary points. Here, we discuss the relative electronic energy PESs summarized in Table 10.3 and Figures 10.2 and 10.3. Note, however, that the PESs including ZPE corrections and those based on relative enthalpies give rise to the same trends (see supporting information of ref. 143).

Relativity stabilizes the PES of all $CH_3X$ oxidative addition reactions to Pd and $PdCl^-$, as illustrated by Figure 10.2 (compare dotted and dashed lines) and Figure 10.3 (compare upper and middle diagrams). Reaction barriers are stabilized by up to 14.6 kcal/mol (for $TS_{S_N2\text{-ra}}$ in case of $CH_3At$ addition to Pd), and reactions become more exothermic by up to 16 kcal/mol (for Pd + $CH_3Cl$; see Table 10.3). The effect increases in most cases as one proceeds along the reaction coordinate (see Figure 10.2; compare the difference between the dotted and the dashed lines for both the reactant complexes and the product). Thus, in the case of Pd + $CH_3Cl$, for example, the $RC_{OxIn}$, $TS_{OxIn}$, and P are relativistically stabilized by –5.5, –6.2, and –15.9 kcal/mol (compare relativistic with nonrelativistic data in Table 10.3). One seemingly exceptional case is $RC_{OxIn}$ for $CH_3F$ addition to $PdCl^-$, which seems to become more stable when relativity is turned off, see Figure 10.2, upper left diagram. But, in fact, the nonrelativistic $RC_{OxIn}$ is very unstable, such that it does not even exist and changes into the more stable $RC_{S_N2}$. One might expect relativistic effects to be more pronounced for the reactions involving the heavier halogens. This expectation is born out of the observation that relativistic effects on the $CH_3$–X bond strengths increase substantially along X = F, Cl, Br, I, and At (*vide infra*). Interestingly, however, the relativistic stabilization of the stationary points becomes overall smaller, not stronger, along this series in X, with only two exceptions, namely, $RC_{S_N2}$ and $TS_{S_N2\text{-ra}}$, for addition to Pd (see Table 10.3).

The relativistic effects originating from the halogen atoms obviously counteract and partially cancel those originating from Pd. Closer inspection of the influence of relativity on the orbital energy levels shows what causes this is. The only observable effect in the valence and subvalence orbitals, both on Pd as on the larger halogens, is the relativistic stabilization of the *s* orbitals. In the case of Pd, the stabilization of the empty 5*s* orbital (from –3.0 eV to –3.4 eV) increases its electron-accepting ability. This enhances the Pd-substrate interaction and is thus responsible for the relativistic stabilization of the stationary points. In the case of the halogens, the increasing stabilization of the filled valence *s* orbital along the series of halogens (e.g., for F from –30.4 to –30.5 eV, for Br from –19.7 to –20.4 eV, and for At from –15.1 to –19.4 eV; not shown in diagrams or tables) causes the electron-donating ability to decrease. Thus, the relativistic effects stemming from the halogen atoms have a weakening effect on the Pd-substrate interaction, which counteracts the stabilizing relativistic effect originating from Pd.

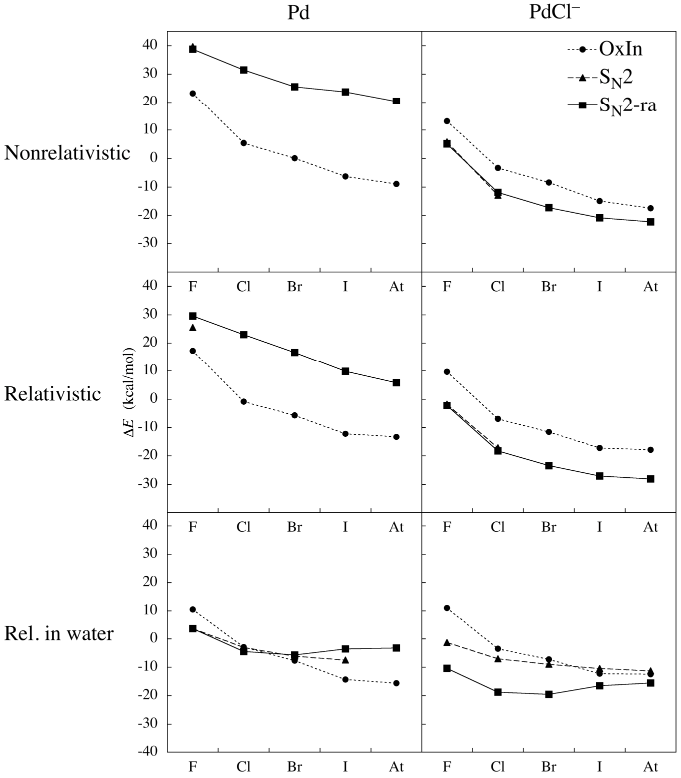

**Figure 10.3** Reaction barriers relative to reactants of the OxIn and $S_N2$-type pathways for Pd and $PdCl^-$ addition to the halomethane C–X bond, with X = F, Cl, Br, I, and At, calculated at different levels of theory

Relativity also affects the geometries of all species involved in the oxidative addition reactions. The most striking and general effect is a shortening of the Pd–X bond distance. In Chapter 9, on the oxidative addition of HX and $X_2$ to Pd, it was shown that geometry-relaxation processes caused by relativity are typically in the order of one kcal/mol or less and, thus, hardly affect the PES along the reaction coordinate. The relativistic stabilization of stationary points along the reaction coordinate can be really directly attributed to the strengthening of the Pd-substrate interaction mentioned above.

### 10.3.3 Solvent effects

Solvent effects, at variance with relativistic effects, profoundly affect and qualitatively modify the characteristics of the reactions, in certain instances to the extent that they change the preference from one to another pathway (see Table 10.3). Solvent effects are also markedly different for the neutral (Pd + $CH_3X$) as compared to the anion-assisted reactions ($PdCl^-$ + $CH_3X$). In the former, solvation stabilizes all stationary points along the reaction coordinate relative to the reactants. Thus, in water, the reactant complexes of Pd + $CH_3X$ become more strongly bound, activation barriers are reduced, and the reaction becomes more exothermic. This becomes clear, for example, by comparing solid lines (water) with dashed lines (gas phase) in Figure 10.2. The stabilization relative to reactants that is caused by solvation can be easily understood from electrostatic arguments. The interaction of neutral Pd with neutral $CH_3X$ induces a charge separation $Pd^{\delta+}\cdots CH_3X^{\delta-}$ which is stabilized by the concomitant polarization of the solvent medium. Likewise, the ionic intermediate structure $PdCH_3^{+}\cdots X^{-}$ ($IM_{S_N2}$), which is labile in the gas phase (or, in the case of Pd + $CH_3F$, exists as $PdCH_2\cdots HX$), is particularly stabilized and reappears as a stable intermediate in water (see Table 10.3).

On the other hand, solvation of the anion-assisted reactions ($PdCl^{-}$ + $CH_3X$) leads in many (but not all) cases to a *destabilization* of stationary points (see Table 10.3 and Figures 10.2 and 10.3). The reason is mainly the strong stabilization of the reactant $PdCl^{-}$ in which the excess negative charge is highly localized, leading to a strongly stabilizing electrostatic and orbital interaction with the solvent.[142] In the other stationary points (i.e., RC, TS, etc.), the negative charge is delocalized, because of the $PdCl^{-}$-substrate interaction, over a larger area, leading to a less favourable electrostatic and orbital interaction. Note however that the $RC_{S_N2}$ structure $PdCl^{-}\cdots CH_3X$, which is labile and thus absent in the gas phase, is stabilized more than $TS_{S_N2}$ and reappears as a stable species in water (see Table 10.3 and Figure 10.3). For $RC_{S_N2}$ and P, the relative energy clearly becomes less negative. For example, in the case of $PdCl^{-}$ + $CH_3Cl$, it changes from –17.7 to –10.8 kcal/mol and from –54.7 to –45.9 kcal/mol, respectively (see Table 10.3 and Figure 10.2). For $RC_{OxIn}$, the effect is somewhat less clear-cut. What is clear, however, is the absence of a pronounced and general stabilization of transition states, at variance with the neutral Pd + $CH_3X$ reactions (see Figure 10.3).

The most striking phenomenon associated with solvation is, however, the change in preference from one to another pathway. Interestingly, the occurrence of this solvation-induced change in reaction mechanism depends on which C–X bond is activated and also on whether anion assistance is present ($PdCl^{-}$) or not (Pd). The neutral reactions of Pd + $CH_3X$ shift because of solvation from OxIn (preferred in the gas phase) to $S_N2$, but this shift occurs only for the smaller halogens, F and Cl (see Figure 10.3). On the other hand, the anion-assisted reactions of $PdCl^{-}$ + $CH_3X$ shift from $S_N2$ (preferred in the gas phase) to OxIn, but this time, the shift happens only for the heavier halogens, I and At (see Figure 10.3). For example, for Pd + $CH_3F$, the barrier for the OxIn pathway is lowered by solvation from 17.2 to 10.5 kcal/mol, but the barrier for the $S_N2$ pathway is lowered much more, from 29.6 to 3.7 kcal/mol (see Table 10.3). On the other hand, for Pd + $CH_3At$, the barrier for the OxIn pathway is lowered by solvation from –13.3 to –15.6 kcal/mol, and the barrier for the $S_N2$ pathway is lowered more, from 5.8 to –3.2 kcal/mol, but not nearly enough to make the $S_N2$ pathway the preferred pathway (see

Table 10.3). For comparison, the $S_N2$ barrier of $PdCl^-$ + $CH_3At$, which is absent in the gas phase, is in water about one kcal/mol higher than the corresponding OxIn barrier (see Table 10.3 and Figure 10.3). Furthermore, the $S_N2$-ra barrier of $PdCl^-$ + $CH_3At$ in water is only slightly, that is, 3 kcal/mol lower than the OxIn barrier, whereas it is more than 10 kcal/mol lower than the OxIn barrier in the gas phase.

Solvation apparently stabilizes the $S_N2$ transition states of the lighter C–X bonds significantly more efficiently than the corresponding OxIn transition states but also more than the $S_N2$ transition states of the heavier C–X bonds (see Table 10.3 and Figure 10.3). Note that this biased solvation stabilization even breaks the intrinsic (i.e., gas-phase) trend of continuously decreasing $S_N2$-ra reactions barriers along the halogens: thus, in water, the $S_N2$-ra barrier still decreases from F to Cl to Br, but thereafter, it increases from Br to I to At (see Figure 10.3).

### 10.3.4 Activation Strain analysis of gas-phase reactivity

In the following, we aim at understanding the origin of the above trends in reactivity, that is, we wish to understand how the feasibility of reaction mechanisms is exactly determined by the nature of the C–X bond, anion assistance and solvent effects. We do this using the Activation Strain model, which, as pointed out earlier, is a fragment approach to understanding activation barriers in terms of properties of the reactants, here, the catalyst [Pd] and the substrate $CH_3X$. Thus, the activation energy $\Delta E^{\neq}$ is decomposed into the activation strain $\Delta E^{\neq}_{\text{strain}}$ associated with deforming the reactants from their equilibrium structures to the geometries they adopt in the TS plus the TS interaction $\Delta E^{\neq}_{\text{int}}$, that is, the interaction between the deformed reactants (see Eq. 10.1; see also Chapter 2).

First, we explore and analyze the metal-substrate bonding in the reactant complexes and the C–X bond strength in the halomethane substrates. This facilitates interpreting the Activation Strain analyses of activation barriers $\Delta E^{\neq}$, as the latter are the result of an interplay between these two quantities which appear as the metal-substrate TS interaction $\Delta E^{\neq}_{\text{int}}$ and the activation strain $\Delta E^{\neq}_{\text{strain}}$ that mainly stems from C–X bond elongation. The metal-substrate interaction between the reactants is provided, among others, by the donor-acceptor orbital interactions between the Pd-4*d* orbitals (or the Pd-4*d*-derived orbitals in $PdCl^-$) and the substrate $\sigma^*_{\text{C–X}}$ LUMO. These orbital interactions are strengthened by relativistic effects because, as is well-known, the latter destabilize the Pd-4*d* orbitals, leading to a smaller, more favourable HOMO-LUMO gap between Pd and the substrate (the effect is further reinforced by relativistic stabilization of the Pd-5*s* acceptor orbital).[22] The relativistic strengthening of the metal-substrate interaction in the reactant complexes can be clearly recognized in Figure 10.2, in which nonrelativistic and relativistic gas-phase energies are connected by dotted and dashed lines, respectively.

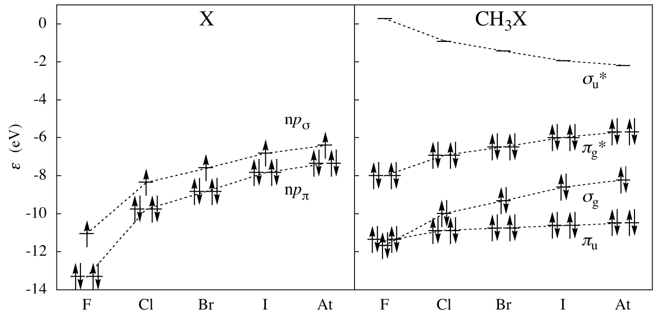

**Figure 10.4** Orbital energies of the frontier orbitals of X and $CH_3X$, with X = F to At, at ZORA-BLYP/QZ4P

The trend of increasing metal-substrate interaction in $RC_{OxIn}$ along X = F to At (Figure 10.2) can be easily understood on the basis of how the electronic structure of the substrate $CH_3X$ depends on the halogen X (Figure 10.4). The frontier orbitals of $CH_3X$ are the degenerate $\pi_g*$ lone-pair HOMOs, which are mainly the halogen $np_\pi$ AOs, and the $\sigma*_{C–X}$ LUMO, which is mainly the C-2*s* halogen-$np_\sigma$ antibonding combination. Along X = F to At, the halogen $np_\pi$ AOs rise in energy (the halogen becomes less electronegative) and become more diffuse. Thus, the halogen $\pi_g*$ lone-pair HOMOs in the substrate also increases in energy (because the halogen $np_\pi$ AO rise) while the antibonding $\sigma*_{C–X}$ LUMO decreases as the $<2s \mid np_\sigma>$ overlap becomes smaller (because the halogen $np_\sigma$ AO becomes more diffuse). This reduces the HOMO-LUMO gaps for donation (substrate $\pi_g*$ lone-pair to metal 5*s*) and backdonation (metal 4*d* to substrate $\sigma*_{C–X}$) between Pd or $PdCl^-$ and $CH_3X$ and strengthens the interaction along this series.

In $RC_{S_N2}$, on the other hand, the metal–substrate interaction depends much less on the halogen atom X in the substrate $CH_3X$. The reason is that in $RC_{S_N2}$ the metal interacts predominantly through an agostic interaction with C–H bonds of the methyl group in $CH_3X$ and therefore depends much less on X (for a detailed discussion, see ref. 20).

Next, we examine the other player, besides metal-substrate interaction, in the Activation Strain model, namely, the geometrical rigidity of the reactants. The latter shows up as the activation strain $\Delta E^{\neq}_{strain}$. It is predominantly determined by the C–X bond stretching in the TS and, thus, by the $CH_3$–X bond strengths $D_{CX}$ in the halomethane substrates. Thus, we have computed $D_{CX}$ associated with the reactions $CH_3–X \rightarrow CH_3^{\bullet} + X^{\bullet}$ at BLYP/QZ4P (see Table 10.4). The bond strength $D_{CX}$ decreases continuously along X = F, Cl, Br, I, and At, from 114.6 (X = F) to 41.0 kcal/mol (X = At), at the spin-orbit corrected relativistic SO-ZORA-BLYP/QZ4P level of theory. This trend is mainly caused by the decreasing charge-stabilization that goes with the decreasing electronegativity difference across the $CH_3$–X bond when the halogen atom becomes less and less electronegative along the series.[144]

**Table 10.4** Homolytic and heterolytic dissociation energies (in kcal/mol) of the $CH_3$–X bond for X = F to At[a]

| Method | F | Cl | Br | I | At |
|---|---|---|---|---|---|
| *Homolytic* | | | | | |
| BLYP//BLYP[b] | 114.7 | 82.9 | 72.1 | 62.1 | 57.5 |
| BLYP | 114.7 | 82.9 | 72.1 | 62.1 | 57.5 |
| ZORA-BLYP | 114.6 | 82.7 | 71.7 | 61.3 | 55.9 |
| SO-ZORA-BLYP | 114.6 | 82.4 | 68.3 | 54.3 | 41.0 |
| SO-ZORA-BLYP in water[c] | 117.9 | 84.2 | 70.7 | 56.1 | 42.5 |
| CCSD(T) | 111.1 | 83.0 | 72.6 | 63.2 | 58.9 |
| SFDC-CCSD(T) | 111.1 | 82.9 | 72.2 | 62.2 | 56.6 |
| DC-CCSD(T) | 110.7 | 82.0 | 68.8 | 55.7 | 41.7 |
| Experiment[d] | 109.8 | 83.8 | 69.8 | 56.9 | |
| *Heterolytic* | | | | | |
| ZORA-BLYP | 262.1 | 227.5 | 220.7 | 214.7 | 213.5 |
| ZORA-BLYP in water[c] | 80.5 | 72.2 | 71.7 | 74.9 | 75.8 |

a At various levels of DFT and *ab initio* theory. Geometries optimized at ZORA-BLYP/QZ4P unless stated otherwise. BLYP = nonrelativistic BLYP/QZ4P. ZORA-BLYP = scalar ZORA-relativistic BLYP/QZ4P. SO-ZORA-BLYP = spin-orbit ZORA-relativistic BLYP/QZ4P. CCSD(T) = nonrelativistic CCSD(T). SFDC-CCSD(T) = CCSD(T) with relativistic spin-free Dirac-Coulomb Hamiltonian excluding spin-orbit coupling. DC-CCSD(T) = CCSD(T) with relativistic unmodified Dirac-Coulomb Hamiltonian including spin-orbit coupling. All CCSD(T) values have been counterpoise-corrected.

b Geometries optimized nonrelativistically at BLYP/QZ4P.

c Solvent effects in water by COSMO.

d Obtained from corresponding enthalpies of formation at 298 K from ref. 136.

Before continuing the discussion of the interplay between metal-substrate interaction and geometrical deformation or strain energy in the Activation Strain model, we briefly evaluate the performance of our approach for computing C–X bond strength. To this end, we have carried out an accurate benchmark study at the CCSD(T) level of *ab initio* theory. Relativistic effects have been assessed for both BLYP and CCSD(T), by carrying out the computations nonrelativistically (BLYP, CCSD(T)), scalar relativistically, i.e., without spin-orbit coupling (ZORA-BLYP, spin-free Dirac-Coulomb or SFDC-CCSD(T)), and relativistically including spin-orbit coupling (SO-ZORA-BLYP, Dirac-Coulomb or DC-CCSD(T)). The BLYP values agree well with those of the CCSD(T) benchmark, and they do so at each level of treating relativistic effects. For example, $D_{\mathrm{CAt}}$ amounts to 57.5, 55.9 and 41.0 kcal/mol at BLYP, ZORA-BLYP and SO-ZORA-BLYP, which agrees within 1.4 kcal/mol with 58.9, 56.6, and 41.7 kcal/mol obtained at CCSD(T), SFDC-CCSD(T) and DC-CCSD(T), respectively, including counterpoise correction (see Table 10.4). The DC-CCSD(T) benchmark in turn agrees within a few kcal/mol with experimental data[136] where available. Note that relativistic effects on the homolytic $D_{\mathrm{CX}}$ are predominantly caused by spin-orbit coupling. The spin-orbit term stems from the species that have a doublet open-shell configuration, i.e., the dissociation products $CH_3^{\bullet}$ and especially $X^{\bullet}$. This is in line with earlier work by Ziegler *et al.*[144] Spin-orbit coupling is a minor term for all closed-shell systems studied, i.e., Pd, $PdCl^-$, $CH_3X$, and the species at the stationary points of our model reactions.[a] Thus, whereas the

---

[a] For example, the relativistic energy with spin-orbit coupling of the product of Pd + $CH_3At$ relative to R is –45.1 kcal/mol. This differs only 2.4 kcal/mol from the scalar relativistic value of –42.7 kcal/mol (Table 10.3).

computation of reliable homolytic bond-dissociation energies requires consideration of spin-orbit effects, the relative energies of stationary points along the PESs of our model reactions (all closed-shell!) can be sufficiently accurately determined through a scalar relativistic approach (i.e., the ZORA-BLYP approach which is used throughout the present chapter).

Interestingly, the Activation Strain analyses, to which we now return, reveal that the trend in activation energies $\Delta E^{\neq}$ of our gas-phase model reactions is mainly determined by the trend in C–X bond strength. The results of the analyses are listed in Table 10.5, both for the gas-phase and the condensed-phase model reactions which are discussed in this section and the following one, respectively. The trend of a decreasing activation energy along X = F, Cl, Br, I and At derives predominantly from the activation strain $\Delta E^{\neq}_{\text{strain}}$ and despite a (in most but not all cases) counteracting trend in metal-substrate TS interaction $\Delta E^{\neq}_{\text{int}}$ (see Table 10.5, relativistic in gas phase). The activation strain $\Delta E^{\neq}_{\text{strain}}$ decreases along X = F, Cl, Br, I and At for all reaction steps and pathways (i.e., OxIn versus $S_N2$ and $S_N2$-ra) of the Pd- and $PdCl^-$-induced reactions. For example, in the case of the OxIn reactions of Pd + $CH_3X$, $\Delta E^{\neq}_{\text{strain}}$ decreases from 37.0 to 10.0 to 7.2 to 5.4 to 4.6 kcal/mol (see Table 10.5). Similar trends exist for the other model reactions with somewhat lower $\Delta E^{\neq}_{\text{strain}}$ values for the $PdCl^-$-induced OxIn reactions (with more eductlike and thus less deformed TSs, *vide infra*) and higher $\Delta E^{\neq}_{\text{strain}}$ values for the $S_N2$-type reactions (which feature TSs in which the substrate $CH_3X$ is significantly more deformed, *vide infra*). This trend of decreasing activation strain along X = F, Cl, Br, I and At and, thus, the trend in activation energies $\Delta E^{\neq}$, is directly inherited from the behaviour of the C–X bond strength, which, as discussed above, also weakens along this series in X. In this context, we note that the activation strain of the Pd-induced reactions arises exclusively from the substrate, in particular, the C–X elongation along the reaction coordinate. That of the $PdCl^-$-induced reactions arises *almost* exclusively from the substrate: the $PdCl^-$ complex never contributes more than a few tenths of a kcal/mol.

Here, we wish to address two phenomena in more detail: (i) the increase in activation energy from OxIn to $S_N2$ pathways and (ii) the much stronger decrease in activation energies due to anion assistance (that is, if one goes from Pd to $PdCl^-$) for the $S_N2$ than for the OxIn reactions, which causes the preferred pathway to shift from OxIn for Pd + $CH_3X$ to $S_N2$ for $PdCl^-$ + $CH_3X$. Note, in connection with the former issue, that the activation strain increases in all cases going from $TS_{\text{OxIn}}$ to $TS_{S_N2\text{-ra}}$. We mentioned already that this is caused by the higher extent of deformation that the substrate undergoes in the $S_N2$ and, especially, the $S_N2$-ra transition states in which the C–X bond is essentially completely broken (see Figure 10.1). Interestingly, the activation strain can become even larger than the C–X bond dissociation energy. For example, the activation strain $\Delta E^{\neq}_{\text{strain}}$ of 62.3 kcal/mol associated with the $S_N2$-ra reaction of Pd + $CH_3At$ (see

Table 10.5) is more than 7 kcal/mol higher than the $CH_3$–At bond dissociation energy of 55.9 kcal/mol (see Table 10.4). The origin of this phenomenon is that, in the transition state $TS_{S_N2\text{-ra}}$, the methyl group stemming from the substrate remains pyramidal with an average H-C-H angle of 111° (in $CH_3At$, the H-C-H angle is 107°), while in a straight bond-dissociation reaction, the methyl group would adopt its own planar equilibrium geometry with a H-C-H angle of 120°.

Finally, we address the phenomenon that anion assistance (i.e., going from Pd to $PdCl^-$) shifts the preference from the OxIn to the $S_N2$ mechanism. This happens as anion

**Table 10.5** Activation Strain analysis for Pd and $PdCl^-$ addition to the $CH_3$–X bond, with X = F to At[a]

| | | Pd | | | | | $PdCl^{-}$[b] | | | | |
|---|---|---|---|---|---|---|---|---|---|---|---|
| | | F | Cl | Br | I | At | F | Cl | Br | I | At |
| *Relativistic in gas phase* | | | | | | | | | | | |
| $TS_{OxIn}$ | $\Delta E^{\neq}$ | 17.2 | –0.8 | –5.7 | –12.2 | –13.3 | 9.7 | –6.9 | –11.6 | –17.2 | –17.9 |
| | $\Delta E^{\neq}_{\text{strain}}$ | 37.0 | 10.0 | 7.2 | 5.4 | 4.6 | 22.2 | 14.1 | 12.5 | 9.4 | 8.3 |
| | $\Delta E^{\neq}_{\text{int}}$ | –19.8 | –10.8 | –12.9 | –17.7 | –17.9 | –12.5 | –21.0 | –24.1 | –26.6 | –26.1 |
| $TS_{S_N2}$ | $\Delta E^{\neq}$ | 25.5 | c | c | c | c | –1.8 | –17.2 | c | c | c |
| | $\Delta E^{\neq}_{\text{strain}}$ | 103.2 | c | c | c | c | 84.5 | 9.1 | c | c | c |
| | $\Delta E^{\neq}_{\text{int}}$ | –77.7 | c | c | c | c | –86.2 | –26.3 | c | c | c |
| $TS_{S_N2\text{–ra}}$ | $\Delta E^{\neq}$ | 29.6 | 22.9 | 16.6 | 9.9 | 5.8 | –2.2 | –18.3 | –23.4 | –27.0 | –28.1 |
| | $\Delta E^{\neq}_{\text{strain}}$ | 95.8 | 82.8 | 76.4 | 67.4 | 62.3 | 98.1 | 85.3 | 78.5 | 72.5 | 68.8 |
| | $\Delta E^{\neq}_{\text{int}}$ | –66.2 | –59.8 | –59.8 | –57.6 | –56.5 | –100.3 | –103.6 | –101.8 | –99.5 | –96.9 |
| *Relativistic in water* | | | | | | | | | | | |
| $TS_{OxIn}$ | $\Delta E^{\neq}(aq)$ | 10.5 | –2.9 | –7.7 | –14.4 | –15.6 | 11.0 | –3.5 | –7.3 | –12.3 | –12.5 |
| | $\Delta E^{\neq}_{\text{strain}}(aq)$ | 47.9 | 10.0 | 7.5 | 5.7 | 4.8 | 23.2 | 13.0 | 10.0 | 7.8 | 6.6 |
| | $\Delta E^{\neq}_{\text{strain,pure}}$ | 53.4 | 11.4 | 8.3 | 5.9 | 5.0 | 28.9 | 14.9 | 11.2 | 8.2 | 6.9 |
| | $\Delta E^{\neq}_{\text{strain,cav}}$ | 0.0 | 0.0 | 0.0 | 0.0 | 0.0 | 0.0 | 0.0 | 0.0 | 0.0 | 0.0 |
| | $\Delta E^{\neq}_{\text{strain,solv}}$ | –5.5 | –1.4 | –0.8 | –0.2 | –0.2 | –5.7 | –1.9 | –1.2 | –0.4 | –0.3 |
| | $\Delta E^{\neq}_{\text{int}}(aq)$ | –37.4 | –12.9 | –15.2 | –20.1 | –20.5 | –12.1 | –16.5 | –17.3 | –20.0 | –19.1 |
| | $\Delta E^{\neq}_{\text{int,desolv}}$ | 0.6 | 0.2 | 0.0 | –0.3 | –0.2 | 2.2 | 1.3 | 1.2 | 0.9 | 0.9 |
| | $\Delta E^{\neq}_{\text{int,cav}}$ | –1.5 | –1.5 | –1.5 | –1.5 | –1.5 | –1.5 | –1.5 | –1.5 | –1.5 | –1.5 |
| | $\Delta E^{\neq}_{\text{int,pure}}$ | –36.5 | –11.6 | –13.8 | –18.3 | –18.8 | –12.8 | –16.4 | –17.0 | –19.5 | –18.6 |
| | $(\Delta E^{\neq}_{\text{int,gas}})$ | (–33.7) | (–12.1) | (–14.0) | (–18.2) | (–18.3) | (–19.5) | (–22.5) | (–23.2) | (–25.9) | (–25.2) |
| $TS_{S_N2}$ | $\Delta E^{\neq}(aq)$ | 3.6 | –3.1 | –6.2 | –7.5 | c | –1.3 | –7.0 | –9.0 | –10.4 | –11.3 |
| | $\Delta E^{\neq}_{\text{strain}}(aq)$ | 23.4 | 13.9 | 10.2 | 9.0 | c | 35.6 | 18.2 | 13.1 | 14.3 | 11.5 |
| | $\Delta E^{\neq}_{\text{strain,pure}}$ | 30.0 | 16.3 | 11.5 | 9.6 | c | 43.1 | 20.7 | 14.6 | 15.1 | 12.0 |
| | $\Delta E^{\neq}_{\text{strain,cav}}$ | 0.0 | 0.0 | 0.0 | 0.0 | c | 0.0 | 0.0 | 0.0 | 0.0 | 0.0 |
| | $\Delta E^{\neq}_{\text{strain,solv}}$ | –6.6 | –2.4 | –1.3 | –0.6 | c | –7.5 | –2.5 | –1.5 | –0.8 | –0.5 |
| | $\Delta E^{\neq}_{\text{int}}(aq)$ | –19.8 | –16.9 | –16.3 | –16.5 | c | –36.9 | –25.2 | –22.1 | –24.7 | –22.8 |
| | $\Delta E^{\neq}_{\text{int,desolv}}$ | 1.8 | 1.0 | 0.7 | 0.4 | c | 2.8 | 2.1 | 1.8 | 1.6 | 1.4 |
| | $\Delta E^{\neq}_{\text{int,cav}}$ | –1.4 | –1.4 | –1.4 | –1.4 | c | –1.5 | –1.5 | –1.5 | –1.5 | –1.5 |
| | $\Delta E^{\neq}_{\text{int,pure}}$ | –20.1 | –16.5 | –15.6 | –15.5 | c | –38.2 | –25.8 | –22.5 | –24.9 | –22.8 |
| | $(\Delta E^{\neq}_{\text{int,gas}})$ | (–13.2) | (–12.9) | (–13.1) | (–13.9) | c | (–49.9) | (–38.8) | (–36.0) | (–39.3) | (–37.4) |
| $TS_{S_N2\text{–ra}}$ | $\Delta E^{\neq}(aq)$ | 3.7 | –4.5 | –5.7 | –3.6 | –3.2 | –10.4 | –18.8 | –19.6 | –16.5 | –15.6 |
| | $\Delta E^{\neq}_{\text{strain}}(aq)$ | 80.6 | 75.5 | 71.7 | 69.4 | 66.6 | 88.6 | 81.0 | 77.0 | 74.0 | 71.1 |
| | $\Delta E^{\neq}_{\text{strain,pure}}$ | 100.4 | 86.2 | 74.8 | 64.9 | 59.8 | 112.9 | 87.0 | 76.3 | 65.9 | 60.5 |
| | $\Delta E^{\neq}_{\text{strain,cav}}$ | 0.1 | 0.1 | 0.1 | 0.1 | 0.1 | 0.1 | 0.1 | 0.1 | 0.1 | 0.1 |
| | $\Delta E^{\neq}_{\text{strain,solv}}$ | –19.9 | –10.8 | –3.2 | 4.4 | 6.7 | –24.4 | –6.1 | 0.6 | 8.0 | 10.5 |
| | $\Delta E^{\neq}_{\text{int}}(aq)$ | –76.9 | –79.9 | –77.4 | –72.9 | –69.9 | –99.1 | –99.8 | –96.5 | –90.4 | –86.6 |
| | $\Delta E^{\neq}_{\text{int,desolv}}$ | 8.0 | 10.2 | 7.5 | 4.1 | 2.6 | 13.1 | 12.4 | 9.5 | 5.1 | 3.7 |
| | $\Delta E^{\neq}_{\text{int,cav}}$ | –1.4 | –1.5 | –1.4 | –1.4 | –1.5 | –1.5 | –1.5 | –1.5 | –1.5 | –1.5 |
| | $\Delta E^{\neq}_{\text{int,pure}}$ | –83.5 | –88.7 | –83.4 | –75.6 | –71.0 | –110.8 | –110.8 | –104.5 | –94.0 | –88.8 |
| | $(\Delta E^{\neq}_{\text{int,gas}})$ | (–57.0) | (–59.7) | (–55.9) | (–53.5) | (–52.0) | (–107.2) | (–102.4) | (–97.2) | (–91.1) | (–87.1) |

[a] See footnote a of Table 10.3.

[b] Activation strain values include strain in $PdCl^-$ species, which is never larger than 0.6 kcal/mol, but mostly around 0.1 kcal/mol.

[c] TS does not exist.

assistance stabilizes the transition states of both pathways, but it does so significantly more effectively for the latter. What happens is the following: The $S_N2$ pathway has in all cases a significantly higher, that is, less favourable activation strain $\Delta E^{\neq}_{\text{strain}}$ than the OxIn pathway. The activation strain $\Delta E^{\neq}_{\text{strain}}$ is a characteristic of each of the two pathways: for each C–X bond, the activation strain is higher for $TS_{S_N2\text{-ra}}$ than for $TS_{\text{OxIn}}$ because the former is inherently more distorted than the latter in which the C–X has to elongate only slightly. Importantly, the activation strain $\Delta E^{\neq}_{\text{strain}}$ changes comparatively little if we add a chloride ligand on Pd or solvent on the reaction system (see Table 10.5). However, the TS interaction $\Delta E^{\neq}_{\text{int}}$ does change significantly. Coordination of the chloride anion effectively pushes up the palladium-4*d* AOs, which leads in most of the reactions to an increase of the metal-substrate TS interaction $\Delta E^{\neq}_{\text{int}}$ by roughly a factor two. In absolute terms, this means a much larger stabilization of $TS_{S_N2\text{-ra}}$ because, in this transition state, $\Delta E^{\neq}_{\text{int}}$ was already larger. The reason is the higher extent of deformation of the substrate in $TS_{S_N2\text{-ra}}$, in particular, the larger C–X bond expansion (see Table 10.1). This stabilizes the substrate $\sigma^*_{\text{C–X}}$ LUMO and thus reinforces the metal-substrate interaction in $TS_{S_N2\text{-ra}}$ as compared to $TS_{\text{OxIn}}$. Thus, the TS interaction always favours $S_N2$-ra, but in the Pd-induced reactions, it is too weak to counteract the unfavourable $\Delta E^{\neq}_{\text{strain}}$. This changes in the $PdCl^-$-induced reactions in which $\Delta E^{\neq}_{\text{int}}$ becomes large enough to overrule the trend in $\Delta E^{\neq}_{\text{strain}}$ and to shift the reactivity to $S_N2$.

In the Pd + $CH_3Br$ reactions, for example, the OxIn barrier (–6 kcal/mol) is lower than the $S_N2$-ra barrier (17 kcal/mol) because of a significantly lower activation strain for the less distortive OxIn reaction, that is, 7 versus 76 kcal/mol (see Table 10.5, relativistic in gas phase). The corresponding TS interactions of –13 and –60 kcal/mol, respectively, are too small to change the order set by the activation strain. Switching on anion assistance (i.e., going to $PdCl^-$ + $CH_3Br$) has little effect on the activation strain values, which go from 7 to 13 kcal/mol (OxIn) and from 76 to 79 kcal/mol ($S_N2$-ra). However, the corresponding TS interactions jump from –13 to –24 kcal/mol (OxIn) and from –60 to –102 kcal/mol ($S_N2$-ra). The in absolute terms larger stabilization of $\Delta E^{\neq}_{\text{int}}$ in $TS_{S_N2\text{-ra}}$ causes this transition state to drop below $TS_{\text{OxIn}}$.

In conclusion, the height of reaction barriers for C–X bond activation decrease as the C–X bond becomes weaker along X = F, Cl, Br, I and At, because of the concomitant decrease in activation strain. The latter is furthermore significantly lower for the OxIn pathway, which therefore has a lower barrier and dominates the $S_N2$ pathway in the Pd-induced reactions. Anion assistance in the $PdCl^-$-induced reactions significantly amplifies the TS interaction which favours the $S_N2$ pathway. This provides us with a rational approach toward tuning the stereochemistry of the C*–X bond activation process from retention (OxIn) to inversion of configuration ($S_N2$), simply by increasing the TS interaction with the help of a chloride ligand (see also Scheme 10.1).

### 10.3.5 Activation Strain model for condensed-phase reactions

Solvation, as pointed out above, pronouncedly changes the intrinsic reactivity trends of C–X bond activation: it causes the neutral reactions of Pd + $CH_3X$ to shift from OxIn to $S_N2$ (for the *smaller* halogens, F and Cl) and the anion-assisted reactions of $PdCl^-$ + $CH_3X$ from $S_N2$ to OxIn (for the *heavier* halogens, I and At; see Figure 10.3). In the following, we aim to understand these solvent effects on the reactivity and stereochemical selectivity of catalytic C–X bond activation, using again the conceptual framework provided by the Activation Strain model. In this way, the height of reaction barriers is again described and understood in terms of the rigidity and bonding capabilities of the reactants, that is, the reactants *in solution*. This enables a consistent comparison with the Activation Strain analyses of the gas-phase reactions. Thus, the activation energy in water, $\Delta E^{\neq}(\mathrm{aq})$, is decomposed into the activation strain of the model catalyst and substrate in water, $\Delta E^{\neq}{}_{\mathrm{strain}}(\mathrm{aq})$, plus the corresponding metal-substrate interaction in water, $\Delta E^{\neq}{}_{\mathrm{int}}(\mathrm{aq})$:

$$\Delta E^{\neq}(\mathrm{aq}) = \Delta E^{\neq}{}_{\mathrm{strain}}(\mathrm{aq}) + \Delta E^{\neq}{}_{\mathrm{int}}(\mathrm{aq}) \tag{10.2}$$

Note that both $\Delta E^{\neq}{}_{\mathrm{strain}}(\mathrm{aq})$ and $\Delta E^{\neq}{}_{\mathrm{int}}(\mathrm{aq})$ contain effects due to solvation. The activation strain in solution, $\Delta E^{\neq}{}_{\mathrm{strain}}(\mathrm{aq})$, is the energy associated with deforming the reactants from their equilibrium structure *in solution* to the geometry they adopt in the TS *in solution*. To reveal which role the solvent plays in this term, the latter is decomposed into three terms (Eq. 10.3): (i) the pure deformation energy, that is, the change in energy associated with the geometrical deformation of the reactants in solution *but in the absence of the solvent*, $\Delta E^{\neq}{}_{\mathrm{strain,pure}}$; (ii) the change in cavitation energy associated with the corresponding deformation of the cavity in the solvent that houses the reactants, $\Delta E^{\neq}{}_{\mathrm{strain,cav}}$; and (iii) the corresponding change in solute–solvent interaction, that is, in solvation stabilization $\Delta E^{\neq}{}_{\mathrm{strain,solv}}$:

$$\Delta E^{\neq}{}_{\mathrm{strain}}(\mathrm{aq}) = \Delta E^{\neq}{}_{\mathrm{strain,pure}} + \Delta E^{\neq}{}_{\mathrm{strain,cav}} + \Delta E^{\neq}{}_{\mathrm{strain,solv}} \tag{10.3}$$

Thus, the activation strain in water depends on the rigidity of the reactants (mainly the substrate), the extent to which the solvent cavities must change in reaction to the geometrical deformation of the reactants, and the effect of all these geometrical deformations of reactants and solvent on the solute-solvent interaction.

The TS interaction in solution, $\Delta E^{\neq}{}_{\mathrm{int}}(\mathrm{aq})$, is the energy associated with bringing the deformed reactants *in solution* together in the TS *in solution*. To also uncover how the solvent affects this term, $\Delta E^{\neq}{}_{\mathrm{int}}(\mathrm{aq})$ is decomposed again into three terms (Eq. 10.4): (i) the change in energy associated with the desolvation of those sites on either reactant that in the TS are bonding and/or in steric contact, $\Delta E^{\neq}_{\text{int,desolv}}$, see also Scheme 10.2; (ii) the change in cavitation energy associated with going from two reactant cavities in the solvent to one cavity that houses the TS, $\Delta E^{\neq}_{\text{int,cav}}$; and (iii) the pure interaction energy between the partially desolvated reactants (i.e., without desolvation and cavitation effects), $\Delta E^{\neq}_{\text{int,pure}}$:

$$\Delta E^{\neq}_{\text{int}}(\text{aq}) = \Delta E^{\neq}_{\text{int,desolv}} + \Delta E^{\neq}_{\text{int,cav}} + \Delta E^{\neq}_{\text{int,pure}} \tag{10.4}$$

The $\Delta E^{\neq}_{\text{int,desolv}}$ is computed as the change in solute-solvent interaction when each of the deformed reactants is brought from its regular cavity to the TS cavity *in the absence of the other reactant* (i.e., by using ghost atoms for the other reactant). The term $\Delta E^{\neq}_{\text{int,pure}}$ is then computed as $\Delta E^{\neq}_{\text{int}}(\text{aq}) - \Delta E^{\neq}_{\text{int,desolv}} - \Delta E^{\neq}_{\text{int,cav}}$.

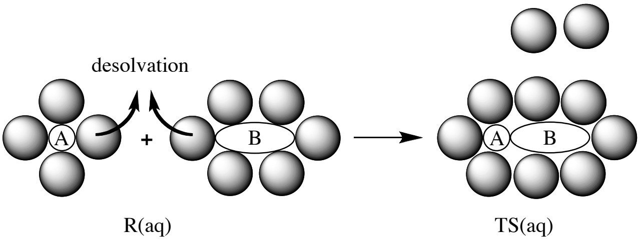

**Scheme 10.2** Desolvation of fragments A and B when complex AB is formed

### 10.3.6 Activation Strain analysis of condensed-phase reactivity

Solvation shifts the preference of the neutral Pd + $CH_3X$ reactions from OxIn to $S_N2$ for two reasons: (i) it weakens the C–X bond regarding heterolytic bond cleavage and thus effectively reduces the rigidity of the substrate, and (ii) it stabilizes the metal-substrate interaction by the concomitant enhancement of the charge separation $C^{\delta+}–X^{\delta-}$ in the substrate. This shows up in a lower activation strain in water, $\Delta E^{\neq}_{\text{strain}}(\text{aq})$, as compared to that in the gas phase, $\Delta E^{\neq}_{\text{strain}}$, as well as in a more stabilizing TS interaction in water, $\Delta E^{\neq}_{\text{int}}(\text{aq})$, as compared to that in the gas phase, $\Delta E^{\neq}_{\text{int}}$ (see Table 10.5). Importantly, this stabilizing effect is stronger for the more deformed $TS_{S_N2\text{-ra}}$ than for $TS_{\text{OxIn}}$ as the former has a more elongated and polarized $C^{\delta+}–X^{\delta-}$ bond (*vide supra*). In the case of Pd + $CH_3Cl$, for example, hydration stabilizes the activation strain and TS interaction of the OxIn pathway by only 0.0 and –2.1 kcal/mol, respectively, whereas it stabilizes the corresponding terms of the $S_N2$-ra reaction by a sizeable –7.3 and –20.1 kcal/mol (Table 10.5: compare $\Delta E^{\neq}_{\text{strain}}(\text{aq})$ with $\Delta E^{\neq}_{\text{strain}}$ and $\Delta E^{\neq}_{\text{int}}(\text{aq})$ with $\Delta E^{\neq}_{\text{int}}$). The solvent-induced stabilization of the activation strain and TS interaction furthermore increases along At to F, that is, going to the smaller and more electronegative halogens. Thus, for Pd + $CH_3I$, the hydration-induced stabilization of the activation strain and TS interaction of the $S_N2$-ra reaction has been reduced to +2.0 (i.e., a slight *destabilization*) and –15.3 kcal/mol. As a result, the barriers of the $S_N2$ pathway approach those of the OxIn pathway, and for F and Cl, $TS_{S_N2\text{-ra}}$ becomes lower in energy than $TS_{OxIn}$.

Further analyses show that the hydration-induced stabilization of the activation strain in the case of the smaller halogens is indeed caused by a better solvation term, $\Delta E^{\neq}_{\text{strain,solv}}$. In the case of the $S_N2$-ra reaction, the latter amounts to –19.9 (F), –10.8 (Cl), –3.2 (Br), +4.4 (I) and +6.7 kcal/mol (At) (see Table 10.5). The cavitation term, $\Delta E^{\neq}_{\text{strain,cav}}$, is nowhere larger than a virtually negligible 0.1 kcal/mol. The reason for the large solvent stabilization in case of $TS_{S_N2\text{-ra}}$ is that solvation in water stabilizes charge separation and opens the possibility for heterolytic bond dissociation of the $CH_3$–X bond, that is, dissociation into the ionic fragments $CH_3^+$ and $X^-$. This is illustrated by the data in Table 10.4, which shows homolytic and heterolytic C–X dissociation energies for both the gas phase and the water phase. In the gas phase, the homolytic dissociation is always more favourable than the heterolytic one. But in water, heterolytic dissociation is significantly more strongly stabilized. In the case of F and Cl, heterolytic dissociation becomes even more favourable than homolytic dissociation. In the cases of Br, I and At, the selective stabilization of the heterolytic dissociation is not strong enough to open this ionic dissociation mode as a more favourable alternative to homolytic dissociation.

The above effects of hydration on the activation strain can be easily understood with the classical electrostatic Born model of a spherical ion in a dielectric continuum:[145]

$$\Delta E_{\text{solv}} = -\frac{q^2}{8\pi\varepsilon_0 a}\left(1-\frac{1}{\varepsilon_{\text{r}}}\right) \tag{10.5}$$

In this equation, $\varepsilon_0$ is the dielectric constant in vacuum, and $\varepsilon_{\text{r}}$ is the relative dielectric constant of the solvent (i.e., 78.4 for water). The charge $q$ is –1 for $X^-$. The appearance of the radius $a$ of the ion in the denominator leads to smaller solvation energies for larger ions. On the basis of this simple model, it is immediately clear why the dissociation of $CH_3X$ into $CH_3^+$ and $X^-$ in water is more favoured for the smaller halogens: the large halogenide anions are in a sense too large to be well stabilized by solvation.

Likewise, further analyses show that the hydration-induced stabilization of the TS interaction in the case of the smaller halogens is indeed caused by a reinforcement of the pure interaction between the solvated reactants, $\Delta E^{\neq}_{\text{int,pure}}$, which dominates all other effects (Table 10.5: compare this term directly with $\Delta E^{\neq}_{\text{int}}$ or $\Delta E^{\neq}_{\text{int,gas}}$). The contribution of the changing cavitation energy $\Delta E^{\neq}_{\text{int,cav}}$ is in all cases small, i.e., around –1.5 kcal/mol. This decrease in cavitation energy is caused by the fact that the deformed reactants occupy less space when they form the complex than when they are apart from each other. The partial desolvation energy $\Delta E^{\neq}_{\text{int,desolv}}$ is (naturally) always destabilizing.

Finally, we extend our analysis to the anion-assisted $PdCl^-$ + $CH_3X$ reactions in water to understand why here solvation shifts the reactivity from $S_N2$ to OxIn, that is, in the opposite direction as compared to the effect of solvation on the neutral reactions. The main effect of solvation appears to be the *weakening* of the metal-substrate TS interaction, at variance with the strengthening in the case of the neutral reactions Pd + $CH_3X$ (*vide infra*). On the other hand, the activation strain behaves quite similar in the anion-assisted and neutral reactions, since the substrates are identical and the strain in Pd and $PdCl^-$ is zero versus negligible.

The TS interaction, as discussed above, is more stabilizing for the $S_N2$ pathway and therefore favours this mechanism over OxIn. In the gas phase, anion assistance amplifies the TS interaction term, which causes the reactivity to switch from OxIn, for Pd + $CH_3X$, to $S_N2$, for $PdCl^-$ + $CH_3X$ (see Figure 10.4 and Table 10.5). Now, if we go from the gas phase to the water phase, the TS interaction becomes again weaker, an effect that favours the OxIn transition states because it destabilizes the barrier of the anion-assisted $TS_{S_N2\text{-ra}}$ more than that of the corresponding $TS_{OxIn}$. For example, for the neutral Pd + $CH_3At$ reaction, solvation *strengthens* the TS interaction of $TS_{OxIn}$ and $TS_{S_N2\text{-ra}}$ by –2.6 and –13.4 kcal/mol, respectively, while for the anion-assisted $PdCl^-$ + $CH_3At$ reaction, solvation *weakens* the TS interaction of $TS_{OxIn}$ and $TS_{S_N2\text{-ra}}$ by +7.0 and +10.3 kcal/mol, respectively (Table 10.5: compare $\Delta E^{\neq}_{int}(aq)$ with $\Delta E^{\neq}_{int}$ values).

Similar solvent effects occur for $TS_{S_N2}$ which, in the case of X = I and At, becomes even higher in energy than $TS_{OxIn}$ (see Figure 10.3 and Table 10.5). But a direct comparison between the gas-phase and water-phase $TS_{S_N2}$ is complicated by the fact that for $PdCl^-$ + $CH_3X$ this transition state exists only for X = F and Cl but not for the other halogens. To nevertheless enable a systematic gas-phase versus condensed-phase comparison, we have also computed the TS interaction in all the *condensed-phase* $TS_{S_N2}$ geometries, *however, in the absence of solvent.* The metal-substrate interaction associated with this structure is designated $\Delta E^{\neq}_{int,gas}$, and serves as a measure for the gas-phase TS interaction $\Delta E^{\neq}_{int}$. Moreover, $\Delta E^{\neq}_{int,gas}$ serves as a point of reference to which the condensed-phase TS interaction $\Delta E^{\neq}_{int}(aq)$ can be compared in a consistent fashion, that is, without strong geometry effects that mask the intrinsic change in the interaction. Indeed, the values of $\Delta E^{\neq}_{int}(aq)$ of –22 to –37 kcal/mol are substantially less stabilizing than those of $\Delta E^{\neq}_{int,gas}$ of –36 to –50 kcal/mol (see Table 10.5).

Further analyses show that the hydration-induced weakening of the TS interaction of the $PdCl^-$ + $CH_3X$ reactions is, in most cases, mainly caused by a weakening of the pure interaction between the solvated reactants, $\Delta E^{\neq}_{int,pure}$, which dominates all other effects (Table 10.5: compare this term directly with $\Delta E^{\neq}_{int}$ or $\Delta E^{\neq}_{int,gas}$). The contribution of the changing cavitation energy $\Delta E^{\neq}_{int,cav}$ is in all cases small: around –1.5 kcal/mol. This decrease in cavitation energy is caused by the fact that the deformed reactants occupy less space when they form the complex than when they are apart from each other. The partial desolvation energy $\Delta E^{\neq}{}_{\text{int,desolv}}$ is always destabilizing but relatively unimportant, that is, about one order of magnitude smaller than $\Delta E^{\neq}{}_{\text{int,pure}}$. The hydration-induced weakening of the pure metal-substrate interaction is ascribed to the polarization of the negative charge on $PdCl^{-}$ (away from the desolvated binding site) and the stabilization of the highest occupied molecular orbitals on $PdCl^{-}$, which reduces the capability of these orbitals to participate in donor-acceptor interactions. Similar effects have been analyzed in detail for the reactions of $F^{-} + CH_3CH_2F$.[142]

## 10.4 Conclusions

Palladium-catalyzed C*–X bond activation in halomethanes can proceed through two stereochemically different pathways: direct oxidative insertion (OxIn, which goes with retention of configuration at C*) and $S_N2$ substitution (which goes with inversion of configuration at C*). Using the Activation Strain model of chemical reactivity, we have shown that the barriers of all pathways decrease along X = F, Cl, Br, I and At because the C–X bond becomes less stable and therefore less rigid along this series. Relativistic effects substantially stabilize the stationary points along the PES but do not change the relative order in barrier heights and reaction energies along the various model reactions.

Interestingly, our Activation Strain analyses provide a very simple and transparent picture of how anion assistance (i.e., going from the model catalyst Pd to $PdCl^{-}$) and solvation (water, described through the COSMO model) affect the overall reactivity and the selectivity between the OxIn and $S_N2$ pathways. The latter pathway is inherently connected with a higher extent of deformation of the substrate in the TS, which leads to a higher activation strain $\Delta E^{\neq}{}_{\text{strain}}$ for $S_N2$ than OxIn. Through the relationship $\Delta E^{\neq} = \Delta E^{\neq}{}_{\text{strain}} + \Delta E^{\neq}{}_{\text{int}}$ this contributes to a higher reaction barrier $\Delta E^{\neq}$ for $S_N2$ than for OxIn.

This situation can now be modulated by the TS interaction $\Delta E^{\neq}{}_{\text{int}}$, which *favours* the $S_N2$ pathway because the more deformed substrate in the latter is also a better partner in electrostatic and donor-acceptor orbital interactions. Thus, whenever the TS interaction $\Delta E^{\neq}{}_{\text{int}}$ is small, the trend in selectivity is determined more by the activation strain $\Delta E^{\neq}{}_{\text{strain}}$, and *vice versa*.

Thus, anion assistance, which increases the bonding capabilities of the model catalyst, favours the $S_N2$ pathway. On the other hand, solvation on top of anion assistance diminishes the bonding capabilities of the model catalyst and therefore favours again the OxIn pathway.

# 11 Transition-state energy and position along the reaction coordinate: towards an extended Activation Strain model

## Abstract

We have studied palladium-catalyzed activation of the C–H, C–C, C–F and C–Cl bonds in methane, ethane, cyclopropane, fluoromethane and chloromethane, using relativistic density functional theory (DFT) at ZORA-BLYP/TZ2P. Our purpose is to arrive at a qualitative understanding, based on accurate calculations, of the trends in activation barriers and transition state (TS) geometries (e.g., early or late along the reaction coordinate) in terms of the reactants' properties. To this end, we have extended the Activation Strain model (in which the activation energy $\Delta E^{\neq}$ is decomposed into the activation strain $\Delta E^{\neq}_{\text{strain}}$ of and the stabilizing TS interaction $\Delta E^{\neq}_{\text{int}}$ between the reactants in the transition state) from a single-point analysis of the TS to an analysis along the reaction coordinate $\zeta$, i.e., $\Delta E(\zeta) = \Delta E_{\text{strain}}(\zeta) + \Delta E_{\text{int}}(\zeta)$. This extension enables us to understand qualitatively trends in the position of the TS along $\zeta$ and, therefore, the values of the activation strain $\Delta E^{\neq}_{\text{strain}} = \Delta E_{\text{strain}}(\zeta^{\text{TS}})$ and TS interaction $\Delta E^{\neq}_{\text{int}} = \Delta E_{\text{int}}(\zeta^{\text{TS}})$ and trends therein. An interesting insight that emerges is that the much higher barrier of catalytic C–C versus C–H activation originates from steric shielding of the C–C bond in ethane by C–H bonds. Thus, before a favourably stabilizing interaction with the C–C bond can occur, the C–H bonds must be bent away which causes the $\Delta E_{\text{strain}}(\zeta)$ in the substrate to be anomalously high and the metal-substrate interaction $\Delta E_{\text{int}}(\zeta)$ in C–C activation to lag behind. Such a steric shielding is not present in the catalytic activation of the C–H bond which is always accessible from the hydrogen side. Other phenomena that are addressed are anion assistance, competition between direct oxidative insertion (OxIn) and the alternative $S_N2$ pathway, and the effect of ring strain.

## 11.1 Introduction

Oxidative addition and reductive elimination (Eq. 11.1) are ubiquitous as elementary reaction steps in homogeneous catalysis[117-120] and have been intensively investigated both experimentally[32-35,120-122] and theoretically.[33,35,42,43,67,108,122,123]

$$\mathrm{ML}_n + \mathrm{R{-}X} \underset{\text{Reductive Elimination}}{\overset{\text{Oxidative Addition}}{\rightleftarrows}} \mathrm{R{-}ML}_n\mathrm{{-}X} \tag{11.1}$$

A well-known class of processes involving oxidative addition is catalytic C–X bond activation.[31,117,118,124,125] The catalytically active species in these reactions are generally coordination complexes of palladium or other transition metals. This process is an efficient tool for selectively converting simple educts, via C–C bond formation, into more complex compounds and is therefore of major importance for synthetic chemistry. The most intensively used substrates for such C–C coupling reactions are aryl halides, whereas it is more difficult in this context to exploit alkyl halides.[115]

Previously, we have studied a series of archetypal carbon-element bond activation reactions (see, for example, ref. 24 and Chapters 8 and 10), using the Activation Strain model of chemical reactivity (see Chapter 2). In that model, activation energies $\Delta E^{\neq}$ are decomposed into the activation strain $\Delta E^{\neq}_{\text{strain}}$ of and the stabilizing transition state (TS) interaction $\Delta E^{\neq}_{\text{int}}$ between the reactants in the activated complex: $\Delta E^{\neq} = \Delta E^{\neq}_{\text{strain}} + \Delta E^{\neq}_{\text{int}}$. The activation strain $\Delta E^{\neq}_{\text{strain}}$ depends on the strength of the activated bond and on the extent to which a particular metal expands the bond in the activated complex. The TS interaction $\Delta E^{\neq}_{\text{int}}$ is directly determined by the bonding capabilities of the reactants. The Activation Strain model concentrates on the decomposition of the activation energy, that is, the energy of the catalyst-substrate complex in the TS geometry.

However, a so far unresolved issue is that the position of the TS along the reaction coordinate has a large effect on the size of the energy components; see for example the discussion in Chapter 8. To get insight into how this position is determined and how this affects the barrier height, we have extended the Activation Strain model from a single-point analysis of the TS to an analysis along the reaction coordinate $\zeta$, i.e., $\Delta E(\zeta) = \Delta E_{\text{strain}}(\zeta) + \Delta E_{\text{int}}(\zeta)$. This extension enables us to understand qualitatively the trends in the position of the TS along $\zeta$ and, therefore, the value of the activation strain $\Delta E^{\neq}_{\text{strain}} = \Delta E_{\text{strain}}(\zeta^{\text{TS}})$ and TS interaction $\Delta E^{\neq}_{\text{int}} = \Delta E_{\text{int}}(\zeta^{\text{TS}})$ and trends therein.

The above extension to the Activation Strain model is brought into practice in our quest to fully understand the following four factors that play a role in determining the activity and selectivity in catalytic bond activation: (i) the nature of the C–X bond; (ii) the competition between direct oxidative insertion (OxIn) and an alternative $S_N2$

pathway; (iii) the effect of anion assistance in the model catalyst; and (iv) the effect of ring strain in the substrate. To investigate how the nature of the C–X bond affects reactivity, we have studied the OxIn reactions of palladium-model catalysts [Pd] into the C–H, C–C, C–F, and C–Cl bonds in methane, ethane, fluoromethane and chloromethane, respectively (Scheme 11.1, OxIn).

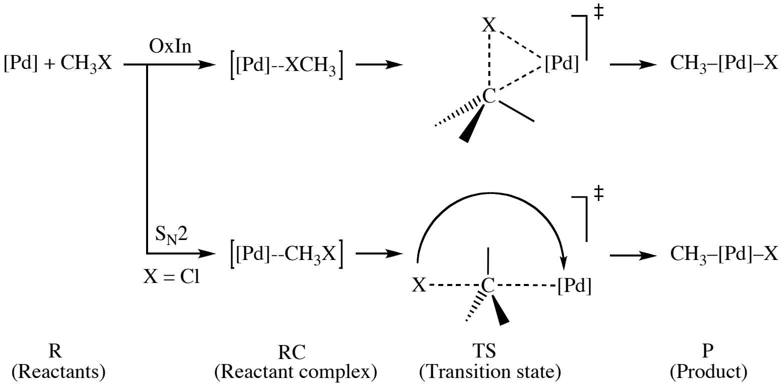

**Scheme 11.1** Model reactions and nomenclature: [Pd] = Pd, PdCl$^-$, X = H, CH$_3$, F, Cl

The competition between OxIn and S$_N$2 pathways has been investigated for the activation of the C–Cl bond as the alternative S$_N$2 pathway was previously shown to be relatively facile for carbon-halogen bonds (Scheme 11.1, OxIn and S$_N$2; see, for example, ref. 20 and Chapter 10). In the gas phase, the reaction barrier for OxIn is lower than that for the S$_N$2 pathway. Interestingly, anion assistance but also solvation (in the case of the lighter halogens, F and Cl) can reverse this order in activation energies shifting reactivity towards S$_N$2 (see Chapter 10).

The effect of ring strain on C–H and C–C bond activation is probed for the OxIn reactions of [Pd] with cyclopropane; see Eqs. 11.2 and 11.3, respectively.

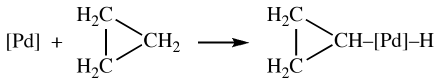

(11.2)

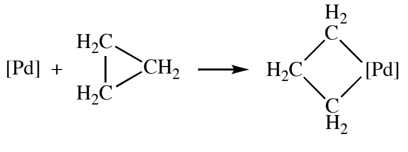

(11.3)

Finally, the effect of anion assistance on all reaction pathways has been investigated by comparing the reactions of the neutral Pd atom with those of the PdCl$^-$ complex.

## 11.2 Methods

All calculations are based on density functional theory (DFT),[6-9] using the ADF program.[49,50,133] The BLYP[52,53] functional was used, in combination with a large uncontracted set of Slater-type orbitals (STOs) containing diffuse functions. This basis set is designated TZ2P: it is of triple-$\zeta$ quality and has been augmented with two sets of polarization functions: $2p$ and $3d$ on H, $3d$ and $4f$ on C, F and Cl, $5p$ and $4f$ on Pd. The core shells of C ($1s$), F ($1s$), Cl ($1s2s2p$), and Pd ($1s2s2p3s3p3d$) were treated by the frozen-core approximation.[49] An auxiliary set of $s$, $p$, $d$, $f$ and $g$ STOs was used to fit the molecular density and to represent the Coulomb and exchange potentials accurately in each SCF cycle.[49] Relativistic effects were accounted for using the zeroth-order regular approximation (ZORA).[19] In Chapters 4 to 7, it was shown that our approach is in good agreement with high-level *ab initio* calculations for oxidative addition reactions to Pd.

Equilibrium and TS geometries were fully optimized using analytical gradient techniques. All structures were verified by frequency calculations. Intrinsic reaction coordinate (IRC)[146] calculations have been performed and the resulting paths were used to compute and analyze the corresponding potential energy surfaces (PESs).

## 11.3 Results and discussion

### 11.3.1 Reaction profiles and geometries

In this section, the reaction profiles of the various reactions as well as the geometries of the stationary points are discussed. The main focus of this chapter is the introduction and application (in the following sections) of the extended version of the Activation Strain model, in which not only the activation energy at the TS is decomposed but the PES along the entire reaction coordinate, from reactant complex (RC) to product (P). Therefore, we restrict the discussion here to the main characteristics. Structural results are summarized in Figure 11.1 (OxIn of [Pd] + $CH_3X$), Figure 11.2 (OxIn of [Pd] + cyclopropane), and Figure 11.3 ($S_N2$ pathway of [Pd] + $CH_3Cl$). Relative energies of the stationary points for all model reactions are collected in Table 11.1.

First, we examine the structural transformations associated with the various reaction pathways followed by a discussion of the main features of the PES, in particular, the activation energies. The OxIn pathway proceeds for all reactions from the reactants R via the formation of a stable reactant complex RC, in which the substrate coordinates to the Pd complex (structures **1a**-**9a**, **11a**), to a TS (**1b**-**12b**) and finally a stable product P (**1c**-**12c**). In the RC, the substrate may coordinate to Pd either via the hydrogen atoms (see structures **1a**, **2a**, **3a**, **5a**, **6a**, **9a** and **11a**) or via the halogen atom (see structures **4a**, **7a** and **8a**).

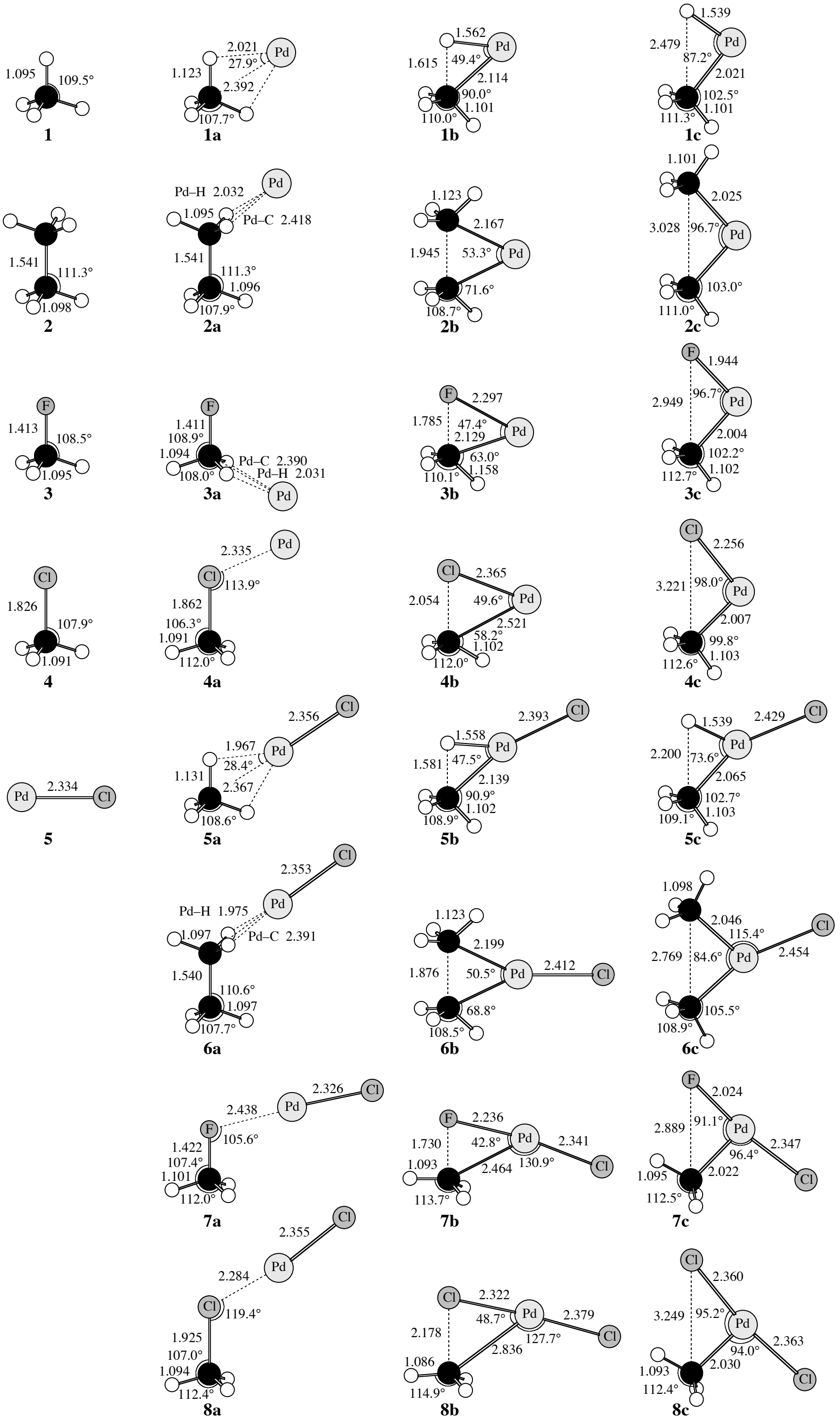

**Figure 11.1** Geometries (in Å, degrees) at ZORA-BLYP/TZ2P of stationary points along the reaction coordinate for oxidative insertion of Pd and $PdCl^-$ into the C–X bond of $CH_3X$, with X = H, $CH_3$, F and Cl

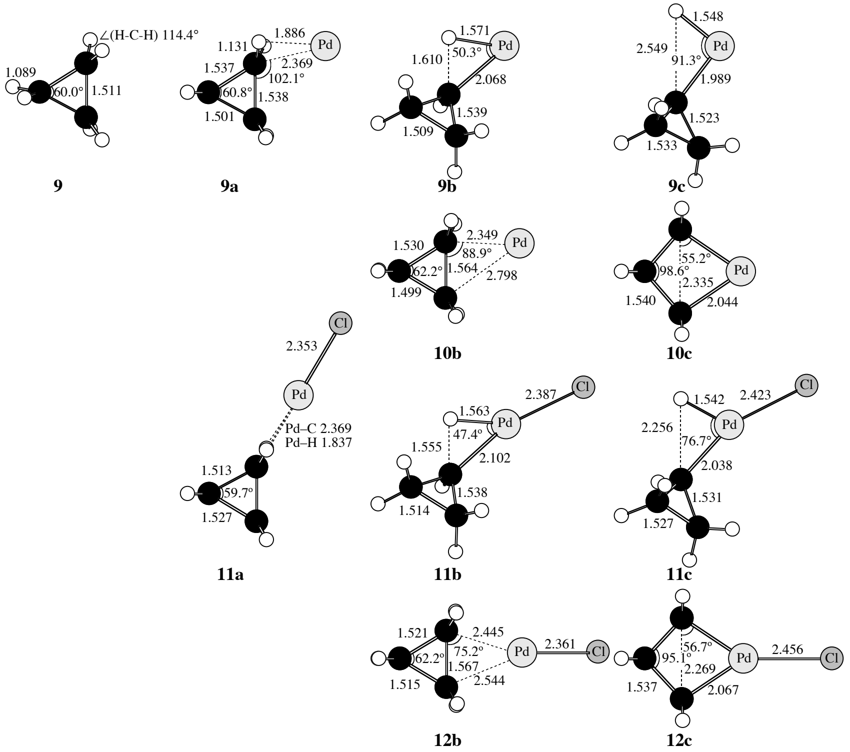

**Figure 11.2** Geometries (in Å, degrees) at ZORA-BLYP/TZ2P of stationary points along the reaction coordinate for oxidative insertion of Pd and $PdCl^-$ into the C–H and C–C bonds of cyclopropane

In the reactions of cyclopropane with both Pd and $PdCl^-$, oxidative insertion into either the C–H or the C–C bond proceed via one and the same RC: **9a** and **11a** in the case of Pd and $PdCl^-$, respectively. The barrier towards insertion into the C–C bond is dramatically reduced if one goes from ethane to cyclopropane, e.g., from 18.3 down to –6.1 kcal/mol in the case of addition to neutral Pd (see Table 11.1). This is a direct consequence of the C–C bond weakening effect of the ring strain in cyclopropane (*vide infra*). The barrier for insertion into the C–H bond is much less affected, i.e., it drops by less than one kcal/mol if one goes from methane to cyclopropane. Interestingly, the TSs for Pd and $PdCl^-$ insertion into the cyclopropane C–C bond do not arise from the actual insertion stage of the process. They are associated with the loss in stabilizing interaction that must be surmounted first as the [Pd] species moves away from its optimal binding site in the RCs. As soon as the model catalyst faces the C–C bond, it spontaneously inserts. We have verified that a direct frontal approach of the C–C bond by [Pd] proceeds indeed spontaneously, i.e., without encountering any barrier along the entire approach.

The alternative $S_N2$ pathway for oxidative addition of $CH_3Cl$ to Pd and $PdCl^-$ proceeds via RCs (structures **13a** and **14a**) that differ from those in the OxIn pathway (**4a** and **8a**) in that chloromethane coordinates to palladium via two hydrogen atoms and

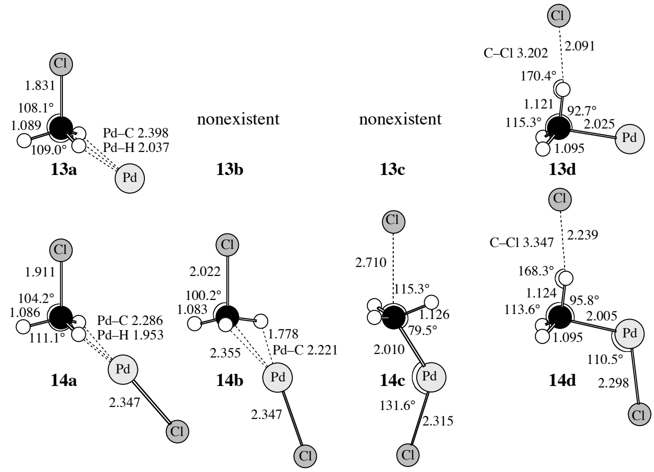

**Figure 11.3** Geometries (in Å, degrees) at ZORA-BLYP/TZ2P of stationary points along the reaction coordinate for the $S_N2$ pathway of oxidative addition of $CH_3Cl$ to Pd and $PdCl^-$

not via the halogen atom. In the case of $PdCl^-$, the reaction proceeds in two separate, elementary reaction steps: first an $S_N2$ TS (**14b**) is encountered, leading to a stable intermediate [$ClPdCH_3$, $Cl^-$] (**14c**). Thereafter, the expelled $Cl^-$ leaving group rearranges via a second TS (**14d**) to form the same product (**8c**) as in the OxIn pathway. In the case of Pd, the $S_N2$ stage of the reaction has no reverse barrier, i.e., there is no $S_N2$ TS, because the energetically highly unfavourable charge separation that builds up as one

**Table 11.1** Energies of stationary points (in kcal/mol; relative to reactants) for the oxidative insertion, $S_N2$ substitution and $S_N2$/Cl-rearrangement reactions of Pd and $PdCl^-$ with various substrates[a]

| Activated bond | Reactants | RC | TS | P |
|---|---|---|---|---|
| *Oxidative insertion* | | | | |
| C–H | Pd + $CH_4$ | −6.7 | 3.9 | −3.4 |
| | $PdCl^-$ + $CH_4$ | −12.4 | −5.4 | −8.7 |
| | Pd + cyclopropane | −6.2 | 3.3 | −5.2 |
| | $PdCl^-$ + cyclopropane | −11.9 | −6.5 | −10.8 |
| C–C | Pd + $C_2H_6$ | −6.8 | 18.3 | −9.3 |
| | $PdCl^-$ + $C_2H_6$ | −12.6 | 15.4 | −9.9 |
| | Pd + cyclopropane | −6.2 | −6.1 | −28.5 |
| | $PdCl^-$ + cyclopropane | −11.9 | −7.8 | −29.0 |
| C–F | Pd + $CH_3F$ | −5.5 | 17.7 | −15.8 |
| | $PdCl^-$ + $CH_3F$ | −2.6 | 8.9 | −40.1 |
| C–Cl | Pd + $CH_3Cl$ | −12.9 | −0.6 | −33.1 |
| | $PdCl^-$ + $CH_3Cl$ | −17.9 | −7.5 | −55.6 |
| *$S_N2$ substitution* | | | | |
| C–Cl | Pd + $CH_3Cl$ | −5.1 | b | b |
| | $PdCl^-$ + $CH_3Cl$ | −18.7 | −18.2 | −22.1[c] |
| *$S_N2$/Cl-rearrangement* | | | | |
| C–Cl | Pd + $CH_3Cl$ | −5.1[d] | 23.1 | −33.1 |
| | $PdCl^-$ + $CH_3Cl$ | −22.1[c] | −18.8 | −55.6 |

a Computed at ZORA-BLYP/TZ2P (see also Figures 11.1 to 11.3).

b Reverse reaction proceeds without a barrier.

c Product complex for $S_N2$ substitution, structure **14c** in Figure 11.3. This is the RC for rearrangement towards the oxidative addition product.

d Structure **13a** in Figure 11.3. Reaction proceeds directly from RC for $S_N2$ substitution to TS for rearrangement.

approaches the fictitious $S_N2$ product complex $PdCH_3^+–Cl^-$ continuously pushes up the PES. Consequently, the $S_N2$ pathway of Pd + $CH_3Cl$ proceeds, from the RC, directly to the TS for $Cl^-$ rearrangement (**13d**) and then to the product (**4c**).

Next, we examine the PESs of the reactions (see Table 11.1). The complexation energy associated with the formation of RCs varies from –3 to –19 kcal/mol but typically adopts values around –7 kcal/mol. All reactions are exothermic with reaction energies ranging from –3 to –56 kcal/mol. In all cases, the reactions involving $PdCl^-$ have lower reaction barriers and are more exothermic than those involving Pd. Note that there is no obvious correlation between the relative order in reaction barriers and that in reaction energies. For example, the insertion of Pd into the methane C–H bond has a relatively low barrier of 3.9 kcal/mol but the reaction energy of –3.4 kcal/mol is not very exothermic. On the other hand, although the insertion of Pd into the ethane C–C bond is clearly more exothermic with a reaction energy that amounts to –9.3 kcal/mol, it goes with a significantly higher barrier, namely, 18.3 kcal/mol.

Finally, we focus on the trends in activation energies along the various model reactions, which are graphically presented in Figure 11.4. For the Pd-induced reactions, the lowest barrier is found for C–C(c), i.e., OxIn into the cyclopropane C–C bond, and the highest barrier for C–Cl($S_N2$), i.e., the $S_N2$ pathway of oxidative addition of the chloromethane C–Cl bond. The activation barrier (in kcal/mol) increases along C–C(c) (–6.1) < C–Cl (–0.6) < C–H(c) (+3.3) ≤ C–H (+3.9) << C–F (+17.7) ≤ C–C (+18.3) < C–Cl($S_N2$) (+23.1), where the affix "(c)" designates a bond in cyclopropane. The barriers of the $PdCl^-$-induced reactions are all lower than the corresponding Pd-induced

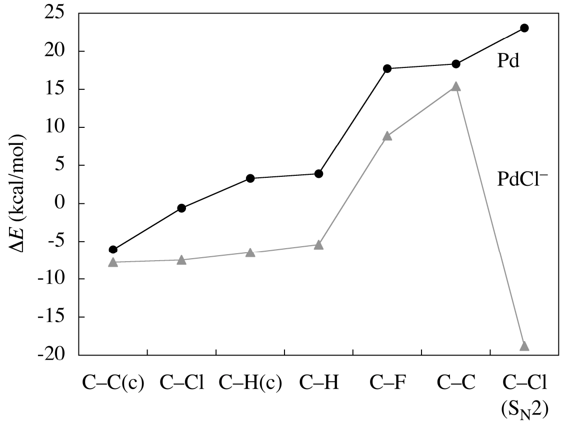

**Figure 11.4** Activation energies relative to reactants at ZORA-BLYP/TZ2P for the oxidative insertion of Pd (circles) and $PdCl^-$ (triangles) into various bonds. C–H(c) and C–C(c) refer to the C–H and C–C bonds in cyclopropane, respectively. C–Cl($S_N2$) refers to the $S_N2$ pathway for oxidative addition of chloromethane.

ones but the reduction in the overall barrier for the $S_N2$ pathway of oxidative addition of the C–Cl bond is dramatic, making it lowest of the entire series of $PdCl^-$-induced model reactions. The activation barrier (in kcal/mol) increases along C–Cl($S_N2$) (–18.8) << C–C(c) (–7.8) ≤ C–Cl (–7.5) ≤ C–H(c) (–6.5) ≤ C–H (–5.4) << C–F (+8.9) < C–C (+15.4).

Thus, the barrier for Pd-induced activation of "regular" C–X bonds, i.e., in unstrained substrates, increases along C–Cl < C–H << C–F ≤ C–C. Here, direct oxidative insertion into the C–Cl bond is by far more favourable than the $S_N2$ pathway. Anion assistance lowers all activation energies but does not affect the order in OxIn barriers. Anion assistance however does turn around the relative height of the overall barriers for the OxIn and $S_N2$ mechanisms making the latter the preferred pathway. Ring strain, that is, going from methane and ethane to cyclopropane, only slightly affects the C–H barrier but it dramatically reduces the barrier for insertion into the C–C bond.

### 11.3.2 Extended Activation Strain model

In previous studies, we have used the Activation Strain model of chemical reactivity (see Chapter 2) to gain insight into how the use of different inserting metal complexes and different substrates affects the activation barriers of different oxidative addition reactions (see, for example, ref. 24 and Chapters 8 and 10). In this model, the activation energy $\Delta E^{\neq}$ is decomposed into the activation strain $\Delta E^{\neq}_{\text{strain}}$ and the TS interaction $\Delta E^{\neq}_{\text{int}}$:

$$\Delta E^{\neq} = \Delta E^{\neq}_{\text{strain}} + \Delta E^{\neq}_{\text{int}} \tag{11.4}$$

$\Delta E^{\neq}_{\text{strain}}$ is the strain energy associated with deforming the reactants from their equilibrium geometry to the geometry they acquire in the activated complex. $\Delta E^{\neq}_{\text{int}}$ is the actual interaction energy between the deformed reactants in the transition state.

However, as pointed out in the introduction to this chapter, a so far unresolved problem is that the position of the TS along the reaction coordinate ($\zeta = \zeta^{\text{TS}}$) has a large effect on the magnitude of $\Delta E^{\neq}_{\text{strain}} = \Delta E_{\text{strain}}(\zeta^{\text{TS}})$ and $\Delta E^{\neq}_{\text{int}} = \Delta E_{\text{int}}(\zeta^{\text{TS}})$ (see for example the discussion in Chapter 8). To illustrate this, we provide in Table 11.2 the single-point (i.e., for the optimized TS structures at $\zeta = \zeta^{\text{TS}}$) activation strain analyses of the activation energies of each of our model reactions. The values of $\Delta E^{\neq}_{\text{strain}}$ and $\Delta E^{\neq}_{\text{int}}$ must be interpreted with great care, since the optimized TS structure is the result of a balance of the components $\Delta E_{\text{strain}}(\zeta)$ and $\Delta E_{\text{int}}(\zeta)$. For example, the activation strain $\Delta E^{\neq}_{\text{strain}}$ for the OxIn reaction of Pd + $H_3C$–F bond has a value of 36.4 kcal/mol, which is much smaller than the corresponding value of 52.2 kcal/mol for Pd + $H_3C$–H. This may erroneously suggest that the C–H bond is more difficult to break than the C–F bond which is, of course, *not* the case (*vide infra*).

**Table 11.2** Analysis of the activation energies for Pd and PdCl$^-$ induced activation of the C–H, C–C, C–F and C–Cl bonds in various substrates, in terms of the Activation Strain model

| | Pd | | | | | | | PdCl$^-$ | | | | | | |
|---|---|---|---|---|---|---|---|---|---|---|---|---|---|---|
| | C–H (CH$_4$) | C–H (Cycl.) | C–C (C$_2$H$_6$) | C–C (Cycl.) | C–F (CH$_3$F) | C–Cl (CH$_3$Cl) | C–Cl (S$_N$2) | C–H (CH$_4$) | C–H (Cycl.) | C–C (C$_2$H$_6$) | C–C (Cycl.) | C–F (CH$_3$F) | C–Cl (CH$_3$Cl) | C–Cl (S$_N$2) |
| *Energy decomposition (in kcal/mol)* | | | | | | | | | | | | | | |
| $\Delta E^{\neq}$ | 3.9 | 3.3 | 18.3 | –6.1 | 17.7 | –0.6 | 23.1 | –5.4 | –6.5 | 15.4 | –7.8 | 8.9 | –7.5 | –18.8 |
| $\Delta E^{\neq}_{\text{strain}}$ | 52.2 | 55.2 | 37.8 | 2.0 | 36.4 | 9.9 | 82.2 | 48.9 | 50.3 | 31.3 | 1.0 | 22.1 | 14.8 | 84.8 |
| $\Delta E^{\neq}_{\text{int}}$ | –48.3 | –51.9 | –19.6 | –8.1 | –18.8 | –10.5 | –59.1 | –54.3 | –56.8 | –16.4 | –8.9 | –13.1 | –22.3 | –103.6 |
| *C–X bond elongation in TS* | | | | | | | | | | | | | | |
| $\Delta$(C–X)$^{\neq}$ (in Å) | 0.52 | 0.52 | 0.40 | 0.05 | 0.37 | 0.23 | 1.38 | 0.49 | 0.47 | 0.34 | 0.06 | 0.32 | 0.35 | 1.52 |
| $\Delta$(C–X)$^{\neq}$ (in %) | 47 | 48 | 26 | 4 | 26 | 12 | 75 | 44 | 43 | 22 | 4 | 22 | 19 | 83 |

To tackle this problem, we have extended the Activation Strain model from a single-point analysis of the TS to an analysis along the reaction coordinate $\zeta$:

$$\Delta E(\zeta) = \Delta E_{\text{strain}}(\zeta) + \Delta E_{\text{int}}(\zeta) \tag{11.5}$$

The energy profile along the reaction coordinate $\zeta$, from the reactant complex to the oxidative-addition product, is computed using the intrinsic reaction coordinate (IRC) method.[146] In the following graphical representations, $\zeta$ is then projected onto the stretch of the C–X bond which is in general one of the dominant components of the reaction coordinate and undergoes a well defined change from intact to dissociated bond.

Note that along the reaction coordinate, $\Delta E_{\text{strain}}(\zeta)$ increases because the substrate becomes increasingly deformed. At the same time, the interaction between catalyst [Pd] and substrate, $\Delta E_{\text{int}}(\zeta)$, also increases. The net result is the total energy profile $\Delta E(\zeta)$ (Eq. 11.5) which achieves its maximum (i.e., the TS) at the point along the reaction coordinate where $\mathrm{d}\Delta E_{\text{strain}}(\zeta)/\mathrm{d}\zeta = -\mathrm{d}\Delta E_{\text{int}}(\zeta)/\mathrm{d}\zeta$. This highlights the importance of the behaviour of the two components, especially their slopes, along the reaction coordinate.

### 11.3.3 Extended Activation Strain analyses

*Oxidative insertion into C–X bonds*

Why does the barrier for oxidative insertion into "regular" C–X bonds increase along C–Cl < C–H << C–F ≤ C–C? This correlates only partially with the physically plausible (yet somewhat naive) idea that stronger bonds require more energy to dissociate and, therefore, go with higher reaction barriers. According to this simple model, one would expect the barrier to increase in the order C–Cl < C–C << C–H ≤ C–F as the bond dissociation energy (BDE) increases in this order from 82 to 90 to 110 to 115 kcal mol$^{-1}$, respectively, computed at ZORA-BLYP/TZ2P. This clearly shows that the catalyst-substrate interaction strongly affects the barrier height.

The extended Activation Strain analyses of the four Pd-induced OxIn reactions (graphically represented in Figure 11.5) confirm that the simple bond-strength model is to some extent correct but, at the same time, these analyses also pinpoint the breakdown of this model. First, we note that the much lower activation energy for C–Cl activation is mainly due to a correspondingly much lower strain ($\Delta E_{\text{strain}}$) curve. The metal-substrate interaction ($\Delta E_{\text{int}}$) curve for C–Cl activation differs much less from those of the other bonds and, in the early stages of the reaction (where the TS is located), it is even *less* favourable, i.e., *less* stabilizing than the $\Delta E_{\text{int}}$ curve for C–H activation. The relatively weakly destabilizing $\Delta E_{\text{strain}}$ curve for C–Cl activation is a direct consequence of the fact that the C–Cl bond is significantly weaker than all other bonds, which causes $\Delta E_{\text{strain}}$ to increase less as this bond expands and eventually dissociates along the reaction coordinate. The other bonds, i.e., C–H, C–F and C–C, have more destabilizing $\Delta E_{\text{strain}}$ curves that mutually differ comparatively little (see Figure 11.5). As far as the C–H and C–F bonds are concerned, this reflects again the relative bond strengths of these bonds which increase only slightly in the order C–H ≤ C–F. The fact that the $\Delta E_{\text{strain}}$ curve for the C–C bond also practically coincides with those of the much stronger C–H and C–F bonds is not what one would expect on the basis of the relative bond strengths. The effect that causes the $\Delta E_{\text{strain}}$ curve for C–C activation to be more destabilizing than the simple C–C bond dissociation energy curve is discussed later on.

Thus, the reaction barrier for C–H activation is higher than that for C–Cl activation because the C–H bond is stronger. However, the further increase of the barrier along

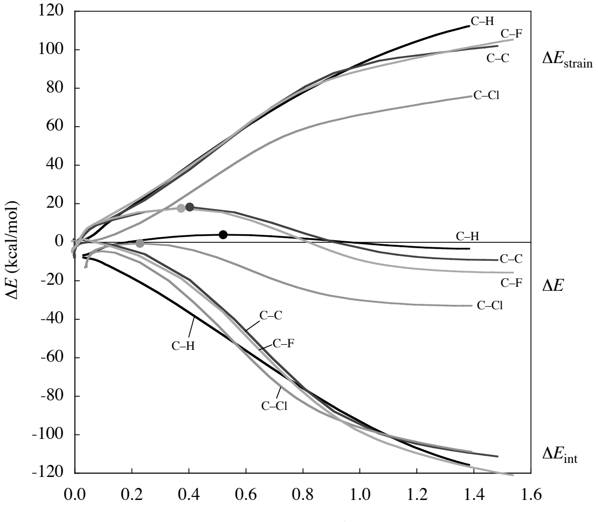

**Figure 11.5** Decomposition of $\Delta E$ for oxidative insertion of Pd into the C–H, C–C, C–F, and C–Cl bonds of methane, ethane, fluoromethane and chloromethane, respectively, along the reaction coordinate projected onto the C–X bond length. Dots indicate TSs.

C–H, C–C and C–F appears to have its origin in the metal-substrate interaction $\Delta E_{\text{int}}$. In Figure 11.5, it can be nicely seen that initially the $\Delta E_{\text{int}}$ curves of the C–C and C–F bonds, and to a lesser extent also that of the C–Cl bond, lag behind that of the C–H bond while, later on, they catch up. This initial lagging behind of the $\Delta E_{\text{int}}$ curves has the effect of pushing up the net energy profile $\Delta E$ which causes the C–F and C–C barriers to be higher than that of C–H activation. The catching up in a somewhat later stage along the reaction coordinate $\zeta$ causes an increased (negative) slope in the $\Delta E_{\text{int}}$ curves. Compared to the situation for C–H, this shifts the stationary point (i.e., the TS) on the net potential energy surface $\Delta E(\zeta) = \Delta E_{\text{strain}}(\zeta) + \Delta E_{\text{int}}(\zeta)$ towards the left.

The origin of the lagging behind of the $\Delta E_{\text{int}}$ curves of C–C, C–F and C–Cl compared to C–H is diverse. The three former bonds have in common that initially Pd must leave its optimal bonding position in the RC to move side-on to the bond into which it is going to insert. This is obvious in the case of the RCs of C–C (**2a**) and C–F activation (**3a**) in which the dihapto coordination with two C–H bonds must first be broken (see Figure 11.1). But a similar phenomenon occurs also in the case of the RC for C–Cl activation (**4a**) which has a relatively large C–Cl–Pd angle of 113.9° and a Pd atom that is somewhat oriented away from the C–Cl bond. The large C–Cl–Pd angle results from a balance between the optimal orientation for donation of the Cl-lone pairs into the Pd-5*s* (i.e., ~90°) and the optimal orientation for backdonation from Pd-4*d* AOs into the $\sigma^*_{\text{C–Cl}}$ with its large lobe pointing along the C–Cl axis and away from chloromethane (i.e., ~180°). This latter bonding mechanism must first be broken as Pd moves towards the C–Cl bond and this causes the initial weakening in the $\Delta E_{\text{int}}$ curve (see Figure 11.5). At variance, in the RC for C–H activation (**1a**), the Pd atom binds from the beginning practically side-on to the C–H bond and can directly begin with inserting as the reaction proceeds. Thus, in the case of C–H, the $\Delta E_{\text{int}}$ curve is stabilized right from the outset.

Next, after initially loosing favourable interactions in the RC, the $\Delta E_{\text{int}}$ curves of C–C, C–F and C–Cl continue to have a delay in building up stabilization which they however catch up. The interaction of palladium with the C–H bond has, from the beginning, a relatively favourable overlap between a metal 4*d* AO and the $\sigma^*_{\text{C–H}}$ acceptor orbital of the substrate with its large, nodeless 1*s* lobe at hydrogen. This overlap situation is shown schematically in **I** (the dashed line indicates the nodal surface of the carbon 2*p* component of the $\sigma^*_{\text{C–H}}$ MO which contributes especially when the C–H bond begins to be stretched):

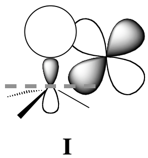
**I**

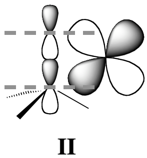
**II**

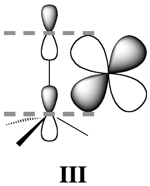
**III**

The corresponding overlap with the $\sigma^*_{\text{C–X}}$ acceptor orbital of C–X bonds in which X is a main-group atom (i.e., C–C, C–F, C–Cl) is less favourable, in the beginning, because now there is also a nodal surface at X which cuts through the metal 4*d* lobe, resulting in cancellation of overlap (see **II**, above). However, the overlap soon catches up as the reaction proceeds and the C–X bond expands because this causes the nodal surfaces of the substrates $\sigma^*_{\text{C–X}}$ MO to move out of the way of the metal 4*d* AO (see **III**, above). The results of quantitative Kohn-Sham MO analyses of this effect are discussed later on. The $\Delta E_{\text{int}}$ curve for C–Cl activation benefits, in addition, from being already longer and thus closer to situation **III** in the RC if compared to the C–F and C–C bonds (C–Cl activation also benefits from having relatively high-energy lone pairs on chlorine that donate charge into the metal 5*s* AO, see also the discussion in Chapter 10.

*C–C versus C–H bond activation*

Interestingly, our analyses show that a special phenomenon occurs in the case of C–C activation: the C–C bond is sterically shielded by the surrounding C–H bonds. Before the metal can achieve direct contact with the C–C bond, the C–H bonds have to be pushed away. This is achieved by C–C bond stretching and, importantly, the well-known tilting of the methyl groups along the reaction path, in particular, in the transition state **2b** (see Figure 11.1). The most eye-catching effect of this “first making room for the metal” is again a delay in the $\Delta E_{\text{int}}$ curve. This is shown again in Figure 11.6a, which compares specifically the C–C with the C–H activation process. Note the snapshots of the Pd + $C_2H_6$ reaction system along the reaction coordinate at $\zeta = 0$, 0.4 and 0.8 Å: around $\zeta =$ 0.4 Å, the tilting is already clearly visible and thereafter, at $\zeta = 0.8$ Å, the $\Delta E_{\text{int}}$ curve for C–C has finally reached that for C–H activation. Another important effect of the methyl tilting, which features may be less prominently in Figure 11.6a, is the increased substrate strain that results. This causes the $\Delta E_{\text{strain}}$ curve of C–C activation to be raised to the same level as that of C–H, even though the former (BDE = 90 kcal/mol) is 20 kcal/mol *weaker* than the latter bond (BDE = 110 kcal/mol).

In conclusion, the steric shielding of the ethane C–C bond by the surrounding C–H bonds is responsible for the fact that activation of the C–C bond has a higher barrier than that of the C–H bond despite the fact that the former is weaker than the latter. One reason is that the steric shielding induces a methyl tilting that raises $\Delta E_{\text{strain}}$. This is in line with previous work in which the higher barrier for C–C activation was ascribed to a higher strain associated with the tilting of two methyl groups for C–C activation versus only one methyl group for C–H activation.[38,96] Note however that, despite the tilting, the strain curve of C–C is not more destabilizing than that of C–H. Therefore, without the delay in interaction between metal and the initially sterically shielded C–C bond, the activation of the latter would not have a higher barrier than C–H activation.

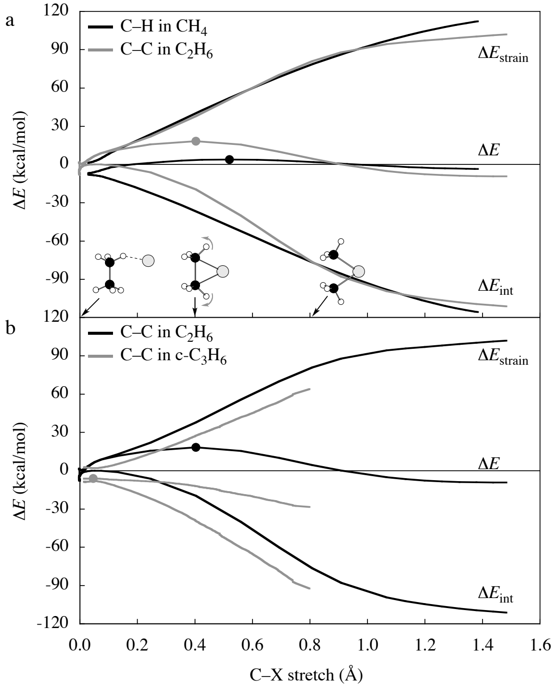

**Figure 11.6** Decomposition of $\Delta E$ for oxidative insertion of Pd into (a) the methane C–H (black lines) and ethane C–C bonds (grey lines), and (b) the C–C bonds of ethane (black lines) and cyclopropane (grey lines), along the reaction coordinate projected onto the C–X bond length. Dots indicate TSs

It is instructive to compare the above C–C bond activation in ethane with the corresponding process in cyclopropane (see Figure 11.6b). Cyclopropane is highly strained, which substantially reduces the barrier for C–C activation. One symptom of ring strain is the dramatic loss in C–C bond strength: the bond dissociation energy of the C–C bond drops from 90 kcal/mol in ethane down to 74 kcal/mol in cyclopropane. The latter is computed at ZORA-BLYP/TZ2P as the energy difference between the singlet biradical propane-1,3-diyl (using the triplet-optimized geometry) and cyclopropane. The lower C–C bond strength in cyclopropane leads to a lower $\Delta E_{\text{strain}}$ curve. Furthermore, there is essentially no steric shielding of the cyclopropane C–C bond by the surrounding C–H bonds. The latter are arranged in cyclopropane (**9**) in an eclipsed conformation with an H–C–C angle of 118° that is clearly larger than the corresponding one in ethane (**2**), which amounts to 111°. In fact, cyclopropane has from the beginning tilted methyl groups that leave room for the approaching Pd to directly interact with the C–C bond. Thus, the retardation that we find in the $\Delta E_{\text{int}}$ curve of ethane practically disappears in the case of cyclopropane. In other words, the cyclopropane C–C bond is more reactive both because it is weaker and because it is exposed to an approaching metal atom.

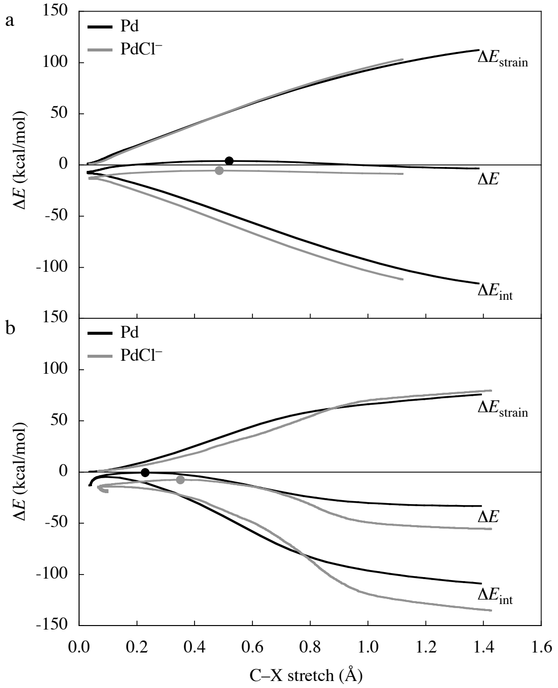

**Figure 11.7** Decomposition of $\Delta E$ for oxidative insertion of Pd (black lines) and PdCl$^-$ (grey lines) into (a) the C–H bond of methane, and (b) the C–Cl bond of chloromethane, along the reaction coordinate projected onto the C–X bond length. Dots indicate TSs

### *Anion assistance*

Anion assistance, that is, going from Pd to PdCl$^-$, lowers all barriers and increases the exothermicity of all studied reactions. Figure 11.7a compares the analyses for insertion of Pd versus that of PdCl$^-$ into the methane C–H bond. The effect of anion assistance on the $\Delta E_{\text{strain}}$ curve is negligible: the lowering of the reaction profile $\Delta E$ from Pd to PdCl$^-$ is exclusively caused by the strengthening in the metal-substrate interaction $\Delta E_{\text{int}}$ along the entire reaction coordinate. Previously, Diefenbach *et al.*[24] showed for the TS of the C–H activation reaction that the increased metal-substrate interaction in the case of PdCl$^-$ originates mainly from a reduced Pauli repulsion because the anionic ligand pushes the Pd-4*d* AOs up in energy: this increases the energy gap with the occupied substrate MOs and weakens the corresponding two-orbital–four-electron repulsions. The donor-acceptor orbital interactions are less affected because of two counteracting effects: (i) the higher energy of the Pd-4*d* AOs makes them better partners in the backdonation to the substrate, but (ii) the higher energy of the Pd-5*s* AO makes it a worse partner in the donation from the substrate to the metal (for details, see ref. 24). Eventually, effect number (ii) slightly outweighs and the orbital interactions slightly weaken due to anion assistance. Here, we find that this holds true along the entire reaction coordinate (data not shown). As can be seen in Figure 11.7a, the more steeply increasing $\Delta E_{\mathrm{int}}$ curve in the case of $PdCl^-$ shifts the TS of the anion-assisted C–H activation to an earlier position along the reaction coordinate.

The other bonds are promoted by anion assistance through a similar electronic mechanism as in the case of C–H and, for most of them, we see besides a lowering of the barrier the shift of the TS towards the educt side, that is, towards an earlier point along the reaction coordinate (see Table 11.1). A striking exception is C–Cl activation: whereas anion assistance lowers again the barrier, it shifts the TS towards the product side and not to the educt side, i.e., the C–Cl bond distance expands from 2.054 Å in the neutral TS **4b** to 2.178 Å in the anionic TS **8b**. This, in a sense, anti-Hammond behaviour, can be ascribed to the following. The Pd-5*s*-derived $\sigma^*_{\mathrm{Pd-Cl}}$ LUMO of $PdCl^-$ has a sizeable (bonding) admixture of the Pd-5$p_\sigma$ AO and is therefore strongly directional, pointing along the Cl–Pd axis away from the catalyst (see below):

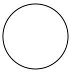

Pd 5*s*

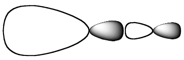

$PdCl^-$ $\sigma^*_{\mathrm{C-Cl}}$

This enhances the model catalyst's inclination to orient and bind to the lone pairs on the chlorine atom of the dissociating C–Cl bond, which, in turn, reduces the tilting of the methyl group. The effect is not large, yet it is clearly monitored in Figure 11.7b: going from Pd to $PdCl^-$ + $CH_3Cl$, we see that the $\Delta E_{\mathrm{strain}}$ curve is initially slightly reduced. The retarded tilting also delays the metal-substrate interaction $\Delta E_{\mathrm{int}}$ because this tilting would otherwise have promoted the overlap for backdonation, as shown schematically in **IV**:

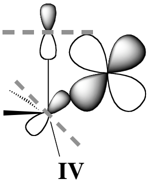

**IV**

The reduced slope in the $\Delta E_{\mathrm{int}}$ curve eventually dominates and promotes the observed shift, due to anion assistance, of the TS for C–Cl activation towards the product side. A similar mechanism for C–F activation is not effective because of the low energy of the fluorine lone pairs, which makes donation into the metal LUMO relatively unimportant.

### *$S_N2$ versus OxIn*

Finally, we address the question *why* oxidative addition of the chloromethane C–Cl bond to Pd proceeds preferentially via OxIn and *why* anion assistance shifts the preference towards the $S_N2$ pathway. The reaction profiles and activation strain analyses for both pathways are shown in Figure 11.8a. The reaction profile $\Delta E(\zeta)$ of the $S_N2$ pathway is always above that of the OxIn pathway, and it is more so the more the reaction proceeds, except for the final stage of the reaction where the energy of the $S_N2$ pathway drops and becomes equal to that of the OxIn pathway. Another characteristic difference between the two pathways is the larger stretching, during the $S_N2$ process, of

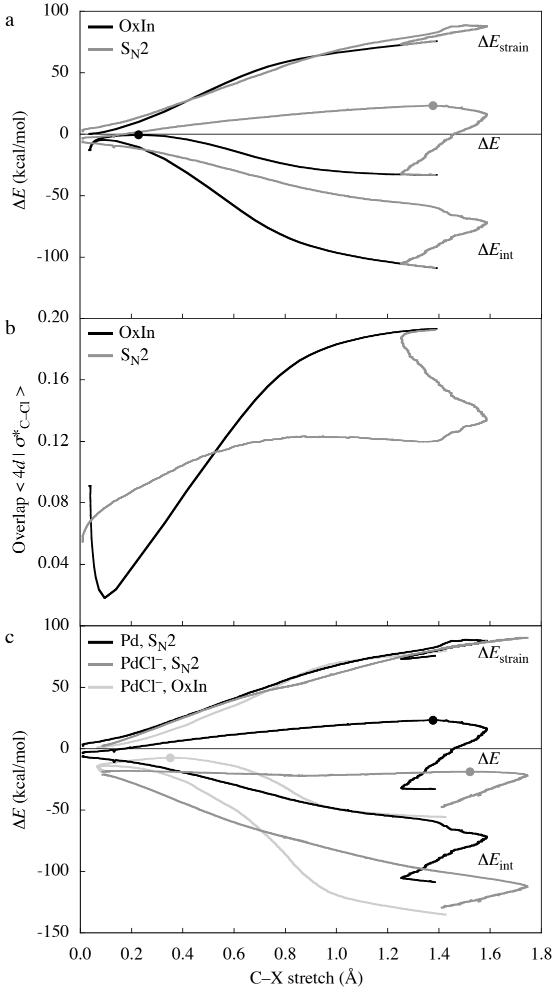

**Figure 11.8** (a) Decomposition of $\Delta E$ for the OxIn (black lines) and the $S_N2$ pathways (grey lines) for oxidative addition of the $CH_3$–Cl bond to Pd; (b) orbital overlap $< 4d \mid \sigma^*_{C-Cl} >$ for the OxIn (black line) and the $S_N2$ pathways (grey line) for oxidative addition of the $CH_3$–Cl bond Pd; (c) decomposition of $\Delta E$ for oxidative addition of the $CH_3$–Cl bond to Pd along the $S_N2$ pathway (black lines), to $PdCl^-$ along the $S_N2$ pathway (grey lines), and to $PdCl^-$ along the OxIn pathway (light-grey lines), along the reaction coordinate projected onto the C–X bond length. Dots indicate TSs

the C–Cl bond, in particular as the rearrangement stage of the latter reaction is entered, in which the expelled leaving group migrates towards palladium. In the corresponding TS **13d**, which is located in this rearrangement stage, the C–Cl bond is stretched by 1.38 Å with respect to isolated chloromethane **4** (see Figures 11.1 and 11.3). This has to be compared with the TS for oxidative insertion (**4b**), in which the C–Cl bond is expanded by only 0.23 Å. The point of largest expansion along the $S_N2$ pathway is reached *beyond* this TS, at a stretch of almost 1.6 Å. Thereafter, in the process of approaching the Pd atom, the expelled $Cl^-$ leaving group also comes closer to carbon and the C–Cl bond somewhat contracts. Interestingly, as the energy drops in this final stage of the $S_N2$ pathway, the corresponding IRC merges with that of the OxIn pathway, already before the product (**4c**) is reached. Thus, after this merger, the C–Cl bond expands again a little. This causes the Z shape to the right in the $\Delta E(\zeta)$ profile of the $S_N2$ pathway.

Interestingly, the difference between the OxIn and $S_N2$ PESs does not come from the $\Delta E_{\text{strain}}$ curves, which, in fact, practically coincide. All differences originate instead from the behaviour of the metal-substrate interaction curves $\Delta E_{\text{int}}$. The $\Delta E_{\text{int}}$ curve of the $S_N2$ pathway is nearly always above that of the OxIn pathway, except for the beginning of the reaction, around $\zeta = 0.1$ Å and in the final stage of the reaction when the two pathways merge on the PES. Thus, the $\Delta E_{\text{int}}$ curve for $S_N2$ is less stabilizing and, importantly, much more shallow than that for OxIn. This causes the TS for the $S_N2$ pathway to shift far to the right, i.e., at a very large C–Cl stretch. This is also the reason why $\Delta E^{\neq}_{\text{strain}}$, i.e., the strain in the TS, is much larger for the $S_N2$ pathway: this is so because the $S_N2$ pathway reaches its highest point at a larger extent of C–Cl stretching, and *not* because the substrate-deformation mode along the $S_N2$ pathway is associated with more strain at a given C–Cl stretch.

But what causes the $\Delta E_{\text{int}}$ curve of the $S_N2$ pathway to be much more shallow than that of the OxIn pathway? A careful analysis shows that the main difference stems from the bonding orbital interactions and in particular from the backdonation from the occupied Pd-4*d* orbitals to the unoccupied $\sigma^*_{\text{C–Cl}}$ LUMO of chloromethane. In the case of the $S_N2$ pathway, this backdonation increases much less as the C–Cl bond expands than in the case of OxIn. This is caused by a much smaller increase of the overlap $< 4d \mid \sigma^*_{\text{C–Cl}} >$ along the $S_N2$ pathway than along the OxIn pathway, as can be seen in Figure 11.8b (OxIn: black line; $S_N2$: grey line). This is related to the nodal structure of the $\sigma^*_{\text{C–Cl}}$ LUMO or, to be more specific, with the extent to which the lobes of the metal 4*d* AOs cross the nodal planes of the chloromethane acceptor orbital. The importance of this nodal structure has already been pointed out above in a different context (see **II** and **III**). Here we present the quantitative results of the analyses: the contour plots in Figure 11.9 visualizes for both pathways how the $\sigma^*_{\text{C–Cl}}$ orbital overlaps with the most important 4*d* orbital (i.e., the one that provides the dominant contribution to the overlap)

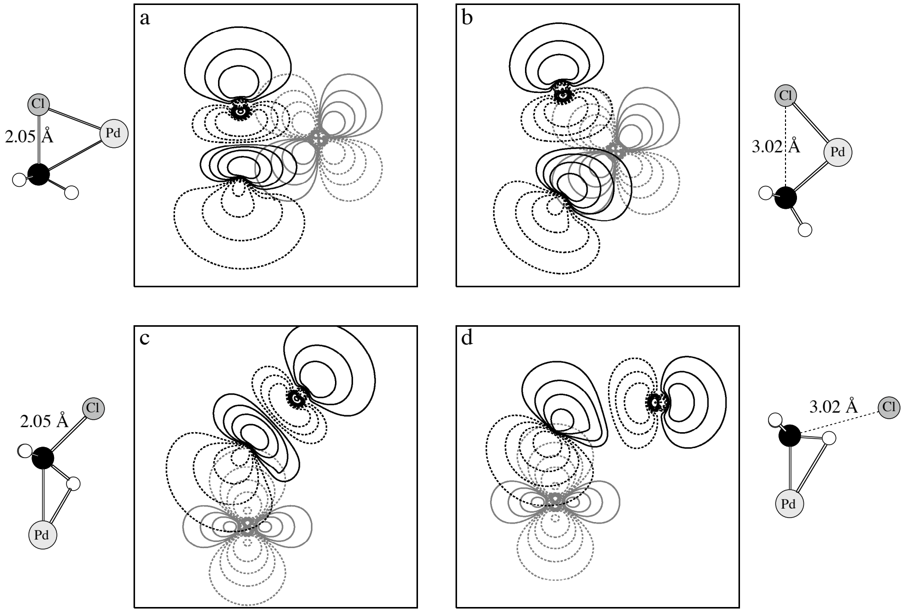

**Figure 11.9** Plots of the $\sigma^*_{\text{C–Cl}}$ orbital (black) and one of the Pd-4*d* orbitals (grey) at selected points along the OxIn (a, b) and $S_N2$ pathways (c, d) (box size 8 Å; contour values: ±0.02, ±0.05, ±0.1, ±0.2, ±0.5 a.u.; atoms oriented as shown)

when the C–Cl distance is 2.05 and 3.02 Å. In the case of the OxIn pathway, as can be seen in Figure 11.9a, the C–Cl distance of 2.05 Å is yet too short to achieve an optimal overlap with the Pd-4$d_{xy}$ orbital. There is cancellation of overlap because the lobes of the 4$d_{xy}$ orbital cross the nodal planes in the $\sigma^*_{\text{C–Cl}}$ orbital. Thus, the $< 4d_{xy} \mid \sigma^*_{\text{C–Cl}} >$ overlap increases steeply as the C–Cl bond further stretches because this reduces the destructive overlap (see Figures 11.8b and 11.9; see also **II** and **III**). At variance, in the case of the $S_N2$ pathway, in which the Pd atom approaches from the backside of the chloromethane C–Cl bond, there is initially much less cancellation of overlap between the Pd-4$d_{z^2}$ AO and the $\sigma^*_{\text{C–Cl}}$ orbital of chloromethane. And, importantly, the overlap situation hardly changes as the C–Cl bond expands. Consequently, the $< 4d_{z^2} \mid \sigma^*_{\text{C–Cl}} >$ overlap and thus the corresponding backdonation increases much less over a wide range of C–Cl bond distances along the $S_N2$ path.

Finally, we address the question *why* anion assistance nevertheless shifts the preference from OxIn to $S_N2$. Anion assistance, i.e., going from Pd to $PdCl^-$, stabilizes the $\Delta E_{\text{int}}$ curve of the OxIn pathway (as discussed above) but, through a similar mechanism, also that of the $S_N2$ pathway: compare the grey $\Delta E_{\text{int}}$ curve ($S_N2$ pathway for $PdCl^-$) with the black $\Delta E_{\text{int}}$ curve ($S_N2$ pathway for Pd) in Figure 11.8c. But since the TS for the $S_N2$ pathway is situated far to the right (see black and grey dots in Figure 11.8c), at large C–Cl expansion where $\Delta E_{\text{int}}$ is inherently more stabilizing, the additional stabilization due to anion assistance in $\Delta E_{\mathrm{int}}$ at that position of the TS (i.e., the effect of anion assistance on the TS interaction $\Delta E^{\neq}_{\mathrm{int}}$) is also larger than for the OxIn pathway (compare grey and light-grey curves in Figure 11.8c). This causes the overall barrier for the $S_N2$ pathway to drop below that of the OxIn pathway.

## 11.4 Conclusions

We have extended the Activation Strain model of chemical reactivity from a single-point analysis of the TS to an analysis along the entire reaction coordinate $\zeta$, i.e., $\Delta E(\zeta) = \Delta E_{\mathrm{strain}}(\zeta) + \Delta E_{\mathrm{int}}(\zeta)$. This extension enables one to understand qualitatively trends in the position of the TS along $\zeta$ and, therefore, the values of the activation strain $\Delta E^{\neq}_{\mathrm{strain}} = \Delta E_{\mathrm{strain}}(\zeta^{\mathrm{TS}})$ and TS interaction $\Delta E^{\neq}_{\mathrm{int}} = \Delta E_{\mathrm{int}}(\zeta^{\mathrm{TS}})$ and trends therein. We have applied this approach to a variety of archetypal C–X bond activation reactions, involving C–H, C–C, C–Cl and C–F bonds in strained and unstrained compounds as well as the effect of anion assistance on the palladium model catalyst. The low reaction barrier, e.g., for C–Cl as compared to C–H bond activation is straightforwardly explained by the lower C–Cl bond strength which manifests itself in a less destabilizing $\Delta E_{\mathrm{strain}}$ curve. Other phenomena that are addressed are anion assistance, competition between direct oxidative insertion (OxIn) and the alternative $S_N2$ pathway and the effect of ring strain.

The extended Activation Strain model also sheds light on a previously not understood anti-Hammond behaviour, under anion assistance, of palladium-catalyzed C–Cl bond activation. Anion assistance reduces the barrier and makes the reaction more exothermic but it shifts the TS towards the product side, not to the educt side as would be expected on the basis of the Hammond postulate.[147] The origin of this anti-Hammond behaviour is an increased affinity of the highly directional $\sigma^*_{\mathrm{C-Cl}}$ LUMO of $\mathrm{PdCl^-}$ towards the chlorine-lone pairs of the activated C–Cl bond. In the early stages of the reaction, this leads to less tilting of the methyl group which causes a delay in the build-up of a favourable $4d_{xz} + \sigma^*_{\mathrm{C-Cl}}$ backdonation. The reduction in (the slope of) the $\Delta E_{\mathrm{int}}$ curve is responsible for the shift of the TS towards the product side.

Another hitherto inaccessible insight is that the much higher barrier of catalytic C–C versus C–H activation originates from steric shielding of the C–C bond in ethane by C–H bonds. Thus, before a favourably stabilizing interaction with the C–C bond can occur the C–H bonds must be bent away which causes the metal-substrate interaction $\Delta E_{\mathrm{int}}(\zeta)$ in C–C activation to lag behind. Such a steric shielding is not present in the activation of the C–H bond which is always directly accessible from the hydrogen side.

# Gearfetting

*Teoretyske stúdzjes nei katalytyske biningsaktivearring*

It ûndersyk yn de teoretyske gemy jout wichtige ynsichten yn it ferrin fan gemyske reaksjes. Yn dit proefskrift wurdt ferslach dien fan in gearhingjende rige stúdzjes nei in klasse fan biningsaktivearringsreaksjes dêr't it oergongsmetaal palladium (Pd) in haadrol yn spilet. Dy oksidative-addysjereaksjes steane model foar in wichtige groep reaksjes op it mêd fan de homogene katalyze.

Yn haadstik 1 wurdt it ûndersyk fan dit proefskrift yn it bredere ramt fan it ûndersyk nei homogene katalyze setten. Yn haadstik 2 wurde de brûkte teoretyske konsepten neier beljochte. Yn termen fan rekkenkundige kosten is it fakentiids te djoer sekuere resultaten út de saneamde '*ab initio*'-teory te heljen. Tichtheidsfunksjonaalteory (dichtheidsfunctionaaltheorie: DFT) is in effisjint en dêrmei ûnmisber alternatyf dat al by steat is relevante modelsystemen te behanneljen. In beswier tsjin guon gongbere DFT-benaderings is in beskate ûnderskatting fan reaksjebarrières. Dêrom binne yn dit proefskrift detaillearre falidaasjestúdzjes útfierd, wêryn't de komputasjonele kondysjes fan kar op harren deugdsumens ûndersocht binne. Foar dat doel binne der ferlikings makke mei sekuere itichwearden dy't út avansearre '*ab initio*'-metoaden weikomme.

It earste part fan it ûndersyk, yn de haadstikken 3 oant 7, hâldt him dwaande mei it krijen fan dy betroubere itichwearden foar inkele ienfâldige modelreaksjes. Dat binne de aktivearrings troch Pd fan de koalstof-wetterstofbining (C–H), de koalstof-koalstofbining (C–C), de koalstof-fluorbining (C–F) en de koalstof-gloarbining (C–Cl). Oan de iene kant krije wy dêrmei betroubere kompleksaasje-, aktivearrings- en reaksjeenergyen, oan de oare kant toane wy ek it belang fan it brûken fan basissets mei foldwaande polarisaasjefunksjes en fan korreksje foar de basissetsuperposysjeflater oan. De itichwearden dy't dêr útkomme, binne brûkt om ús DFT-oanpak te falidearjen. Sa is oantoand dat foar DFT basissetkonverginsje flugger berikt wurdt en dat it brûken fan de beferzen-rompbenadering gjin ferskil útmakket. In útwrydske rige tichtheidsfunksjonalen is hifke. Opmerklik is dat de ferskate aktivearringsenergyen troch guon GGA-funksjonalen as BLYP en OLYP, lykas ek troch it populêre hybrid-funksjonaal B3LYP, yn it bestek fan inkele kcal/mol reprodusearre wurde. Om't BLYP as in robúst funksjonaal goed bekend stiet, is it brûkt yn it twadde part fan it ûndersyk, yn de haadstikken 8 oant 11.

Yn haadstik 8 binne inkele oergongsmetalen, wêrûnder Pd, ferlike mei inkele haadgroepmetalen yn de aktivearring fan C–H- en C–Cl-binings. Mei help fan it aktivearringsspanningsmodel, wêryn't de reaksjebarrière ûntlede wurdt yn de aktivearringsspanning fan de yn de oergongstastân ferfoarme reaktanten en de stabilisearjende wikselwurking tusken dy reaktanten, kinne de ferskillen yn reaktiviteit analysearre en begrepen wurde yn termen fan eigenskippen fan de reaktanten. Fan de ûndersochte metalen kringt Pd it maklikst yn de binings troch de grutte stabilisearjende wikselwurking. Soks kin op de poerbêste elektrondonearjende en elektronakseptearjende fermogens fan Pd weromlaat wurde.

Yn haadstik 9 is in oersjoch jûn fan de ynsersje fan Pd yn de rige fan wetterstofhalogeniden en dihalogenen. It ferrin fan de reaktiviteit bylâns de rige fan halogenen blykt in meïnoar opspyljen fan biningssterkte en wikselwurkingsmooglikheden dy't op de elektroanyske struktuer fan de substraten weromlaat wurde kinne. It is fierder nijsgjirrich dat de ynfloed fan in relativistyske oanpak op aktivearrings- en reaksjeenergyen ôfnimt foar de swierdere halogenen troch inoar tsjinwurkjende relativistyske effekten.

Yn haadstik 10 is it aktivearjen fan de koalstof-halogeenbining yn de rige fan halogeenmetanen troch Pd en it anion-assistearre $PdCl^-$ ûndersocht. It docht bliken dat der twa stereogemysk ferskillende reaksjepaden binne: (i) direkte oksidative ynsersje (OxIn) en (ii) in alternatyf $S_N2$-meganisme. Yn de gasfaze foar Pd is de barrière it leechst foar it OxIn reaksjepaad. Anionassistinsje feroaret de foarkar foar alle halogeenmetanen nei it alternative $S_N2$-paad. Oplosmiddeleffekten yn wetter feroarje yn it gefal fan Pd de foarkar foar de lichtere halogenen fan OxIn nei $S_N2$, mar yn it gefal fan $PdCl^-$ foar de swierdere halogenen fan $S_N2$ nei OxIn. Mei help fan it aktivearringsspanningsmodel, en benammen ek fan in útwreiding fan dit model foar de kondinsearre faze, binne dizze feroaringen yn reaksjefoarkar ynsichtlik makke.

Yn haadstik 11, ta beslút, is in wêzentlike útwreiding fan it aktivearringsspanningsmodel yntrodusearre, wêryn't de energydekomposysje net allinnich yn de oergongstastân, mar yn 'e rin fan it folsleine reaksjepaad fan reaktantkompleks ta produkt analysearre wurdt. Dy útwreiding makket it mooglik ferskillen yn posysje fan de oergongstastân bylâns de reaksjekoördinaat te begripen yn termen fan it ferrin yn spanning en de wikselwurking tusken de reaktanten bylâns de reaksjekoördinaat. Under de fenomenen dy't dêrmei ferklearre wurde koenen, binne it anti-Hammond-gedrach fan de C–Cl-biningsaktivearring ûnder anionassistinsje, de kompetysje tusken OxIn en $S_N2$ en de aardich hegere barrière foar de C–C- yn ferliking mei de C–H-biningsaktivearring, soks nettsjinsteande de swakkere biningssterkte fan de C–C-bining. Nijsgjirrich is dat blykt dat de hegere barrière gearhinget mei it feit dat de C–C bining yn etaan sterysk ôfskerme wurdt troch de seis C–H-binings deromhinne.

# Samenvatting

*Theoretische studies aan katalytische bindingsactivering*

Het onderzoek in de theoretische chemie levert belangrijke inzichten in het verloop van chemische reacties. In dit proefschrift wordt verslag gedaan van een samenhangende reeks studies naar een klasse van bindingsactiveringsreacties waarin het overgangsmetaal palladium (Pd) een hoofdrol speelt. Deze oxidatieve-additiereacties staan model voor een belangrijke groep reacties op het gebied van de homogene katalyse.

In hoofdstuk 1 wordt het onderzoek in dit proefschrift geplaatst in het bredere verband van het onderzoek naar homogene katalyse. In hoofdstuk 2 worden de gebruikte theoretische concepten nader toegelicht. Het verkrijgen van nauwkeurige resultaten uit zogeheten '*ab initio*'-theorie is vaak te duur in termen van rekenkundige kosten. Dichtheidsfunctionaaltheorie (DFT) is een efficiënt en daarom onontbeerlijk alternatief dat wel in staat is relevante modelsystemen te behandelen. Een bezwaar tegen sommige gangbare DFT-benaderingen is een zekere onderschatting van reactiebarrières. Daarom zijn in dit proefschrift gedetailleerde validatiestudies verricht, waarin de gekozen computationele condities op hun deugdelijkheid zijn onderzocht. Hiertoe is vergeleken met nauwkeurige ijkwaarden, verkregen met geavanceerde '*ab initio*'-methoden.

Het eerste deel van het onderzoek, beschreven in de hoofdstukken 3 tot 7, concentreert zich op het verkrijgen van die betrouwbare ijkwaarden voor enkele eenvoudige modelreacties. Dit zijn de Pd-gekatalyseerde activeringen van de koolstof-waterstofbinding (C–H), de koolstof-koolstofbinding (C–C), de koolstof-fluorbinding (C–F) en de koolstof-chloorbinding (C–Cl). Naast het feit dat betrouwbare complexatie-, activerings- en reactieenergieën zijn verkregen, is ook het belang van het gebruik van basissets met voldoende polarisatiefuncties en van correctie voor de basissetsuperpositiefout aangetoond. De verkregen ijkwaarden zijn gebruikt om onze DFT-aanpak te valideren. Zo is aangetoond dat, voor DFT, basissetconvergentie sneller bereikt wordt en het gebruik van de bevroren-rompbenadering een verwaarloosbaar effect heeft. Een uitgebreide reeks dichtheidsfunctionalen is getoetst. Opmerkelijk is dat de verschillende activeringsenergieën door zowel sommige GGA-functionalen zoals BLYP en OLYP alsook door het populaire hybrid-functionaal B3LYP binnen enkele kcal/mol gereproduceerd worden. Omdat BLYP een robuust en welbekend functionaal is, is dit gebruikt in het tweede deel van het onderzoek, beschreven in de hoofdstukken 8 tot 11.

In hoofdstuk 8 zijn enkele overgangsmetalen, waaronder Pd, vergeleken met enkele hoofdgroepmetalen in de activering van C–H- en C–Cl-bindingen. Met behulp van het activeringsspanningsmodel, waarin de reactiebarrière wordt ontleed in de activeringsspanning van de in de overgangstoestand vervormde reactanten en de stabiliserende wisselwerking tussen deze reactanten, kunnen de verschillen in reactiviteit geanalyseerd en begrepen worden in termen van eigenschappen van de reactanten. Onder de onderzochte metalen, dringt Pd het gemakkelijkst de bindingen binnen door de grote stabiliserende wisselwerking. Dit kan herleid worden tot de uitstekende electrondonerende en electronaccepterende capaciteiten van Pd.

In hoofdstuk 9 is een overzicht gegeven van de insertie van Pd in de reeks van waterstofhalogeniden en dihalogenen. Het verloop van de reactiviteit langs de reeks van halogenen blijkt een samenspel van bindingssterkte en wisselwerkingsmogelijkheden die herleid kunnen worden tot de electronische structuur van de substraten. Interessant is verder dat de invloed van een relativistische aanpak op activerings- en reactieënergieën afneemt voor de zwaardere halogenen door elkaar tegenwerkende relativistische effecten.

In hoofdstuk 10 is de activering van de koolstof-halogeenbinding in de reeks van halogeenmethanen door Pd en het anion-geassisteerde $PdCl^-$ onderzocht. Er blijken twee stereochemisch verschillende reactiepaden te zijn: (i) directe oxidatieve insertie (OxIn) en (ii) een alternatief $S_N2$-mechanisme. In de gasfase voor Pd is de barrière het laagst voor het OxIn reactiepad. Anionassistentie verandert de voorkeur voor alle halogeenmethanen naar het alternatieve $S_N2$-pad. Oplosmiddeleffecten in water veranderen in geval van Pd de voorkeur voor de lichtere halogenen van OxIn naar $S_N2$, maar in geval van $PdCl^-$ voor de zwaardere halogenen van $S_N2$ naar OxIn. Met behulp van het activeringsspanningsmodel, en met name ook van een uitbreiding van dit model voor de gecondenseerde fase, zijn deze veranderingen in reactievoorkeur inzichtelijk gemaakt.

In hoofdstuk 11, tot besluit, is een wezenlijke uitbreiding van het activeringsspanningsmodel geïntroduceerd, waarin de energiedecompositie niet alleen in de overgangstoestand, maar langs het gehele reactiepad van reactantcomplex tot product wordt geanalyseerd. Deze uitbreiding maakt het mogelijk verschillen in positie van de overgangstoestand langs de reactiecoördinaat te begrijpen in termen van het verloop in spanning in en wisselwerking tussen de reactanten langs de reactiecoördinaat. Verschillende fenomenen die hiermee verklaard konden worden, zijn het anti-Hammond-gedrag van de C–Cl-bindingsactivering onder anionassistentie, de competitie tussen OxIn en $S_N2$ en de beduidend hogere barrière voor C–C- dan voor C–H-bindingsactivering, ondanks de zwakkere bindingssterkte van de C–C-binding. Interessant genoeg blijkt de hogere barrière samen te hangen met het feit dat de C–C-binding in ethaan sterisch afgeschermd wordt door de zes omringende C–H-bindingen.

# Zusammenfassung

*Theoretische Studien zur katalytischen Bindungsaktivierung*

Die Forschung in der theoretischen Chemie liefert Einsichten in den Verlauf chemischer Reaktionen. Diese Doktorarbeit beinhaltet eine zusammenhängende Reihe Studien über eine Klasse von Bindungsaktivierungsreaktionen in welchen das Übergangsmetall Palladium (Pd) eine wichtige Rolle spielt. Diese oxidativen Additionsreaktionen sind exemplarisch für eine wichtige Klasse von Reaktionen in der homogenen Katalyse.

In Kapitel 1 werden die Ergebnisse dieser Doktorarbeit in den größeren Kontext der Forschung im Bereich der homogenen Katalyse gestellt. Kapitel 2 beschäftigt sich näher mit den verwendeten theoretischen Konzepten. Genaue Resultate aus der sogenannten „*ab initio*“-Theorie zu erlangen ist oft zu teuer. Die Dichtefunktionaltheorie (DFT) ist eine effiziente und deswegen unentbehrliche Alternative, die in der Lage ist, relevante Modellsysteme zu behandeln. Ein Einwand gegen gängige DFT-Näherungen ist eine gewisse Unterschätzung von Reaktionsbarrieren. Aus diesem Grund sind in dieser Doktorarbeit ausführliche Validierungsstudien durchgeführt worden, um die gewählten Rechenmethoden auf ihre Genauigkeit zu prüfen. Zu diesem Zweck wurden sie mit genauen Referenzwerten verglichen, die sich aus sophistizierten „*ab initio*“-Methoden ergaben.

Der erste Teil dieser Arbeit, Kapitel 3 bis 7, konzentriert sich auf die Erzeugung jener zuverlässigen Referenzwerte für einige Modellreaktionen, nämlich die Pd-katalysierten Aktivierungen der Kohlenstoff-Wasserstoffbindung (C–H), der Kohlenstoff-Kohlenstoffbindung (C–C), der Kohlenstoff-Fluorbindung (C–F) und der Kohlenstoff-Chlorbindung (C–Cl). Es wurden jedoch nicht nur zuverlässige Komplexierungs-, Aktivierungs- und Reaktionsenergien erzeugt. Obendrein wurde auch die Bedeutung der Verwendung von Basissätzen mit hinreichenden Polarisationsfunktionen und der Korrektur des Basissatzsuperpositionsfehlers aufgezeigt. Die erhaltenen Referenzwerte wurden verwendet um unser DFT-Verfahren zu validieren. So zeigte sich, daß bei DFT Basissatzkonvergenz schneller erreicht wird und die Verwendung der Starr-Rumpf-Näherung eine vernachlässigbare Auswirkung hat. Eine beträchtliche Anzahl von Funktionalen wurde geprüft. Bemerkenswert ist, daß die verschiedenen Aktivierungsenergien sowohl durch einige GGA-Funktionale wie BLYP und OLYP, als auch durch das beliebte Hybrid-Funktional B3LYP innerhalb einiger kcal/mol reproduziert werden. Weil BLYP robust und wohlbekannt ist, wurde es im zweiten Teil dieser Arbeit, in Kapitel 8 bis 11, verwendet.

In Kapitel 8 werden einige Übergangsmetalle, unter anderem Pd, mit einigen Hauptgruppenmetallen bezüglich der Aktivierung von C–H- und C–Cl-Bindungen verglichen. Mit Hilfe des Aktivierungsspannungsmodells, in dem die Reaktionsbarriere in die Aktivierungsspannung der im Übergangszustand verzerrten Ausgangsstoffe und in die stabilisierenden Wechselwirkung zwischen diesen zerlegt wird, können die Unterschiede in der Reaktivität anhand der Eigenschaften der Ausgangsstoffe begriffen werden. Von den untersuchten Metallen dringt Pd wegen seiner großen stabilisierenden Wechselwirkung am einfachsten in die Bindungen ein. Dies kann auf die ausgezeichneten elektrondonierenden und -akzeptierenden Eigenschaften des Pd zurückgeführt werden.

In Kapitel 9 wird eine Übersicht über die Insertion des Pd in die Reihe der Wasserstoffhalogenide und Dihalogene gegeben. Der Verlauf der Reaktivität entlang der Halogenreihe zeigt ein Zusammenspiel von Bindungsstärke und Wechselwirkungsmöglichkeiten, die auf die elektronische Struktur der Substrate zurückgeführt werden können. Interessant ist ferner, daß der Einfluß eines relativistischen Verfahrens auf die Aktivierungs- und Reaktionsenergien für die schwereren Halogene wegen einander entgegenwirkender relativistischer Einwirkungen abnimmt.

In Kapitel 10 wird die Aktivierung der Kohlenstoff-Halogenbindung in Halogenmethanen durch Pd und das anionassistierte $PdCl^-$ untersucht. Es ergibt sich, daß zwei stereochemisch unterschiedliche Reaktionspfade existieren: (i) direkte oxidative Insertion (OxIn) und (ii) ein alternativer $S_N2$-Mechanismus. In der Gasphase ist für Pd die Barriere für den OxIn-Pfad am niedrigsten. Anionassistenz ändert die Präferenz für alle Halogenmethane zugunsten des $S_N2$-Pfades. Lösungsmitteleffekte in Wasser verändern im Falle des Pd die Präferenz für die leichteren Halogene von OxIn zu $S_N2$, im Falle des $PdCl^-$ aber für die schwereren Halogene von $S_N2$ zu OxIn. Mit Hilfe des Aktivierungsspannungsmodells, und besonders einer Erweiterung dieses Modells für die kondensierte Phase, werden diese Änderungen in der Reaktionspräferenz verständlich gemacht.

Schließlich wird in Kapitel 11 eine wesentliche Erweiterung des Aktivierungsspannungsmodells eingeführt, in der die Energiezerlegung nicht nur im Übergangszustand, sondern entlang des ganzen Reaktionspfades, von Reaktandkomplex bis Produkt, analysiert wird. Diese Erweiterung macht es möglich, Unterschiede in der Lage des Übergangszustandes auf der Reaktionskoordinate anhand des Verlaufs der Spannung in und Wechselwirkung zwischen den Ausgangsstoffen entlang der Reaktionskoordinate zu verstehen. Einige hiermit erklärte Phänomene sind das anti-Hammond-Verhalten der C–Cl-Bindungsaktivierung unter Anionassistenz, die Konkurrenz zwischen OxIn und $S_N2$ und die bedeutend höhere Barriere für C–C- als für C–H-Bindungsaktivierung, trotz der schwächeren Bindungsstärke der C–C-Bindung. Interessanterweise ergibt sich, daß die höhere Barriere damit zusammenhängt, daß die C–C-Bindung in Ethan von den sechs umringenden C–H-Bindungen sterisch abgeschirmt wird.

# Dankwoord

Tot slot wil ik iedereen danken die, direct of indirect, aan de totstandkoming van dit proefschrift heeft bijgedragen. Een aantal mensen wil ik met name noemen:

Allereerst wil ik mijn copromotor dr. Matthias Bickelhaupt danken. Zonder zijn inspiratie en ondersteuning was dit onderzoek in het geheel niet mogelijk geweest. Het is aan zijn vertrouwen en vasthoudendheid te danken dat ik doorzette wanneer ik niet meer overzag waar onze resultaten toe moesten leiden. Zijn snelle analytische vermogen, chemische intuïtie en praktische doelgerichtheid waren op zulke momenten onmisbaar. Daarnaast wil ik hem ook vooral danken voor de vele goede gesprekken op allerlei gebied en de raad en bijstand waar die nodig waren.

Mijn promotor prof. dr. Evert Jan Baerends dank ik voor het in mij gestelde vertrouwen. Hij was degene die mij als eerste vertrouwd maakte met de theoretische chemie en mij op een cruciaal ogenblik adviseerde het waagstuk van een promotieonderzoek aan te gaan. Ik ben dankbaar dat ik zo lang heb mogen vertoeven in zijn afdeling.

Belangrijke bijdragen aan het onderzoek zijn geleverd door dr. Axel Diefenbach, prof. dr. Miquel Solà, dr. Luuk Visscher, prof. dr. Attila Kovács, Daan Geerke, Ruud Visser en Willem-Jan van Zeist. Ik dank hun voor de publicaties die hieruit voortgevloeid zijn.

Prof. dr. K. Lammertsma, prof. dr. N. M. M. Nibbering, dr. C. Oostenbrink en dr. J. N. H. Reek dank ik voor het kritisch lezen van het manuscript van dit proefschrift.

De collega's van de afdeling Theoretische Chemie, uit verleden en heden, dank ik voor de goede sfeer op het werk. In het bijzonder wil ik noemen Patricia Bento, Paula van Berkum, dr. Leonardo Bernasconi, dr. Célia Bickelhaupt, Marc van Bochove, Nanda Bramer, dr. Rosa Bulo, dr. Bernd Ensing, dr. Timo Fleig, dr. Stan van Gisbergen, dr. Oleg Gritsenko, dr. Wolfgang Hieringer, dr. Ivan Infante, Kitty Kleinlein, Manuel Louwerse, Klaas Giesbertz, dr. Marcello Luppi, dr. Drew McCormack, dr. Johannes Neugebauer, Paul Nicu, dr. Laura Orian, dr. Kasia Pernal, dr. Pier Philipsen, dr. Jordi Poater, Simon Pierrefixe, Jetze Sikkema, dr. Joost van Stralen, dr. Marcel Swart, Tushar van der Wijst, Maxim Zacharov en alle anderen, medewerkers en gasten, die de koffie- en lunchpauzes maakten tot iets om naar uit te kijken.

Dr. Andreas Götz en Christoph Jacob dank ik voor hun hulp bij het vertalen van de samenvatting in het Duits. Henk Wolf dank ik voor zijn Friese vertaling.

Hylke de Jong en Sönke Roterberg dank ik voor het mij terzijde willen staan als paranimfen.

Een belangrijke rol in het volhouden van het promotieonderzoek speelden ook mensen van buiten. Met name wil ik noemen de studentenpredikanten ds. André Fox en dr. Geert van der Bom en studentenpastor Tjeerd Jansen SJ. Zij bezorgden mij inspirerende avonden in het pand aan de Van Eeghenstraat 90 en bezinningsvolle kloosterweekeinden. Deze afwisseling heeft veel voor mij betekend. Jan Bakker dank ik voor de boeiende ontmoetingen die we op het studentenpastoraat of elders, zoals bij cantatediensten, meemaakten. Het is aan hem te danken dat er een Friese samenvatting in dit proefschrift staat. Dr. Margriet Gosker dank ik voor haar inzet en gastvrijheid. De avonden en weekeinden met de jongeren uit de gemeente bij haar thuis betekenden veel voor mij.

Ik dank ook alle andere vrienden, kennissen en familieleden die mij geholpen hebben en wier namen ik hier onmogelijk allemaal op kan noemen. Om niemand te vergeten, wil ik hen allen op deze wijze danken.

Wiebke Roterberg dank ik voor haar niet aflatende steun. Ze heeft mijn leven als promovendus bijna vanaf het begin mee mogen maken en de frustratie op momenten dat het allemaal tegenzat geduldig verdragen. Ze gaf de inspiratie om door te zetten en alles goed af te ronden.

Tenslotte, mijn grootste dank gaat uit naar heit en mem, die immer een onvoorwaardelijk vertrouwen in me hebben gehad. Zij hebben me altijd de mogelijkheden gegeven het beste uit me te halen dat mogelijk was. Ik hoop dat ze trots op me kunnen zijn.

# List of publications

1. G. Th. de Jong, L. Visscher
   *Theor. Chem. Acc.* **2002**, *107*, 304
   "Using the locality of the small-component density in molecular Dirac-Hartree-Fock calculations"

2. G. Th. de Jong, M. Solà, L. Visscher, F. M. Bickelhaupt
   *J. Chem. Phys.* **2004**, *121*, 9982
   "*Ab initio* benchmark study for the oxidative addition of $CH_4$ to Pd: Importance of basis-set flexibility and polarization"

3. A. Diefenbach, G. Th. de Jong, F. M. Bickelhaupt
   *Mol. Phys.* **2005**, *103*, 995
   "Fragment-oriented design of catalysts based on the activation strain model"

4. A. Diefenbach, G. Th. de Jong, F. M. Bickelhaupt
   *J. Chem. Theory Comput.* **2005**, *1*, 286
   "Activation of H–H, C–H, C–C and C–Cl bonds by Pd and $PdCl^-$. Understanding anion assistance in C–X bond activation"

5. G. Th. de Jong, D. P. Geerke, A. Diefenbach, F. M. Bickelhaupt
   *Chem. Phys.* **2005**, *313*, 261
   "DFT benchmark study for the oxidative addition of $CH_4$ to Pd. Performance of various density functionals"

6. G. Th. de Jong, D. P. Geerke, A. Diefenbach, M. Solà, F. M. Bickelhaupt
   *J. Comp. Chem.* **2005**, *26*, 1006
   "Oxidative addition of the ethane C–C bond to Pd. An *ab initio* benchmark and DFT validation study"

7. G. Th. de Jong, F. M. Bickelhaupt
   *J. Phys. Chem. A* **2005**, *109*, 9685
   "Oxidative addition of the fluoromethane C–F bond to Pd. An *ab initio* benchmark and DFT validation study"

8. G. Th. de Jong, F. M. Bickelhaupt
   *J. Chem. Theory Comput.* **2006**, *2*, 322
   "Oxidative addition of the chloromethane C–Cl bond to Pd, an *ab initio* benchmark and DFT validation study"

9. G. Th. de Jong, R. Visser, F. M. Bickelhaupt
   *J. Organomet. Chem.* **2006**, *691*, 4341
   "Oxidative addition to main group versus transition metals: Insights from the Activation Strain model"

10. G. Th. de Jong, A. Kovács, F. M. Bickelhaupt
    *J. Phys. Chem. A* **2006**, *110*, 7943
    "Oxidative addition of hydrogen halides and dihalogens to Pd. Trends in reactivity and relativistic effects"

11. G. Th. de Jong, F. M. Bickelhaupt
    *J. Chem. Theory Comput.* **2007**, *3*, in press
    "Catalytic carbon-halogen bond activation. Trends in reactivity, selectivity and solvation"

12. G. Th. de Jong, F. M. Bickelhaupt
    Submitted for publication
    "Transition-state energy and position along the reaction coordinate in an extended Activation Strain model. Application to catalytic carbon-element bond activation"

# Bibliography

1 A. Diefenbach *Fragment-oriented Design of Catalysts. A theoretical study on bond activation*, Doctoral dissertation, Philipps-Universität, Marburg, 2000.

2 J. Tsuji *Palladium reagents and catalysts*, Wiley, Chichester, 1995.

3 L. S. Hegedus *Transition Metals in the Synthesis of Complex Organic Molecules. Second Edition*, University Science Books, Sausalito, California, 1999.

4 J. P. Collman, L. S. Hegedus *Principles and Applications of Organotransition Metal Chemistry*, University Science Books, Mill Valley, California, 1980.

5 D. Forster *J. Am. Chem. Soc.* **1975**, *97*, 951.

6 P. Hohenberg, W. Kohn *Phys. Rev.* **1964**, *136*, B864.

7 W. Kohn, L. J. Sham *Phys. Rev.* **1965**, *140*, A1133.

8 R. G. Parr, W. Yang *Density-Functional Theory of Atoms and Molecules*, Oxford University Press, New York, 1989.

9 W. Koch, M. C. Holthausen *A Chemist's Guide to Density Functional Theory*, Wiley-VCH Verlag, Weinheim, 2000.

10 J. Baker, M. Muir, J. Andzelm *J. Chem. Phys.* **1995**, *102*, 2063; V. Barone, C. Adamo *J. Chem. Phys.* **1996**, *105*, 11007; H. T. Thümmel, C. W. Bauschlicher Jr. *J. Phys. Chem. A* **1997**, *101*, 1188; R. D. Bach, M. N. Glukhovtsev, C. Gonzales *J. Am. Chem. Soc.* **1998**, *120*, 9902; O. V. Gritsenko, B. Ensing, P. R. T. Schippers, E. J. Baerends *J. Phys. Chem. A* **2000**, *104*, 8558; J. Poater, M. Solà, M. Duran, J. Robles *Phys Chem Chem Phys* **2002**, *4*, 722.

11 F. Jensen *Introduction to computational chemistry*, John Wiley & Sons, Chichester, 1999; Ch. J. Cramer *Essentials of computational chemistry: theories and models*, John Wiley & Sons, Chichester, 2002.

12 S. F. Boys, F. Bernardi *Mol. Phys.* **1970**, *19*, 553.

13 R. E. Moss *Advanced molecular quantum mechanics: an introduction to relativistic quantum mechanics and the quantum theory of radiation*, Chapman and Hall, London, 1973.

14 G. Th. de Jong *Research report: Benaderingen in relativistische moleculaire berekeningen. Naar een lineaire schaling in de kleine componenten in het programma DIRAC*, Vrije Universiteit, Amsterdam, 2001.

15 G. Th. de Jong, L. Visscher *Theor. Chem. Acc.* **2002**, *107*, 304.

16 L. Visscher *Theor. Chem. Acc.* **1997**, *98*, 68.

17 K. G. Dyall *J. Chem. Phys.* **1994**, *100*, 2118.

18 J. M. Lévy-Leblond *Commun. Math. Phys.* **1967**, *6*, 286.

19 E. van Lenthe, E. J. Baerends, J. G. Snijders *J. Chem. Phys.* **1994**, *101*, 9783.

20 F. M. Bickelhaupt, T. Ziegler, P. von Ragué Schleyer *Organometallics* **1995**, *14*, 2288.

21 F. M. Bickelhaupt *J. Comput. Chem.* **1999**, *20*, 114.

22 A. Diefenbach, F. M. Bickelhaupt *J. Chem. Phys.* **2001**, *115*, 4030.

23 A. Diefenbach, F. M. Bickelhaupt *J. Phys. Chem. A* **2004**, *108*, 8460.

24 A. Diefenbach, G. Th. de Jong, F. M. Bickelhaupt *J. Chem. Theory Comput.* **2005**, *1*, 286.

25 A. Diefenbach, G. Th. de Jong, F. M. Bickelhaupt *Mol. Phys.* **2005**, *103*, 995.

26 A. Klamt, G. Schüürmann *J. Chem. Soc., Perkin Trans. 2* **1993**, 799; A. Klamt *J. Phys. Chem.* **1995**, *99*, 2224.

27 B. Ensing, F. Buda, P. Blöchl, E. J. Baerends *Angew. Chem. Int. Ed.* **2001**, *40*, 2893.

28 R. H. Crabtree *Chem. Rev.* **1995**, *95*, 987; B. A. Arndtsen, R. G. Bergman, T. A. Mobley, Th. H. Peterson *Acc. Chem. Res.* **1995**, *28*, 154.

29 A. E. Shilov, G. B. Shul'pin *Chem. Rev.* **1997**, *97*, 2879.

30 C. Hall, R. N. Perutz *Chem. Rev.* **1996**, *96*, 3125.

31 A. Dedieu *Chem. Rev.* **2000**, *100*, 543.

32 P. Fayet, A. Kaldor, D. M. Cox *J. Chem. Phys.* **1990**, *92*, 254.

33 J. C. Weisshaar *Acc. Chem. Res.* **1993**, *26*, 213.

34 J. J. Carroll, J. C. Weisshaar *J. Am. Chem. Soc.* **1993**, *115*, 800.

35 J. J. Carroll, K. L. Haug, J. C. Weisshaar, M. R. A. Blomberg, P. E. M. Siegbahn, M. Svensson *J. Phys. Chem.* **1995**, *99*, 13955.

36 M. L. Campbell *Chem. Phys. Lett.* **2002**, *365*, 361.

37 J. J. Low, W. A. Goddard III *J. Am. Chem. Soc.* **1984**, *106*, 8321.

38 J. J. Low, W. A. Goddard III *Organometallics* **1986**, *5*, 609.

39 M. R. A. Blomberg, P. E. M. Siegbahn, U. Nagashima, J. Wennerberg *J. Am. Chem. Soc.* **1991**, *113*, 424.

40 M. Svensson, M. R. A. Blomberg, P. E. M. Siegbahn *J. Am. Chem. Soc.* **1991**, *113*, 7076.

41 M. R. A. Blomberg, P. E. M. Siegbahn, M. Svensson *J. Am. Chem. Soc.* **1992**, *114*, 6095.

42 P. E. M. Siegbahn, M. R. A. Blomberg, M. Svensson *J. Am. Chem. Soc.* **1993**, *115*, 1952.

43 A. M. C. Wittborn, M. Costas, M. R. A. Blomberg, P. E. M. Siegbahn *J. Chem. Phys.* **1997**, *107*, 4318.

44 E. D. Smurnyi, I. P. Gloriozov, Yu. A. Ustynuk *Russ. J. Phys. Chem.* **2003**, *77*, 1699.

45 P. E. M. Siegbahn, M. R. A. Blomberg, M. Svensson *Chem. Phys. Lett.* **1994**, *223*, 35.

46 P. J. Hay *J. Am. Chem. Soc.* **1981**, *103*, 1390.

47 S. Huzinaga *J. Chem. Phys.* **1977**, *66*, 4245.

48 R. C. Raffenetti *J. Chem. Phys.* **1973**, *58*, 4452.

49 E. J. Baerends, D. E. Ellis, P. Ros *Chem. Phys.* **1973**, *2*, 41.

50 C. Fonseca Guerra, J. G. Snijders, G. te Velde, E. J. Baerends *Theor. Chem. Acc.* **1998**, *99*, 391; G. te Velde, F. M. Bickelhaupt, E. J. Baerends, C. Fonseca Guerra, S. J. A. van Gisbergen, J. G. Snijders, T. Ziegler *J. Comput. Chem.* **2001**, *22*, 931.

51 E. J. Baerends *et al.*, *ADF2002.03*, SCM, Theoretical Chemistry, Vrije Universiteit, Amsterdam, The Netherlands, 2002.

52 A. D. Becke *Phys. Rev. A* **1988**, *38*, 3098.

53 C. Lee, W. Yang, R. G. Parr *Phys. Rev. B* **1988**, *37*, 785.

54 M. J. Frisch *et al.*, *GAUSSIAN 03, Rev. A.11*, Gaussian Inc., Pittsburgh, PA, 2003.

55 L. Visscher, T. J. Lee, K. G. Dyall *J. Chem. Phys.* **1996**, *105*, 8769.

56 T. Saue, T. Helgaker *J. Comput. Chem.* **2002**, *23*, 814; T. Saue *et al.*, *DIRAC, Release 3.2*, Syddansk Universitet, Odense, Denmark, 2000.

57 C. Møller, M. S. Plesset *Phys. Rev.* **1934**, *46*, 618.

58 R. Krishnan, J. A. Pople *Int. J. Quantum Chem.* **1978**, *14*, 91; R. Krishnan, M. J. Frisch, J. A. Pople *J. Chem. Phys.* **1980**, *72*, 4244.

59 G. D. Purvis III, R. J. Bartlett *J. Chem. Phys.* **1982**, *76*, 1910.

60 K. Raghavachari, G. W. Trucks, J. A. Pople, M. Head-Gordon *Chem. Phys. Lett.* **1989**, *157*, 479.

61 A. D. Becke *J. Chem. Phys.* **1993**, *98*, 5648; P. J. Stephens, F. J. Devlin, C. F. Chabalowski, M. J. Frisch *J. Phys. Chem.* **1994**, *98*, 11623.

62 Th. H. Dunning Jr. *J. Chem. Phys.* **1989**, *90*, 1007.

63 R. A. Kendall, Th. H. Dunning Jr., R. J. Harrison *J. Chem. Phys.* **1992**, *96*, 6796.

64 P. J. Hay, W. R. Wadt *J. Chem. Phys.* **1985**, *82*, 299.

65 V. Jonas, G. Frenking, M. T. Reetz *J. Comput. Chem.* **1992**, *13*, 919.

66 A. W. Ehlers, M. Böhme, S. Dapprich, A. Gobbi, A. Höllwarth, V. Jonas, K. F. Köhler, R. Stegmann, A. Veldkamp, G. Frenking *Chem. Phys. Lett.* **1993**, *208*, 111.

67 M. Torrent, M. Solà, G. Frenking *Chem. Rev.* **2000**, *100*, 439.

68 S. R. Langhoff, L. G. M. Petterson, C. W. Bauschlicher Jr. *J. Chem. Phys.* **1987**, *86*, 268.

69 K. Faegri Jr., personal communication.

70 L. Visscher, P. J. C. Aerts, O. Visser, W. C. Nieuwpoort *Int. J. Quantum Chem.: Quantum Chem. Symp.* **1991**, *25*, 131.

71 Y. Osanai, M. Sekiya, T. Noro, T. Koga *Mol. Phys.* **2003**, *101*, 65.

72 G. Frenking, I. Antes, M. Böhme, S. Dapprich, A. W. Ehlers, V. Jonas, A. Neuhaus, M. Otto, R. Stegmann, A. Veldkamp, S. F. Vyboishchikov in *Reviews in Computational Chemistry*, Kenny B. Lipkowitz, Donald B. Boyd, Eds.; VCH Publishers Inc., New York, 1996, Vol. 8, pp 63.

73 Th. R. Cundari, M. T. Benson, M. L. Lutz in *Reviews in Computational Chemistry*, Kenny B. Lipkowitz, Donald B. Boyd, Eds.; VCH Publishers Inc., New York, 1996, Vol. 8, pp 145.

74 T. Ziegler *Chem. Rev.* **1991**, *91*, 651; T. Ziegler *Can. J. Chem.* **1995**, *73*, 743.

75 N. M. M. Nibbering *Adv. Phys. Org. Chem.* **1988**, *24*, 1; F. M. Bickelhaupt *Mass Spectrom. Rev.* **2001**, *20*, 347.

76 J. P. Perdew *Phys. Rev. B* **1986**, *33*, 8822.

77 J. P. Perdew in *Electronic structure of solids '91*, P. Ziesche, H. Eschrig, Eds.; Akademie Verlag, Berlin, 1991; J. P. Perdew, Y. Wang *Phys. Rev. B* **1992**, *45*, 13244; J. P. Perdew, J. A. Chevary, S. H. Vosko, K. A. Jackson, M. R. Pederson, D. J. Singh, C. Fiolhais *Phys. Rev. B* **1992**, *46*, 6671; J. P. Perdew, J. A. Chevary, S. H. Vosko, K. A. Jackson, M. R. Pederson, D. J. Singh, C. Fiolhais *Phys. Rev. B* **1993**, *49*, 4978(E).

78 J. P. Perdew, K. Burke, M. Ernzerhof *Phys. Rev. Lett.* **1996**, *77*, 3865; J. P. Perdew, K. Burke, M. Ernzerhof *Phys. Rev. Lett.* **1997**, *78*, 1396(E).

79 Y. Zhang, W. Yang *Phys. Rev. Lett.* **1998**, *80*, 890.

80 B. Hammer, L. B. Hansen, J. K. Nørkov *Phys. Rev. B* **1999**, *59*, 7413.

81 N. C. Handy, A. J. Cohen *Mol. Phys.* **2001**, *99*, 403.

82 S. H. Vosko, L. Wilk, M. Nusair *Can. J. Phys.* **1980**, *58*, 1200.

83 A. D. Becke *J. Chem. Phys.* **1988**, *88*, 1053; A. D. Becke, M. R. Roussel *Phys. Rev. A* **1989**, *39*, 3761.

84 M. Filatov, W. Thiel *Mol. Phys.* **1997**, *91*, 847.

85 F. A. Hamprecht, A. J. Cohen, D. J. Tozer, N. C. Handy *J. Chem. Phys.* **1998**, *109*, 6264.

86 T. Tsuneda, T. Suzumura, K. Hirao *J. Chem. Phys.* **1999**, *110*, 10664.

87 A. D. Boese, N. L. Doltsinis, N. C. Handy, M. Sprik *J. Chem. Phys.* **2000**, *112*, 1670.

88 A. D. Boese, N. C. Handy *J. Chem. Phys.* **2001**, *114*, 5497.

89 E. I. Proynov, S. Sirois, D. R. Salahub *Int. J. Quantum Chem.* **1997**, *64*, 427.

90 T. van Voorhis, G. E. Scuseria *J. Chem. Phys.* **1998**, *109*, 400.

91 J. B. Krieger, J. Chen, G. J. Iafrate, A. Savin in *Electron correlation and material properties*, A. Gonis, N. Kioussis, Eds.; Plenum, New York, 1999.

92 J. P. Perdew, S. Kurth, A. Zupan, P. Blaha *Phys. Rev. Lett.* **1999**, *82*, 2544; J. P. Perdew, S. Kurth, A. Zupan, P. Blaha *Phys. Rev. Lett.* **1999**, *82*, 5179(E).

93 E. Proynov, H. Chermette, D. R. Salahub *J. Chem. Phys.* **2000**, *113*, 10013.

94 J. Tao, J. P. Perdew, V. N. Staroverov, G. E. Scuseria *Phys. Rev. Lett.* **2003**, *91*, 146401; V. N. Staroverov, G. E. Scuseria, J. Tao, J. P. Perdew *J. Chem. Phys.* **2003**, *119*, 12129.

95 R. H. Hertwig, W. Koch *Chem. Phys. Lett.* **1997**, *268*, 345.

96 P. E. M. Siegbahn, M. R. A. Blomberg *J. Am. Chem. Soc.* **1992**, *114*, 10548.

97 C. H. Jun *Chem. Soc. Rev.* **2004**, *33*, 610.

98 J. Cizek *J. Chem. Phys.* **1966**, *45*, 4256.

99 H. J. Aa. Jensen, T. Saue, L. Visscher, *DIRAC, Release 4.0*, Syddansk Universitet, Odense, Denmark, 2004.

100 S. S. Yi, E. L. Reichert, M. C. Holthausen, W. Koch, J. C. Weisshaar *Chem. Eur. J.* **2000**, *6*.

101 S. H. Robertson, D. M. Wardlaw, D. M. Hirst *J. Chem. Phys.* **1993**, *99*, 7748.

102 M. Pesa, M. J. Pilling, S. H. Robertson *J. Phys. Chem. A* **1998**, *102*, 8526.

103 F. Lorant, F. Behar, W. A. Goddard III, Y. Tang *J. Phys. Chem. A* **2001**, *105*, 7896.

104 B. E. Smart in *The Chemistry of Functional Groups, Supplement D*, S. Patai, Z. Rappoport, Eds.; Wiley, New York, 1983, pp 603.

105 J. L. Kiplinger, Th. G. Richmond, C. E. Osterberg *Chem. Rev.* **1994**, *94*, 373.

106 J. Burdeniuc, B. Jedlicka, R. H. Crabtree *Chem. Ber.* **1997**, *130*, 145.

107 V. P. W. Böhm, C. W. K. Gstöttmayr, Th. Weskamp, W. A. Herrmann *Angew. Chem. Int. Ed.* **2001**, *40*, 3387.

108 H. M. Senn, T. Ziegler *Organometallics* **2004**, *23*, 2980.

109 F. M. Bickelhaupt, T. Ziegler, P. v. Ragué Schleyer *Organometallics* **1995**, *14*, 2288.

110 K. Albert, Ph. Gisdakis, N. Rösch *Organometallics* **1998**, *17*, 1608; A. Sundermann, O. Uzan, J. M. L. Martin *Chem. Eur. J.* **2001**, *7*, 1703; M. Reinhold, J. E. McGrady, R. N. Perutz *J. Am. Chem. Soc.* **2004**, *126*, 5268.

111 A. J. Cohen, N. C. Handy *Mol. Phys.* **2001**, *99*, 607.

112 X. Xu, W. A. Goddard III *Proc. Natl. Acad. Sci. USA* **2004**, *101*, 2673.

113 NIST Computational Chemistry Comparison and Benchmark Database, NIST Standard Reference Database Number 101, Release 11, May 2005, R. D. Johnson III, Ed.; http://srdata.nist.gov/cccbdb.

114 J. J. Wiener, P. Politzer *J. Mol. Struct. (Theochem)* **1998**, *427*, 171.

115 A. C. Frisch, M. Beller *Angew. Chem.* **2005**, *117*, 680.

116 G. Th. de Jong, F. M. Bickelhaupt *J. Chem. Theory Comput.* **2006**, *2*, 322.

117 J. P. Collman, L. S. Hegedus, J. R. Norton, R. G. Finke *Principles and Applications of Organotransition Metal Chemistry*, University Science Books, Mill Valley, California, 1987.

118 Ch. A. Elschenbroich, A. Salzer *Organometallics: A Concise Introduction*, VCH, Weinheim, 1992.

119 V.V. Grushin, H. Alper *Chem. Rev.* **1994**, *94*, 1047; C. Amatore, A. Jutand *Acc. Chem. Res.* **2000**, *33*, 314.

120 T.-Y. Luh, M.-k. Leung, K.T. Wong *Chem. Rev.* **2000**, *100*, 3187.

121 D. Ritter, J. C. Weisshaar *J. Am. Chem. Soc.* **1990**, *112*, 6425; A.L. Casado, P. Espinet *Organometallics* **1998**, *17*, 954; R. Stürmer *Angew. Chem.* **1999**, *111*, 3509; R. Z. Hinrichs, J. J. Schroden, H. F. Davis *J. Am. Chem. Soc.* **2003**, *125*, 860; B. C. de Pater, E. J. Zijp, H.-W. Frühauf, J. M. Ernsting, C. J. Elsevier, K. Vrieze *Organometallics* **2004**, *23*, 269; P. Espinet, A. Echavarren *Angew. Chem.* **2004**, *116*, 4808; G. Wang, M. Chen, M. Zhou *Chem. Phys. Lett.* **2005**, *412*, 46; M. Lersch, M. Tilset *Chem. Rev.* **2005**, *105*, 2471.

122 M. Porembski, J. C. Weisshaar *J. Phys. Chem. A* **2000**, *104*, 1524; A. Haynes, P. M. Maitlis, G. E. Morris, G. J. Sunley, H. Adams, P. W. Badger, C. M. Bowers, D. B. Cook, P. I. P. Elliott, T. Ghaffar, H. Green, T. R. Griffin, M. Payne, J. M. Pearson, M. J. Taylor, P. W. Vickers, R. J. Watt *J. Am. Chem. Soc.* **2004**, *126*, 2847.

123 T. R. Griffin, D. B. Cook, A. Haynes, J. M. Pearson, D. Monti, G. E. Morris *J. Am. Chem. Soc.* **1996**, *118*, 3029; P. E. M. Siegbahn *J. Am. Chem. Soc.* **1996**, *118*, 1487; Q. Cui, D. G. Musaev, K. Morokuma *J. Chem. Phys.* **1998**, *108*, 8418; L.J. Gooßen, D. Koley, H. Hermann, W. Thiel *Chem. Commun.* **2004**, 2141; S. Kozuch, S. Shaik, A. Jutand, C. Amatore *Chem. Eur. J.* **2004**, *10*, 3072.

124 J. March *Advanced Organic Chemistry*, McGraw-Hill, Tokyo, 1977.

125 K. C. Nicolaou, P. G. Bulger, D. Sarlah *Angew. Chem.* **2005**, *117*, 4516.

126 P. Knochel, J.J. Almena Perea, P. Jones *Tetrahedron* **1998**, *54*, 8275.

127 K. P. C. Vollhardt, N. E. Schore *Organic Chemistry*, W. H. Freeman and Company, New York, 1994.

128 P. S. Skell, J. E. Girard *J. Am. Chem. Soc.* **1972**, *94*, 5518; A. W. Ehlers, G. P. M. van Klink, M. J. van Eis, F. Bickelhaupt, P. H. J. Nederkoorn, K. Lammertsma *J. Mol. Model.* **2000**, *6*, 186.

129 V.V. Grushin *Chem. Rev.* **1996**, *96*, 2011.

130 C. Amatore, A. Jutand, G. Meyer, I. Carelli, I. Chiarotto *Eur. J. Inorg. Chem.* **2000**, 1855.

131 J. A. M. Beek, G. van Koten, W. J. J. Smeets, A. L. Spek *J. Am. Chem. Soc.* **1986**, *108*, 5010; G. van Koten *Pure Appl. Chem.* **1990**, *62*, 1155; F. M. Bickelhaupt, E. J. Baerends, W. Ravenek *Inorg. Chem.* **1990**, *29*, 350.

132 F. M. Bickelhaupt, E. J. Baerends in *Reviews in Computational Chemistry*, Kenny B. Lipkowitz, Donald B. Boyd, Eds.; VCH Publishers Inc., New York, 2000, Vol. 15, pp 1.

133 E. J. Baerends *et al.*, *ADF2005.01*, SCM, Theoretical Chemistry, Vrije Universiteit, Amsterdam, The Netherlands, 2005.

134 K. Dyall *Theor. Chem. Acc.* **2002**, *108*, 335.

135 L. Visscher, K. Dyall *J. Chem. Phys.* **1996**, *104*, 9040; L. Visscher, J. Styszyñski, W. C. Nieuwpoort *J. Chem. Phys.* **1996**, *105*, 1987.

136 NIST Standard Reference Database Number 69, June 2005 Release, Eds. P. J. Linstrom and W. G. Mallard; http://webbook.nist.gov/chemistry.

137 A. Kovács, C. Esterhuysen, G. Frenking *Chem. Eur. J.* **2005**, *11*, 1813.

138 C. C. Pye, T. Ziegler *Theor. Chem. Acc.* **1999**, *101*, 396.

139 R. S. Bon, B. van Vliet, N. E. Sprenkels, R. F. Schmitz, F. J. J. de Kanter, Chr. V. Stevens, M. Swart, F. M. Bickelhaupt, M. B. Groen, R. V. A. Orru *J. Org. Chem.* **2005**, *70*, 3542.

140 N. L. Allinger, X. Zhou, J. Bergsma *J. Mol. Struct. (Theochem)* **1994**, *312*, 69.

141 P. T. van Duijnen, F. C. Grozema, M. Swart *J. Mol. Struct. (Theochem)* **1999**, *464*, 191.

142 F. M. Bickelhaupt, E. J. Baerends, N. M. M. Nibbering *Chem. Eur. J.* **1996**, *2*, 196.

143 G. Th. de Jong, F. M. Bickelhaupt *J. Chem. Theory Comput.* **2007**, *3*, in press.

144 L. Deng, V. Branchadell, T. Ziegler *J. Am. Chem. Soc.* **1994**, *116*, 10645.

145 M. Born *Z. Phys.* **1920**, *1*, 45; P. W. Atkins *Physical Chemistry*, Oxford University Press, Oxford, 1994.

146 L. Deng, T. Ziegler, L. Fan *J. Chem. Phys.* **1993**, *99*, 3823.

147 G. S. Hammond *J. Am. Chem. Soc.* **1955**, *77*, 334.